Photochemical and Electrochemical Switching of Overcrowded Alkenes

Brian Pieter Corbet

rijksuniversiteit
groningen

The work described in this thesis was carried out at the Stratingh Institute for Chemistry, University of Groningen, The Netherlands

This work was financially supported by the European Research Council

Print: Ipskamp Printing

Cover: The cover colour is taken from the apparent colour of a solution of oxidised bisthioxanthylidene (Chapter 3, compound $\mathbf{6}^{2+}$) in acetonitrile.

rijksuniversiteit groningen

Photochemical and Electrochemical Switching of Overcrowded Alkenes

Proefschrift

ter verkrijging van de graad van doctor aan de
Rijksuniversiteit Groningen
op gezag van de
rector magnificus prof. dr. C. Wijmenga
en volgens besluit van het College voor Promoties.

De openbare verdediging zal plaatsvinden op

maandag 13 december 2021 om 14.30 uur

door

Brian Pieter Corbet

geboren op 5 februari 1993
te Hoogeveen, Nederland

Promotor
Prof. dr. B. L. Feringa

Copromotor
Dr. S. J. Wezenberg

Beoordelingscommissie
Prof. dr. R. J. M. Nolte
Prof. dr. ir. A. J. Minnaard
Prof. dr. N. H. Katsonis

Table of Contents

Chapter 1

Introduction: Chiroptical Molecular Switches and Motors

Acknowledgement
This chapter was written jointly with Dr. Anouk S. Lubbe (Section 4) and Dr. Stefano Crespi (general contributions). I would like to thank both co-authors for their collaboration and their input and discussion on other parts of this chapter.

Parts of this chapter are published as: Brian P. Corbet, Anouk S. Lubbe, Stefano Crespi and Ben L. Feringa, *Chiroptical Molecular Switches and Motors* in *Molecular Photoswitches: Synthesis, Properties, and Applications,* Z. L. Pianowski (Ed.), 2021, Wiley-VCH, Weinheim, DE, *in press*.

1. Introduction

Photoswitches are molecules that are able to undergo a reversible transformation between different isomeric forms upon light absorption.[1] The photoisomerisation of azo, imine or alkene double bonds is one of the most widely used reactions in photoswitches. The application of light as the external trigger promoting the photochemical isomerisation has several distinct advantages. Light stands out as a quintessential stimulus, which can be precisely tuned in space, time, intensity, wavelength and polarisation. Furthermore, the photon is the ideal traceless reagent that does not add or remove any mass from a closed system.[2]

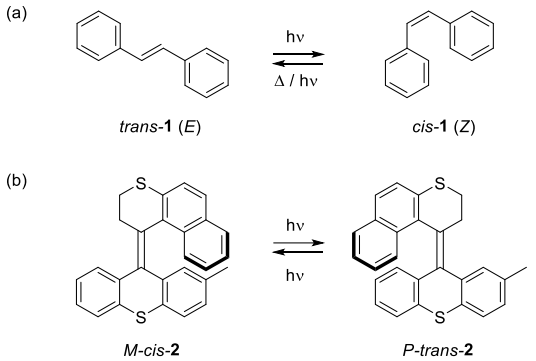

Scheme 1. a) Stilbene photoswitch, b) Overcrowded alkene based chiroptical molecular switch.

In alkene-based photoswitches (Scheme 1), the fixed geometry at the two sp^2 centres gives rise to two configurations indicated *E* and *Z* (*Entgegen/Zusammen)* or *trans* and *cis*. Irradiation of the photoswitch leads to a π→π*-transition, promoting an electron from a π-bonding to a π*-antibonding orbital. In this excited state, the increased single bond character allows isomerisation between the two stereoisomers by rotation around its C=C axis. Switching in the reverse direction can be achieved via another photochemical isomerisation. With sufficient irradiation, the system reaches an equilibrium between the photochemical forward and backward reactions, i.e. the photostationary state (PSS). At a given wavelength, the equilibrium ratio depends on the respective absorptivity of the isomers involved and the quantum yields of the forward and backward photochemical steps.

For some photoswitches, such as stilbene **1** in Scheme 1a, a thermal *E/Z*-isomerisation is also possible, where the higher energy *Z*-stilbene can interconvert into the lower energy *E* isomer.[3] Furthermore, *Z*-stilbene can undergo a photocyclisation[4,5] which will not be discussed further in this

chapter. Stilbene represents the archetype of a class of widely studied alkene photoswitches[4,6] and many of the structures discussed in this chapter have a stilbene-like photoswitching motif. Other fascinating switches sharing a similar mode of action have been developed, such as the imine-based motors by Lehn and co-workers[7] or the hemithioindigo motors by the group of Dube.[8] This chapter will focus on alkene-based chiroptical switches and molecular rotary motors. For an extensive discussion of other classes of photoswitches, the reader is referred to additional books and reviews.[1,4,6,9-14]

Chiroptical switches (e.g. *M-cis*-**2** in Scheme 1b) are overcrowded alkene-based chiral molecules with an intrinsic stilbene-type chromophore, that can be isomerised from one stereoisomer to another (*P-trans*-**2** in Scheme 1b). These switches typically change helicity while preserving chiral information within the operating conditions, without racemisation even after performing multiple switching cycles. This makes fatigue-resistance a prerequisite for this class of molecules.[1] This class owes its name to the possibility to study them with chiroptical techniques, i.e. involving anisotropic radiation.[15] The photochemical control of chiral information provides unique opportunities towards application of these molecules in many fields where chirality is of utmost importance.[16–18]

2. From helical overcrowded alkenes to unidirectional rotary molecular motors

The first light-driven rotary molecular motor was reported in 1999 by Feringa and co-workers.[19] Since then, molecular motors[20–22] have been extensively studied and further developed, making them a versatile class of nanoscale machines.[9–12] In this section, we will first briefly discuss the relevant chiroptical molecular switches from which the motors have evolved, and continue with the research towards overcrowded alkene-based molecular rotary motors. Figure 1 provides a timeline with an overview of alkene-based chiroptical switches (**3** and **4**) and molecular rotary motors (**5** – **7**).

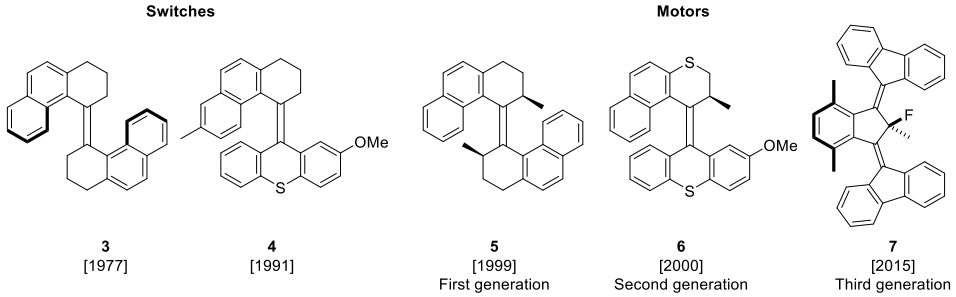

Figure 1. Timeline with illustrative examples of molecular switches towards first, second, and third generation molecular motors.[19,23–26]

Unidirectional rotary molecular motors are generally classified by their generation, based on the number of stereogenic centres present in the molecule. The first generation (Figure 1, compound **5**) is C_2-symmetric over the central alkene bond and has two stereogenic centres, one in each half. The second generation motor **6** has only one stereogenic centre in its rotor half. Finally, the third generation molecular motor **7** is a meso-compound, with a pseudo-asymmetric centre that drives its unidirectionality.

2.1 Chiroptical molecular switches

In 1977 Feringa and Wynberg reported an inherently chiral overcrowded alkene (Figure 1, Scheme 2, compound **3**).[23,27] The steric hindrance between the naphthalene- and the cyclohexane units causes the molecule to adopt a helical conformation in both the *cis*- and *trans* configurations. This feature leads to torsion around the central C=C axle. Four isomers (*P,P*)-*E*, (*M,M*)-*E*, (*P,P*)-*Z*, (*M,M*)-*Z* (Scheme 2) were isolated by chiral HPLC and analysed by UV-vis and CD spectroscopy, as well as X-ray crystallography.[28] A crucial discovery was the room temperature racemisation of the (*M,M*)-*Z* isomer. CD and NMR spectroscopy and additional theoretical analysis[29,30] revealed the purely thermal nature of the process, which inverts the helicity of *Z*-**3** with a barrier of $\Delta G^{\ddagger}$ = 90 kJ mol^{-1} (Scheme 2). No thermal *E*/*Z*-isomerisation or radical processes are involved in this racemisation mechanism. In a similar way, the *E*-isomer racemised at elevated temperatures with a barrier of $\Delta G^{\ddagger}$ = 105 kJ mol^{-1}.[30] This thermal helix inversion (THI) is a fundamental step inherent to this type of chiroptical switch and its rationalisation is a milestone for the development of unidirectional rotation in molecular motors.

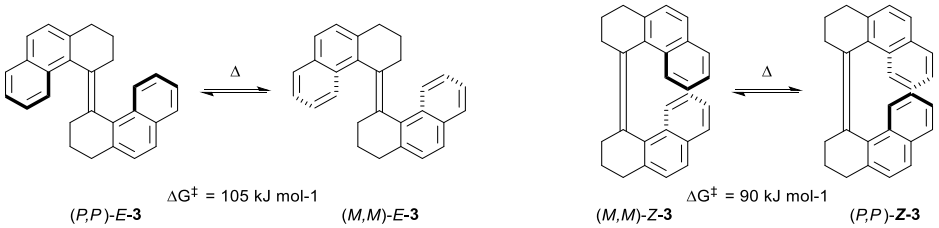

Scheme 2. Stereoisomers of chiroptical switch **3** and their thermal helix inversions.

A different class of chiroptical switches has a non-symmetric structure with respect to the central overcrowded alkene motif (Figure 2a). These switches are characterised by a relatively high barrier for helix inversions, which means that isolated enantiomers do not racemise under ambient conditions. On the other hand, the helicity of the initial state can be inverted by photochemical *E*/*Z*-isomerisation. This process can be readily followed by optical rotatory dispersion (ORD) and circular dichroism (CD) (Figure 2b), as the pseudo-enantiomers *cis-P*-**8** and *trans-M*-**8** possess an inherent dissymmetric helical chromophore and show strong and approximately mirror-image CD spectra.

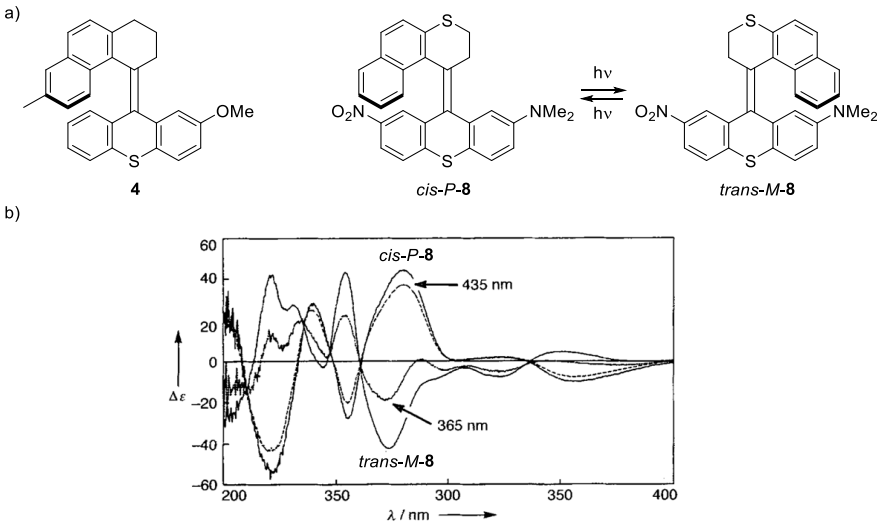

Figure 2. a) Non-symmetrical chiroptical switches and b) CD spectra of *cis-P*-**8**, *trans-M*-**8** and the PSS mixtures obtained by their irradiation with 365 and 435 nm light, respectively.[24,31,32] Figure adapted with permission from Ref 32, Copyright John Wiley and Sons.

By irradiating with different wavelengths of light, different PSS mixtures can be obtained in an altered ratio of pseudo-enantiomers.[24] For compound **4** (Figure 2a), irradiation of the *M-cis* isomer with 300 nm led to a PSS of 64:35 (*M-cis*:*P-trans*) and subsequent irradiation of this mixture with 250 nm light modified the PSS to 68:32.[33] By installing a dimethylamino and a nitro

substituent in **8**, a donor/acceptor system was introduced, which red-shifted the operational irradiation wavelengths to 365 and 435 nm.[32] Protonation of the amine functionality stopped the photoswitching in both directions forming a proton-gated chiroptical photoswitch that could be read out by fluorescence or ORD spectroscopy.[34]

2.2 First and second generation molecular motors

The addition of methyl groups to both cyclohexane rings of **3** introduced stereogenic centres to determine the absolute configuration of the molecule, which led to the synthesis of the overcrowded alkene **5** (Figure 3).[35] The additional methyl groups imposed a further element of asymmetry to the system, also providing improved PSS ratios for the photochemical *E*/*Z*-isomerisations and directional thermal helix inversions. By demonstrating the individual steps in the isomerisation sequence, **5** was identified as the first artificial molecule to perform photochemical-driven unidirectional rotary motion.[19]

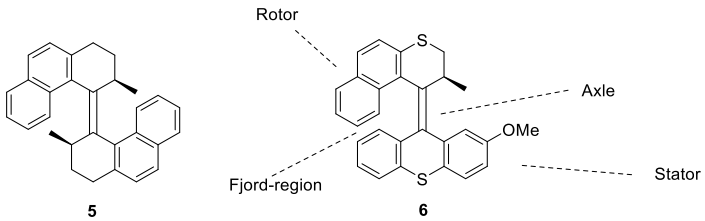

Figure 3. First and second generation molecular motors.[19,36]

First generation molecular motors are C_2-symmetrical across the central axis of rotation and both halves contain a stereogenic centre. Their symmetry provides relatively straightforward synthetic options, such as reductive dimerisation of ketones by McMurry coupling[37] to obtain the central overcrowded alkene. Forging the sterically congested, tetra-substituted double bond is often the crucial step in the synthesis of many switches and motors described in this chapter.[38]

Second generation molecular rotary motors are non-symmetrical over the central double bond axis and are similar to the previously described unsymmetrical chiroptical switches, with an additional stereogenic centre at the allylic position.[26] These structures (**6**, Figure 3) have only one stereogenic centre in their *rotor* (or upper) half, while the lower half – the *stator* – typically consists of a fluorenyl or tricyclic motif.[36] The stereogenic carbon in the *rotor* governs the unidirectional rotation with respect to the *stator* around the *axle* of rotation. The sterically congested space between the aromatic parts of the *rotor* and the *stator* is called the *fjord-region*.

The Barton-Kellogg reaction is commonly used to form the unsymmetrical overcrowded alkene motif of the second generation motors. A thioketone and a diazo compound react in a 1,3-dipolar cycloaddition followed by nitrogen evolution. The obtained thiirane is subsequently desulfurised to provide the overcrowded non-symmetrical alkenes.[36,39]

For both first and second generation molecular motors, the combination of helical chirality and point chirality due to the aforementioned stereogenic elements allows access to multiple diastereomers.

2.3 Fundamental rotational steps

First and second generation overcrowded alkene-based molecular motors undergo rotation, populating four distinct isomers sequentially, as illustrated in Schemes 3 and 4,[20,36,40,41] via a combination of photochemical and thermal reactions.[9,22,42]

Rotary molecular motor **9** (Scheme 3) is C_2-symmetrical over the central double bond axis and contains two naphthalene units, which introduce helical chirality and two stereogenic methyl substituents that determine the directionality of rotation. These stereogenic elements are the cause for the diastereomers and their distinct energies involved in this rotational cycle.[9,22,42]

Following the rotational direction, the fundamental steps involved are as follows. The energetically lowest stereoisomer *(P,P)-trans*-**9**, known as the *stable trans* isomer, undergoes photochemical *E*/*Z*-isomerisation (step 1) to the *metastable cis* isomer upon irradiation with the appropriate wavelength of light. This new configuration is energetically less favourable because of increased steric hindrance. Note that the stereogenic methyl substituents are now in a pseudo-equatorial position. From the metastable isomer, THI occurs, inverting the helicity of the molecule leading to a *stable cis* isomer (step 2). The THI step is discussed in further detail in Section 3.1.

After this 180° rotation, the *stable cis* isomer undergoes another photochemical *E*/*Z*-isomerisation (step 3) to obtain the *metastable trans* isomer. A THI step again inverts the helicity (step 4), completing the 360° unidirectional rotation. The rates for the two THI steps are significantly different for first generation molecular motors, as the metastable isomers experience a notably different steric hindrance (as an example, for motor **9** $t_{1/2}$ = 45 min and 22 d for step 2 and 4 at 293.15 K, respectively).[20,21,41]

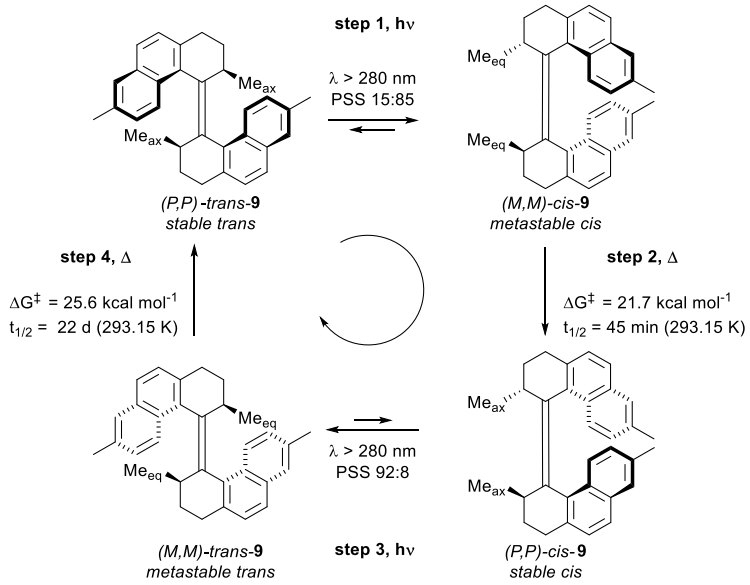

Scheme 3. Rotation cycle for first generation molecular motor **9**.[43]

For second generation molecular rotary motors the fundamental steps of photochemical isomerisation are comparable to the ones observed for the first generation, as illustrated in Scheme 4. Upon irradiation at the appropriate wavelength, the energetically most stable isomer *trans-M*-**6** (*stable trans*), undergoes a photochemical *E*/*Z*-isomerisation of the central double bond to form *cis-P*-**6** (step 1). In this step, the naphthalene motif of the rotor (for rotor, axle, stator nomenclature, see section 2.2) remains on the same side with respect to the stator (i.e. above the plane of the paper). The photoisomerisation leads to an inversion of helicity (*M*- to *P*-helicity*)* and a pseudo-equatorial orientation of the stereogenic methyl group. This metastable state is energetically unfavoured because of increased steric repulsion between both halves, raising the ground state energy level.[44,45]

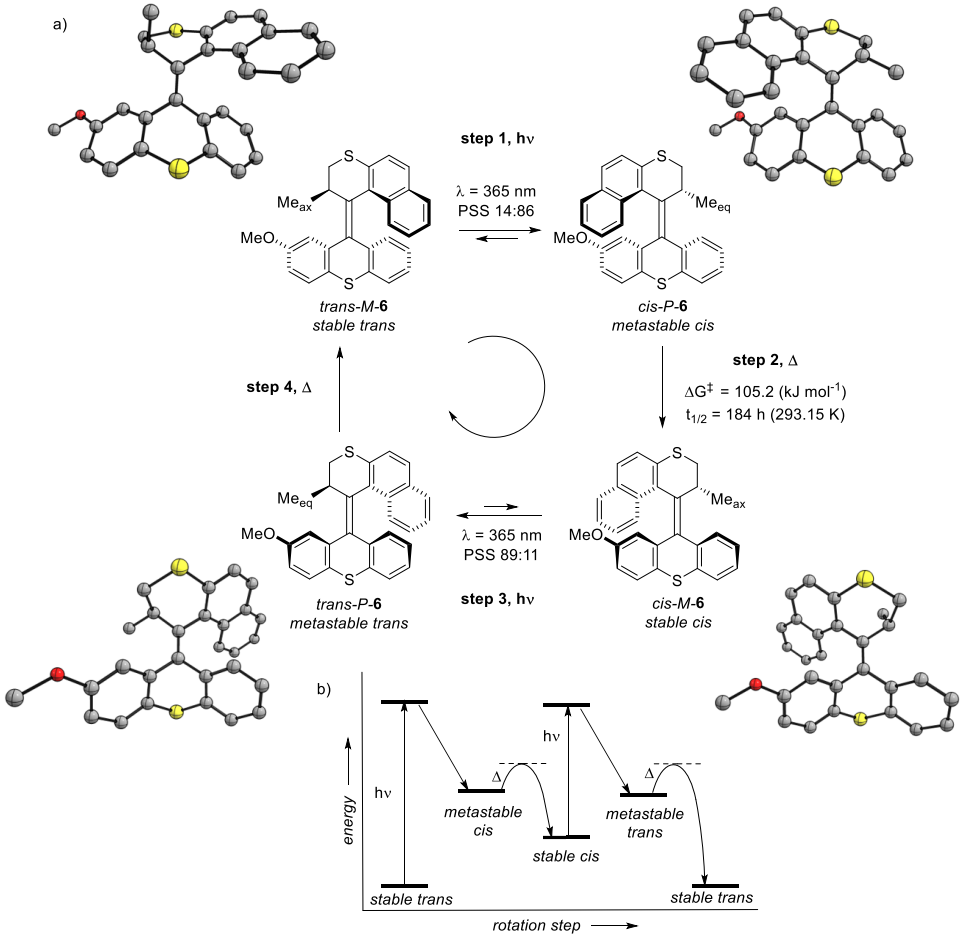

Scheme 4. a) Rotation cycle for second generation molecular motor **6** including 3D representations. b) Corresponding energy diagram.[36,41]

From the metastable state, a THI occurs (step 2) to a more favoured orientation, nearly identical to the initial geometry, but distinguishable by the relative *cis*-orientation of the rotor with respect to the methoxy substituent that desymmetrises the stator. A repetition of the same sequence of photochemical *E*/*Z*-isomerisation (step 3) and thermal helix inversion (step 4) completes the full 360° cycle, returning to the original state. As the extent of steric hindrance in both metastable states and both stable states is nearly identical, the energetic landscape for THI and the respective barriers in step 2 and 4 are practically the same.

Overall, the 360° rotation of molecular motors is non-reciprocal motion, hence the molecule has performed work. The complex combination of conformational and configurational changes of the intermediates influences

the dynamics of the individual steps. The relative energies of each "station" of the motor relate to the rigidity and steric hindrance of rotor and stator halves. There are general trends and rules for the dynamics of molecular motors, which are not ubiquitous. This will be discussed in further detail in section 3.1. The full mechanistic details of all known variations of molecular rotary motors are intricate and not always fully unraveled.[45] However, the thorough study on the motion of various molecular motors allows an increasingly more precise picture of each step of their cycle,[46] which will be discussed further in section 3 of this chapter.

2.4 Third generation rotary molecular motors

The previously mentioned motors have an element of point chirality as a characteristic feature controlling unidirectional rotation. A further challenge was to demonstrate the possibility of directional rotary motion in achiral systems. With one stereocentre with point chirality fewer than the second generation molecular motors, the third generation molecular motors achieve this goal. These meso-compounds differ from previous motor generations by having one central stator core, two axles and two rotors (Figure 4).

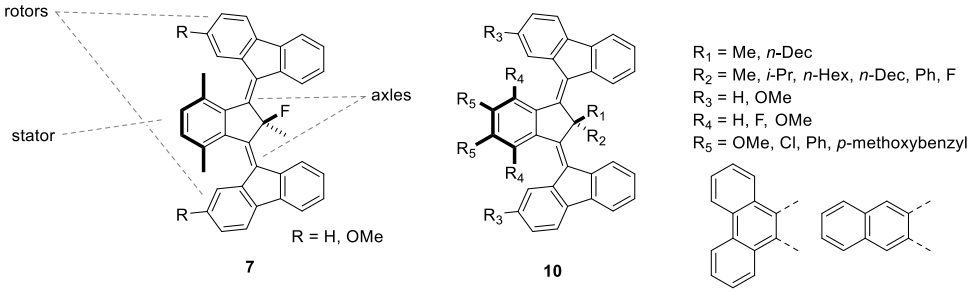

Figure 4. Third generation molecular motors.[25,47,48]

In 2015 Feringa and co-workers showed that the use of a pseudo-asymmetric carbon atom was sufficient for directional rotary motion around two axles.[25] Using a central stator with a pseudo-asymmetric centre and two identical fluorenyl rotors (Figure 4, compound **7**), it was demonstrated that a directional disrotatory motion occurs upon irradiation. Both stators are influenced by a different face of the pseudo-asymmetric centre which provides a bias for the direction of *E*/*Z*-photoisomerisation. This preference originates from the size difference in the doubly allylic position (e.g. motor **10**, R_1 and R_2), where the larger substituent takes a "pseudo-axial" orientation. The presence of this pseudo-asymmetric centre is essential for the occurrence of any directionality.[47] Unidirectionality was proven using desymmetrised rotor motifs by the introduction of a methoxy group (R in

motor **7**, R_3 in motor **10**) and analysis of the products of each step of the photochemical and thermal isomerisations.[25,47]

The size of the core unit (Figure 4, compound **10**, R_4) is the main factor influencing the speed of rotation for these motors. A smaller core unit leads to lower barriers for thermal helix inversion.[47] By modification of the bridgehead groups (Figure 4, compound **10**, R_1 and R_2) the direction of rotation could be precisely controlled. Interestingly, a reversal of directionality occurs when R_1 = Me, R_2 = *i*-Pr are substituted with R_1 = H, R_2 = F.[47] The distal side of the core unit (R_5) can be modified in a modular synthesis route.[48] These modifications can increase the solubility and red-shift the absorption wavelength. Importantly, distal functionalisation provides opportunities for further functionalisation and future application in molecular cargo transport.

3. Dynamics and kinetics of molecular motors

3.1 Thermal isomerisation

For molecular motors in general, the extent of unidirectionality depends on a combination of all steps in the rotary cycle, but can be fully dominated by the directionality of a single step. In practically all of the overcrowded alkene-based molecular motors, such as the motors developed by Feringa and co-workers, the energetic difference of the metastable- and stable states of the THI step drives the unidirectionality of the motors. For fully photochemically driven molecular motors, such as motors introduced in sections 3.5 and 3.6, the quantum yields of individual forward and backward photoisomerisation steps are crucial for unidirectionality.

For some structures, a step in the opposite rotational direction such as a thermal *E*/*Z*-isomerisation can readily occur.[49] Usually, for molecular motors, as for structurally similar stilbenes, the barrier for thermal *E*/*Z*-isomerisation is high (commonly exceeding 150 kJ mol^{-1}).[50] Some molecular motors have a more favourable thermal *E*/*Z*-isomerisation than THI, albeit only when barriers for THI are notably high.[50] This distinct thermal behaviour is undesired for unidirectional rotation.

There are good indications that the extent of accommodation of folding in the rings adjacent to the central double bond is a crucial factor in the energetic profiles of THI, where more flexibility with respect to folding leads to a more facile slipping of the rotor over the stator.[45] A striking example is represented by the mechanistic pathways for thermal helix inversion for second generation molecular motors, which involve a ring flip of the rotor

followed by a slipping of the rotor over the stator and a ring flip of the stator. The structure of the molecular motor determines the stability of the intermediates and transition states and can therefore influence the most likely pathway for THI as well as the speed of the overall process.[45]

An additional factor to be taken into consideration is the nature of the solvent. Many solvent parameters were investigated to probe the influence of the medium on the kinetics of molecular motors.[51] Most molecular motors are apolar and do not interact strongly with the solvent. THI rates are reduced in the presence of hydrogen bonding or π-π interactions between the motor and the solvent. The main kinetic effect of the medium was found to stem from the rearrangement of the solvent shell. Indeed, viscosity has a strong influence on the rate of THI.[51] A study of first generation molecular motors with varying lengths of rigid "stirrer" substituents further shows the strong viscosity dependence. This effect increases with higher solvent displacement caused by longer substituents.[52]

3.2 Tuning the speed of rotation

Understanding the factors that regulate the speed of rotation of molecular motors is crucial to apply or study these molecules. The speed of each individual step composing the rotational cycle determines the overall rate on a molecular level. Additionally, for an ensemble of molecules, the speed is influenced by the input of energy. As both thermal and photochemical steps are involved, external factors such as the temperature, photon flux and absorption have the potential to be the determining factor to the overall speed.

For an individual molecule of a molecular motor, the THI is by far the slowest step. For an ensemble of molecular motors, there are two rate-limiting regimes. Motors with a high barrier for THI they are *thermally rate limited*, meaning the speed of rotation, or frequency of rotational events, is mostly governed by the temperature.[44]

For motors with a low energetic barrier for THI, the rotation process can become *photochemically rate limited* at common experimental conditions. At these conditions the quantum yield for isomerisation and absorptivity of the motor become more influential to the overall rotational frequency. The strongest influence in this regime becomes the light intensity of the irradiation source and it is expected that under common experimental conditions (irradiation intensity of 20 W cm^{-2}), a speed of up to $\sim 10^2$ Hz is achievable.[44] Solution-based molecular motors have been reported with a

THI speed in orders of magnitude ranging from 10^{-11} to 10^{8} Hz at room temperature.[44,53]

As alkene photoisomerisation of stilbenes and motors occurs within picoseconds after photon absorption (for a more detailed discussion see section 3.3),[54] the rate-limiting step on a molecular level is the thermal helix inversion (a detailed overview on THI is presented in Schemes 3 and 4, section 2.3 and additional discussion of this step can be found in section 3.1). For example, for motor **6** (Figure 5), discussed earlier in section 2.3, Eyring analysis by means of ^{1}H NMR spectroscopy provided a THI activation barrier of 105.2 kJ mol^{-1}.[41] Being characterised by first order kinetics, this barrier corresponds to a half-life of 7.6 d at 293.15 K (or a frequency of 1.51 μHz). The THI is, consequently, the rate-limiting step of the rotational cycle of the motor. Hence it is used as the descriptor of the motor speed in terms of activation energy, half-life or frequency. For a clear comparison of the rotary speed, in this section the half-life at 293.15 K is used.

In first generation molecular motors the two THI steps differ greatly in the *cis*- and *trans*- isomers (section 2.3, Scheme 3). As a result of this asymmetry, structural modifications on first generation molecular motors have an independent influence on both THI steps, where an increase in speed in one THI step can lead to a decrease in speed for the other THI step.[55,56]

Figure 5 illustrates a non-exhaustive selection of second generation molecular motors, highlighting trends generally observed in the speeds of THI steps. Many additional factors than the ones described in this section have been shown to influence the THI rates.[53] For example, changing the nature of the heteroatom in the rings adjacent to the central double bond[57] or introducing a donor-acceptor motif in conjugation with the double bond, changing the single bond character of the alkene group.[58] Estimating THI rates *a priori* is a non-trivial task, where careful experimental and theoretical investigations are necessary for all new motor scaffolds.

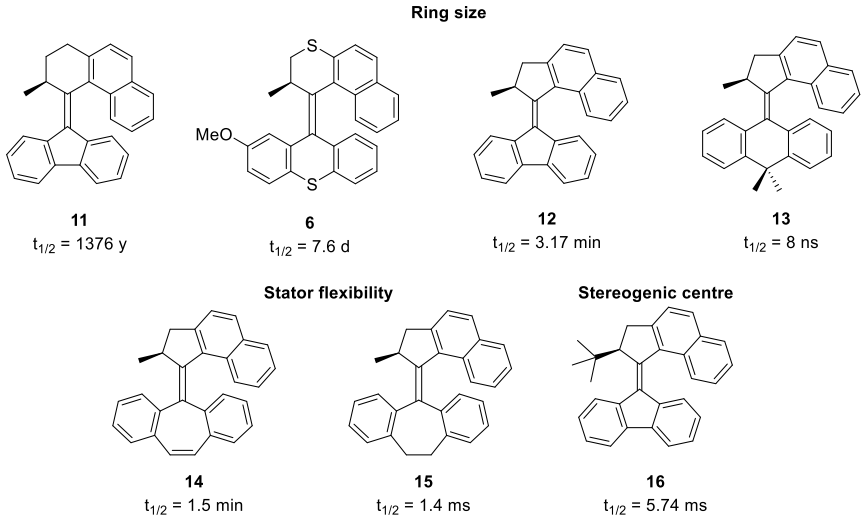

Figure 5. Selected examples of various speeds, indicated by the half-life at 293.15 K, for second generation molecular motors.[41,53,59–62]

The size and flexibility of the rings linked to the C=C axle and the size of the allylic substituent affect the THI half-lives significantly, so there is a delicate balance of steric and conformational effects. The most commonly used second generation molecular motors have 5- or 6-membered rings connected to the axle. With a 6-membered ring in the rotor and a 5-membered ring in the stator, motor **11** (Figure 5) has relatively low steric hindrance in the fjord-region. However, this motor shows a remarkable low speed for rotation with a half-life of more than a thousand years.[62] Motor **6**, containing two 6-membered rings, has a slightly higher amount of steric hindrance in the fjord region, but a much faster THI, likely caused by more facile ring folding of the stator part.[45]

When both rings adjacent to the C=C axle are 5-membered rings, such as in fluorenyl-based motor **12**, the speed is higher than the previously mentioned examples with 6-membered rotors. With 5-membered rings, conformational flexibility is lost. Consequently, the metastable states are most likely further destabilised, as steric hindrance cannot be accommodated by ring folding. With a higher energy level of the metastable state compared to the energetic barrier of THI, the speed of this step increases.[55]
The fastest overcrowded alkene-based motors reported to date, are found in motors containing a 5-membered ring in the rotor and a 6-membered ring in the stator, as illustrated in motor **13** with a half-life of only 8 ns.[53]

The significant difference in speed between the more rigid stator of **14** and the more flexible stator of **15** (half-lives of 1.5 min and 1.4 ms, respectively)

shows that ring flexibility is a major contributor to the overall speed of THI. The considerable difference in speed between *tert*-butyl functionalised motor **16** and motor **12** (half-lives of 5.74 ms and 3.17 min, respectively) is illustrative of the strong influence of the allylic stereogenic group. This speed increase is caused by the relative rise in the energy level of the metastable state.[60,63]

3.3 Photoisomerisation

The study of the excited state photochemistry of overcrowded alkene-based molecular motors represents a more significant challenge, compared to the ground state chemistry of the thermal isomerisation steps. Absorption spectroscopy allows the steady-state photochemical E/Z-isomerisation to be followed with relative ease. The irradiation of a molecular motor in its stable state leads to a more strained, red-shifted and higher energy metastable state in a unimolecular process. However, as these processes occur in a picosecond timescale,[54] ultrafast transient spectroscopy is required to record experimental data on the mechanisms during photoisomerisation.[64] Alternatively, theoretical studies have shown to be a useful tool for the understanding of the photochemical pathways.[65]

In the most commonly described situation for molecular motors (Figure 6), after absorption of a photon of the appropriate wavelength, an $S_1 \leftarrow S_0$ excitation, corresponding to a π→π* transition, occurs,[65] which leads to a reduced double bond character and elongation of the axle olefinic bond.[67] This excitation is a vertical transition starting from the stable state of the motor to a Frank-Condon (FC) state. The initial excited state is a bright, fluorescent state that is limitedly affected by solvent polarity. This finding suggests the absence of significant change in dipole moment of the molecule upon light absorption and that charge transfer is not a key driving force for this excitation.[68]

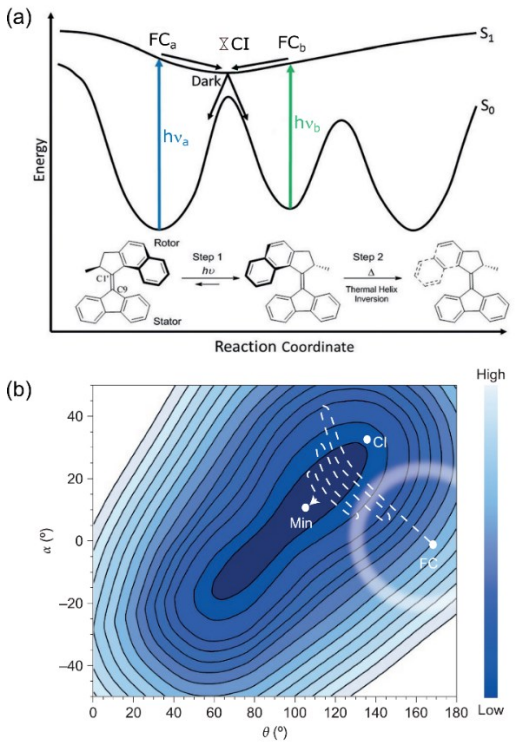

Figure 6. a) Schematic one-dimensional potential energy surface for a second generation molecular motor. Figure adapted with permission from Ref 66, Copyright John Wiley and Sons (2018). b) Schematic representation of the primary dynamics on the excited state surface along the central double bond dihedral angle (θ) and C9-pyramidalisation (α).[64] (For explanation of the terms FC, CI, Min, see text).

As it is typical in alkene photochemistry,[69] conical intersections (CI) play a central role in the photoisomerisation mechanism of molecular motors.[65,70] Transient spectroscopy, supported by calculations indicates that the sloped topology of the excited state potential energy surface for molecular motors shows a preference for unidirectional rotation in the photochemical step.[71] The twisted nature of the central double bond axle, caused by the chirality of the molecular rotary motors, plays a crucial part in the motion during photorearrangement.[65,72]

In the excited state, the motor undergoes a barrierless, ultrafast relaxation towards a CI or an S_1 minimum on the order of 100 fs.[64] This process is likely a volume-conserved structural change as shown in ultrafast absorption studies revealing that this process is solvent friction independent.[68] It is confirmed that at the CI, a moderate twisting of the central olefinic axis occurs with increased pyramidalisation of the stator axle carbon atom.[73] This mechanism of photoisomerisation with pyramidalisation and twisting

is similar to other known stilbene photoisomerisation dynamics.[6,64,74] The pyramidalisation and twisting describe an inherently asymmetrical potential energy surface that leads to rotation around the axle in the excitation-relaxation step.[54]

It is interesting to notice that the region where the S_0/S_1 CIs and S_1 minimum are located, which is populated after the ultrafast relaxation from the bright FC state, is a dark state. The lack of radiative relaxation is consistent with the relatively long lifetime of the dark state.[73] The exact nature and structure of this dark state is crucial for a full understanding of the photodynamics, but remains a topic of debate.[67] An S_2 excited state, reached via excitation to S_1 and an S_1/S_2 conical intersection, has been suggested to be the dark state.[75]

A fingerprint of the excited state of first and second generation molecular rotary motors can be obtained using ultrafast spectroscopic measurements, in the form of an oscillation superimposed on the emission decay profile.[64,67,68,75–77] This oscillation is reported to be caused by coherently excited vibrational modes in the excited state.[64,76] Additionally, similar oscillations have been observed in the transient absorption spectra of both the bright and dark state.[67,78] These observed vibrations survive the structural relaxation starting from the FC to the dark state.[67,68] An alternative explanation for the oscillations is the involvement of a dark S_2 excited state and repopulation of the bright S_1 excited state.[75] Other multistate models have been proposed for the excited state dynamics of molecular motors.[71]

From the CI between the excited and ground state, there is a "dark" relaxation that involves a large structural change within the molecule, consistent with the completion of the rotation around the central double bond axis.[68] This transition to the ground state leads to a vibrationally hot ground state where the motor can continue the pathway of rotation to the metastable state.[75] This excess energy relaxes first via ultrafast intramolecular vibrational redistribution and is subsequently released to the environment.[67]

Excitation of the stable state can also result in a relaxation pathway back to the initial state via radiative or non-radiative relaxation through CI or energetically lower lying excited states. The reverse photoreaction, that is from the metastable to the stable state can occur when the metastable state is irradiated. The pathway for reverse photoisomerisation is distinct from the forward reaction and proceeds through a different CI.[66]

The overall "efficiency" of the photochemical step can be expressed with the ratio of the isomers in the photostationary state, where the rates of the

forward and reverse photoreaction are equal. The PSS is dependent on the quantum yield of either step and the absorptivity of each isomer. Consequently, the PSS is wavelength-dependent.[76] Because of the wavelength dependence of absorption and quantum yields, a favourable PSS can be obtained by selective irradiation where the stable state absorbs considerably more than the metastable state.[68] However, there often is significant overlap in absorption spectra of the stable and metastable isomers.

Quantum yields for helical overcrowded alkene molecular motor isomerisation range from low to moderately high (experimentally determined in the range of 0.55–20%).[45,64,68,79] The electronic nature of a substituent that is not involved in the thermal steps can have a pronounced effect in the excited state potential energy landscape and substituent-dependent quantum yields of isomerisation have been reported.[68]

A number of different effects and processes have been described or suggested in additional studies focusing on the details of the photochemical steps of various molecular motors. For a second generation motor with a xanthylidene stator the data was consistent with an initial fast relaxation to a local minimum on the S_1 excited state energy surface.[54] A motor with rigid substituents was used to show that the movement during the photochemical step is mainly localised on the core structure of the motor, rather than the outer substituents.[76] For first generation molecular motors, a similar twisting/pyramidalisation mechanism for photoisomerisation occurs and comparable involvement of conical intersections and ultrafast initial relaxation steps. Notable differences are a longer lived excited state, a red-shifted emissive state and overall higher quantum yields.[71,77]

3.4 Tuning the absorption wavelength

A significant amount of work in the field of molecular motors and other photoswitches[80] has been performed into the tuning of the excitation wavelength. For the use of molecular motors in soft materials and biomedical applications, the ability to function without the use of UV irradiation would be highly beneficial. For biological or medicinal uses, an excitation wavelength inside the "therapeutic window" of 600–1200 nm is desired to avoid cell damage and have sufficient tissue penetration of light.[81,82]

A number of common strategies for red-shifting chromophores, such as the introduction of donor-acceptor motifs, the extension of the π-system, metal complexation and intramolecular energy transfer have been applied to

molecular motors. A few examples are illustrated in Figure 7. In this section, all the photostationary state (PSS) ratios of metastable:stable state are reported at the indicated wavelengths.

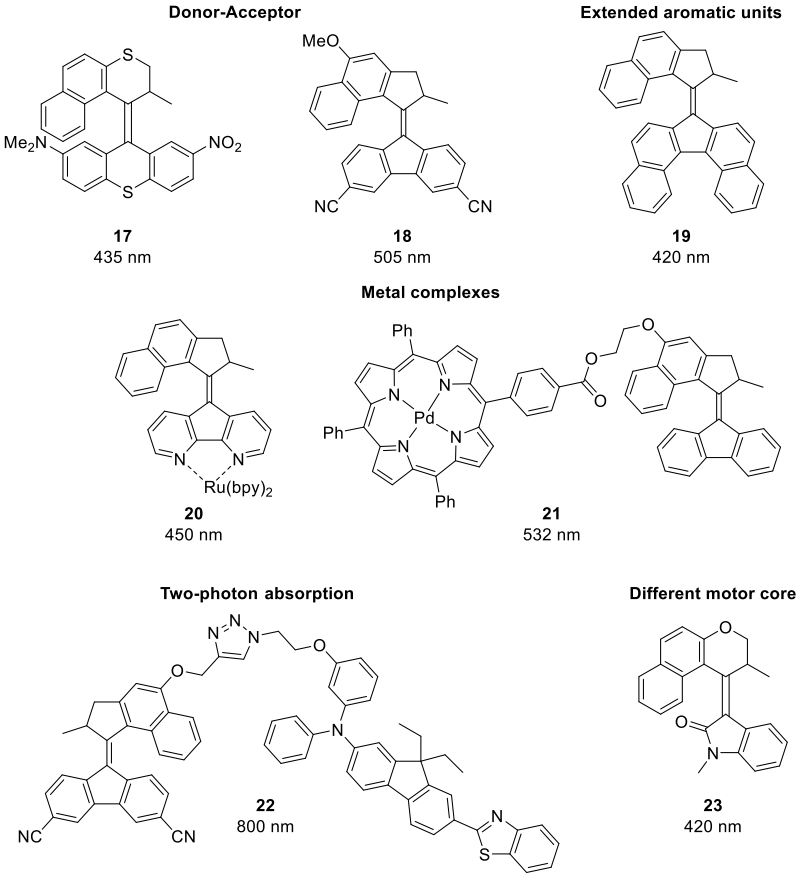

Figure 7. Different strategies for red-shifted photon absorption to the visible light-driven molecular motors and their operational irradiation wavelength.

The introduction of a dimethylamino- and a nitro-substituent on the stator half of second generation motor **17** shows the versatility of a donor-acceptor motif. A red-shift to an operational irradiation wavelength of 435 nm (PSS 90:10) compared to the parent motor (312 nm, PSS 92:8) was achieved.[45,83] Further development of donor-acceptor motifs in molecular motors has led to absorbance up to 505 nm (PSS 24:76) for motor **18**.[79]

Molecular motor **19** uses the strategy of extension of the π-system with a new, larger aromatic core in the stator. This synthetic modification has led to a red-shift of the operational wavelength up to 490 nm with a quite low

PSS, but a commonly acceptable PSS of 76:24 at 420 nm. The parent motor with a fluorenyl stator has a PSS of 75:25 at 365 nm.[84,85]

Metal complexes have been used both directly conjugated to the C=C axle and connected via a linker. Molecular motor **20**, containing a 4,5-diazofluorenyl motif, was used as a ligand in a Ru(II) complex, leading to a shift in absorption spectrum up to 450 nm (PSS 36:64).[86] By linking a palladium porphyrin complex to motor **21** as a "visible light antenna", molecular rotational motion was achieved with irradiation up to 532 nm (PSS 33:67) by absorption at the palladium porphyrin sensitiser and subsequent energy transfer to the motor core.[87]

Using an organic two-photon absorber as a sensitiser linked to a second generation molecular motor (**22**), allows using near-infrared light (800 nm) with an intensity and wavelength compatible with in vivo studies. It operates by two-photon excitation of the sensitiser and resonance energy transfer to the molecular rotary motor.[88]

Finally, another strategy to achieve absorption wavelength alteration is to use a different photochromic core. Oxindole-based molecular motor **23** is functioning via the same fundamental steps as second generation molecular motors, but has a significantly different, non-symmetric stator. This introduces a difference for both E/Z-photoisomerisations and both THIs akin to first generation motors. The motor operates with an irradiation wavelength of 420 nm (PSS 94:6 and 62:38 for Z and E, respectively).[89]

3.5 All-photochemical driven motors

It is possible for molecular motors to perform unidirectional rotation with exclusively photochemical isomerisations, such as the hemithioindigo-based motor developed by Dube and co-workers.[90] In another, recent example Feringa and co-workers reported an overcrowded alkene-based molecular rotary motor based on only photochemical isomerisations (Scheme 5, **24**). This all-photochemical driven, second generation molecular motor with a phosphorus centre in the stator can be converted into the four diastereomers by irradiation. A "shortcut" for rotation involving only three steps was achieved by thermal phosphine inversion.[46] Furthermore, for motor **24**, X-ray crystal structures have been obtained for all four diastereomeric states.[46]

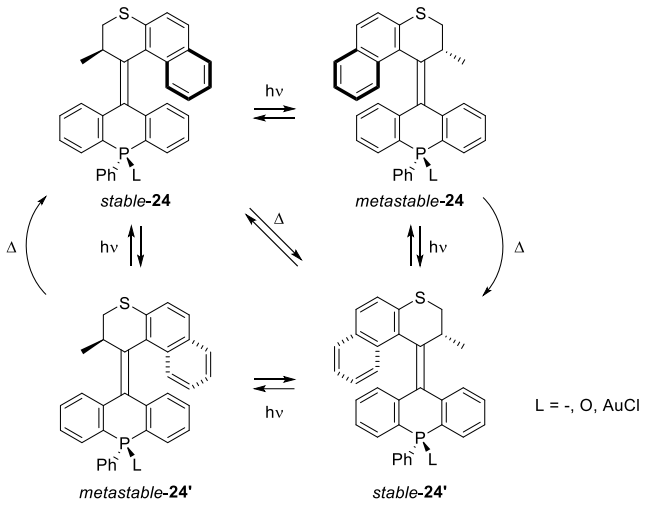

Scheme 5. All-photochemical molecular motor.[46]

3.6 Novel motor core designs

The expansion of computational studies into molecular rotational motion in recent years has shown to be a powerful tool for new motor designs and study of the analytically challenging photochemical steps. Several structures have been proposed and investigated, mainly based on theoretical and computational studies (Figure 8). In many of these novel motor designs, the main challenges addressed are the improvement of quantum yields of the photochemical steps, fast photochemical steps and the removal of thermal steps in the rotation mechanism. As the thermal steps in the rotary mechanism are rate-limiting for the rotation, a fully photochemical motor could be faster and temperature-independent. The thermal step is no longer the main ratchet and driving force for unidirectionality. Instead, unidirectionality is governed solely by the photochemical steps.

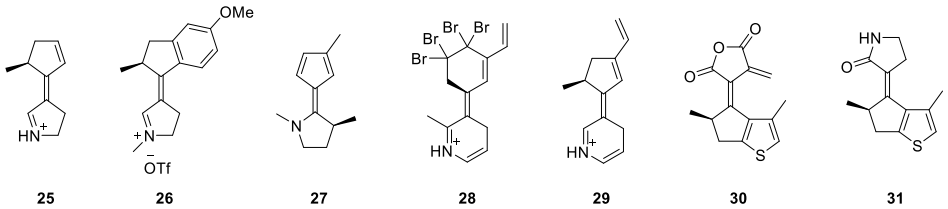

Figure 8. Novel motor core designs.

Olivucci and co-workers reported light-activated molecular motors based on a biomimetic indanylidene-pyrrolinium (IP) framework[72,91,92] inspired by natural photoswitchable molecules, such as rhodopsin, that operate in a unidirectional rotational way with high quantum yields.[93] In minimalistic IP

25 the allylic methyl only provides a small pretwisting of approximately 2° for the rotation axle, but this is sufficient to show rotational directionality of photoisomerisation.[91] In the further development using the same framework, the computational[72] and experimental[92] studies show that IP **26** could in principle work as a fast light-driven unidirectional molecular motor. The *Z*-to-*E* photoisomerisation shows full clockwise unidirectional rotation. However, the unidirectionality of the *E*-to-*Z* isomerisation is lacking. Indeed, a different degree of planarisation and steric repulsion induce both clockwise and anticlockwise rotation.

Bicyclic enamine motor **27** was designed by Durbeej and co-workers and evaluated in molecular dynamics simulations and quantum chemical calculations as a fully photochemical molecular motor.[94,95] The theoretical research into this motor shows unidirectional rotation for both *Z*-to-*E* and *E*-to-*Z* photoisomerisation. These enamine motors could have relatively high quantum yields because the formation of excited state aromaticity drives their rotation.

Durbeej and co-workers further designed visible light absorbing conjugated imine-based molecular motors such as **28** and **29**. Theoretical investigations predict high quantum yields and fast photoisomerisations for these type of motors.[96,97]

From quantum chemical calculations and molecular dynamics simulations Filatov and co-workers showed that motors **30** and **31**, based on fulgide motifs, have the characteristics to operate as rotational molecular motors with high quantum yields and fast photochemical dynamics.[98,99]

These novel motor core designs can serve as an attractive stepping stone for mechanistic further understanding of photochemically-driven molecular rotation and the development of motors with new properties.

4. Applications

As already predicted by Lehn in 2002,[100] the past decades have seen a general movement of the chemical sciences into the supramolecular realm. Some of the most promising applications for chiroptical molecular switches and motors, towards out-of-equilibrium and autonomous dynamic behaviour in particular, are based on organised systems[101] and complex systems featuring collective action.[102] For applications in the extensive and thriving field of supramolecular systems or smart materials, such as responsive polymers,[103] gels and liquid crystals,[104] the reader is referred to the following reviews.[105–110]

4.1 Transfer of chirality

The inherent ability to change stereochemical information by inverting helicity in both photochemical and thermal steps is a unique property of chiroptical molecular switches and motors, that has found some fascinating applications in the previous decade. The chiral information stored in a chiroptical molecular motor or switch can be transferred to a second system, such as a newly formed stereogenic centre or complex (*vide infra*). However, in contrast to commonly used chiral auxiliaries, the absolute chirality can be inverted by a fast and highly efficient helix inversion. Since this inversion is induced by a simple stimulus such as light (stable to metastable) and/or temperature (metastable to stable), the process is orthogonal to many chemical reactions and (supra)molecular interactions, which means that *in situ* switching is often possible in reaction mixtures and complex systems.

The ability of a molecular motor to transfer chiral information at the single molecular level was first demonstrated in 2011.[111] A first generation xylene-based molecular motor **32** (Figure 9) with a highly efficient rotation cycle was functionalised with 4-dimethylaminopyridine (DMAP) and thiourea groups, and can cooperate to form a bifunctional organocatalyst.[112] In both *trans* isomers, these moieties are remote, but in the *cis* isomers, they are in close proximity. Moreover, the relative spatial orientation of the DMAP and thiourea groups adopts the helicity of the motor backbone. The ability of **32** to function as an enantioselective organocatalyst was demonstrated in an organocatalytic Michael addition of 2-methoxythiophenol to cyclohexenone (Figure 9c). In the presence of stable (2*R*,2'*R*)-(*P*,*P*)-*trans*-**32**, the racemic thiol product was formed slowly as the DMAP and thiourea groups cannot cooperate, while the rate could be significantly enhanced by using either *cis* isomer. Remarkably, using the metastable (2*R*,2'*R*)-(*M*,*M*)-*cis* ligand led to selective formation of the (*S*)-enantiomer of the product (e.r. (*S*/*R*) 75:25), while using the stable (2*R*,2'*R*)-(*P*,*P*)-*cis* ligand inverted the enantioselectivity of the reaction (e.r. (*S*/*R*) 23:77). Photochemical isomerisation from stable *trans*-**32** to metastable *cis*-**32**, i.e. switching from stage *I* to stage *II* of the catalyst (Figure 9), is highly efficient (>99%). By heating the catalyst at 70 °C for 40 min, the metastable stage *II*, *M*-helical catalyst could be converted to the stable stage *III*, *P*-helical catalyst. By irradiating stable *trans*-**32** in the presence of the reagents, the asymmetric Michael addition could be 'switched on' *in situ*, leading to a comparable enantioselectivity and a slightly diminished reaction rate compared to the isolated metastable *cis* isomer. Summarised, motor **32** can be used as a multistage chiral catalyst which, through a specific switching sequence, can be used for the formation of the racemic product or either of the *S*- or *R*-enantiomers selectively.

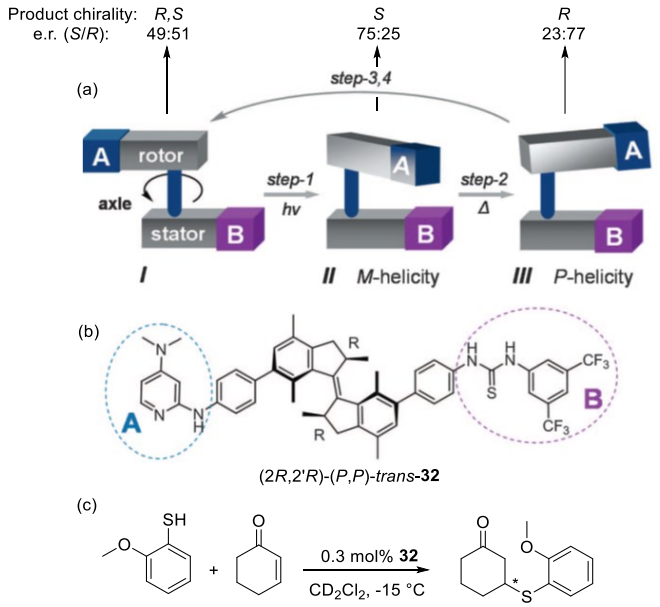

Figure 9. Photoswitchable asymmetric catalysis. (a) Conceptual overview. (b) Molecular structure of catalytic motor **32**. (c) Michael addition of 2-methoxy thiophenol to cyclohexanone. Figure adapted with permission from Ref 111, Copyright AAAS.

Following this successful example, the same principle was applied to various molecular motors, reactions and substrates.[113] Highlights include switchable, motor-based phosphine ligands, which have been used in asymmetric palladium catalysis[114] (Figure 10, **33**) and anion binding catalysis (Figure 10, **34**).[115] In a recent example, a photoresponsive phosphoramidite ligand based on bistable chiroptical switch **35** (Figure 10) was successfully used to tune the rate and stereochemical outcome of a copper-catalysed conjugate addition.[116] In this complex, chiral information is transferred over five stereochemical elements: the fixed stereogenic carbon centre of the switch, the helicity of the overcrowded alkene, the dynamic helical geometry and axial chirality of the attached biaryl unit and stereogenic phosphorus centre, which is thermally stable at room temperature. In Figure 10b, the schematic overview shows the coupled inversion of helical and axial chirality. A maximum *ee* of 97% and maximum Δ*ee* of 106% were achieved for the copper-catalysed addition of diethyl zinc to cyclohexanone. While such results are not yet able to compete with traditional (non-responsive) phosphoramidite ligands, this particular example beautifully demonstrates the possibility of transferring the chiral information of a chiroptical switch or motor not simply from one molecule to the other, but across an intricate network of dynamic elements.

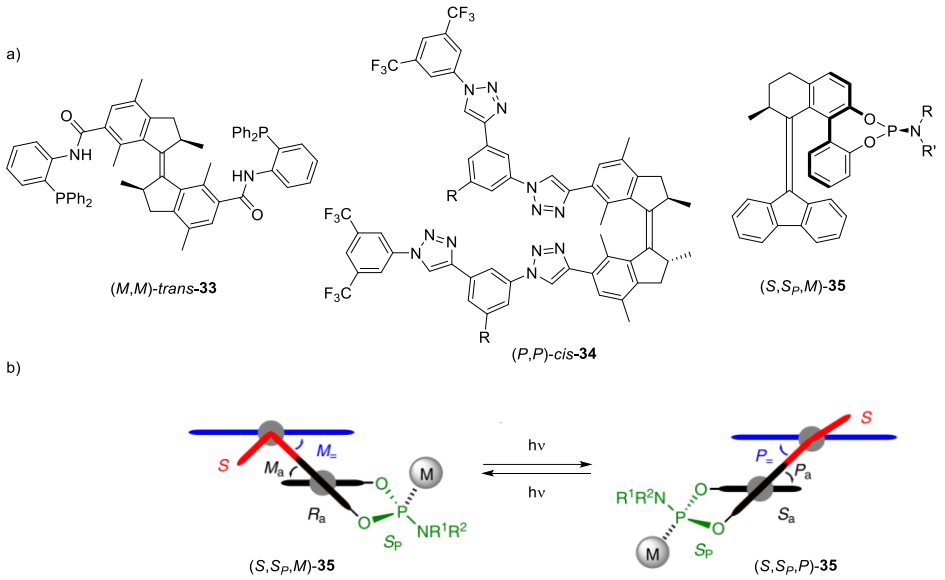

Figure 10. a) Several molecular motor based photoswitchable catalysts. b) Schematic top-down view of the switching of motor **35** upon metal complexation. Figure adapted with permission from Ref 116.

In the field of catalysis, future applications of photoresponsive systems may include *in situ* switching of selectivity and activity for sequential synthesis. Moreover, the transfer of chirality from chiroptical motors or switches to other responsive systems may prove to be a cornerstone in the design of more sophisticated molecular machinery or complex systems. For a discussion on the efforts towards dynamic transfer of chiral information on larger systems, such as polymeric and liquid crystalline materials, the reader is referred to the following reviews.[110,117] On a molecular scale, the principle was recently demonstrated using a short double-stranded helical copper complex (Figure 11).[118] Taking inspiration from Lehn's supramolecular double helicates,[119] a first generation molecular motor was functionalised with two bipyridine ligands, which upon complexation to Cu^{+} form a double helix. The stable (*P,P'*)-*trans* isomer forms oligomers in which the copper-complexed ligands adopt a defined *P* helical chirality. By irradiation with 312 nm light and subsequent heating the metastable (*M,M'*)-*cis* and stable (*P,P'*)-*cis* isomers, respectively, can be generated, which both form a dinuclear complex. CD spectroscopy was used to demonstrate that the THI is accompanied by an inversion of helical chirality. While this double helical system is relatively small, related work by Clayden[120] and Feringa[121], among others, already shows that chiral information may be transferred across single strands at multiple length scales.

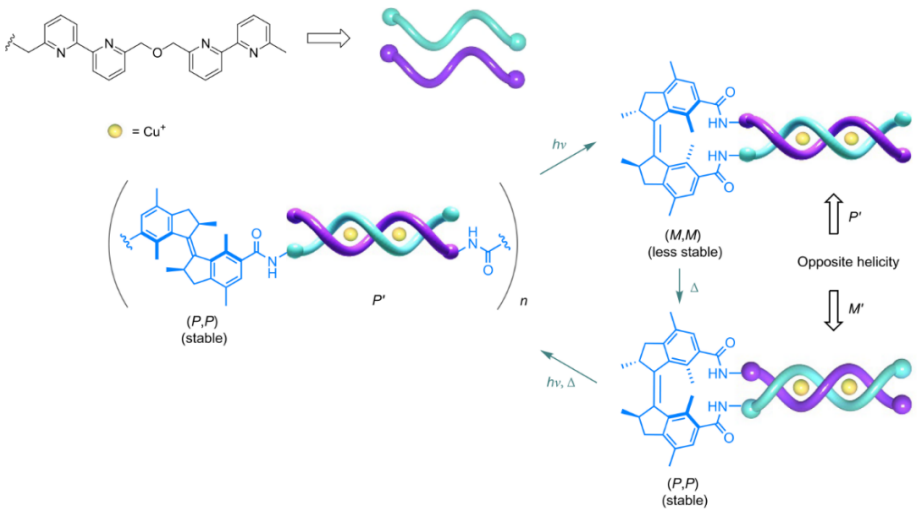

Figure 11. Schematic overview of the switching of the helicity of oligomeric metal-ligand complexes. The switching of the helicity is governed by the motor core structure.[118]

4.2 Transfer of motion

Coupled rotary systems

Much like the machines of the macroscopic world are fuelled by motors via a complex network of cogwheels, ratchets and pulleys, there is a sincere hope that one day, molecular motion on the single molecular scale may be transferred and amplified to fuel the nanomachinery of the future. The regulation and transfer of rotary motion are of essential importance to such systems, and the unidirectional rotation cycle of a light-driven molecular motor is perfectly suited to drive any envisioned machine on the nanoscale.[122] Even so, early explorations towards controlling rotary motion using overcrowded alkenes precede the development of the molecular motor. In 1997, an overcrowded alkene-based chiroptical switch was functionalised with a xylene rotor (Figure 12a, **36**).[123] EXSY-NMR spectroscopy was used to investigate the rate of rotation around the biaryl axis of the xylene unit. Unexpectedly, the *trans* isomer has a higher barrier ($\Delta\Delta G_{303K}^{\ddagger}$ = 2.9 kJ mol^{-1}) than the *cis* isomer for xylene rotation. This design provided a starting point for the development of a range of more advanced coupled rotary systems, several of which are depicted in Figure 12. In the motor-based molecular 'gearbox' **37** the *cis* isomers have a faster xylene biaryl rotation than the *trans* isomers, akin to **36**. Additionally, the *stable* isomers show faster xylene rotation than the respective *metastable* isomers, attributed to increased steric hindrance enforced by the pseudo-equatorial orientation of the rotor methyl substituents.[124] In first generation motor-based coupled rotary system **38** (Figure 12a), rotation of the anisyl

substituents was unhindered in three out of four of the isomers in the rotary cycle, but significantly slowed down in the metastable *trans* isomer.[125]

While the speed of rotation of a secondary rotor may be regulated by the systems described above, there is no directionality. The molecular motors incorporated in structures **37** and **38** (Figure 12a) effectively function as four state switches.

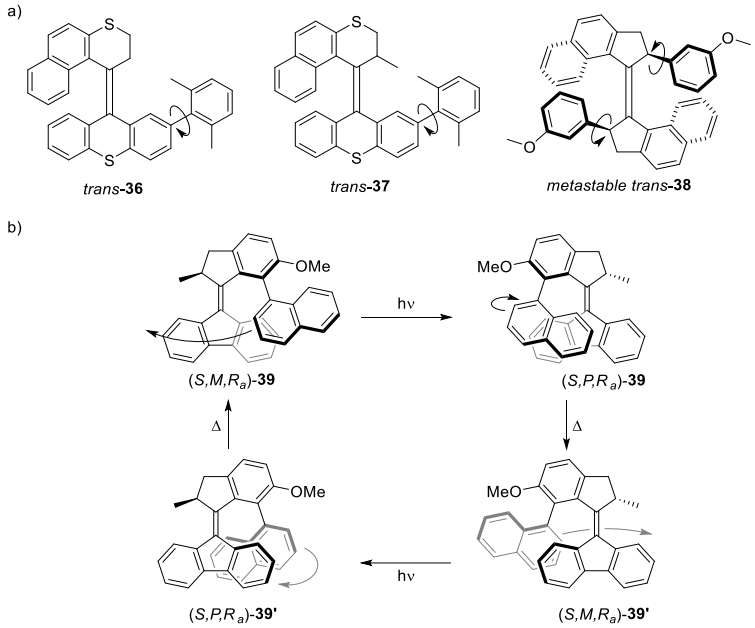

Figure 12. a) Several coupled rotary systems and b) overview of the rotary cycle of locked synchronous motion of motor **39**.

An important step in the direction of truly coupled rotary systems was achieved with the development of a second generation motor functionalised with a naphthyl rotor (**39**), which displays a locked, synchronous rotary motion (Figure 12b).[126] The design of **39** perfectly balances the barriers for motor and rotor rotation. Random thermal rotation around the biaryl axis is effectively blocked at the operating temperature. Instead, the rotor follows the rotation of the motor in a sequence of rotating and sliding motions, ensuring that the naphthyl unit always faces the motor with the same side. As the authors remark, this locked synchronous rotation is reminiscent of the rotation of the moon around the earth, and brings us a step closer to the design of more sophisticated geared molecular systems.

Translation of motion

While coupled rotary systems may, one day, drive complex artificial molecular machines, the direct conversion of unidirectional rotary motion

to translational motion has already yielded impressive results. Nanocars are molecules consisting of wheels on a chassis which were designed with the objective of moving them across a surface.[127] The first nanocar (Figure 13, **40**) was reported by Tour and co-workers and consisted of a central frame connecting four fullerene 'wheels', which could be rolled across a flat gold surface by pulling with an STM tip.[128] Shortly thereafter, the group proposed a design for a motorised nanocar, containing a single light-driven rotary motor in the centre of the chassis.[129] Further studies revealed that this design would not move on a copper surface, neither upon irradiation of the motor unit or via STM tip pulling.[130] It was argued that the surface interactions for this particular nanocar were simply too high to allow for lateral movement.

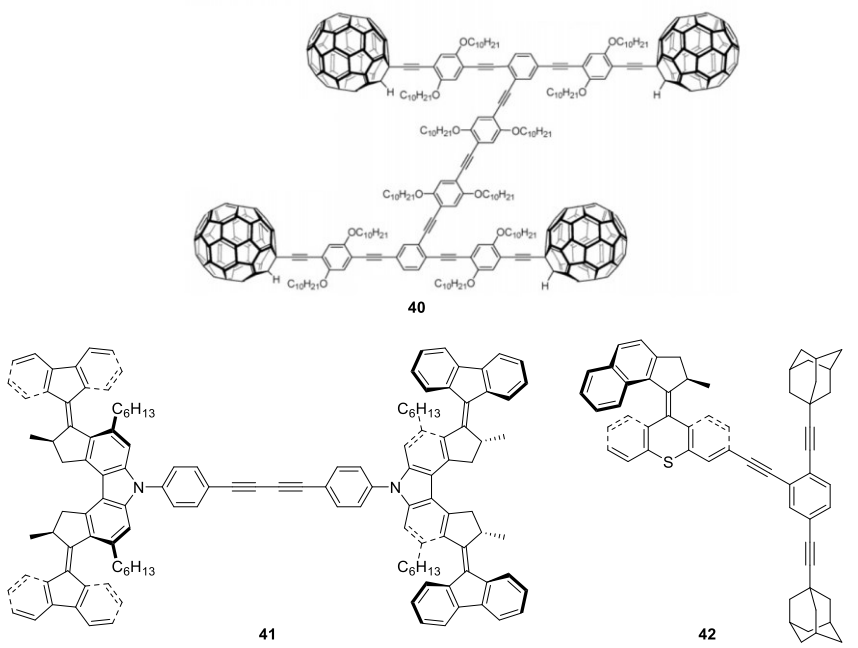

Figure 13. Non-motorised (top), electrically driven (bottom left) and light driven (bottom right) nanovehicles. Structure **40** was adapted from with permission from Ref 128, Copyright ACS.

In the meantime, successful motorised motion on a surface had been demonstrated by Feringa and co-workers.[131] In this design **41** (Figure 13), four molecular motors were incorporated, functioning as the wheels. This design significantly reduces surface interactions, as the motor 'paddlewheels' are both small and distorted. Electric pulses applied by the STM tip were used to fuel the nanocar on a 10-step, 6 nm long linear trajectory across the copper surface. Although motor rotation upon application of a voltage is thought to proceed *via* the same mechanism as

light-induced rotation, movement of nanocar **41** across a surface upon irradiation has not yet been demonstrated. Recently, Tour, Grill and co-workers reported light-induced translation across a surface for their 'nanoroadster' **42** (Figure 13), thus demonstrating that overcrowded alkene-based molecular motors may be rotated by UV light while adsorbed on a surface.[132] While directional movement could not be observed, rotation of the motor led to an increased rate of diffusion across the copper surface.

Important steps for the future of nanoscale machinery and nanocars are to further develop the directional motion. Where nature has developed kinesin "walkers" to transport cargo in a guided unidirectional way,[133] artificial molecular nanocars can strive to get closer to the level of control that nature has.

Control over motion

Fuelling nanomachines is on its own a challenge that will occupy chemists for years to come, but in order to perform complex operations, we will also need to exercise some degree of control over this motion. Feringa and co-workers have developed gated systems, which have the power to reversibly halt rotation and thus act like brakes. These systems each comprise a second generation molecular motor functionalised with either a pseudorotaxane[134,135] or a dithienylethene switch.[136] In each case, the 'braking' functionality is turned on and off with a trigger that is orthogonal to the light used to rotate the motor, i.e. acid/base and higher wavelength light, respectively. In addition, the group reported a molecular motor in which the direction of rotation could be changed by a base mediated epimerisation of the asymmetric centre responsible for determining the direction of rotation.[137]

4.3 Biological applications

The ability to switch a molecular structure and therefore its function using a trigger orthogonal to most processes in the cell, e.g. light, offers tremendous opportunities for biological applications.[138,139] Containing an aromatic system at their core, overcrowded alkene-based molecular motors and switches are inherently hydrophobic, making applications in an aqueous environment challenging. The four-state switching cycle and unidirectional rotation of a molecular motor may be applied to create intriguing responsive systems with mechanical properties, hitherto impossible to achieve using two-state switches, such as azobenzenes, diarylethenes or spiropyrans.

The use of chiroptical switches and molecular motors in an aqueous environment using aggregated systems, such as amphiphiles,[106] is outside of

the scope of this section. For applications of molecular motors on the single molecular scale, solubilisation using hydrophilic substituents has proven to be a largely successful strategy.[140] Addition of two choline moieties to a first or second generation molecular motor was proven to be sufficient to completely dissolve the motors at concentrations up to 0.1 mM.[141] While first generation motor **43** (Figure 14) suffered from minor degradation upon irradiation, most likely due to photoinduced water addition to the central double bond, second generation motor **44** (Figure 14) remained stable upon prolonged irradiation.[141] Notably, the solubilisation of **44** was achieved by functionalizing only the lower half of the motor, leaving the possibility to further functionalise the top half for potential future application.

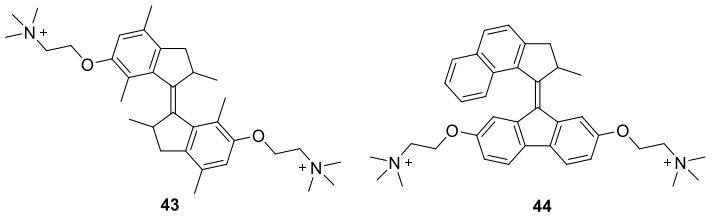

Figure 14. Water soluble light driven molecular motors.

The hydrophobic nature of molecular motors can also be circumvented by incorporation into a much larger biomolecule. First generation molecular motors were successfully adapted into building blocks for both peptides and oligonucleotides. In both cases, it was demonstrated that the large geometrical change associated with *trans*-to-*cis* isomerisation of the relatively small motor unit could reversibly modify the secondary structure of the larger biohybrid system. For a motor-functionalised peptide, the *trans* isomer exists in a monomeric state, while isomerisation to the *cis* isomer induces formation of a β-hairpin structure (see Figure 15).[142] In an 8 base pair-long motor-functionalised oligonucleotide, both *cis* and *trans* isomers form a hairpin structure.[143] Isomerisation of the motor proceeds despite its incorporation in a highly stable hybridised (double stranded) system, and a remarkable difference in duplex stability is observed upon 180° rotation.

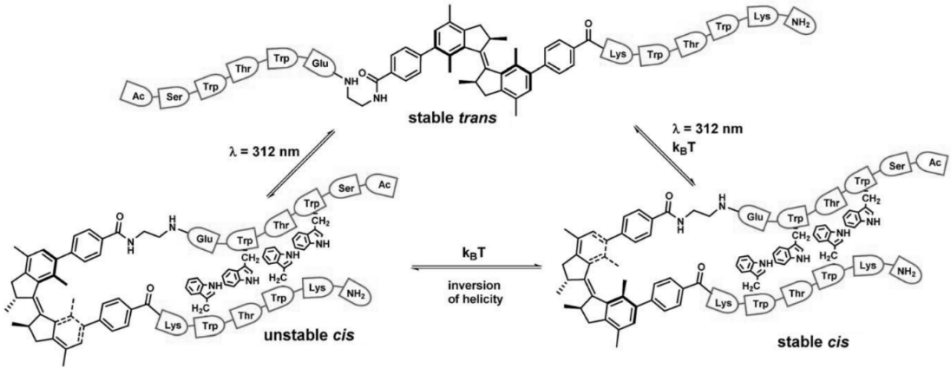

Figure 15. First generation molecular motor forming a β-hairpin structure.[142]

In the non-aqueous parts of biological systems, the use of molecular motors is much more straightforward. Despite the limited amount of free space, both photochemical and thermal isomerisation processes occur readily in aggregated systems such as nanofibers, nanotubes and artificial muscles,[144-146] making molecular motors ideal candidates for application in non-aqueous environments, such as cell membranes. Tour and co-workers loaded second generation molecular motors modified with fluorescent tags in the cell membrane, and demonstrated that these are non-toxic.[147] They found that upon UV irradiation, the motors move across the membrane. As expected, exposure to UV light caused cell death, but the authors demonstrated that apoptosis was accelerated by more than 50% in the presence of molecular motors. This effect was attributed to disruption of the membrane by motor rotation. By modification of the motors with short peptides, specific cells could be targeted. In follow-up research, the group demonstrated that cell death can also be induced using molecular motors that rotate through two-photon excitation in the near infrared domain, thus eliminating the need for damaging UV irradiation.[148] Finally, in vivo studies showed that light-activated molecular motors can cause severe damage in small eukaryotes, i.e. increased mortality in invertebrates such as *C. Elegans* and *Daphnia*, and skin lesions in hairless mice.[149]

In a recent example, molecular rotary motion from motors attached to a glass surface was used to dynamically alter a surface, mediating a protein adhesion layer. This ultimately directed the fate of human bone marrow-derived mesenchymal stem cells. The dynamic motor surface led to an increased differentiation into osteoblasts, while a non-rotating surface maintained higher multipotency.[150]

Due to their conceptual similarity with biological molecular motors, application of artificial molecular motors in biological nanotechnology intuitively feels obvious. However, major challenges remain. While the

possibility to target specific cells for cell death is certainly appealing, it needs to be determined whether the implied apoptosis will be an inevitable side effect to other *in vivo* applications. Meanwhile, solubility and stability remain an issue in aqueous environments.

4.4 Other applications

The vast majority of research into chiroptical molecular switches and motors takes place in solution, where molecules are randomly oriented and continuously moving due to Brownian motion. As such, taking full advantage of their properties is challenging. Unidirectional rotation or chiral information can be easily transferred within the single molecule or complex, but in order to create an effect at larger length scales, orientational order needs to be imposed.

Surface functionalisation is a straightforward method of creating large two-dimensional arrays of identically ordered molecules. Molecular motors have been functionalised to be attached to surfaces while ensuring enough free space around the motor to allow for unidirectional rotation.[151,152] Taking inspiration from the landmark experiment of Kinosita and co-workers, in which rotation of a single ATPase protein motor was visualised on a surface,[153] Cockroft, Feringa, Hofkens and co-workers collaborated to visualise single molecular artificial motor rotation on a surface, using a tetrapodal second generation molecular motor functionalised with a perylene diimide fluorophore, which is attached to the glass surface via electrostatic interaction.[154,155] Using wide-field defocused fluorescence microscopy, the diffraction limit could be circumvented and the behaviour of the motors upon irradiation with UV light could be observed. Although rotation was observed, it appeared that during the THI, the entire molecule was rotating with respect to the surface. This unexpected behaviour was attributed to transient dissociation and reassociation of the surface attachment "feet". Covalent attachment of the legs to the surface is expected to solve this issue.

The evolution of data storage is a continuous story of shrinking bits into smaller spaces. Soon after the initial development of chiroptical molecular switches, optical data storage came to mind as an attractive potential application.[32,156] A single bistable molecular switch could function as a bit and a functionalised surface would possess tremendous storage capacity. For four-state rotary motors, the effect could be even more dramatic. Although such applications have not yet been realised using chiroptical switches and motors, synthesis of large, ordered arrays of photoswitches and motors is easily achieved in two or three dimensions,[101] while the

advance of nanophotonics has opened opportunities for overcoming the diffraction limit and enabling light-matter interactions at the nanoscale.[157]

5 Perspective & Outlook

Chiroptical switches based on overcrowded alkenes have slowly been surpassed by rotary molecular motors, both in terms of understanding and applications. A molecular motor is undoubtedly the more versatile photoactive molecule of the two, but is also more complex to synthesise and to study. While the most exciting innovations may require to exploit the full potential of rotary molecular motors, it is beneficial to have tailor-made molecular switches or motors for the envisioned use.

Considering the broad scope of molecular motors available, the current research into new motors and the increasing insights in the fundamental processes of molecular motion, a myriad of robust tools for the selection and design of functional motors now exists. The development of new core designs, such as oxindole- or pyrrolinium-based systems, has the potential to evolve into new families of motors with unique properties.

The full understanding of the details of the photochemical steps in molecular motors is challenging, but has seen impressive progress taking advantage of ultrafast spectroscopy and theoretical chemistry. This knowledge has facilitated in the design of more and more efficient molecular unidirectional rotary motors. The tuning of the operational irradiation wavelengths opens up new possibilities for application, notably in biological systems and smart materials. The continually improving insight into motor photochemistry will advance new designs, widening the potential applications and tuning the motors to their specific applications.

The addressability of specific stereochemical information in molecular motors, which can be amplified or used in supramolecular systems or catalytic reactions, has been shown to be a powerful principle. This can serve as an interesting starting point for selectively modifying the chiral information present in molecular systems for information storage or using it in more complex programmable (supra-)molecular systems.

The application of chiroptical switches and motors in catalysis has as of yet seen several promising studies, but there is still significant potential for future investigation. Different states of the molecular motor can be used to tune the chirality of the motor and its environment specifically. The prospect of these catalytic motors to be applied *in situ* has already been demonstrated, leaving the door wide open for the development of highly efficient, green,

photoswitchable catalytic systems for e.g. multitasking catalysis or sequential asymmetric synthesis.

Many reported and envisioned applications of motors require the translation of motion from the nano- to the meso- or macroscale, which needs amplification or coordination of the molecular machinery. The use of motors in supramolecular or multicomponent systems is a significant step into bridging the length scales where we can develop responsive systems and interactive materials. Overcoming the Brownian storm, increasing the quantum yields, as nature has done and developing tools to prove nanoscale motion in detail are challenges that remain. Rotary molecular motors are among the most exciting candidates for applications in nanotechnology. Several proof-of-principle coupled rotary systems have already been reported. The motorised directional motion of a nanocar across a surface and the unidirectional rotation of a micro rod on a soft, liquid crystal surface, have demonstrated just how far a combination of synthetic experience, fundamental knowledge and imagination can take us.

While molecular motors are unique in their unidirectional rotational motion, there have been limited direct uses of this type of motion. There are ample opportunities to take advantage of the fact that molecular motors are excellent to achieve rotary motion and can serve a crucial role in devices of the future based on nanoscale machines.

6. Aim of this research and thesis outline

The field of overcrowded alkene-based molecular switches and motors has seen a great deal of progress in the last few decades, with many versatile structures and various applications. A number of further developments of overcrowded alkenes are presented in this thesis.

An important goal of this work was to study the use of electrochemical stimuli for unidirectional molecular rotary motors. We investigated the modification of known molecular motor scaffolds, the functionalisation of a previously developed electrochemical switch and the design of a new, helical chirality based switch. Another focus point of this work was to further develop the research into the conformational redox switches based on bisthioxanthylidenes. A new synthesis method is explored as well as bridged and ligand functionalised variants of bisthioxanthylidenes.

Chapter 2 describes the development of molecular rotary motors with quaternary stereogenic centres for electrochemically driven rotation. The synthesis of fluorinated and alkylated motors is discussed and a number of targets were analysed by cyclic voltammetry, UV-vis spectroscopy and transient absorption spectroscopy.

Chapters 3, 4 and 5 are studies on bisthioxanthylidenes and related compounds. Chapter 3 presents a new and rapid method for the synthesis of bisthioxanthylidenes with various substituents. With this new useful method, a library of compounds was constructed and their differences in electrochemical properties was investigated. In Chapter 4, two extended bisthioxanthylidenes are described using DFT calculations and electrochemical and spectroscopic data. These bridged species are used as conformational switches and have stable neutral folded, orthogonal diradical and orthogonal dicationic states. We found that the bridging unit has a strong influence on the overall switching behaviour. Chapter 5 describes the use of pyridyl ligand functionalised bisthioxanthylidenes with alkyl linkers for the modulation of their redox driven conformational switching. The metal complexation influences the optical and electrochemical properties of previously developed bisthioxanthylidenes.

Chapter 6 shows computational and experimental studies into *N*,*N*'-substituted isoindigos for the development of a reliable method for the prediction of their optical and electronical properties. The combination of UV-vis and cyclic voltammetry data in combination with several computational methods provided such a method. This can be used for tuning

the properties of isoindigos with various substituents, which is a functional tool in the development of organic photovoltaics.

In Chapter 7, fluorenyl-helicene based overcrowded alkenes are investigated for molecular rotary motion, controlled by exclusively helical chirality. This would constitute a new class of molecular motors without any stereogenic centres and could be promising electrochemical and optical molecular switches.

7. References

1 B. L. Feringa and W. R. Browne, *Molecular Switches*, Wiley-VCH, Hoboken, USA, 2nd edn., 2011.
2 A. Albini and M. Fagnoni, *ChemSusChem*, 2008, **1**, 63–66.
3 P. Bortolus and G. Cauzzo, *Trans. Faraday Soc.*, 1970, **66**, 1161–1164.
4 D. H. Waldeck, *Chem. Rev.*, 1991, **91**, 415–436.
5 F. B. Mallory and C. W. Mallory, in *Organic Reactions, Vol. 30*, ed. W. G. Dauben, John Wiley & Sons, 1984, pp. 1–151.
6 D. Villarón and S. J. Wezenberg, *Angew. Chem. Int. Ed.*, 2020, **59**, 13192–13202.
7 L. Greb and J. M. Lehn, *J. Am. Chem. Soc.*, 2014, **136**, 13114–13117.
8 M. Guentner, M. Schildhauer, S. Thumser, P. Mayer, D. Stephenson, P. J. Mayer and H. Dube, *Nat. Commun.*, 2015, **6**, 8406.
9 S. Kassem, T. van Leeuwen, A. S. Lubbe, M. R. Wilson, B. L. Feringa and D. A. Leigh, *Chem. Soc. Rev.*, 2017, **46**, 2592–2621.
10 J. P. Sauvage, *Angew. Chem. Int. Ed.*, 2017, **56**, 11080–11093.
11 Y. Qiu, Y. Feng, Q. H. Guo, R. D. Astumian and J. F. Stoddart, *Chem*, 2020, **6**, 1952–1977.
12 M. Baroncini, S. Silvi and A. Credi, *Chem. Rev.*, 2020, **120**, 200–268.
13 J. P. Sauvage and P. Gaspard, Eds., *From Non-Covalent Assemblies to Molecular Machines*, Wiley-VCH, Weinheim, DE, 2010.
14 C. J. Burns and J. Fraser Stoddart, Eds., *The Nature of the Mechanical Bond: From Molecules to Machine*, John Wiley & Sons, Hoboken, NJ, USA, 2016.
15 G. P. Moss, in *Basic terminology of stereochemistry (IUPAC Recommendations 1996)*, 1996, vol. 68, p. 2203.
16 S. Mason, *Chem. Soc. Rev.*, 1988, **17**, 347–359.
17 F. Crick, *Life Itself*, McDonald & Co, London, 1981.
18 E. L. Eliel and S. H. Wilen, *Stereochemistry of Organic Compounds*, Wiley, New York, 1994.
19 N. Koumura, R. W. J. Zijistra, R. A. van Delden, N. Harada and B. L. Feringa, *Nature*, 1999, **401**, 152–155.
20 W. R. Browne and B. L. Feringa, *Nat. Nanotechnol.*, 2006, **1**, 25–35.
21 B. L. Feringa, *J. Org. Chem.*, 2007, **72**, 6635–6652.
22 B. L. Feringa, *Angew. Chem. Int. Ed.*, 2017, **56**, 11060–11078.
23 B. L. Feringa and H. Wynberg, *J. Am. Chem. Soc.*, 1977, **99**, 602–603.
24 B. L. Feringa, W. F. Jager, B. de Lange and E. W. Meijer, *J. Am. Chem. Soc.*, 1991, **113**, 5468–5470.
25 J. C. M. Kistemaker, P. Štacko, J. Visser and B. L. Feringa, *Nat. Chem.*, 2015, **7**, 890–896.
26 N. Koumura, E. M. Geertsema, A. Meetsma and B. L. Feringa, *J. Am. Chem. Soc.*, 2000, **122**, 12005–12006.
27 P. U. Biedermann and I. Agranat, *Top. Curr. Chem.*, 2014, **350**, 177–278.
28 N. Harada, A. Saito, N. Koumura, H. Uda, B. De Lange, W. F. Jager, H. Wynberg and B. L. Feringa, *J. Am. Chem. Soc.*, 1997, **119**, 7241–7248.
29 R. W. J. Zijlstra, W. F. Jager, B. de Lange, P. T. van Duijnen, B. L. Feringa, H. Goto, A. Saito, N. Koumura and N. Harada, *J. Org. Chem.*, 1999, **64**, 1667–1674.

30 N. Harada, A. Saito, N. Koumura, D. C. Roe, W. F. Jager, R. W. J. Zijlstra, B. de Lange and B. L. Feringa, *J. Am. Chem. Soc.*, 1997, **119**, 7249–7255.
31 B. L. Feringa, N. P. M. Huck and H. A. van Doren, *J. Am. Chem. Soc.*, 1995, **117**, 9929–9930.
32 W. F. Jager, J. C. de Jong, B. de Lange, N. P. M. Huck, A. Meetsma and B. L. Feringa, *Angew. Chem. Int. Ed. Engl.*, 1995, **34**, 348–350.
33 E. W. Meijer and B. L. Feringa, *Mol. Cryst. Liq. Cryst.*, 1993, **235**, 169–180.
34 N. P. M. Huck and B. L. Feringa, *J. Chem. Soc. Chem. Commun.*, 1995, 1095–1096.
35 N. Harada, N. Koumura and B. L. Feringa, *J. Am. Chem. Soc.*, 1997, **119**, 7256–7264.
36 N. Koumura, E. M. Geertsema, M. B. van Gelder, A. Meetsma and B. L. Feringa, *J. Am. Chem. Soc.*, 2002, **124**, 5037–5051.
37 J. E. McMurry, *Chem. Rev.*, 1989, **89**, 1513–1524.
38 B. L. Feringa, *Acc. Chem. Res.*, 2001, **34**, 504–513.
39 M. K. J. ter Wiel, J. Vicario, S. G. Davey, A. Meetsma and B. L. Feringa, *Org. Biomol. Chem.*, 2005, **3**, 28–30.
40 M. Klok, L. P. B. M. Janssen, W. R. Browne, B. L. Feringa, *Faraday Discuss.*, 2009, **143**, 9–14.
41 M. M. Pollard, M. Klok, D. Pijper and B. L. Feringa, *Adv. Funct. Mater.*, 2007, **17**, 718–729.
42 R. D. Astumian, *Chem. Sci.*, 2017, **8**, 840–845.
43 M. K. J. ter Wiel, R. A. van Delden, A. Meetsma and B. L. Feringa, *J. Am. Chem. Soc.*, 2005, **127**, 14208–14222.
44 M. Klok, W. R. Browne and B. L. Feringa, *Phys. Chem. Chem. Phys.*, 2009, **11**, 9124–9131.
45 A. Cnossen, J. C. M. Kistemaker, T. Kojima and B. L. Feringa, *J. Org. Chem.*, 2014, **79**, 927–935.
46 G. B. Boursalian, E. R. Nijboer, R. Dorel, L. Pfeifer, O. Markovitch, A. Blokhuis and B. L. Feringa, *J. Am. Chem. Soc.*, 2020, **142**, 16868–16876.
47 J. C. M. Kistemaker, P. Štacko, D. Roke, A. T. Wolters, G. H. Heideman, M.-C. C. Chang, P. van der Meulen, J. Visser, E. Otten and B. L. Feringa, *J. Am. Chem. Soc.*, 2017, **139**, 9650–9661.
48 J. A. Berrocal, L. Pfeifer, D. Heijnen and B. L. Feringa, *J. Org. Chem.*, 2020, **85**, 10670–10680.
49 S. Kuwahara, Y. Suzuki, N. Sugita, M. Ikeda, F. Nagatsugi, N. Harada and Y. Habata, *J. Org. Chem.*, 2018, **83**, 4800–4804.
50 J. C. M. Kistemaker, S. F. Pizzolato, T. van Leeuwen, T. C. Pijper and B. L. Feringa, *Chem. Eur. J.*, 2016, **22**, 13478–13487.
51 A. S. Lubbe, J. C. M. Kistemaker, E. J. Smits and B. L. Feringa, *Phys. Chem. Chem. Phys.*, 2016, **18**, 26725–26735.
52 J. Chen, J. C. M. Kistemaker, J. Robertus and B. L. Feringa, *J. Am. Chem. Soc.*, 2014, **136**, 14924–14932.
53 J. Bauer, L. Hou, J. C. M. Kistemaker and B. L. Feringa, *J. Org. Chem.*, 2014, **79**, 4446–4455.

54 R. Augulis, M. Klok, B. L. Feringa and P. H. M. van Loosdrecht, *Phys. Stat. Sol.*, 2009, **6**, 181–184.
55 D. Roke, S. J. Wezenberg and B. L. Feringa, *Proc. Natl. Acad. Sci. U.S.A.*, 2018, **115**, 9423–9431.
56 M. M. Pollard, A. Meetsma and B. L. Feringa, *Org. Biomol. Chem.*, 2008, **6**, 507–512.
57 A. Cnossen, W. R. Browne and B. L. Feringa, *Top. Curr. Chem.*, 2014, **354**, 139–162.
58 D. Pijper, R. A. van Delden, A. Meetsma and B. L. Feringa, *J. Am. Chem. Soc.*, 2005, **127**, 17612–17613.
59 J. Vicario, A. Meetsma and B. L. Feringa, *Chem. Commun.*, 2005, 5910–5912.
60 J. Vicario, M. Walko, A. Meetsma and B. L. Feringa, *J. Am. Chem. Soc.*, 2006, **128**, 5127–5135.
61 M. Klok, N. Boyle, M. T. Pryce, A. Meetsma, W. R. Browne and B. L. Feringa, *J. Am. Chem. Soc.*, 2008, **130**, 10484–10485.
62 M. Klok, PhD Thesis, Rijksuniversiteit Groningen, 2009.
63 M. Klok, M. Walko, E. M. Geertsema, N. Ruangsupapichat, J. C. M. Kistemaker, A. Meetsma and B. L. Feringa, *Chem. Eur. J.*, 2008, **14**, 11183–11193.
64 J. Conyard, K. Addison, I. A. Heisler, A. Cnossen, W. R. Browne, B. L. Feringa and S. R. Meech, *Nat. Chem.*, 2012, **4**, 547–551.
65 A. Kazaryan, J. C. M. Kistemaker, L. V. Schäfer, W. R. Browne, B. L. Feringa and M. Filatov, *J. Phys. Chem. A*, 2010, **114**, 5058–5067.
66 C. R. Hall, W. R. Browne, B. L. Feringa and S. R. Meech, *Angew. Chem. Int. Ed.*, 2018, **57**, 6203–6207.
67 C. R. Hall, J. Conyard, I. A. Heisler, G. Jones, J. Frost, W. R. Browne, B. L. Feringa and S. R. Meech, *J. Am. Chem. Soc.*, 2017, **139**, 7408–7414.
68 J. Conyard, A. Cnossen, W. R. Browne, B. L. Feringa and S. R. Meech, *J. Am. Chem. Soc.*, 2014, **136**, 9692–9700.
69 B. G. Levine and T. J. Martínez, *Annu. Rev. Phys. Chem.*, 2007, **58**, 613–634.
70 A. Kazaryan, Z. Lan, L. V. Schäfer, W. Thiel and M. Filatov, *J. Chem. Theory Comput.*, 2011, **7**, 2189–2199.
71 F. Liu and K. Morokuma, *J. Am. Chem. Soc.*, 2012, **134**, 4864–4876.
72 M. Filatov and M. Olivucci, *J. Org. Chem.*, 2014, **79**, 3587–3600.
73 X. Pang, X. Cui, D. Hu, C. Jiang, D. Zhao, Z. Lan and F. Li, *J. Phys. Chem. A*, 2017, **121**, 1240–1249.
74 S. Takeuchi, S. Ruhman, T. Tsuneda, M. Chiba, T. Taketsugu and T. Tahara, *Science*, 2008, **322**, 1073–1077.
75 S. Amirjalayer, A. Cnossen, W. R. Browne, B. L. Feringa, W. J. Buma and S. Woutersen, *J. Phys. Chem. A*, 2016, **120**, 8606–8612.
76 J. Conyard, P. Stacko, J. Chen, S. McDonagh, C. R. Hall, S. P. Laptenok, W. R. Browne, B. L. Feringa and S. R. Meech, *J. Phys. Chem. A*, 2017, **121**, 2138–2150.
77 A. S. Sardjan, P. Roy, W. Danowski, G. Bressan, L. Nunes dos Santos Comprido, W. R. Browne, B. L. Feringa and S. R. Meech, *ChemPhysChem*, 2020, **21**, 594–599.

78 D. R. S. Pooler, R. Pierron, S. Crespi, R. Costil, L. Pfeifer, J. Léonard, M. Olivucci and B. L. Feringa, *Chem. Sci.*, 2021, **12**, 7486–7497.
79 L. Pfeifer, M. Scherübl, M. Fellert, W. Danowski, J. Cheng, J. Pol and B. L. Feringa, *Chem. Sci.*, 2019, **10**, 8768–8773.
80 M. J. Hansen, M. M. Lerch, W. Szymanski and B. L. Feringa, *Angew. Chem. Int. Ed.*, 2016, **55**, 13514–13518.
81 K. Kalka, H. Merk and H. Mukhtar, *J. Am. Acad. Dermatol.*, 2000, **42**, 389–413.
82 J. Broichhagen, J. A. Frank and D. Trauner, *Acc. Chem. Res.*, 2015, **48**, 1947–1960.
83 R. A. van Delden, N. Koumura, A. Schoevaars, A. Meetsma and B. L. Feringa, *Org. Biomol. Chem.*, 2003, **1**, 33–35.
84 T. van Leeuwen, J. Pol, D. Roke, S. J. Wezenberg and B. L. Feringa, *Org. Lett.*, 2017, **19**, 1402–1405.
85 M. M. Pollard, P. V. Wesenhagen, D. Pijper and B. L. Feringa, *Org. Biomol. Chem.*, 2008, **6**, 1605–1612.
86 S. J. Wezenberg, K. Y. Chen and B. L. Feringa, *Angew. Chem. Int. Ed.*, 2015, **54**, 11457–11461.
87 A. Cnossen, L. Hou, M. M. Pollard, P. V. Wesenhagen, W. R. Browne and B. L. Feringa, *J. Am. Chem. Soc.*, 2012, **134**, 17613–17619.
88 L. Pfeifer, N. V. Hoang, M. Scherübl, M. S. Pshenichnikov and B. L. Feringa, *Sci. Adv.*, 2020, **6**, eabb6165.
89 D. Roke, M. Sen, W. Danowski, S. J. Wezenberg and B. L. Feringa, *J. Am. Chem. Soc.*, 2019, **141**, 7622–7627.
90 A. Gerwien, P. Mayer and H. Dube, *J. Am. Chem. Soc.*, 2018, **140**, 16442–16446.
91 G. Marchand, J. Eng, I. Schapiro, A. Valentini, L. M. Frutos, E. Pieri, M. Olivucci, J. Léonard and E. Gindensperger, *J. Phys. Chem. Lett.*, 2015, **6**, 599–604.
92 I. Schapiro, M. Gueye, M. Paolino, S. Fusi, G. Marchand, S. Haacke, M. E. Martin, M. Huntress, V. P. Vysotskiy, V. Veryazov, J. Léonard and M. Olivucci, *Photochem. Photobiol. Sci.*, 2019, **18**, 2259–2269.
93 A. Strambi, B. Durbeej, N. Ferré and M. Olivucci, *Proc. Natl. Acad. Sci. U.S.A.*, 2010, **107**, 21322–21326.
94 J. Wang, B. Oruganti and B. Durbeej, *ChemPhotoChem*, 2019, **3**, 450–460.
95 B. Oruganti, J. Wang and B. Durbeej, *Org. Lett.*, 2017, **19**, 4818–4821.
96 J. Wang and B. Durbeej, *ChemistryOpen*, 2018, **7**, 583–589.
97 J. Wang and B. Durbeej, *Comput. Theor. Chem.*, 2019, **1148**, 27–32.
98 M. Filatov, M. Paolino, S. K. Min and K. S. Kim, *J. Phys. Chem. Lett.*, 2018, **9**, 4995–5001.
99 M. Filatov, M. Paolino, S. K. Min and C. H. Choi, *Chem. Commun.*, 2019, **55**, 5247–5250.
100 J.-M. Lehn, *Proc. Natl. Acad. Sci. U.S.A.*, 2002, **99**, 4763–4768.
101 W. Danowski, T. van Leeuwen, S. Abdolahzadeh, D. Roke, W. R. Browne, S. J. Wezenberg and B. L. Feringa, *Nat. Nanotechnol.*, 2019, **14**, 488–494.
102 R. Eelkema, M. M. Pollard, J. Vicario, N. Katsonis, B. S. Ramon, C. W. M. Bastiaansen, D. J. Broer and B. L. Feringa, *Nature*, 2006, **440**, 163.
103 T. van Leeuwen, G. H. Heideman, D. Zhao, S. J. Wezenberg and B. L. Feringa, *Chem. Commun.*, 2017, **53**, 6393–6396.

104 A. Bosco, M. G. M. Jongejan, R. Eelkema, N. Katsonis, E. Lacaze, A. Ferrarini and B. L. Feringa, *J. Am. Chem. Soc.*, 2008, **130**, 14615–14624.

105 J. C. M. Kistemaker, A. S. Lubbe and B. L. Feringa, *Mater. Chem. Front.*, 2021, **5**, 2900–2906.

106 S. Chen, R. Costil, F. K.-C. Leung and B. L. Feringa, *Angew. Chem. Int. Ed.*, 2021, **60**, 11604–11627.

107 R. Costil, A. Guinart and B. L. Feringa, *Chem*, 2020, **6**, 2868–2870.

108 I. Aprahamian, *ACS Cent. Sci.*, 2020, **6**, 347–358.

109 W. Danowski, T. van Leeuwen, W. R. Browne and B. L. Feringa, *Nanoscale Adv.*, 2021, **3**, 24–40.

110 D. Dattler, G. Fuks, J. Heiser, E. Moulin, A. Perrot, X. Yao and N. Giuseppone, *Chem. Rev.*, 2020, **120**, 310–433.

111 J. Wang and B. L. Feringa, *Science*, 2011, **331**, 1429–1432.

112 A. G. Doyle and E. N. Jacobsen, *Chem. Rev.*, 2007, **107**, 5713–5743.

113 R. Dorel and B. L. Feringa, *Chem. Commun.*, 2019, **55**, 6477–6486.

114 D. Zhao, T. M. Neubauer and B. L. Feringa, *Nat. Commun.*, 2015, **6**, 6652.

115 R. Dorel and B. L. Feringa, *Angew. Chem. Int. Ed.*, 2020, **59**, 785–789.

116 S. F. Pizzolato, P. Štacko, J. C. M. Kistemaker, T. van Leeuwen and B. L. Feringa, *Nat. Catal.*, 2020, **3**, 488–496.

117 F. Lancia, A. Ryabchun and N. Katsonis, *Nat. Rev. Chem.*, 2019, **3**, 536–551.

118 D. Zhao, T. van Leeuwen, J. Cheng and B. L. Feringa, *Nat. Chem.*, 2016, **9**, 250–256.

119 R. Krämer, J.-M. Lehn and A. Marquis-Rigault, *Proc. Natl. Acad. Sci. U.S.A.*, 1993, **90**, 5394–5398.

120 R. A. Brown, V. Diemer, S. J. Webb and J. Clayden, *Nat. Chem.*, 2013, **5**, 853–860.

121 D. Pijper and B. L. Feringa, *Angew. Chem. Int. Ed.*, 2007, **46**, 3693–3696.

122 R. Costil, M. Holzheimer, S. Crespi, N. A. Simeth and B. L. Feringa, *Chem. Rev.*, 2021, **121**, 13213–13237.

123 A. M. Schoevaars, W. Kruizinga, R. W. J. Zijlstra, N. Veldman, A. L. Spek and B. L. Feringa, *J. Org. Chem.*, 1997, **62**, 4943–4948.

124 M. K. J. ter Wiel, R. A. van Delden, A. Meetsma and B. L. Feringa, *Org. Biomol. Chem.*, 2005, **3**, 4071–4076.

125 A. S. Lubbe, N. Ruangsupapichat, G. Caroli and B. L. Feringa, *J. Org. Chem.*, 2011, **76**, 8599–8610.

126 P. Štacko, J. C. M. Kistemaker, T. van Leeuwen, M. Chang, E. Otten and B. L. Feringa, *Science*, 2017, **356**, 964–968.

127 Y. Shirai, J.-F. Morin, T. Sasaki, J. M. Guerrero and J. M. Tour, *Chem. Soc. Rev.*, 2006, **35**, 1043–1055.

128 Y. Shirai, A. J. Osgood, Y. Zhao, K. F. Kelly and J. M. Tour, *Nano Lett.*, 2005, **5**, 2330–2334.

129 J. F. Morin, Y. Shirai and J. M. Tour, *Org. Lett.*, 2006, **8**, 1713–1716.

130 P. T. Chiang, J. Mielke, J. Godoy, J. M. Guerrero, L. B. Alemany, C. J. Villagómez, A. Saywell, L. Grill and J. M. Tour, *ACS Nano*, 2012, **6**, 592–597.

131 T. Kudernac, N. Ruangsupapichat, M. Parschau, B. MacIá, N. Katsonis, S. R. Harutyunyan, K. H. Ernst and B. L. Feringa, *Nature*, 2011, **479**, 208–211.

132 A. Saywell, A. Bakker, J. Mielke, T. Kumagai, M. Wolf, V. García-López, P. T. Chiang, J. M. Tour and L. Grill, *ACS Nano*, 2016, **10**, 10945–10952.
133 P. Xie, *ACS Omega*, 2020, **5**, 5721–5730.
134 D. H. Qu and B. L. Feringa, *Angew. Chem. Int. Ed.*, 2010, **49**, 1107–1110.
135 J. J. Yu, L. Y. Zhao, Z. T. Shi, Q. Zhang, G. London, W. J. Liang, C. Gao, M. M. Li, X. M. Cao, H. Tian, B. L. Feringa and D. H. Qu, *J. Org. Chem.*, 2019, **84**, 5790–5802.
136 D. Roke, C. Stuckhardt, W. Danowski, S. J. Wezenberg and B. L. Feringa, *Angew. Chem. Int. Ed.*, 2018, **57**, 10515–10519.
137 N. Ruangsupapichat, M. M. Pollard, S. R. Harutyunyan and B. L. Feringa, *Nat. Chem.*, 2011, **3**, 53–60.
138 W. Szymanski, J. M. Beierle, H. A. V Kistemaker, W. A. Velema and B. L. Feringa, *Chem. Rev.*, 2013, **113**, 6114–6178.
139 M. M. Lerch, M. J. Hansen, G. M. van Dam, W. Szymanski and B. L. Feringa, *Angew. Chem. Int. Ed.*, 2016, **55**, 10978–10999.
140 J. Volarić, W. Szymanski, N. A. Simeth and B. L. Feringa, *Chem. Soc. Rev.*, 2021, **50**, 12377–12449.
141 A. S. Lubbe, C. Böhmer, F. Tosi, W. Szymanski and B. L. Feringa, *J. Org. Chem.*, 2018, **83**, 11008–11018.
142 C. Poloni, M. C. A. Stuart, P. van der Meulen, W. Szymanski and B. L. Feringa, *Chem. Sci.*, 2015, **6**, 7311–7318.
143 A. Herrmann, A. H. de Vries, J. W. de Vries, J. C. M. Kistemaker, I. Faustino, A. S. Lubbe, B. L. Feringa, Q. Liu, W. Szymanski, S. J. Smith and Z. Meng, *J. Am. Chem. Soc.*, 2018, **140**, 5069–5076.
144 A. C. Coleman, J. M. Beierle, M. C. A. Stuart, B. Maciá, G. Caroli, J. T. Mika, D. J. van Dijken, J. Chen, W. R. Browne and B. L. Feringa, *Nat. Nanotechnol.*, 2011, **6**, 547–552.
145 D. Zhao, Y. Wei, E. J. Boekema, M. C. A. Stuart, B. L. Feringa, L. E. Franken and J. Chen, *J. Am. Chem. Soc.*, 2018, **140**, 7860–7868.
146 J. Chen, F. K. C. Leung, M. C. A. Stuart, T. Kajitani, T. Fukushima, E. Van Der Giessen and B. L. Feringa, *Nat. Chem.*, 2018, **10**, 132–138.
147 V. García-López, F. Chen, L. G. Nilewski, G. Duret, A. Aliyan, A. B. Kolomeisky, J. T. Robinson, G. Wang, R. Pal and J. M. Tour, *Nature*, 2017, **548**, 567–572.
148 D. Liu, V. Garcia-Lopez, R. S. Gunasekera, L. Greer Nilewski, L. B. Alemany, A. Aliyan, T. Jin, G. Wang, J. M. Tour and R. Pal, *ACS Nano*, 2019, **13**, 6813–6823.
149 R. S. Gunasekera, T. Galbadage, C. Ayala-Orozco, D. Liu, V. García-López, B. E. Troutman, J. J. Tour, R. Pal, S. Krishnan, J. D. Cirillo and J. M. Tour, *ACS Appl. Mater. Interfaces*, 2020, **12**, 13657–13670.
150 Q. Zhou, J. Chen, Y. Luan, P. A. Vainikka, S. Thallmair, S. J. Marrink, B. L. Feringa and P. Van Rijn, *Sci. Adv.*, 2020, **6**, eaay2756.
151 K.-Y. Chen, O. Ivashenko, G. T. Carroll, J. Robertus, J. C. M. Kistemaker, G. London, W. R. Browne, P. Rudolf and B. L. Feringa, *J. Am. Chem. Soc.*, 2014, **136**, 3219–3224.
152 K. Y. Chen, S. J. Wezenberg, G. T. Carroll, G. London, J. C. M. Kistemaker, T. C. Pijper and B. L. Feringa, *J. Org. Chem.*, 2014, **79**, 7032–7040.
153 K. Adachi, R. Yasuda, H. Noji, H. Itoh, Y. Harada, M. Yoshida and K. Kinosita, *Proc. Natl. Acad. Sci. U.S.A.*, 2000, **97**, 7243–7247.

154 J. Chen, J. Vachon and B. L. Feringa, *J. Org. Chem.*, 2018, **83**, 6025–6034.
155 B. Krajnik, J. Chen, M. A. Watson, S. L. Cockroft, B. L. Feringa and J. Hofkens, *J. Am. Chem. Soc.*, 2017, **139**, 7156–7159.
156 B. L. Feringa, N. P. M. Huck and A. M. Schoevaars, *Adv. Mater.*, 1996, **8**, 681–684.
157 M. Gu, X. Li and Y. Cao, *Light Sci. Appl.*, 2014, **3**, e177.

Chapter 2

Fluorinated and Alkylated Quaternary, Second Generation Molecular Motors for Electrochemically Driven Rotary Motion

Unidirectional rotation of photochemically driven overcrowded alkene-based motors is a fascinating and well-established field. The ability to control unidirectional rotary motion with different stimuli would provide great potential and insight for the development of complex responsive and smart materials. Previous work showed that the presence of an acidic proton at the allylic position of second generation molecular motors was detrimental for electrochemically-triggered unidirectional rotation. Rooted in our previous studies on electrochemical switches and photochemically driven motors, modifications of existing motors by quaternarisation at the allylic position and novel designs of second-generation molecular motors are presented. Fluorinated quaternary molecular motors are shown to be sensitive molecules and are prone to degradation. Nevertheless, we could observe some photochemical and electrochemical switching, but unidirectional rotation was not achieved due to the high barriers for the required thermal interconversions. Quaternary benzothiophene-based molecular motors show that the electrochemical oxidation also results in a chemical deprotonation at the benzylic position and double bond shift. Transient absorption spectroscopy indicated that benzothiophene-based motors with a six-membered stator half are fast photochemical molecular motors. The obtained photochemical and electrochemical results have given new insights for our continuing programme towards electrochemically-driven unidirectional molecular motion.

Acknowledgement
I would like to thank Dr. Ruth Dorel for her contribution to the synthesis of alkylated quaternary motors (Section 2.7) and Dr. Stefano Crespi, Prof. Dr. Wybren Jan Buma and Ing. Michiel Hilbers, for the transient spectroscopy experiments on the benzothiophene motors (Section 2.9).

1. Introduction

In the development of molecular unidirectional motors,[1–6] the use of multi-stimuli responsive structures is highly attractive. The molecular motors previously developed in our group are driven by light and heat, based on a photochemical *E*/*Z*-isomerisation and a thermal helix inversion (for detailed information, see Chapter 1 of this thesis).[1,7,8] In nature, molecular motors are mostly driven by chemical energy[9] or an ion flux.[10] Using the movement of charge, i.e. current, to create unidirectional molecular motion in a synthetic molecule is a fascinating challenge to take on.

Various other electrochemical or redox-driven molecular switches are known.[11,12] Electrochemical switches can be based on electrocyclisation reactions,[13,14] metal coordination chemistry[15] or organic redox-active motifs.[16] A special class of electrochemical switches are the molecular machines based on mechanically interlocked molecules, where the redox events cause motion on the molecular scale. The redox-chemistry of Cu-complexes has been used successfully for such switches. By electrochemically switching between a tetravalent Cu^{I} complex and a pentavalent Cu^{II} complex, relative motion of the interlocking rings is induced.[17] The same Cu complexation redox-switching can be used in rotaxanes (Figure 1a).[18,19] Alternatively, in catenanes such as compound **1** (Figure 1b), motion of a macrocycle can be driven by oxidation of a tetrathiafulvalene unit, causing repulsion of a paraquat-motif.[20]

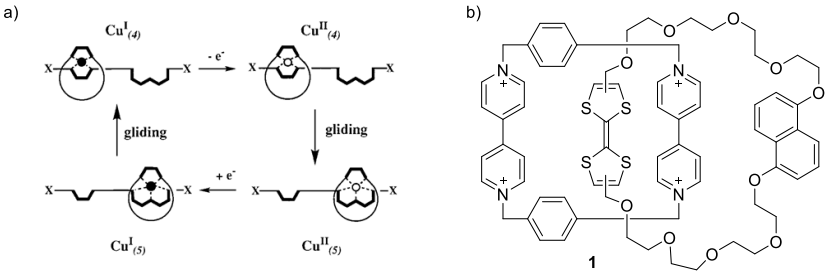

Figure 1. a) Schematic overview of a rotaxane redox switch.[18] Figure adapted with permission from Ref 18, Copyright ACS. b) Catenane redox-switch **1**.[20]

As the unidirectional molecular motors developed in our group have been based on double bond isomerisations, it is of great interest to develop switches that utilise an electrochemical *E*/*Z*-isomerisation. A number of electrochemical double bond isomerisations have previously been described. Oxidative *Z*-to-*E*-isomerisation of N=N double bonds is known for azonorbornane[21] and azobenzenes.[22] However, azobenzene reduction is

more commonly studied and indeed, azobenzenes can be switched in a reductive fashion from a *Z*- to an *E*-isomer.[23] Additionally, for C=C double bonds, *Z*-to-*E*-isomerisation is possible, as shown in examples using oxidative electrochemistry of stilbenes and stilbene derivatives.[24–26]

With scanning tunnelling microscopy (STM), it is possible to isomerise double bonds via STM tip voltage pulses by a tunnelling current or an electric field.[27,28] A nanocar (**2**, Figure 2), based on four overcrowded alkene motors as wheels, was shown to perform isomerisation and movement through the application of a voltage bias with the STM tip of > 600 mV under low temperature (7 K) STM conditions, on a Cu(111) surface.[29]

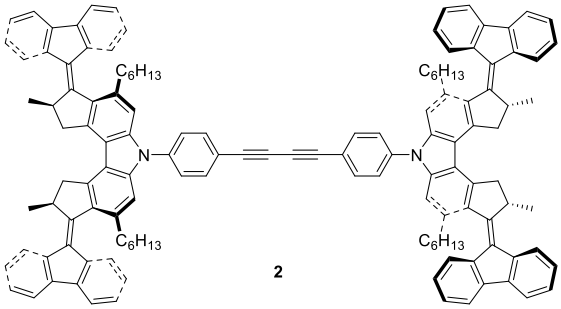

Figure 2. Nanocar **2** was used for driving on a Cu(111) surface by STM tip voltage bias.[29]

A common photochemical unidirectional molecular motor (compound **3**, Scheme 1) contains a stilbene motif and is comparable to a bisthioxanthylidene. The electrochemistry of bisthioxanthylidenes is robust and shows reversible and stable electrochemical switching.[30,31] Bisthioxanthylidenes are describe in more detail in Chapter 3 of this thesis.

Second generation molecular motor **3** was investigated by our group for its potential as an electrochemically-driven unidirectional molecular motor.[32] Oxidation of motor **3** at 1.0 V vs. SCE resulted in the expected dicationic $\mathbf{3}^{2+}$. Unfortunately, at this stage an irreversible chemical reaction, i.e., deprotonation occurs, resulting in $\mathbf{4}^{+}$ where, crucially, the point chirality of the methyl substituted stereogenic centre is no longer present. As the chirality of this stereogenic centre is of fundamental importance to the unidirectional molecular motion (see Chapter 1 of this thesis for further details), this strategy did not prove successful for the final goal of electrochemically driven molecular motion, but did provide important insight into the requirements to obtain an “electromotor”.

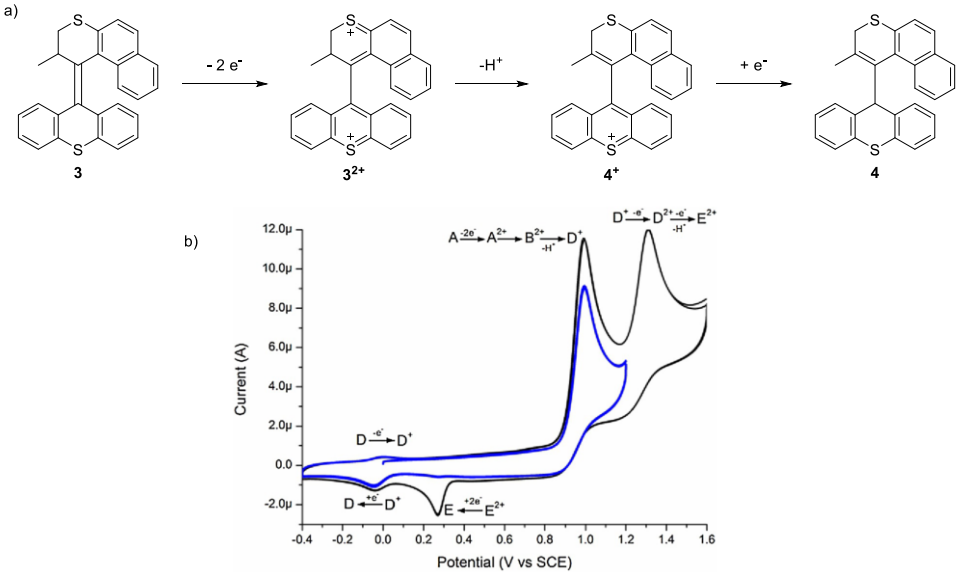

Scheme 1. a) Electrochemical pathway of second generation motor **3**.[32] b) Cyclic voltammetry of **3**, scan rate = 0.1 V s^{-1}, 0.1 M $TBAPF_6$ in CH_3CN. Reproduced with permission from Ref 32, copyright John Wiley and Sons.

The deprotonation event and subsequent loss of chiral information needs to be avoided for successful electrochemically driven directional molecular motion. Our attempts towards this goal are initially further developed with blocking the deprotonation by replacing the allylic hydrogen atom for more inert substituents.

The stereogenic centre in molecular motors has been a point of investigation in a few previous studies.[33–35] The difference in size and orientation of the group can have a strong influence on the speed of the motor rotation. Enhanced torsional strain caused by the steric hindrance of the substituent at the stereogenic centre can increase the speed of rotation by destabilising the *metastable* state, as was shown with Me, Ph, *i*-Pr and *t*-Bu substituents (for further information on speed of molecular motors, see Chapter 1 of this thesis).[33,34]

Molecular motors with a quaternary allylic centre adjacent to the overcrowded alkene motif, "quaternary motors" are less common than their analogues with a tertiary allylic centre: "tertiary motors". A study in 2017 by Štacko and co-workers presented fluorinated quaternary molecular motors (Figure 3).[35] Fluorine was chosen as a small substituent, suitable as a replacement for the hydrogen atom in the previously studied molecular motors. The introduction of the fluorinated centre caused a significant decrease in motor rotation speed, by increased strain in the transition state

for THI. The increase in rotational barrier was shown to be approximately 20–25 kJ mol^{-1}.[35]

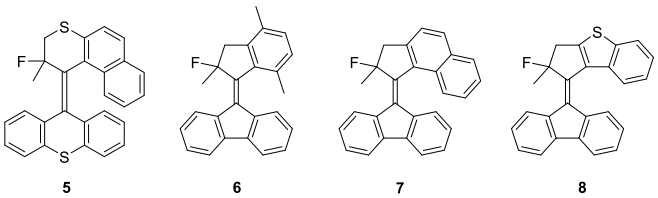

Figure 3. Previously synthesised fluorinated molecular motors.

In the present study, further attempts and new designs are made for electrochemically-driven, unidirectional, molecular rotary motion. The goal is to develop a molecular motor with robust, repeatable and reliable electrochemical switching. Notably, this includes the retention of the chirality required for selective rotation around the central axis. Finally, the unidirectionality of the redox motor needs to be demonstrated using only electrochemical and thermal steps to induce rotary motion.

2. Results & Discussion

In order to find a molecular motor suitable for electrochemically driven, unidirectional molecular motion, we first set out to adapt known molecular motor scaffolds and modify them to fit the requirements of redox-driven switching. As shown previously, the hydrogen at the stereogenic centre is a highly sensitive position and substituting it for a less labile substituent seems an important next step.

2.1 Fluorinated motors

The bisthioxanthylidene scaffold with two sulfur atoms in conjugation to the central double bond has shown to be a robust motif for redox switching (see Chapter 3 for further information).[30,36] The combination of the fluorinated stereogenic centre and the use of two sulfur atoms in conjugation with the central double bond prompted us initially to look into molecular motor **5** for investigation as potential redox-driven molecular motor (Figure 4). The increased barrier for thermally induced helix inversion and, as a consequence, rotation is an expected problem. Motors **9** and **10** are designed with a reduced steric hindrance in the fjord-region in the hope of alleviating the issues with high rotation barriers. Motor **11** is designed to have a further decrease in steric hindrance in the fjord-region and has a rotor half sulfur atom introduced as part of a benzothiophene motif.

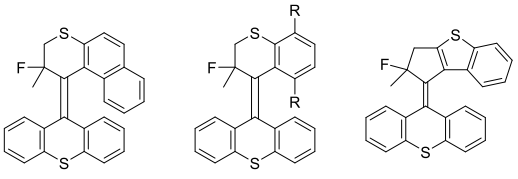

Figure 4. Fluorinated molecular motor targets designed for electrochemically driven motion.

The first strategy towards substitution of the allylic hydrogen in second generation molecular motors is to use a fluorine atom, such as described above (Figure 3, compounds **5–8**). The synthesis of these motors follows a common strategy with a Barton-Kellogg synthesis as its final step.[35] The fluorine atom is installed in an α-fluorination step via α-deprotonation and the use of electrophilic N–F reagents as a well-established method for fluorine introduction.[37,38]

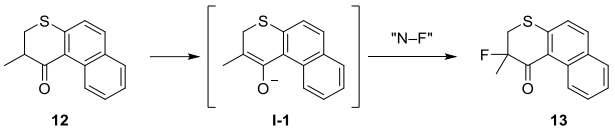

Scheme 2. α-fluorination.

For the synthesis of **5** (Figure 3), the strategy reported in previous work by our group[35] was used as a starting point and was optimised for a few steps. The main steps involve the thiol-alkene reaction of 2-naphthalenethiol with methacrylic acid, followed by Friedel-Crafts cyclisation to obtain thiochromenone **12** (Scheme 3).

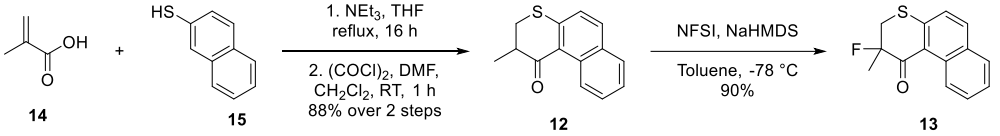

Scheme 3. Synthesis of α-fluorinated ketone **13**.

Ketone **9** was fluorinated in a modified procedure by deprotonation and addition of electrophilic fluorine reagent *N*-fluorosuccinimide (NFSI). The choice of solvent is of crucial importance to the outcome of the reaction as the presence of THF as a solvent led to the formation of α,β-unsaturated ketone or complex mixtures of products. A small optimisation resulted in the best option for the α-fluorination of **12** using the commercially available NaHMDS in toluene as a base, dry toluene as the reaction solvent and the portion wise addition of solid NFSI at low temperature. Note that commercially available NaHMDS is commonly found in THF, which is

unfeasible for this reaction. It is possible that the cause for the significant change in reactivity in different solvents is the relative rate of nucleophilic substitution versus electron transfer between the sodium enolate and the fluorinating agent.[39–41] The formed radical could result in an elimination reaction leading to the α,β-unsaturated ketone or via potential radical termination reaction to the complex mixture of products observed.

The required thioketone (compound **16**, Scheme 4) for the Barton-Kellogg reaction to obtain the central olefinic bond is not sufficiently stable to be isolated. Therefore, it is made *in situ* and used directly in the next reaction. The thionation to obtain **16** was followed by TLC (silica, 3% EtOAc/*n*-pentane) and by taking aliquots, filtration over silica gel with Et_2O and ^{1}H-NMR spectroscopy. Here, 3.0 equivalents of Lawesson's reagent and 3.0 equivalents of P_2S_5 were used in toluene heated at reflux. The only signals of the expected thioketone product **16** that could be identified and followed were found at a chemical shift (400 MHz, $CDCl_3$) of 8.44 (d, J = 8.4 Hz, 1H) and 1.92 ppm (d, $J_{H\text{-}F}$ = 20.4 Hz, 3H). The optimal conversion found for this reaction was approximately 70%, before degradation became significant. For the synthesis of motor **5**, the conversion of **13** to **16** was followed by TLC and the thioketone product was directly used as soon as degradation was observable.

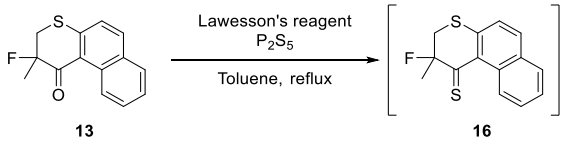

Scheme 4. Thionation of **13**.

The diazo coupling partner for the Barton-Kellogg reaction **20** could be obtained *in situ* from the oxidation of hydrazone **19**. The hydrazone was synthesised using a literature procedure by thionation of thioxanthone (**17**), followed by hydrazine formation using hydrazine monohydrate.[42]

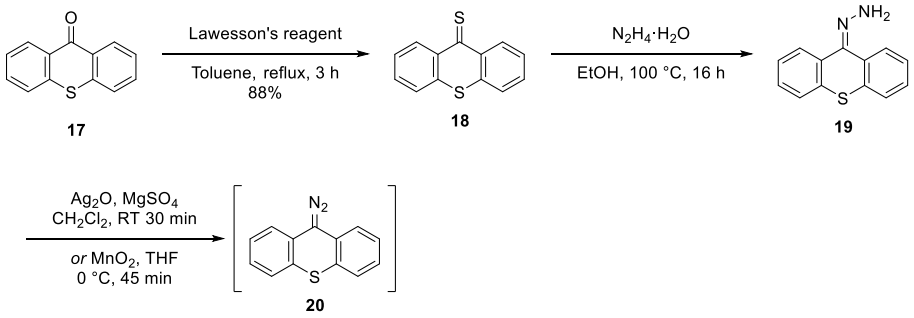

Scheme 5. Synthesis of diazo compound **20**.

As both components **16** and **20**, required for the Barton-Kellogg reaction, are not stable enough to be isolated, both need to be synthesised *in situ* and directly mixed. This was done by careful timing to obtain simultaneously the optimal conversion for both reagents. The thioketone **16**, after optimal conversion, was filtered over a plug of silica gel under N_2 outflow directly into a Schlenk flask containing the freshly made solution of the diazo compound **20**. Conversion towards the episulfide **21** could be observed, which was subsequently desulfurised using $P(NMe_2)_3$. Following the formation and conversion of episulfide **21** was performed using ^{19}F-NMR spectroscopy. The sterically congested, fluorinated molecules **21** and **5** are both sensitive compounds prone to elimination and other degradation pathways during the reaction and purification steps. Purification of a small amount of target **5** was successfully done by careful, but rapid flash column chromatography on basified silica followed by trituration with cold *n*-hexane and the product was characterised by ^{1}H-, ^{13}C- and ^{19}F-NMR spectroscopy, which was in agreement with the literature.[35]

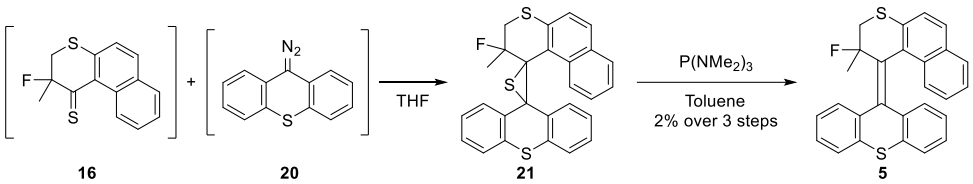

Scheme 6. Barton-Kellogg coupling towards fluorinated motor **5**.

2.2 Computational chemistry of the THI of a fluorinated motor

With an understanding that the barrier for thermal helix inversion of fluorinated molecular motors is high, it is worthwhile to obtain information about this fundamental step. By DFT calculations at B3LYP/6-31G** level of theory, a likely pathway for THI of motor **5** was analysed (Figure 5).[43] Starting from the *metastable* state, the first transition is the movement of the methyl group over the stator ring, leading to a more twisted conformation for I1. Next, the naphthyl motif moves over the stator half, which corresponds to the highest point in the overall reaction (127.7 kJ mol^{-1}), as expected. This leads to an intermediate, still twisted state of the molecule at I2, which can interconvert via TS3 to the *anti*-folded structure of the *stable* state.

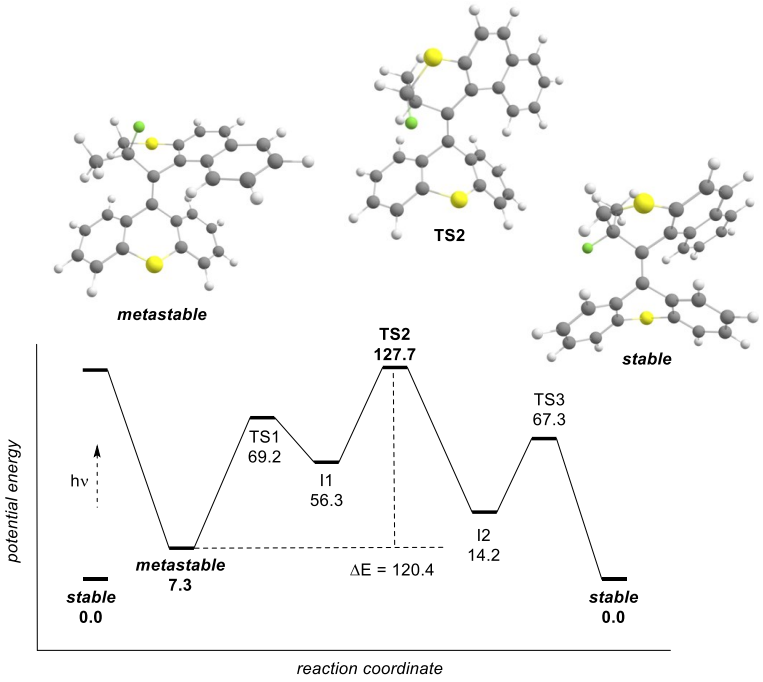

Figure 5. Schematic overview of the reaction coordinate for the thermal helix inversion of **5**, based on DFT calculations at B3LYP/6-31G** level of theory.

The overall THI has a relative energy barrier of 120.4 kJ mol^{-1}, which via the Eyring equation corresponds to a barrier of $t_{1/2}$ = 10.2 years at room temperature. The non-fluorinated "parent motor" has an experimental barrier for THI of 106 kJ mol^{-1} ($t_{1/2}$ = 240 d at room temperature),[44] indicating an estimated increase of 14.4 kJ mol^{-1} due to the introduction of the fluorine substituent. This high barrier for rotation can lead to unfortunate effects. At the temperature required for rotation, thermal pathways for isomerisation, such as thermal *E*/*Z*-isomerisation or thermal degradation, are increasingly likely.

A possible effect on the stability of the conformers of fluorinated motors such as **5** can be the interaction of the fluorine atom with the sulfur atom. The fluorine-gauche effect[45,46] is a known feature for organofluorine compounds, where the fluorine atom prefers a *gauche* conformation with respect to another heteroatom. A number of examples with a S–C–C–F motif are known.[47,48] The S-C-C-F motif found in motor **5** and its precursors likely has consequences for destabilising conformations where this fluorine-gauche orientation cannot be present. The strong electronegativity of the fluorine atom can have a significant influence on the conformer stability.

2.3 Electrochemistry of a fluorinated motor

The redox properties of fluorinated motor **5** were investigated by cyclic voltammetry, in a standard three-electrode setup (Figure 6) with tetrabutylammonium hexafluorophosphate ($TBAPF_6$) as supporting electrolyte in CH_2Cl_2. In the positive potential direction, a current is observed with an $E_{p,a}$ = 0.75 V vs. Ag/AgCl. The reverse direction shows a current at $E_{p,c}$ = 0.32 V vs. Ag/AgCl. This provides a hysteresis between the oxidation and reduction signals for this compound of 0.43 V. The expected cause of this electrochemical response is similar to the response found in bisthioxanthylidenes (for further details, see Chapter 3 of this thesis).

Likely, upon two-electron oxidation,[32] a geometrical change occurs from the most stable *anti*-folded state towards a more twisted state (Figure 6b), allowing for a planar stator half. As the reduction of this conformer is less facile, the reduction potential is shifted towards 0.32 V vs. SCE. A small reduction signal is visible at -0.4 V vs. SCE, which is an indication that there is some degradation of the sample occurring. The initial colourless sample turned faintly pink after a number of cycles.

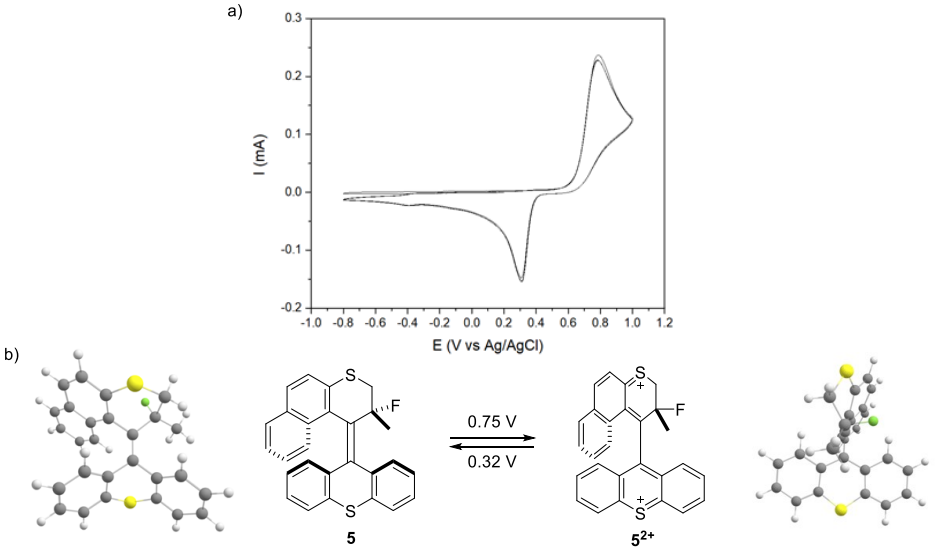

Figure 6. a) Cyclic voltammogram of fluorinated molecular motor **5**. GC working electrode, Pt wire counter electrode, Ag/AgCl reference electrode, 0.1 V s^{-1}, 5 (0.1 mM), $TBAPF_6$ (0.1 M), CH_2Cl_2, RT. b) Representation of the hypothesised conformational switching.

The electrochemical results are promising that a quaternary molecular motor can be used for electrochemical switching, although a more stable structure than **5** would be favourable.

2.4 Absorption spectroscopy of a fluorinated motor

Motor **5** was further investigated by absorption spectroscopy. As it is expected that the THI needs elevated temperatures, solvents with relatively high boiling points are chosen. In acetonitrile three absorption maxima are observed at 222 nm, 255 nm and 315 nm (Figure 7a). Upon irradiation with 312 nm light, a shoulder appears around 280 nm and we observe increased absorption around 390 nm. We expect that this significant redshift, tailing towards 430 nm, is indicative of a degradation pathway. In tetrachloroethane the initial spectrum has maxima at 282 nm and 319 nm (Figure 7b). Upon irradiation with 312 nm light there is a significant increase in absorption of the 282 nm signal. Additionally, a new absorption bands appears at 388 nm and a broad absorption is observed tailing towards 570 nm. This is again indicative that there is no stable photoswitching, but rather another degradation pathway.

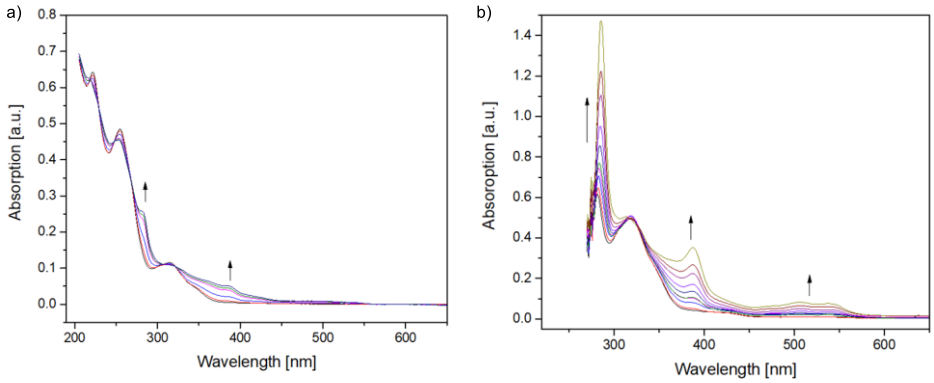

Figure 7. a) Motor **5**, MeCN, 15 µM, RT, irradiation 312 nm. b) Motor **5**, tetrachloroethane, 15 µM, RT, irradiation 312 nm.

The absorption spectrum in *n*-heptane is very similar to the initial spectrum in acetonitrile with absorption maxima at 224 nm, 257 nm and 316 nm. However, when the sample of **5** in *n*-heptane was irradiated with 312 nm light, photoswitching was observed (Figure 8) with clear isosbestic points (Figure 8, inset). The sample was irradiated to PSS and subsequently heated to 50 °C in the dark for 5 h. Unfortunately, heating the sample did not show any indication of THI, but indicated a degradation at elevated temperatures.

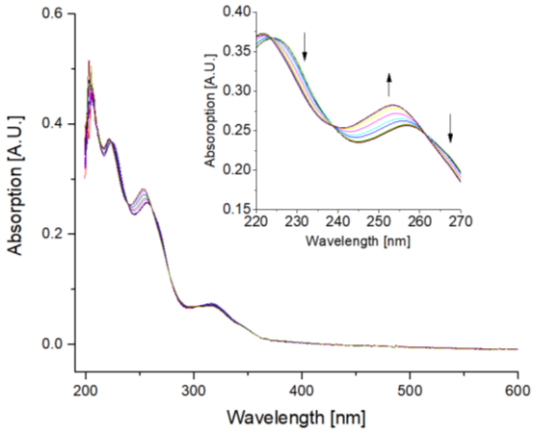

Figure 8. Motor **5**, *n*-heptane, 9 μM, RT, irradiation 312 nm.

From these UV-vis and irradiation studies we conclude that motor **5** seems to function as a photoswitch but is limited by its propensity towards degradation in polar solvents and upon heating.

2.5 Decreasing the size of the rotor half

With the establishment of the unfeasible high barrier for THI, alternatives to **5** were designed (Figure 4). Decreasing the barrier to THI can be done in a number of ways (for further details see Chapter 1 of this thesis), one of which is the decrease of steric hindrance in the fjord region. The reliability of the electrochemistry of bisthioxanthylidene-type structures is well established, leading to a design which persisted in the thioxanthene stator half and the use of a thiochromenone structure in the rotor half. The fluorine substituent was maintained to avoid the problems arising from the allylic deprotonation upon oxidation.

The benzannulated structure in compound **5** is also replaced by a methyl or methoxy substituent. The use of *para*-disubstituted structures increases the ease of synthesis of the rotor halves by avoiding the possibility of the formation of regioisomers in the Friedel-Crafts acylation step (Scheme 4).

Previous studies have shown that the replacement of the rotor naphthalene motif with a *para*-xylene motif had an accelerating effect on the THI.[49] A substituent at this position remains necessary to avoid photocyclisation reactions.[50] A methoxy-substituted design was chosen to potentially increase the effect of lower steric hindrance in the fjord region. A methoxy group has a lower effective steric size,[51,52] because of the ability of a methoxy substituent to adapt a more favourable conformation in contrast to the methyl substituent, which is more rigidly pointed towards the stator half.

The synthesis of **25** and **28** were performed in a parallel method (Scheme 7). Starting from the *para*-dimethyl and *para*-dimethoxy benzene thiols, respectively, a combination of thiol-olefin addition and Friedel-Crafts reaction could be used to obtain the two rotor halves **25** and **29** in good or moderate yields. For these reactions an established procedure was used with triethylamine, methacrylic acid in THF to form the thioether connection. The intermediate carboxylic acids were used directly by conversion of the carboxylic acid into an acyl chloride functionality, followed by Friedel-Crafts acylation using $AlCl_3$.

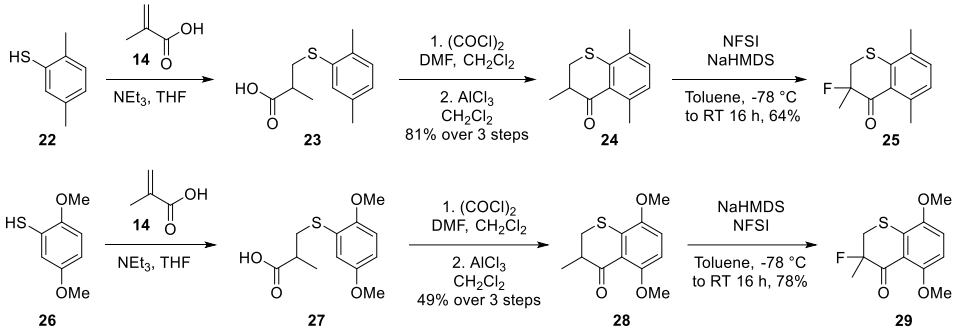

Scheme 7. Synthesis of ketones **25** and **29**.

For the purposes of this research the α-position requires substitution. For other projects ketones **24** and **28** could be used as rotors for molecular motors without further substitution. The substitution of **24** and **28** were performed with the same method as the benzannulated analogue, using NFSI as electrophilic fluoride source and NaHMDS in toluene as a base. Likewise, the use of THF should be avoided to exclude the degradation pathway found in α-fluorination of γ-sulfur carbonyl motifs discussed above. Attempted fluorination of **24** with NaHMDS in THF resulted in the observation of the eliminated product by GC-MS (m/z = 204). Using toluene exclusively, fluorinated ketones **25** and **29** could be obtained in good to excellent yields.

Proceeding to synthesise the corresponding molecular motors, fluorinated ketone **25** was submitted to various conditions to form the thioketone. The thioketones were found to be unstable and degraded rapidly. As diazo-compound **20** is unstable as well, both thioketone and diazo coupling partner for the Barton-Kellogg synthesis had to be obtained *in situ* and simultaneously. For the thioketone formation, a toluene solution of **25** was heated at reflux with 2 equivalents of both P_2S_5 and Lawesson's reagent and the conversion was monitored closely by TLC analysis. Upon the first indication of degradation the coupling partners were combined after removal of the thionation reagents using filtration over either Celite or silica under N_2 flow.

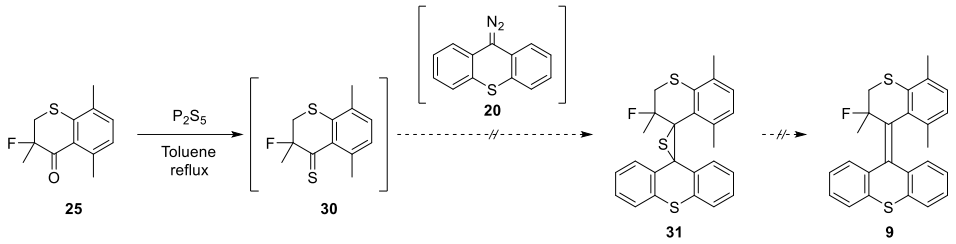

Scheme 8. Attempted synthesis of fluorinated motor **9**.

Analysis of the resulting mixtures indicated the formation of many compounds after these reactions. Purification by flash column chromatography did not lead to any measurable level of isolated episulfide **31** or overcrowded alkene **9**. It is unknown if the lack of obtained product is caused by a lack of conversion towards the episulfide or due to instability and decomposition of the final product upon purification attempts. Using dimethoxy ketone **29** instead of dimethyl ketone **25** resulted in a similar complex mixture of products after the reaction and no isolated product.

2.6 Benzothiophene-based fluorinated motor

The third type of target for the fluorinated molecular motors to be used for electrochemically driven molecular motion is the structure containing a benzothiophene motif (Figure 4, compound **11**). In order to obtain the necessary rotor half for Barton-Kellogg coupling, first benzothiophene was reacted with methacrylic acid in polyphosphoric acid. This leads to a mixture of regioisomers **33** and **34** (Scheme 9) that can be separated by a combination of flash column chromatography and crystallisation from ethanol.

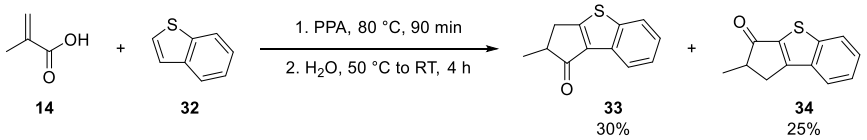

Scheme 9. Synthesis of rotor half building block **33**.

The benzothiophene-based ketone **33**, does not suffer from the same reactivity problems as the thiochromenone-based ketones discussed above. Likely, the electron transfer pathway is significantly slower than the nucleophilic substitution. Therefore, the fluorination of **33** could be done in a more straightforward method using LDA and NFSI in THF to afford **35** in a good yield. The fluorinated ketone **35** could be converted to a thioketone prior to reaction with diazo compound **20**. The desired overcrowded alkene could be observed after this Barton-Kellogg reaction. However, the product

is highly susceptible to HF-elimination and no significant amount of **11** could be isolated as a pure compound.

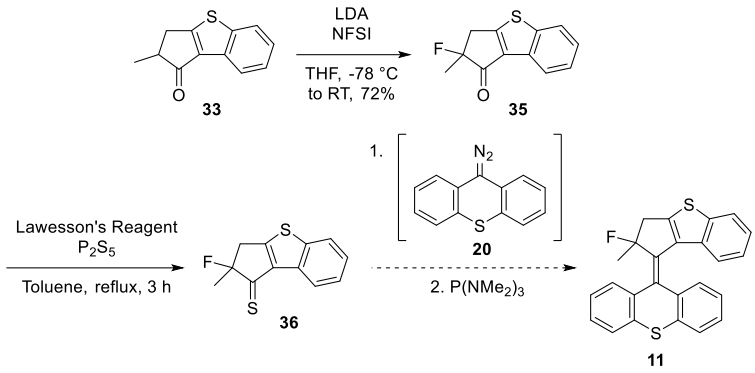

Scheme 10. Attempted synthesis route towards molecular motor **11**.

2.7 Alkylated quaternary motors

Because of the observed sensitivity of the fluorinated molecular motors, in combination with the considerable effect of increasing the THI to unfeasible levels, we opted to change the fluorine atom for an alkyl substituent. Maintaining the same core architecture of a thioxanthone and a thiochromenone half, the target compounds **37–40** (Figure 7) were designed. Compounds **41** and **42** are proposed as analogues of the previously described fluorinated motor **11** (Figure 4). As second generation quaternary bis-alkyl motors have not previously been studied, we investigated the R = Me analogues (**37**, **39**, Figure 7) in parallel for synthesis purposes and as potential switches.

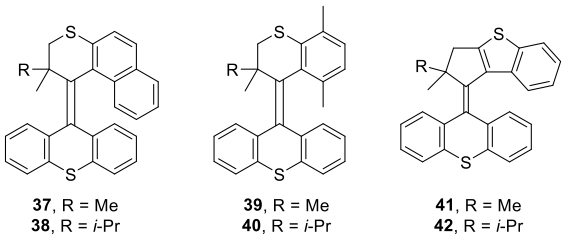

Figure 7. Alkylated molecular motor targets of interest for electrochemically driven motion.

After the direct α-alkylation of the previously made rotor half ketones **12** (Scheme 2), **24** and **28** (Scheme 7) had proven to be unsuccessful, due to low reactivity or degradation, a new synthesis route was explored. By employing a strategy with earlier incorporation of the α-quaternary position we could obtain the target ketones (*vide infra*).

Dimethyl malonate derivative **44** was synthesised, starting from commercially available **43**. By a straightforward tosylation the hydroxy group is functionalised for use in a nucleophilic substitution reaction. 2,5-Dimethyl benzenethiol could be used as a nucleophile to make the thioether linkage to obtain **45**. The methyl ester could be deprotected by hydrolysis under basic conditions and carboxylic acid **46** was obtained after reprotonation. By using *para*-dimethyl benzene thiol **22** in the thioether formation step, the Friedel-Crafts acylation become more facile as it does not allow for regioisomeric products. The methyl group that is not pointing towards the fjord region is not strictly necessary for the motor design. The Friedel-Crafts acylation via the acyl chloride intermediate was successful and dimethyl ketone **47** was obtained in a good yield.

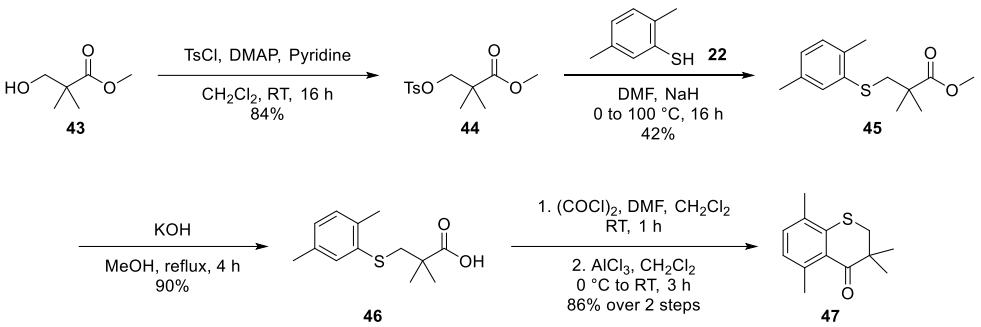

Scheme 11. Synthesis route of ketone **47**.

The methyl/isopropyl analogue was obtained in a similar manner by early-stage alkylation. From the methylation of commercially available isopropyl malonate **48**, compound **49** (Scheme 12) was obtained in quantitative yield. One side of the malonate is envisioned to be used for later Friedel-Crafts acylation and the other to be functionalised as a thioether. In this pursuit, **49** was carefully reduced to obtain as much of the mono alcohol as possible. Using sequential reduction steps with DIBAL-H and $NaBH_4$ respectively, conversion to the mono alcohol compound **50** was possible, albeit in somewhat reduced yield. The reduction has also been attempted before the alkylation step, but this did not result in sufficient amount of material to continue in that strategy.

From the β-dialkylated alcohol **50**, the synthesis follows the previously explained pathway of tosylation towards **51**, substitution with dimethyl thiophenol **22**, followed by deprotection of the ester and finally Friedel-Crafts acylation to obtain methyl isopropyl ketone **54**.

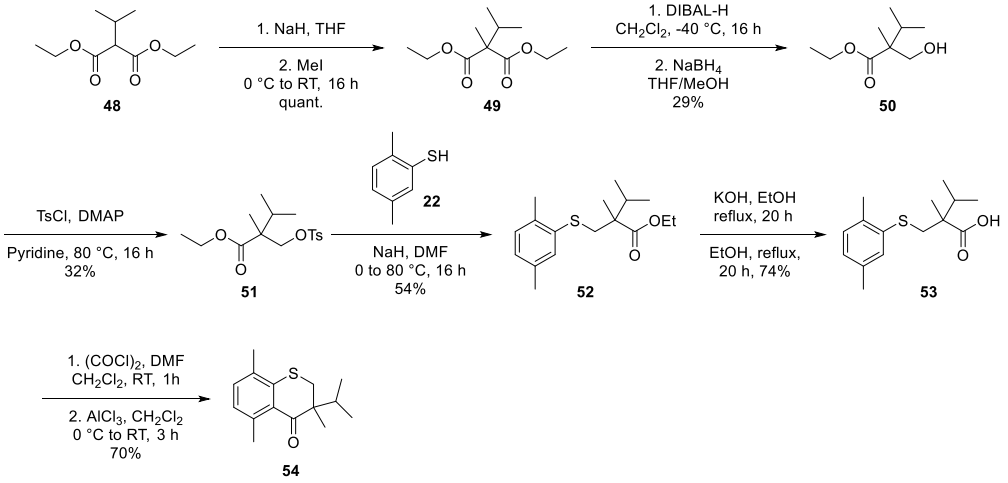

Scheme 12. Synthesis route of ketone **54**.

With the quaternary alkylated ketones **47** and **54** in hand we proceeded to find conditions for the Barton-Kellogg reaction (Scheme 13). Starting with **47** as the compound best suited to find the optimal conditions, the first attempts used thioketone **55**, which was made directly before use by thionation of **47** with a combination of Lawesson's reagent and P_2S_5 in toluene with microwave irradiation at 130 °C. No conversion towards episulfide **56** or overcrowded alkene **39** (Figure 7) was observed.

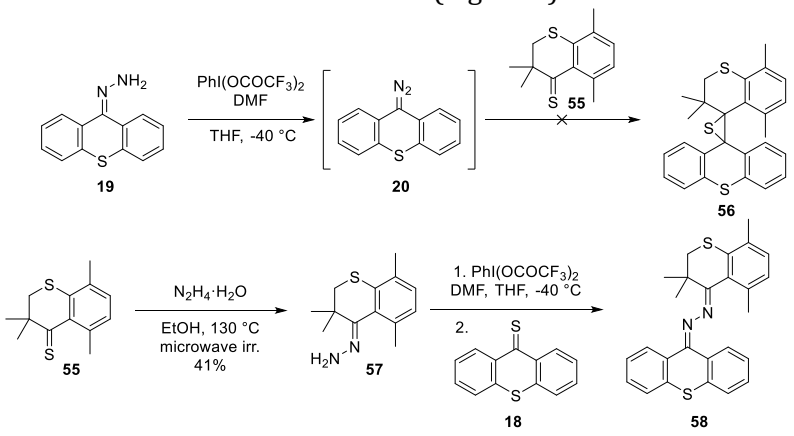

Scheme 13. Attempted Barton-Kellogg couplings and the transformation towards azine **58**.

As an alternative strategy the coupling partners for the Barton-Kellogg reaction were reversed. Freshly synthesised thioketone **55** was converted to the corresponding hydrazone **57**. The hypervalent iodine oxidant, bis(trifluoroacetoxy)iodobenzene was added at -40 °C to a solution of the hydrazone, after which the thioketone **18** was added. This method was used for other Barton-Kellogg reactions successfully. We could observe

conversion of the starting materials and we initially thought to have conversion towards the episulfide. Attempts at desulfurisation using $P(NMe_2)_3$ showed no further conversion. Careful analysis showed that this reaction formed azine **58** and no conversion towards the desired overcrowded alkene **39** was observed. It seems that the steric hindrance inhibits Barton-Kellogg coupling and azine **58** is formed. The azine formation, potentially occurs under the influence of an *in situ* formed iodine species or via protonation of reaction intermediates. From these results we concluded that the formation of dialkyl quaternary overcrowded alkenes with two sulfur-containing six-membered rings is not feasible for these approaches.

The benzothiophene scaffold design with an alkylated quaternary centre for molecular motors uses the previously described strategy of a Barton-Kellogg reaction to form the overcrowded alkene central olefinic bond. The synthesis of compound **33** has been described above (Scheme 9).

Ketone **33** does not suffer from any of the issues encountered in the thiochromenone-based systems and the alkylation could be performed by straightforward α-alkylation using LDA and the respective alkyl iodides to get the quaternary dimethyl and methyl/isopropyl ketones **59** and **60** in excellent and moderate yields of 95% and 45%, respectively. The isopropylation has a lower yield because of a lower conversion, a significant amount of starting material **33** was retrieved that could be resubmitted.

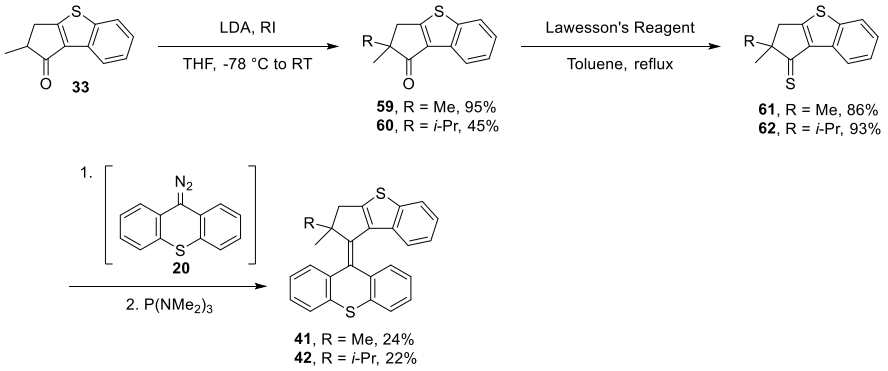

Scheme 14. Synthesis route of motors **41** and **42**.

The α-quaternary ketones could be converted to the respective thioketones **61** and **62** as strongly pink solids, which appeared relatively bench stable in comparison with other thioketones. The Barton-Kellogg reaction of **61** with diazo compound **20** provided the overcrowded alkene **41** with some unreacted thioketone starting material present. The thioketone and overcrowded alkene were not separable by flash column chromatography.

The mixture was submitted to phase transfer catalysed hydrolysis conditions[53] to transform thioketone **61** back into ketone **59**. The ketone and overcrowded alkene could then be separated by flash column chromatography and the product was obtained in a yield of 24%, acceptable for Barton-Kellogg reactions towards overcrowded alkenes. Thioketone **62** was transformed successfully into overcrowded alkene **42** via the same method in a yield of 22%.

2.8 Electrochemistry of a dialkyl benzothiophene-based overcrowded alkene

The electrochemistry of dimethyl benzothiophene-based overcrowded alkene **41** was investigated by cyclic voltammetry in a standard three electrode setup with a GC working electrode, Pt wire counter electrode and SCE reference electrode in dry CH_2Cl_2 (1.0 mM substrate concentration) with $TBAPF_6$ (0.1 M) as supporting electrolyte. We observe, in the oxidative direction, two signals (Figure 9a, 0.59 and 1.28 V vs. SCE) and in the reductive direction we observe two, significantly smaller signals, that nearly overlap (0.01 and 0.05 V vs. SCE). With a narrower range for cyclic voltammetry (Figure 9b), we observe that the first oxidation wave has a corresponding reduction wave at the same potential (0.05 V vs. SCE) as the first observed reduction wave in Figure 9a. These observations correspond with the oxidation of **41** around an expected potential and a subsequent formation of a new species, which is oxidised at a higher potential.

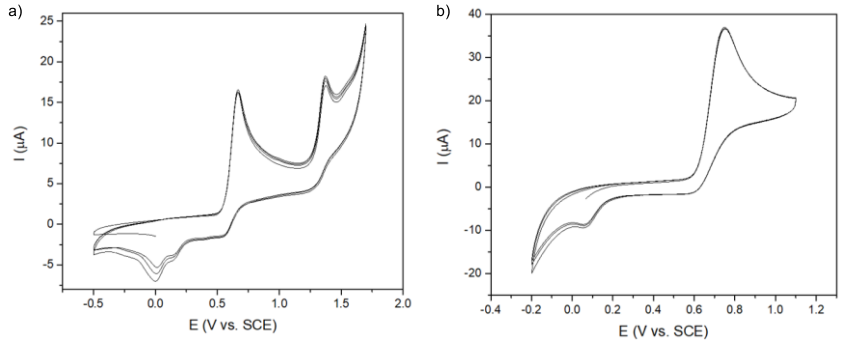

Figure 9. Cyclic voltammograms (CH_2Cl_2, 1.0 mM, diffusion limited conditions, 0.1 V s^{-1}) of **41** with a potential range of: a) -0.5 – 1.6 V vs. SCE and b) -0.2 – 1.1 V vs. SCE.

To investigate the processes occurring during CV, **41** was submitted to bulk oxidation at 0.9 V vs. SCE in $MeCN/CH_2Cl_2$ with KPF_6 as supporting electrolyte. The bulk oxidation was stopped when the oxidation signal was no longer observable by CV. The solution turned noticeably to a deep red colour. The resulting solid was washed with CH_2Cl_2 to remove KPF_6.

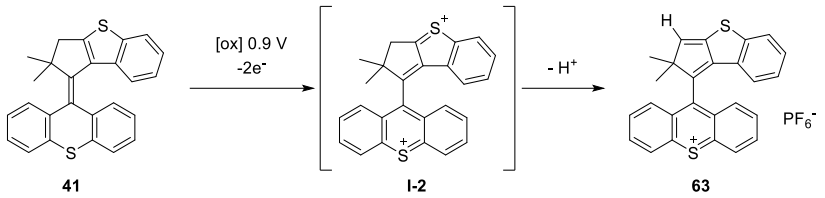

Scheme 15. Expected pathway of electrochemical oxidation followed by deprotonation.

The ^{1}H-NMR spectrum in CD_3CN (Figure 10) is highly indicative of a compound containing a symmetrised lower half thioxanthylidene motif (signals at 8.82, 8.74, 8.39 and 8.02 ppm), a benzothiophene motif, as well as a new signal at 6.71 ppm (s, 1H), corresponding to an sp^2-hybridised CH (indicated H in Scheme 15, compound **63**). From this data, it seems likely that, after oxidation of **41**, a deprotonation occurs, causing a double bond shift, ultimately resulting in compound **63**. This shows that the benzylic position in our benzothiophene-motif molecular motors is highly susceptible to deprotonation upon oxidation.

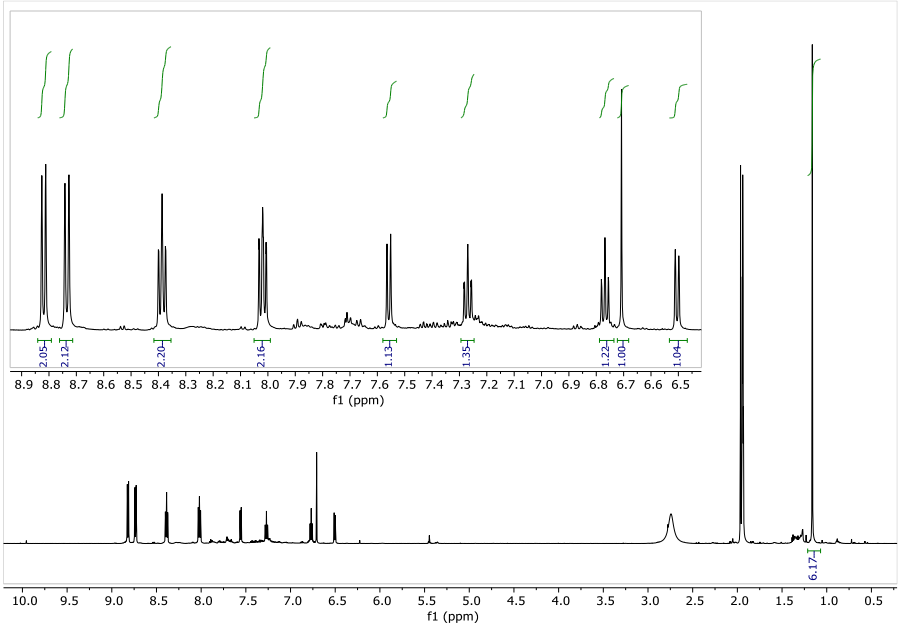

Figure 10. ^{1}H NMR spectrum of **63** (600 MHz, CD_3CN).

The cyclic voltammogram obtained for **41** is reminiscent of the electrochemical and chemical behaviour of motor **3** (Scheme 1) where a chemical reaction follows electrochemical oxidation. Unfortunately, this shows that the benzothiophene motif molecular motor does not seem have the right characteristics for an electrochemical molecular motor.

2.9 Transient absorption spectroscopy

By conventional UV-vis analysis the typical motor isomerisation steps were not observed for the benzothiophene-based molecular motors. We hypothesised that the barrier for thermal isomerisation of these compounds is too low at room temperature. With transient spectroscopic methods it is possible to observe switching behaviour on a vastly different time scale. Motor **42** (Scheme 14) was selected to be analysed with transient absorption spectroscopy.

Motor **65** was synthesised using a Barton-Kellogg reaction, similar to the previously described benzothiophene-based motors (Scheme 16) as a model compound for comparison with other benzothiophene-based motors.

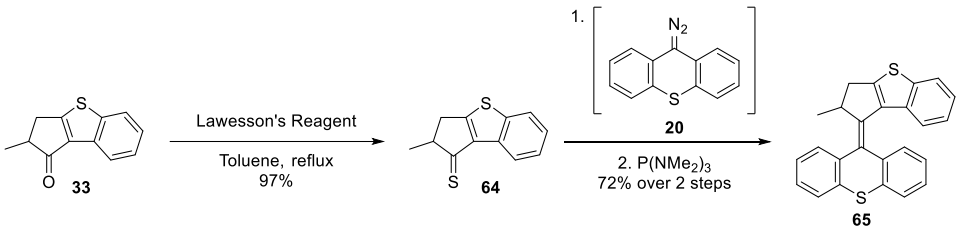

Scheme 16. Synthesis of motor **65**.

From preliminary transient absorption spectroscopy measurements of **65** we could detect the formation of a transient signal with an absorption maximum at 369 nm after excitation of **65** at 334 nm (Figure 11). The transient signal was identified as a spectroscopic signature of the *metastable* state of **65**.[54] Its decay afforded a lifetime of 24 μs from global fitting analysis (Figure 11b, 11c). The ground state bleaching of the stable state of **65** could not be observed because of instrumental limitations of the ICCD camera used for this experiment. This formation of the *metastable* state and fast decay indicate that motor **65** is likely operating as a fast unidirectional molecular motor.

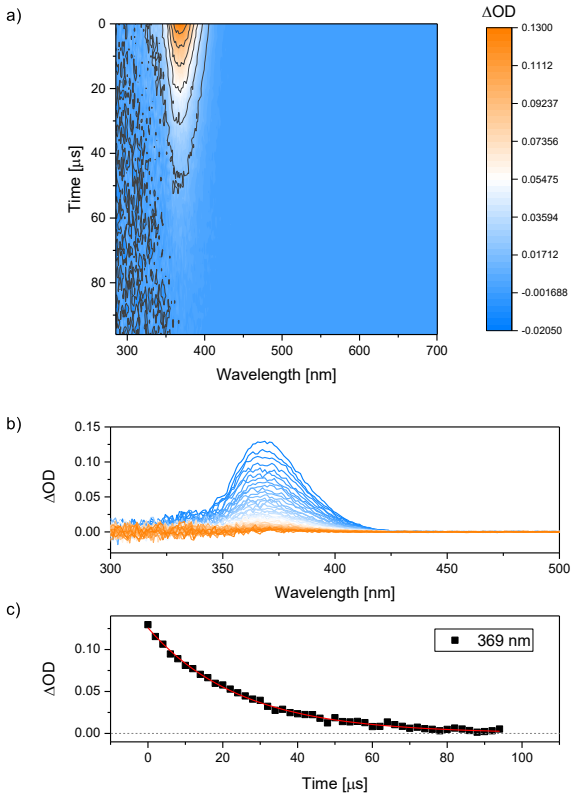

Figure 11. a) Heatmap of the transient absorption signal generated after excitation of **65** with a pulse at 334 nm over 96 µs in toluene. b) Decay of the transient absorption signal generated after excitation of **65** with a pulse at 334 nm over 96 µs in toluene. c) Global fitting analysis of the signal detected at 369 nm. The kinetic constant of the decay of the transient is k = 0.0410 (0.00025) μs^{-1} with a lifetime τ = 24 µs.

Motor **42** was analysed in the same transient absorption spectroscopy setup, however, no photoswitching was observed. There is a possibility that the speed of the isomerisation and back isomerisation is such that the change in absorption spectrum is not visible with the chosen detector setup.

3. Conclusions & Outlook

With the aim to achieve electrochemically driven unidirectional rotation we have worked on the modification of second-generation molecular motors. The introduction of quaternary centres with either fluorine or alkyl substituents has demonstrated to be synthetically challenging. Nevertheless, a number of overcrowded alkenes with quaternary centres have been synthesised.

The electrochemistry and photochemistry of the fluorinated molecular motor **5** shows that it operates as a fascinating molecular switch as it shows switching using either electro- or photochemical stimuli. Unfortunately, compound **5** suffers from a susceptibility to degradation at higher temperatures and in some solvents. The calculated high barrier for THI, in combination with the low stability makes it an unattractive candidate for electrochemically driven unidirectional rotation.

A successful synthetic strategy for quaternary alkylated rotor halves is presented, which could be used in the development of new photoswitches. Unfortunately, the synthesis of overcrowded alkenes with these halves in combination with thioxanthene motifs has been unsuccessful so far.

The benzothiophene-based quaternary, alkylated overcrowded alkenes have been synthesised successfully and a number of them have been investigated by cyclic voltammetry and transient absorption spectroscopy. The electrochemical switching of the dialkylated overcrowded alkenes upon oxidation, is followed by a benzylic deprotonation and double bond shift, reminiscent of the common second-generation molecular motors. This changes the nature of the electrochemical switch to the extent that this is no longer a viable candidate for unidirectional molecular rotation. Interestingly, preliminary studies indicate that the tertiary benzothiophene molecular motor **65** shows fast photoswitching.

In order to obtain a functional redox-driven molecular motor, new strategies need to be developed. From this work and earlier reports, the sensitive allylic- and benzylic positions on the molecular motors are a significant challenge. For successful, robust molecular electromotors it is of interest to investigate structures that are unlikely to undergo a chemical reaction after electrochemical oxidation, such as the structures discussed in Chapter 7 of this thesis.

4. Experimental

4.1 General comments

All reagents and solvents were purchased from Sigma Aldrich, TCI Europe, Acros Organics, Fluorochem or Alfa Aesar and were used without further purification. Dry solvents were obtained from an MBraun SPS-800 solvent purification system. All reactions were performed in oven-dried glassware under a nitrogen atmosphere unless otherwise noted. Flash column chromatography was performed on silica gel (Merck, type 9385, 230-400 mesh). NMR spectra (^{1}H, ^{13}C and ^{19}F) were recorded on a Varian Mercury-Plus 400 spectrometer or a Bruker Avance 600 NMR spectrometer at 298K. Data are reported in term of chemical shift (δ), multiplicity (s = singlet, d = doublet, t = triplet, q = quartet, p = pentet, m = multiplet, br. = broad), coupling constants (Hz), and integration. GC-MS was performed on (GC, HP6890; MS HP5973) with an HP1 or HP5 column (Agilent Technologies, Palo Alto, CA). High resolution mass spectroscopy (HRMS) was performed on a LTQ Orbitrap XL spectrometer with electrospray ionisation (ESI) or atmospheric pressure chemical ionisation (APCI) as ionisation technique. Cyclic voltammograms were recorded using a three-electrode setup on a CHI600C electrochemical workstation (CH Instruments) or a VSP-300 Potentiostat/Galvanostat (Biologic Science Instruments) using a saturated calomel electrode (SCE), a freshly polished glassy carbon (3 mm diameter) disc working electrode (WE), and a platinum wire as counter electrode (CE). All CVs were recorded at room temperature with tetrabutylammonium hexafluorophosphate (0.1 M) as supporting electrolyte in CH_2Cl_2 or CH_3CN, unless otherwise stated. UV-vis spectroscopy was measured using a Hewlett-Packard 8453 spectrometer with irradiation using Thorlabs LEDs at the indicated wavelengths with a controlled temperature.

4.2 Transient absorption spectroscopy

Nanosecond transient absorption spectra were recorded with an in-house assembled setup. An excitation wavelength of 334 nm was used to excite a sample with OD=0.95 at 334 nm. The excitation wavelength was generated using a tuneable Nd:YAG-laser system (NT342B, Ekspla) comprising the pump laser (NL300) with harmonics generators (SHG, THG) producing 355 nm to pump an optical parametric oscillator (OPO) with SHG connected in a single device. The laser system was operated at a repetition rate of 10 Hz with a pulse length of 5 ns. The power generated by the pump was 1 mJ. The probe light running at 20 Hz was generated by a high-stability short arc xenon flash lamp (FX-1160, Excelitas Technologies) using a modified PS302 controller (EG&G). Using a 50/50 beam splitter, the probe light was split

equally into a signal beam and a reference beam and focused (bi-convex lens 75mm) on the entrance slit of a spectrograph (SpectraPro-150, Princeton Instruments) with a grating of 150 ln mm^{-1}, blaze at 500 nm. The probe beam (A = 1 mm^2) was passed through the sample cell and orthogonally overlapped with the excitation beam on a 1 mm × 1 cm area. The excitation energy was recorded by measuring the excitation power at the back of an empty sample holder. In order to correct for fluctuations in the flash lamp spectral intensity, the reference was used to normalise the signal. Both beams were recorded simultaneously using a gated intensified CCD camera (PI-MAX3, Princeton Instruments) which has an adjustable gate of minimal 2.9 ns, normally a gate of 20 ns and software binning is used to improve the dynamic range and signal to noise ratio. Two delay generators (DG535 and DG645, Stanford Research Systems, Inc.) were used to trigger the excitation and to change the delay of the flash lamp together with the gate of the camera during the experiment. The setup was controlled by an in-house written Labview program. The global fitting analysis of the transients was performed using Glotaran.[55]

4.3 Synthesis and characterisation of compounds

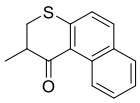

2-methyl-2,3-dihydro-1H-benzo[f]thiochromen-1-one (**12**). 2-naphthalenethiol (320 mg, 2.0 mmol, 1.0 equiv.), methacrylic acid (4.0 mmol, 2.0 equiv.) and NEt_3 (0.56 mL, 4.0 mmol, 2.0 equiv.) were dissolved in THF (6 mL, 0.33 M) and the mixture was heated at reflux for 16 h. The reaction mixture was allowed to cool down to room temperature and 1.0 M HCl (aq) was added. The mixture was extracted with EtOAc, washed with brine and dried over $MgSO_4$.

Freshly crystallised carboxylic acid intermediate (*n*-heptane) was dissolved in CH_2Cl_2 (15 mL, 0.15 M) and a few drops of DMF were added. $(COCl)_2$ (0.5 mL, 5.9 mmol, 3.0 equiv.) was added dropwise and the reaction mixture was stirred at room temperature for 1 h. Volatiles were removed under reduced pressure and remaining $(COCl)_2$ was removed by the aid of co-evaporation with *n*-heptane. The crude oxalyl chloride intermediate was dissolved in CH_2Cl_2 (15 mL) and cooled to 0 °C. $AlCl_3$ (347 mg, 2.6 mmol, 1.3 equiv.) was added portion wise and the mixture was stirred at 0 °C for 3 h. The reaction was quenched with 1.0 M HCl (aq), extracted with CH_2Cl_2 and dried over $MgSO_4$. The product was purified by flash column chromatography (silica, 3–5% EtOAc/*n*-pentane) and obtained as a yellow oil (395 mg, 1.73 mmol) in 88% yield. ^{1}H NMR (400 MHz, $CDCl_3$) δ 9.07 (dd, *J* = 8.7, 0.9 Hz, 1H), 7.82 –

7.69 (m, 2H), 7.58 (ddd, *J* = 8.7, 6.9, 1.5 Hz, 1H), 7.44 (ddd, *J* = 8.0, 6.9, 1.1 Hz, 1H), 7.24 (d, *J* = 8.7 Hz, 1H), 3.30 – 3.05 (m, 3H), 1.40 (d, *J* = 6.5 Hz, 3H). Compound data is in accordance with literature.[44]

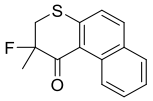

2-fluoro-2-methyl-2,3-dihydro-1H-benzo[f]thiochromen-1-one (**13**). 2-methyl-2,3-dihydro-1H-benzo[f]thiochromen-1-one (**12**, 96 mg, 0.42 mmol, 1.0 equiv.) was dissolved in toluene (0.1 M) and cooled to -78 °C. NaHMDS (0.6 M in toluene) was added and the mixture was stirred for 15 min. NFSI (1.2 equiv.) was added portion wise over 5 min and the mixture was stirred until full conversion of the starting material (TLC, 5% EtOAc/*n*-pentane). The reaction was quenched at -78 °C using MeOH (1 mL) and the mixture was allowed to warm up to room temperature. Volatiles were removed under reduced pressure and the product was purified by rapid flash column chromatography (silica gel, slurry prepared using 1% NEt_3 in *n*-pentane, compound eluted with EtOAc/*n*-pentane, 3%) and obtained as a yellow oil in 90% yield (93 mg, 0.38 mmol). ^{1}H NMR (400 MHz, $CDCl_3$) δ 9.09 (d, *J* = 8.8 Hz, 1H), 7.83 (d, *J* = 8.7 Hz, 1H), 7.80 – 7.74 (m, 1H), 7.63 (ddd, *J* = 8.6, 6.9, 1.5 Hz, 1H), 7.48 (ddd, *J* = 8.1, 6.9, 1.2 Hz, 1H), 7.21 (d, *J* = 8.7 Hz, 1H), 3.79 – 3.71 (m, 1H), 3.25 (dd, *J* = 13.1, 11.7 Hz, 1H), 1.81 (d, *J* = 21.5 Hz, 3H). ^{19}F NMR (376 MHz, $CDCl_3$) δ -149.61 (m). Compound data is in accordance with literature.[35]

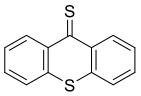

9H-thioxanthene-9-thione (**18**). To a solution of thioxanthene-9-one (212 mg, 1.0 mmol) in toluene (10 mL, 0.1 M) was added Lawesson's reagent (480 mg, 1.05 mmol, 1.05 equiv.). The mixture was heated at reflux for 3 h. Upon completion as monitored by TLC, volatiles were removed under reduced pressure and the mixture was filtered over silica gel and was flushed with EtOAc/*n*-pentane, 5%. The product was obtained as a green solid (200 mg, 0.88 mmol) in 88% yield. ^{1}H NMR (400 MHz, $CDCl_3$) δ 9.01 (dd, *J* = 8.5, 1.4 Hz, 2H), 7.64 – 7.56 (m, 4H), 7.44 (ddd, *J* = 8.4, 6.5, 1.8 Hz, 2H). Compound data is in accordance with literature.[42]

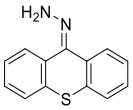

(9H-thioxanthen-9-ylidene)hydrazine (**19**). 9H-thioxanthene-9-thione (**18**, 100 mg, 0.44 mmol, 1.0 equiv.) was dissolved in EtOH (3 mL, 0.15 M)

and hydrazine monohydrate (1.1 mL, 50 equiv.) was added. The mixture was stirred at 100 °C overnight. The mixture was allowed to cool down to room temperature and EtOAc was added. The mixture was washed with water, the aqueous phase was extracted with EtOAc and the combined organic fractions were washed with brine and dried over $MgSO_4$. The product was crystallised from EtOH and obtained as a yellow solid in 64% yield (64 mg, 0.28 mmol). ^{1}H NMR (400 MHz, $CDCl_3$) δ 8.08 – 8.00 (m, 1H), 7.80 (dd, *J* = 7.5, 1.7 Hz, 1H), 7.59 – 7.51 (m, 1H), 7.39 – 7.26 (m, 5H), 5.85 (s, 2H). Compound data is in accordance with literature.[42]

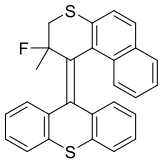

2-fluoro-2-methyl-1-(9H-thioxanthen-9-ylidene)-2,3-dihydro-1H-benzo[f]thiochromene (**5**). 2-fluoro-2-methyl-2,3-dihydro-1H-benzo[f]thiochromen-1-one (**13**, 265 mg, 1.08 mmol, 1.0 equiv.) was dissolved in dry toluene (12 mL, 0.09 M). P_2S_5 (719 mg, mmol, 3.0 equiv.) and Lawesson's reagent (1309 mg, mmol, 3.0 equiv.) were added and the mixture was heated at reflux for 5 h. The thioketone mixture was filtered over a plug of silica under N_2 flow and flushed with THF. The filtrate was concentrated under reduced pressure.

During the thionation of **13**, (9H-thioxanthen-9-ylidene)hydrazine (**19**, 271 mg, 1.2 mmol, 1.1 equiv.) was dissolved in CH_2Cl_2 (14 mL, 0.09 M) and the mixture was cooled to -10 °C. Ag_2O (557 mg, mmol, 2.0 equiv.), $MgSO_4$ (500 mg, mmol, equiv.) and a fresh, saturated solution of KOH in MeOH (1.2 mL) were added and the mixture was stirred at -10 °C for 40 min. The mixture was filtered through a frit (P4) under N_2 flow into a Schlenk flask at -10 °C. The thioketone was added to the diazo solution with a small amount of THF at -10 °C. The mixture was allowed to warm up to room temperature and stirred for 16 h. Volatiles were removed under reduced pressure to afford a crude episulfide mixture. The episulfide was dissolved in toluene (15 mL, 0.07 M) and $P(NMe_2)_3$ (0.60 mL, 3.3 mmol, 3.0 equiv.) was added to the mixture, which was subsequently heated to 90 °C for 16 h. Volatiles were removed under reduced pressure and the product was purified by rapid flash column chromatography (silica gel, slurry prepared using 2% NEt_3 in *n*-pentane, compound eluted with NEt_3/CH_2Cl_2/*n*-pentane, 2:10:88), as the product is poorly stable on silica. After trituration with cold *n*-hexane, the product was obtained as a pale-yellow solid in 2% yield (9 mg, 0.02 mmol). ^{1}H NMR (600 MHz, $CDCl_3$) δ 7.76 (ddd, *J* = 9.3, 7.7, 1.4 Hz, 1H), 7.64 (d, *J* = 8.4 Hz, 1H), 7.60 (d, *J* = 8.5 Hz, 1H), 7.58 – 7.53 (m, 2H), 7.43 (d, *J* = 8.4 Hz, 1H),

7.29 – 7.21 (m, 3H), 7.14 (dd, *J* = 8.1, 6.8, Hz, 1H), 7.08 – 7.05 (m, 1H), 6.65 (dd, *J* = 7.5, 1.4 Hz, 1H), 6.35 (dd, *J* = 7.5, 1.2 Hz, 1H), 6.30 (dd, *J* = 7.8, 1.5 Hz, 1H), 3.66 (dd, *J* = 23.1, 12.1 Hz, 1H), 3.27 (dd, *J* = 13.3, 12.1 Hz, 1H), 1.34 (d, *J* = 21.6 Hz, 3H). ^{19}F NMR (565 MHz, $CDCl_3$) δ -127.8 – -128.0 (m, 1F). Compound data in accordance with literature.[35]

Note: episulfide intermediate: ^{1}H NMR (400 MHz, $CDCl_3$) δ 8.92 (d, *J* = 8.8 Hz, 1H), 8.04 – 7.95 (m, 1H), 7.53 – 7.39 (m, 3H), 7.35 – 7.21 (m, 4H), 7.07 – 7.02 (m, 1H), 6.89 (d, *J* = 8.6 Hz, 1H), 6.87 – 6.83 (m, 1H), 6.70 (dd, *J* = 7.7, 1.2 Hz, 1H), 6.25 (dd, J = 8.1, 7.4 Hz, 1H), 2.99 (dd, J = 18.1, 11.7 Hz, 1H), 2.88 (dd, J = 11.7, 5.1 Hz, 1H), 1.55 (d, $J_{H\text{-}F}$ = 21.4 Hz, 3H). ^{19}F NMR (376 MHz, $CDCl_3$) – 130.1 – 130.4 (m, 1F).

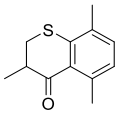

3,5,8-trimethylthiochroman-4-one (**24**). 2,5-Dimethylbenzenethiol (6.0 mmol, 829 mg, 1.0 equiv.), methacrylic acid (12.0 mmol, 1.02 mL, 2.0 equiv.) and NEt_3 (12.0 mmol, 1.67 mL, 2.0 equiv.) were added to THF (10 mL, 0.6 M) and the mixture was heated at reflux for 16 h. The reaction mixture was allowed to cool to room temperature and quenched with 1.0 M HCl (aq). The product was extracted with EtOAc, washed with brine and dried over $MgSO_4$. Volatiles were removed under reduced pressure and the product was dried under vacuum. The intermediate carboxylic acid was obtained as a colourless oil and was used directly in the next step.

The intermediate carboxylic acid was dissolved in CH_2Cl_2 (10 mL, 0.6 M) with a few drops of DMF, $(COCl)_2$ (1.27 mL, 15 mmol, 2.5 equiv.) was added dropwise to the mixture which was then stirred for 1 h. Volatiles were removed under reduced pressure and excess $(COCl)_2$ was further removed with co-evaporation of *n*-heptane. The crude acyl chloride was dissolved in CH_2Cl_2 (30 mL, 0.2 M) and $AlCl_3$ (1040 mg, 7.8 mmol, 1.3 equiv.) was added portion wise to the mixture at 0 °C. The reaction mixture was stirred at this temperature for 2 h. Upon completion, the reaction was quenched with 1.0 M HCl (aq), the mixture was extracted with CH_2Cl_2, washed with brine and the organic phase was dried over $MgSO_4$. Volatiles were removed under reduced pressure and the product was purified by flash column chromatography (silica gel, EtOAc/*n*-pentane, 10%) and obtained as a pale-yellow oil (1130 mg, 5.5 mmol) in 81% yield. ^{1}H NMR (400 MHz, $CDCl_3$) δ 7.11 (d, *J* = 7.6 Hz, 1H), 6.88 (d, *J* = 7.6 Hz, 1H), 3.14 (dd, *J* = 12.4, 3.9 Hz, 1H), 3.06 (d, *J* = 10.9 Hz, 1H), 3.03 – 2.93 (m, 1H), 2.53 (s, 3H), 2.27 (s, 3H), 1.30 (d, *J* = 6.4 Hz, 3H). ^{13}C NMR (101 MHz, $CDCl_3$) δ 199.9, 141.6, 139.9, 133.0, 132.8, 130.4, 128.2, 43.0, 32.3, 23.5, 20.1, 15.3. Compound data is in accordance with literature.[56]

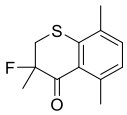

3-fluoro-3,5,8-trimethylthiochroman-4-one (**25**). 3,5,8-trimethylthiochroman-4-one (**24**, 160 mg, 0.78 mmol, 1.0 equiv.) was added dropwise to a solution of NaHMDS (0.6 M in toluene, 1.55 mL, 0.93 mmol, 1.2 equiv.) at -78 °C and the mixture was stirred for 15 min. NFSI (295 mg, 0.94 mmol, 1.2 equiv.) was added portion wise over 10 min at -78 °C, after which the mixture was allowed to warm up to room temperature and was stirred at room temperature overnight. The reaction was quenched with 1.0 M HCl (aq), the mixture was extracted with CH_2Cl_2, and the combined organic phases were washed with brine and dried over $MgSO_4$. Volatiles were removed under reduced pressure and the product was purified by rapid flash column chromatography (silica gel, EtOAc/*n*-pentane, 5%) and obtained as a pale-yellow oil in 80% yield (140 mg, 0.62 mmol). ^{1}H NMR (400 MHz, $CDCl_3$) δ 7.15 (d, J = 7.7 Hz, 1H), 6.94 (d, J = 7.6 Hz, 1H), 3.57 (dd, $J_{H\text{-}H}$ = 13.1, $J_{H\text{-}H}$ = 7.6 Hz, 1H), 3.16 (dd, $J_{H\text{-}H}$ = 13.1, $J_{H\text{-}F}$ 11.6 Hz, 1H), 2.55 (s, 3H), 2.27 (s, 3H), 1.73 (d, $J_{H\text{-}F}$ = 21.5 Hz, 3H). ^{19}F NMR (376 MHz, $CDCl_3$) δ -149.93 (qdd, $J_{H\text{-}F}$ = 21.4, 11.5, 7.6 Hz). ^{13}C NMR (101 MHz, $CDCl_3$) δ 194.0 (d, $J_{C\text{-}F}$ = 18.7 Hz), 141.5 (d, $J_{C\text{-}F}$ = 1.3 Hz), 140.1, 133.9, 132.7, 128.8, 128.7, 92.3 (d, $J_{C\text{-}F}$ = 185.9 Hz) , 35.0 (d, $J_{C\text{-}F}$ = 27.4 Hz), 23.3, 20.7 (d, $J_{C\text{-}F}$ = 25.3 Hz), 19.9.

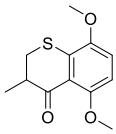

5,8-dimethoxy-3-methylthiochroman-4-one (**28**). 2,5-dimethoxy benzenethiol (8 mmol, 1906 mg, 1.0 equiv.), methacrylic acid (16 mmol, 1.36 mL, 2.0 equiv.) and NEt_3 (16 mmol, 2.23 mL, 2.0 equiv.) were added to THF (14 mL, 0.6 M) and the mixture was heated at reflux overnight. The reaction mixture was cooled to room temperature and quenched with 1.0 M HCl (aq), extracted with EtOAc, washed with brine and dried over $MgSO_4$. Volatiles were removed under reduced pressure and the product was dried under vacuum. The crude carboxylic acid intermediate was obtained as a white solid and was used immediately.

The intermediate carboxylic acid was dissolved in CH_2Cl_2 (11 mL, 0.7 M) with a few drops of DMF, $(COCl)_2$ was added dropwise to the mixture which was then stirred for 1 h. Volatiles were removed under reduced pressure and excess $(COCl)_2$ was further removed with co-evaporation of *n*-heptane. The crude acyl chloride intermediate was dissolved in CH_2Cl_2 (40 mL, 0.2 M) and $AlCl_3$ (10.4 mmol, 1.39 g, 1.3 equiv.) was added portion wise to the mixture at 0 °C. The mixture was stirred at 0 °C for 2 h. Upon completion, the reaction

was quenched with 1.0 M HCl (aq), the mixture was extracted with CH_2Cl_2, and the combined organic phase was washed with brine and dried over $MgSO_4$. The product was purified by flash column chromatography (silica gel, EtOAc/*n*-pentane, 20–50%). The product was obtained as yellow solid in 49% yield (933 mg, 3.92 mmol). ^{1}H NMR (400 MHz, $CDCl_3$) δ 6.89 (d, *J* = 9.0 Hz, 1H), 6.66 (d, *J* = 9.0 Hz, 1H), 3.87 (s, 3H), 3.84 (d, *J* = 1.2 Hz, 3H), 3.15 – 2.93 (m, 3H), 1.30 (d, *J* = 6.3 Hz, 3H). ^{13}C NMR (101 MHz, $CDCl_3$) δ 197.1, 155.1, 148.8, 132.9, 121.9, 114.6, 108.2, 56.8, 56.7, 42.6, 32.0, 15.1. HRMS (ESI Pos): for $[C_{12}H_{15}O_3S]^+$ calcd. m/z = 239.0736, found m/z = 239.0738.

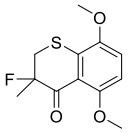

3-fluoro-5,8-dimethoxy-3-methylthiochroman-4-one (**29**). 5,8-dimethoxy-3-methylthiochroman-4-one (**28**, 94 mg, 0.4 mmol) was dissolved in toluene (6.0 mL, 0.07 M) and added to a solution of NaHMDS (0.6 M in toluene, 0.87 mL, 1.3 equiv.) at -78 °C and the mixture was stirred for 10 min. NFSI (189 mg, 0.6 mmol, 1.5 equiv.) was added portion wise over 10 min. The reaction mixture was allowed to warm up to room temperature and was stirred overnight. The reaction was quenched with 1.0 M HCl (aq), the mixture was extracted with CH_2Cl_2, the combined organic phase was washed with brine, dried over $MgSO_4$ and volatiles were removed under reduced pressure. The product was purified by rapid flash column chromatography (silica gel, EtOAc/*n*-pentane, 20–40%) and obtained as a yellow solid in 78% yield (80 mg, 0.31 mmol). ^{1}H NMR (400 MHz, $CDCl_3$) δ 6.93 (d, *J* = 9.0 Hz, 1H), 6.69 (d, *J* = 9.0 Hz, 1H), 3.86 (s, 3H), 3.85 (s, 3H), 3.51 (dd, $J_{H\text{-}H}$ = 13.3 Hz, $J_{H\text{-}F}$ = 7.3 Hz, 1H), 3.14 (dd, $J_{H\text{-}F}$ = 14.1 Hz, $J_{H\text{-}H}$ = 13.3 Hz, 1H), 1.73 (d, $J_{H\text{-}F}$ = 21.4 Hz, 3H). ^{19}F NMR (376 MHz, $CDCl_3$) δ -151.90 (qdd, *J* = 21.5, 14.0, 7.4 Hz). ^{13}C NMR (101 MHz, $CDCl_3$) δ 191.1, 190.9, 155.9, 148.5, 131.6, 120.1, 115.4, 108.7, 92.5, 90.7, 56.9, 56.8, 34.8, 34.6, 20.8, 20.5. GC-MS: found m/z = 256 $[M]^+$, 196 $[M\text{-}C_3H_5F]^+$.

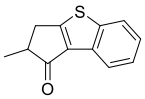

2-methyl-2,3-dihydro-1H-benzo[b]cyclopenta[d]thiophen-1-one (**33**). Benzothiophene (1230 mg, 10.0 mmol, 1.0 equiv.) was added to 20 mL polyphosphoric acid with mechanical stirring and the mixture was heated to 80 °C. Methacrylic acid (1000 mg, 11.6 mmol, 1.16 equiv.) was added to the mixture and the mixture was stirred for 90 min and subsequently the heating was removed and the mixture was allowed to cool down to 50 °C. Cold water was added carefully and the mixture was stirred for another 4 h.

The product was extracted with EtOAc, the combined organic phase was washed with brine and dried over $MgSO_4$. The product was first purified by flash column chromatography (silica, EtOAc/*n*-pentane, 3%) followed by recrystallisation from EtOH to afford the product as a white solid in 30% yield (600 mg, 2.97 mmol). Column chromatography results in two closely overlapping fractions, of which the first fraction is the title compound, the second fraction is the regioisomer (see below). Product: ^{1}H NMR (400 MHz, $CDCl_3$) δ 8.25 (ddd, *J* = 7.9, 1.4, 0.7 Hz, 1H), 7.81 (d, *J* = 8.1 Hz, 1H), 7.48 – 7.43 (m, 1H), 7.41 – 7.35 (m, 1H), 3.54 (dd, *J* = 17.8, 6.9 Hz, 1H), 3.15 – 3.05 (m, 1H), 2.89 (dd, *J* = 17.8, 2.7 Hz, 1H), 1.40 (d, *J* = 7.5 Hz, 3H). ^{13}C NMR (101 MHz, $CDCl_3$) δ 200.9, 172.7, 144.6, 139.1, 131.7, 126.0, 125.6, 123.2, 123.2, 47.6, 34.2, 16.9. Compound data in accordance with literature.[57]

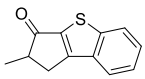

Note: the regioisomeric product **34** obtained in the same reaction in 25% yield (507 mg, 2.51 mmol): ^{1}H NMR (400 MHz, $CDCl_3$) δ 7.94 – 7.86 (m, 2H), 7.55 – 7.38 (m, 2H), 3.48 (dd, *J* = 17.3, 6.8 Hz, 1H), 3.18 – 3.05 (m, 1H), 2.81 (dd, *J* = 17.4, 2.6 Hz, 1H), 1.42 (d, *J* = 7.5 Hz, 3H).

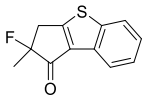

2-fluoro-2-methyl-2,3-dihydro-1H-benzo[b]cyclopenta[d]thiophen-1-one (**35**). 2-methyl-2,3-dihydro-1H-benzo[b]cyclopenta[d]thiophen-1-one (**33**, 100 mg, 0.50 mmol, 1.0 equiv.) was dissolved in THF (5 mL, 0.1 M) and the solution was cooled to -78 °C. LDA (1.0 M in THF, 0.64 mL, 0.64 mmol, 1.3 equiv.) was added to the cold mixture and the mixture was stirred for 30 min. NFSI (237 mg, 0.75 mmol, 1.5 equiv.) was added to the cold mixture which was subsequently allowed to warm up to room temperature followed stirring 1 h at room temperature. The reaction was quenched by the addition of water and the product was extracted with CH_2Cl_2 and the combined organic phase was dried over $MgSO_4$. Volatiles were removed under reduced pressure and the product was purified by flash column chromatography (silica, CH_2Cl_2/*n*-pentane, 10–30%) and obtained as a pale-yellow oil in 72% yield (79 mg, 0.36 mmol). ^{1}H NMR (400 MHz, $CDCl_3$) δ 8.24 (d, *J* = 7.8 Hz, 1H), 7.82 (d, *J* = 8.0 Hz, 1H), 7.52 – 7.36 (m, 2H), 3.68 – 3.39 (m, 2H), 1.71 (d, $J_{H\text{-}F}$ = 23.0 Hz, 3H). Compound data in accordance with literature.[35]

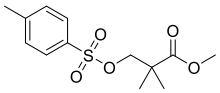

Methyl 2,2-dimethyl-3-(tosyloxy)propanoate (**44**). Methyl 3-hydroxy-2,2-dimethylpropanoate (5000 mg, 37.8 mmol, 1.0 equiv.), *p*-toluene sulfonyl chloride (7571 mg, 39.7 mmol, 1.05 equiv.), 4-dimethylaminopyridine (231 mg, 1.89 mmol, 0.05 equiv.) and pyridine (9.2 mL, 113 mmol, 3.0 equiv.) were added to CH_2Cl_2 (160 mL, 0.24 M) and the mixture was stirred at room temperature for 16 h. The mixture was washed with water and the aqueous phase was reextracted with CH_2Cl_2. The combined organic phases were dried over $MgSO_4$ and volatiles were removed under reduced pressure. The product was purified by recrystallisation from *n*-hexane and obtained as a white solid in 84% yield (9.09 g, 31.8 mmol). ^{1}H NMR (400 MHz, $CDCl_3$) δ 7.76 (d, *J* = 8.0 Hz, 2H), 7.35 (d, *J* = 7.4 Hz, 2H), 3.99 (s, 2H), 3.60 (s, 3H), 2.44 (s, 3H), 1.17 (s, 6H). ^{13}C NMR (101 MHz, $CDCl_3$) δ 175.1, 145.0, 132.8, 130.0, 128.1, 75.3, 52.3, 42.9, 22.1. GC-MS: found m/z = 286 $[M]^+$, 227 $[M\text{-}CO_2CH_3]^+$, 155 $[M\text{-}Ts]^+$.

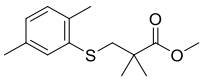

Methyl 3-((2,5-dimethylphenyl)thio)-2,2-dimethylpropanoate (**45**). 2,5-dimethyl benzene thiol (1.85 mL, 13.6 mmol, 1.3 equiv.) was added to DMF (50 mL, 0.27 M) and the solution was cooled to 0 °C. NaH (60% dispersion in mineral oil, 500 mg, 12.6 mmol, 1.2 equiv.) was added and the mixture was stirred while at that temperature. Methyl 2,2-dimethyl-3-(tosyloxy)propanoate (**44**, 3.00 g, 10.5 mmol, 1.0 equiv.) was added to mixture, which was heated to 100 °C for 16 h. The reaction was quenched with water, the product was extracted with CH_2Cl_2 and the combined organic phase was dried over $MgSO_4$. Volatiles were removed under reduced pressure and the product was purified by flash column chromatography (silica, EtOAc/*n*-pentane, 1–5%) and obtained as a yellow oil in 42% yield (1.11 g, 4.41 mmol). ^{1}H NMR (400 MHz, $CDCl_3$) δ 7.17 (d, *J* = 1.7 Hz, 1H), 7.04 (d, *J* = 7.6 Hz, 1H), 6.94 – 6.88 (m, 1H), 3.58 (s, 3H), 3.11 (s, 2H), 2.35 (s, 3H), 2.30 (s, 3H), 1.31 (s, 6H). ^{13}C NMR (151 MHz, $CDCl_3$) δ 176.9, 136.0, 135.7, 135.5, 130.7, 130.1, 127.3, 52.0, 44.6, 43.9, 25.1, 21.1, 20.2.

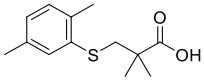

3-((2,5-dimethylphenyl)thio)-2,2-dimethylpropanoic acid (**46**). Methyl 3-((2,5-dimethylphenyl)thio)-2,2-dimethylpropanoate (**45**, 1.01 g, 4.00 mmol, 1.0 equiv.) and KOH (1.12 g, 20.0 mmol, 5.0 equiv.) were added to methanol (20 mL, 0.2 M) and the mixture was heated at reflux for 4 h. The mixture was allowed to cool down to room temperature and methanol was

removed under reduced pressure. The crude product was dissolved in 10% aqueous KOH and washed with Et_2O. The aqueous phase was acidified to pH = 1 with 3 M aqueous HCl and was extracted with EtOAc. The combined organic phase was washed with brine, dried over $MgSO_4$ and volatiles were removed under reduced pressure. The product was purified by trituration with *n*-pentane and obtained as a white solid in 90% yield (856 mg, 3.59 mmol). ^{1}H NMR (600 MHz, DMSO-d_6) δ 12.38 (br. s, 1H), 7.19 – 7.13 (m, 1H), 7.06 (d, *J* = 7.6 Hz, 1H), 6.92 – 6.86 (m, 1H), 3.11 (s, 2H), 2.25 (s, 3H), 2.24 (s, 3H), 1.21 (s, 6H). ^{13}C NMR (151 MHz, DMSO) δ 177.2, 135.9, 135.6, 133.4, 129.8, 128.5, 126.3, 42.8, 42.8, 24.7, 20.6, 19.6. HRMS (ESI Neg) for $[C_{13}H_{17}O_2S]^-$ calcd. 237.0944, found 237.0956.

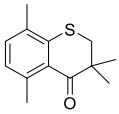

3,3,5,8-tetramethylthiochroman-4-one (**47**). 3-((2,5-dimethylphenyl)thio)-2,2-dimethylpropanoic acid (**46**, 400 mg, 1.68 mmol, 1.0 equiv.) was dissolved in CH_2Cl_2 (2 mL, 0.8 M) with two drops of DMF. Oxalyl chloride (0.28 mL, 3.36 mmol, 2.0 equiv.) was added and the mixture was stirred at room temperature for 1 h. The crude mixture was diluted with heptane and volatiles were removed under reduced pressure. Excess oxalyl chloride was removed by adding heptane and evaporation twice more. The formed acyl chloride intermediate was dissolved in CH_2Cl_2 (10 mL, 0.2 M) and cooled to 0 °C. $AlCl_3$ (314 mg, 2.35 mmol, 1.4 equiv.) was added at that temperature, after which the mixture was allowed to warm to room temperature and stirred at room temperature for 3 h. The reaction was quenched with water and the product was extracted with CH_2Cl_2 and the combined organic phases were washed with brine and dried over $MgSO_4$. The product was purified by flash column chromatography (silica, EtOAc/*n*-pentane, 2–5%) and obtained as a pale-yellow oil in 86% yield (318 mg, 1.44 mmol). ^{1}H NMR (600 MHz, $CDCl_3$) δ 7.09 (d, *J* = 7.6 Hz, 1H), 6.89 (d, *J* = 7.6 Hz, 1H), 3.03 (s, 2H), 2.49 (s, 3H), 2.28 (s, 3H), 1.31 (s, 6H). ^{13}C NMR (151 MHz, $CDCl_3$) δ 202.2, 141.3, 140.1, 132.8, 132.6, 130.1, 128.3, 42.5, 39.1, 24.0, 23.3, 20.0. HRMS (ESI Pos) for $[C_{13}H_{17}OS]^+$, calcd 221.0995, found 221.0998.

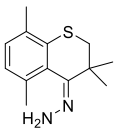

(3,3,5,8-tetramethylthiochroman-4-ylidene)hydrazine (**57**). 3,3,5,8-tetramethyl-thiochroman-4-one (**47**, 200 mg, 0.91 mmol, 1.0 equiv.) was dissolved in toluene (2.0 mL, 0.5 M). Lawesson's reagent (736 mg, 1.82 mmol, 2.0 equiv.) and P_2S_5 (405 mg, 1.82 mmol, 2.0 equiv.) were added. The mixture

was heated to 130 °C with microwave irradiation for 2 h. The mixture was filtered over Celite and purified by flash column chromatography (silica, CH_2Cl_2/*n*-pentane, 5%) to afford a dark purple oil that was used immediately in the next transformation.

The thioketone was dissolved in ethanol (3 mL, 0.3 M) and hydrazine monohydrate (3 mL, 62 mmol, 68 equiv.) was added. The reaction mixture was heated at reflux for 2 h. The product was extracted with EtOAc, the combined organic phase was washed with water and brine, dried over $MgSO_4$ and volatiles were removed under reduced pressure. The product was purified by flash column chromatography (silica, EtOAc/*n*-pentane, 20%) and obtained as a white solid in 31% yield (66 mg, 0.28 mmol). ^{1}H NMR (400 MHz, $CDCl_3$) δ 6.91 (s, 2H), 2.62 (s, 2H), 2.39 (s, 3H), 2.28 (s, 3H), 1.59 (s, 6H). ^{13}C NMR (151 MHz, $CDCl_3$) δ 150.12, 139.60, 136.36, 133.10, 128.90, 127.86, 48.78, 42.17, 22.57, 22.55, 19.80. Note: C=N-NH_2 signal could not be identified by ^{1}H-NMR. HRMS (ESI Pos), for $[C_{13}H_{19}N_2S]^+$, calcd. 235.1264, found 235.1268.

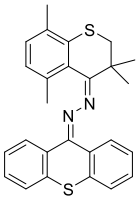

1-(3,3,5,8-tetramethylthiochroman-4-ylidene)-2-(9H-thioxanthen-9-ylidene)hydrazine (**58**). To a solution of (3,3,5,8-tetramethylthiochroman-4-ylidene)hydrazine (**57**, 57 mg, 0.24 mmol, 1.4 equiv.) in DMF (5 mL, 0.05 M) at -40 °C was added $PhI(OCOCF_3)_2$ (97 mg, 0.23 mmol, 1.3 equiv.) in DMF (2 mL) and the mixture stirred at -40 °C until it turned pink. 9H-thioxanthene-9-thione (18, 39 mg, 0.17 mmol, 1.0 equiv.) was added to the cold mixture which was allowed to warm up to room temperature. Volatiles were removed under reduced pressure and the product was purified by flash column chromatography (silica, EtOAc/*n*-pentane, 5%). The product was obtained as a yellow solid in 37% yield (27 mg, 0.06 mmol). ^{1}H NMR (600 MHz, $CDCl_3$) δ 8.15 (dd, *J* = 8.0, 1.5 Hz, 1H), 7.62 (dd, *J* = 7.9, 1.4 Hz, 1H), 7.46 (dd, *J* = 7.9, 1.4 Hz, 1H), 7.38 – 7.27 (m, 4H), 7.21 (ddd, *J* = 8.3, 7.3, 1.3 Hz, 1H), 7.07 (d, *J* = 7.7 Hz, 1H), 6.96 (d, *J* = 7.7 Hz, 1H), 2.92 (d, *J* = 12.6 Hz, 1H), 2.82 (d, *J* = 12.5 Hz, 1H), 2.29 (s, 3H), 2.24 (s, 3H), 1.34 (s, 6H). ^{13}C NMR (151 MHz, $CDCl_3$) δ 166.1, 150.4, 137.9, 135.8, 135. 0, 133.4, 133.2, 133.0, 132.8, 132.7, 130.0, 129.4, 128.9, 128.0, 127.2, 126.7, 126.6, 126.1, 125.2, 124.8, 44.1, 43.4, 27.1, 25.1, 20.8, 19.8. HRMS (APCI Pos): for $[C_{26}H_{25}N_2S_2]^+$ calcd. m/z = 429.1454, found m/z = 429.1457.

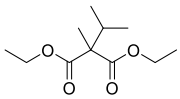

Diethyl 2-isopropyl-2-methylmalonate (**49**). Diethyl 2-isopropylmalonate (10 g, 49 mmol, 1.0 equiv.) was dissolved in THF (240 mL, 0.2 M) and the solution was cooled to 0 °C. NaH (60% dispersion in mineral oil, 2.4 g, 1.2 equiv.) was added to the mixture while stirring at 0 °C. Methyl iodide (4.6 mL, 74 mmol, 1.5 equiv.) was added and the mixture was stirred at room temperature for 16 h. Water was added to the reaction mixture and the product was extracted with Et_2O. The organic phase was washed with water and the aqueous phase was back-extracted with Et_2O. The combined organic phases were dried over $MgSO_4$ and volatiles were removed under reduced pressure. The product was purified by flash column chromatography and obtained as a pale-yellow oil in quantitative yield (10.6 g, 49 mmol). ^{1}H NMR (600 MHz, $CDCl_3$) δ 4.19 – 4.14 (m, 4H), 2.49 (hept, *J* = 6.8 Hz, 1H), 1.32 (s, 3H), 1.24 (t, *J* = 7.1 Hz, 6H), 0.93 (d, *J* = 6.9 Hz, 6H). Compound data is in accordance with literature.[58]

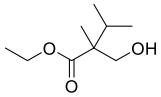

Ethyl 2-(hydroxymethyl)-2,3-dimethylbutanoate (**50**). Diethyl 2-isopropyl-2-methylmalonate (**49**, 4.0 g, 18.5 mmol. 1.0 equiv.) was dissolved in CH_2Cl_2 (40 mL. 0.6 M) and cooled to -40 °C. Diisobutylaluminium hydride (1.2 M in toluene, 30.8 mL, 37.0 mmol, 2.0 equiv.) was added to the mixture, which was stirred at -40 °C for 16 h. The reaction was quenched with an aqueous solution of Rochelle salt and the mixture was extracted with CH_2Cl_2 and dried over Na_2SO_4. Volatiles were removed under reduced pressure, the crude mixture was dissolved in a mixture of THF/MeOH (30 mL/20mL), and $NaBH_4$ (350 mg, 9.25 mmol, 0.5 equiv.) was added to the mixture. The mixture was stirred at room temperature until full conversion of the starting material. The reaction was quenched with saturated aqueous NH_4Cl and the product was extracted with CH_2Cl_2, washed with brine and dried over Na_2SO_4. The product was purified by flash column chromatography (silica, EtOAc/*n*-pentane, 1-15%) and obtained as a colourless oil in 29% yield (935 mg, 5.37 mmol). ^{1}H NMR (400 MHz, $CDCl_3$) δ 4.23 – 4.15 (m, 2H), 3.76 (d, *J* = 11.3 Hz, 1H), 3.47 (d, *J* = 11.3 Hz, 1H), 2.40 (br. s, 1H), 2.10 (hept, *J* = 7.0 Hz, 1H), 1.28 (t, *J* = 7.1 Hz, 3H), 1.09 (s, 3H), 0.93 – 0.85 (m, 6H).

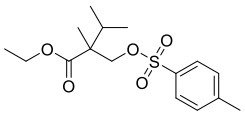

Ethyl 2,3-dimethyl-2-((tosyloxy)methyl)butanoate (**51**). Ethyl 2-(hydroxymethyl)-2,3-dimethylbutanoate (**50**, 730 mg, 4.19 mmol, 1.0 equiv.), *p*-toluene sulfonyl chloride (879 mg, 4.61 mmol, 1.1 equiv.) and 4-dimethylaminopyridine (26 mg, 0.21 mmol, 0.05 equiv.) were added to pyridine (20 mL, 0.2 M). The mixture was stirred at 80 °C for 16 h. After the mixture was cooled to room temperature, it was washed with water, extracted with CH_2Cl_2 and dried over $MgSO_4$. The product was purified by flash column chromatography (silica, EtOAc/*n*-pentane, 15%) and obtained as a colourless oil in 32% yield (440 mg, 1.34 mmol). ^{1}H NMR (400 MHz, $CDCl_3$) δ 7.80 – 7.74 (m, 2H), 7.34 (d, *J* = 8.0 Hz, 2H), 4.19 (d, *J* = 9.0 Hz, 1H), 4.13 – 4.02 (m, 2H), 4.00 (d, *J* = 9.0 Hz, 1H), 2.45 (s, 3H), 1.94 (hept, *J* = 6.9 Hz, 1H), 1.19 (t, *J* = 7.1 Hz, 3H), 1.11 (s, 3H), 0.87 – 0.78 (m, 6H). ^{13}C NMR (151 MHz, $CDCl_3$) δ 173.9, 144.9, 133.1, 129.9, 128.1, 74.4, 60.9, 49.8, 32.6, 21.8, 18.0, 17.5, 15.2, 14.3.

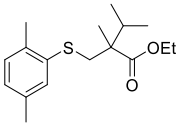

Ethyl 2-(((2,5-dimethylphenyl)thio)methyl)-2,3-dimethylbutanoate (**52**). 2,5-dimethyl benzenethiol (0.39 mL, 2.88 mmol, 1.1 equiv.) and NaH (60% dispersion in mineral oil, 115 mg, 2.88 mmol, 1.1 equiv.) were added to DMF (17 mL, 0.17 M) at 0 °C and the mixture was stirred at this temperature until completion (TLC). A solution of ethyl 2,3-dimethyl-2-((tosyloxy)methyl)butanoate (**51**, 860 mg, 2.62 mmol, 1.0 equiv.) in DMF (8 mL, 0.33 M) was added to the mixture, which was subsequently stirred at 80 °C for 16 h. The reaction was quenched with water, the product was extracted with CH_2Cl_2 and the combined organic phase was dried over $MgSO_4$. Volatiles were removed under reduced pressure and the product was purified by flash column chromatography (silica, EtOAc/*n*-pentane, 1–10%) and obtained as a pale-yellow oil in 54% yield (420 mg, 1.43 mmol). ^{1}H NMR (600 MHz, $CDCl_3$) δ 7.16 (s, 1H), 7.04 (d, *J* = 7.6 Hz, 1H), 6.90 (d, *J* = 7.3 Hz, 1H), 4.10 (dq, *J* = 10.8, 7.1 Hz, 1H), 4.00 (dq, *J* = 10.8, 7.2 Hz, 1H), 3.22 (d, *J* = 12.0 Hz, 1H), 3.02 (d, *J* = 11.9 Hz, 1H), 2.34 (s, 3H), 2.30 (s, 3H), 2.08 (d, *J* = 6.8 Hz, 1H), 1.20 (t, *J* = 7.1 Hz, 3H), 1.18 (s, 3H), 0.92 (d, *J* = 6.9 Hz, 3H), 0.88 (d, *J* = 6.8 Hz, 3H). ^{13}C NMR (151 MHz, $CDCl_3$) δ 175.6, 136.1, 136.0, 135.6, 130.8, 130.1, 127.2, 60.6, 50.9, 42.8, 35.2, 21.1, 20.3, 18.6, 17.3, 16.2, 14.3.

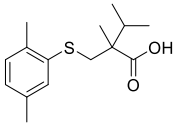

2-(((2,5-dimethylphenyl)thio)methyl)-2,3-dimethylbutanoic acid (**53**). Ethyl 2-(((2,5-dimethylphenyl)thio)methyl)-2,3-dimethylbutanoate (**52**, 40 mg, 0.14 mmol, 1.0 equiv.) and KOH (76.3 mg, 1.4 mmol, 10 equiv.) were added to EtOH (3 mL, 0.47 M) and heated to reflux for 20 h. Ethanol was removed under reduced pressure and the crude product was dissolved in 10% aqueous KOH and the solution was washed with Et_2O. The aqueous phase was acidified to pH = 1 with 3 M HCl (aq) and the product was extracted with EtOAc. The combined organic phase was washed with brine, dried over $MgSO_4$ and volatiles were removed under reduced pressure. The product was obtained as a white solid in 74% yield (27 mg, 0.10 mmol). ^{1}H NMR (400 MHz, $CDCl_3$) δ 7.17 (s, 1H), 7.04 (d, *J* = 7.6 Hz, 1H), 6.91 (d, *J* = 7.6 Hz, 1H), 3.20 (d, *J* = 11.9 Hz, 1H), 3.07 (d, *J* = 11.9 Hz, 1H), 2.35 (s, 3H), 2.30 (s, 3H), 2.17 – 2.05 (m, 1H), 1.21 (s, 3H), 0.99 – 0.93 (m, 6H). ^{13}C NMR (151 MHz, $CDCl_3$) δ 181.5, 136.1, 135.9, 135.6, 130.8, 130.1, 127.4, 51.0, 42.3, 35.2, 21.1, 20.2, 18.5, 17.3, 16.4.

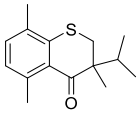

3-isopropyl-3,5,8-trimethylthiochroman-4-one (**54**). 2-(((2,5-dimethylphenyl)thio)methyl)-2,3-dimethylbutanoic acid (**53**, 20 mg, 0.08 mmol, 1.0 equiv.) was dissolved in CH_2Cl_2 (1 mL, 0.08 M) with a drop of DMF. Oxalyl chloride (13 µL, 0.15 mmol, 2.0 equiv.) was added and the mixture was stirred at room temperature for 1 h. The crude mixture was diluted with heptane and volatiles were removed under reduced pressure. Excess oxalyl chloride was removed, by co-evaporation with *n*-heptane under reduced pressure. The formed acyl chloride intermediate was dissolved in CH_2Cl_2 (1 mL, 0.08 M) and cooled to 0 °C. $AlCl_3$ (14 mg, 0.11 mmol, 1.4 equiv.) was added and the mixture was allowed to warm up to room temperature and stirred for 3 h. The reaction was quenched with water and the product was extracted with CH_2Cl_2, washed with brine and dried over $MgSO_4$. The product was purified by flash column chromatography (silica, EtOAc/*n*-pentane, 1–5%) and obtained as a colourless oil in 70% yield (13 mg, 0.05 mmol). ^{1}H NMR (400 MHz, $CDCl_3$) δ 7.07 (d, *J* = 7.7 Hz, 1H), 6.87 (d, *J* = 7.6 Hz, 1H), 3.13 (d, *J* = 13.8 Hz, 1H), 3.05 (d, *J* = 13.8 Hz, 1H), 2.47 – 2.45 (m, 4H), 2.26 (s, 3H), 1.14 (s, 3H), 0.96 (d, *J* = 6.8 Hz, 3H), 0.75 (d, *J* = 6.9 Hz, 3H). ^{13}C NMR (151 MHz, $CDCl_3$) δ 203.6, 141.0, 139.3, 132.4, 132.3, 130.7, 128.1, 47.7, 35.4, 29.8, 22.8, 19.9, 17.8, 17.3, 16.3. GC-MS: found m/z = 248 $[M]^+$, 164 $[M\text{-}C_6H_{12}]^+$.

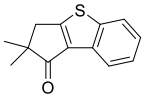

2,2-dimethyl-2,3-dihydro-1H-benzo[b]cyclopenta[d]thiophen-1-one (**59**). 2-methyl-2,3-dihydro-1H-benzo[b]cyclopenta[d]thiophen-1-one (**33**, 202 mg, 1.0 mmol, 1.0 equiv.) was dissolved in THF (1 mL, 1.0 M) and added to a fresh solution of lithium diisopropyl amide (1.2 mmol, 1.2 equiv.) in THF (1.2 mL, 1.0 M) at -78 °C and the mixture was stirred for 15 min. Methyl iodide (93 µL, 1.5 mmol, 1.5 equiv.) was added dropwise to the mixture, after which it was allowed to warm to room temperature followed by stirring for 16 h. The reaction was quenched with saturated NH_4Cl (aq), the mixture was extracted with EtOAc, the combined organic phase was washed with brine and dried over $MgSO_4$. The product was purified by flash column chromatography (silica, EtOAc/*n*-pentane, 3%) and obtained as a yellow oil in 96% yield (208 mg, 0.96 mmol). ^{1}H NMR (400 MHz, $CDCl_3$) δ 8.24 (d, *J* = 7.9 Hz, 1H), 7.81 (d, *J* = 8.0 Hz, 1H), 7.48 – 7.43 (m, 1H), 7.41 – 7.35 (m, 1H), 3.15 (s, 2H), 1.33 (s, 6H). ^{13}C NMR (101 MHz, $CDCl_3$) δ 203.0, 171.3, 144.6, 137.7, 132.0, 125.9, 125.6, 123.3, 123.2, 51.9, 41.8, 25.6. HRMS (APCI Pos): for $[C_{13}H_{13}OS]^+$ calcd. m/z = 217.0682, found m/z = 217.0683.

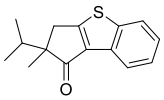

2-isopropyl-2-methyl-2,3-dihydro-1H-benzo[b]cyclopenta[d] thiophen-1-one (**60**). 2-methyl-2,3-dihydro-1H-benzo[b]cyclopenta [d]thiophen-1-one (**33**, 202 mg, 1.0 mmol, 1.0 equiv.) was dissolved in THF (4.3 mL) and added to a fresh solution of lithium diisopropyl amide (2.4 mL, 1.2 mmol, 1.2 equiv., 0.5 M in THF) at -78 °C and the mixture was stirred for 15 min. 2-Iodopropane (0.14 mL, 1.4 mmol, 1.4 equiv.) was added dropwise to the mixture, after which it was allowed to warm up to room temperature and stirred for 16 h. The reaction was quenched with saturated NH_4Cl (aq), the mixture was extracted with EtOAc and the combined organic phase was washed with brine. Volatiles were removed under reduced pressure and the product was purified by flash column chromatography (silica, EtOAc/*n*-pentane, 3%) and obtained as a yellow oil in 48% yield (116 mg, 0.48 mmol). ^{1}H NMR (400 MHz, $CDCl_3$) δ 8.27 – 8.23 (m, 1H), 7.85 – 7.77 (m, 1H), 7.49 – 7.42 (m, 1H), 7.38 (dd, *J* = 8.5, 7.2 Hz, 1H), 3.27 (d, *J* = 18.1 Hz, 1H), 2.81 (d, *J* = 18.1 Hz, 1H), 2.12 (hept, *J* = 6.9 Hz, 1H), 1.31 (s, 3H), 1.00 (d, *J* = 6.9 Hz, 3H), 0.80 (d, *J* = 6.8 Hz, 3H). ^{13}C NMR (101 MHz, $CDCl_3$) δ 203.5, 172.4, 144.6, 139.1, 131.8, 125.9, 125.6, 123.3, 123.2, 59.2, 35.3, 34.0, 23.5, 18.1, 17.8. HRMS (ESI Pos), for $[C_{15}H_{17}OS]^+$ calcd. m/z = 245.0995, found m/z = 245.0999.

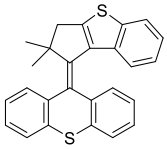

9-(2,2-dimethyl-2,3-dihydro-1H-benzo[b]cyclopenta[d]thiophen-1-ylidene)-9H-thioxanthene (**41**). Thioketone intermediate preparation: 2,2-dimethyl-2,3-dihydro-1H-benzo[b]cyclopenta[d]thiophen-1-one (**59**, 200 mg, 0.93 mmol, 1.0 equiv.) was dissolved in toluene (5 mL, 0.19 M) and Lawesson's reagent (451 mg, 1.12 mmol, 1.2 equiv.) was added. The mixture was heated at reflux for 16 h. The mixture was filtered over silica and flushed with 3% EtOAc/*n*-pentane to afford the thioketone as a pink solid (185 mg, 0.80 mmol, 86% yield) which was used directly in the next transformation.

Barton-Kellogg coupling: (9H-thioxanthen-9-ylidene)hydrazine (**19**, 199 mg, 0.88 mmol, 1.1 equiv.) and $MgSO_4$ (528 mg, 4.4 mmol, 5.5 equiv.) were added to THF (9 mL, 0.1 M) followed by the addition of MnO_2 (383 mg, 4.4 mmol, 5.5 equiv.) and the mixture was stirred for 45 min at 0 °C. A solution of the thioketone intermediate (185 mg, 0.80 mmol, 1.0 equiv.) in THF (5 mL, 0.16 M) was added to the cold mixture, which was allowed to warm up to room temperature and the mixture was stirred for 16 h. Volatiles were removed under reduced pressure and the residue was dissolved in toluene (6 mL, 0.16 M) and $P(NMe_2)_3$ (0.43 mL, 2.9 mmol, 3.6 equiv.) was added. The mixture was stirred at 60 °C for 20 h and subsequently allowed to cool down to room temperature, filtered over silica and flushed with 5% EtOAc/*n*-pentane to afford a mixture of the product and the thioketone intermediate. Volatiles were removed under reduced pressure and the mixture was dissolved in CH_2Cl_2 (10 mL) and 2 M NaOH (aq) solution (10 mL) was added. Tetrabutylammonium hydrogen sulfate (300 mg, 0.88 mmol, 1.1 equiv.) was added and the mixture was vigorously stirred for 16 h at room temperature. The mixture was diluted with CH_2Cl_2, washed with brine and dried over $MgSO_4$. Volatiles were removed under reduced pressure and the product was purified by flash column chromatography (silica, EtOAc/*n*-pentane, 0–5%) and obtained as a white solid in 24% yield (76 mg, 0.19 mmol). ^{1}H NMR (600 MHz, $CDCl_3$) δ 7.69 (dd, *J* = 7.6, 1.5 Hz, 1H), 7.66 (dd, *J* = 7.8, 1.2 Hz, 1H), 7.62 (d, *J* = 8.1 Hz, 1H), 7.60 (dd, *J* = 7.6, 1.4 Hz, 1H), 7.25 – 7.14 (m, 4H), 7.07 – 7.03 (m, 2H), 6.72 – 6.69 (m, 1H), 5.29 (d, *J* = 8.3 Hz, 1H), 1.55 (s, 6H). ^{13}C NMR (151 MHz, $CDCl_3$) δ 150.8, 144.4, 144.0, 143.8, 140.0, 138.5, 138.4, 137.6, 134.5, 130.5, 129.5, 128.5, 128.5, 127.9, 127.4, 126.3, 126.0, 125.1, 124.7, 123.7, 123.1, 122.7, 52.7, 46.6. HRMS (ESI Pos): for $[C_{26}H_{21}S_2]^+$, calcd. m/z = 397.1079, found m/z = 397.1072.

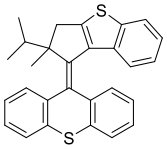

9-(2-isopropyl-2-methyl-2,3-dihydro-1H-benzo[b]cyclopenta[d] thiophen-1-ylidene)-9H-thioxanthene (**42**). Thioketone intermediate preparation: 2,2-dimethyl-2,3-dihydro-1H-benzo[b]cyclopenta[d]thiophen-1-one (**60**, 79 mg, 0.36 mmol, 1.0 equiv.) was dissolved in toluene (2 mL, 0.18 M). Lawesson's reagent (158 mg, 0.39 mmol, 1.2 equiv.) was added and the mixture was heated at reflux for 16 h. The mixture was allowed to cool down to room temperature and was filtered over a plug of silica gel, eluted with CH_2Cl_2. Volatiles were removed under reduced pressure and the thioketone was purified by flash column chromatography (silica, *n*-pentane) and obtained as a pink oil (79 mg, 0.34 mmol, 93% yield).

Barton-Kellogg coupling: (9H-thioxanthen-9-ylidene)hydrazine (**19**, 45 mg, 0.20 mmol, 1.1 equiv.) and $MgSO_4$ (120 mg, 1.0 mmol, 5.5 equiv.) were added to THF (2 mL) and MnO_2 (87 mg, 1.0 mmol, 5.5 equiv.) was added and the mixture was stirred for 45 min at room temperature. A solution of the thioketone intermediate (47 mg, 0.18 mmol, 1.0 equiv.) in THF (2.0 mL, 0.09 M) was added to the mixture, which was stirred at 35 °C for 16 h. The mixture was allowed to cool to room temperature, filtered and volatiles were removed under reduced pressure. The mixture was taken up in toluene (2 mL, 0.18 M) and $P(NMe_2)_3$ (0.11 ml, 0.6 mmol, 3.0 equiv.) is added. The mixture was heated at reflux for 16 h. Volatiles were removed under reduced pressure and the product was purified by flash column chromatography (silica, CH_2Cl_2/*n*-pentane, 10%) and obtained as a white solid in 22% yield (17 mg, 0.04 mmol). ^{1}H NMR (500 MHz, C_6D_6, 65 °C) δ 7.63 (d, *J* = 7.7 Hz, 1H), 7.53 – 7.40 (m, 3H), 7.20 – 7.19 (m, 1H), 6.96 – 6.81 (m, 4H), 6.76 (dd, *J* = 7.7, 7.5 Hz, 2H), 5.70 (d, *J* = 8.4 Hz, 1H), 2.81 (d, *J* = 16.7 Hz, 1H), 2.73 (d, *J* = 16.7 Hz, 1H), 1.51 (s, 3H), 1.31 (m, 1H), 0.66 (d, J = 6.6 Hz, 3H), 0.63 (d, J = 6.6 Hz, 3H). ^{13}C NMR (151 MHz, $CDCl_3$, 25 °C) δ 144.5, 144.2, 143.8, 138.7, 138.4, 136.4, 135.8, 134.3, 130.0, 129.7, 128.5, 127.9, 127.4, 127.3, 126.9, 126.3, 125.8, 125.2, 124.6, 123.7, 123.1, 122.6, 36.1, 34.3, 22.5, 18.5, 17.8, 14.2. GC-MS: found m/z = 424 $[M]^+$, 381 $[M\text{-}C_3H_7]^+$.

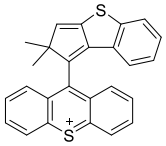

9-(2,2-dimethyl-2H-benzo[b]cyclopenta[d]thiophen-1-yl) thioxanthylium (**63**). In a three-electrode setup with a porous carbon working electrode, a carbon rod counter electrode and an SCE reference electrode. Compound **41** (12 mg, 0.03 mmol) was suspended in acetonitrile (30 mL) and CH_2Cl_2 was added until all material was dissolved (~20 mL). KPF_6 (500 mg, 2.72 mmol, 0.05 M) was added as supporting electrolyte. The compound was electrochemically oxidised with continuous stirring at 0.90 V vs. SCE until cyclic voltammetry indicated full conversion of the starting material. Volatiles were removed under reduced pressure. The oxidised product was dissolved in a minimal amount of acetonitrile and CH_2Cl_2 was carefully added to precipitate the excess KPF_6. The precipitation procedure was repeated twice and a small amount of product was obtained as a red solid. ^{1}H NMR (600 MHz, CD_3CN) δ 8.82 (d, *J* = 8.5 Hz, 2H), 8.73 (d, *J* = 8.8 Hz, 2H), 8.43 – 8.34 (m, 2H), 8.04 – 7.93 (m, 2H), 7.56 (d, *J* = 8.1 Hz, 1H), 7.30 – 7.24 (m, 1H), 6.80 – 6.73 (m, 1H), 6.71 (s, 1H), 6.50 (d, *J* = 7.9 Hz, 1H), 1.16 (s, 6H).

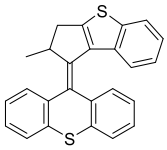

9-(2-methyl-2,3-dihydro-1H-benzo[b]cyclopenta[d]thiophen-1-ylidene)-9H-thioxanthene (**65**). Thioketone preparation: 2-methyl-2,3-dihydro-1H-benzo[b]cyclopenta[d]thiophen-1-one (**33**, 200 mg, 1.0 mmol, 1.0 equiv.) was dissolved in toluene (10 mL, 0.1 M) and Lawesson's reagent (485 mg, 1.2 mmol, 1.2 equiv.) was added. The mixture was heated at reflux for 16 h. The mixture was allowed to cool down to room temperature and was purified by filtration over a short pad of silica gel and flushed with 3% EtOAc/*n*-pentane. Volatiles were removed and the thioketone intermediate was obtained as a pink solid in 97% yield (211 mg, 0.97 mmol).

Barton-Kellogg coupling: (9H-thioxanthen-9-ylidene)hydrazine (**19**, 86 mg, 0.38 mmol, 1.05 equiv.) and $MgSO_4$ (228 mg, mmol, 5.25 equiv.) were added to dry THF (4 mL, 0.1 M) and cooled to 0 °C. MnO_2 (165 mg, mmol, 5.25 equiv.) was added and the mixture was stirred at 0 °C for 30 min. The mixture was filtered over a glass frit (size P4) under N_2 flow into a dry Schlenk flask at 0 °C. A solution of the thioketone intermediate (78 mg, 0.36 mmol, 1.0 equiv.) in THF (3.7 mL, 0.1 M) was added to the mixture which was

subsequently stirred at room temperature for 16 h. Volatiles were removed under reduced pressure and the resulting crude episulfide mixture was dissolved in toluene (5 mL, 0.07 M). $P(NMe_2)_3$ (196 mg, 1.08 mmol, 3.0 equiv.) was added and the mixture was stirred at 80 °C for 16 h. Volatiles were removed under reduced pressure and the product was purified by flash column chromatography (silica, CH_2Cl_2, *n*-pentane, 10%). The product was obtained as a white solid in 72% yield (97 mg, 0.25 mmol). ^{1}H NMR (400 MHz, $CDCl_3$) δ 7.79 (dd, *J* = 7.6, 1.4 Hz, 1H), 7.66 (d, *J* = 8.0 Hz, 1H), 7.61 (dd, *J* = 8.2, 1.3 Hz, 1H), 7.55 (dd, *J* = 7.8, 1.3 Hz, 1H), 7.31 (ddd, *J* = 7.6, 7.5, 1.4 Hz, 1H), 7.25 – 7.16 (m, 3H), 7.13 – 7.07 (m, 1H), 7.07 – 7.02 (m, 1H), 6.82 – 6.75 (m, 1H), 5.67 (d, *J* = 8.3 Hz, 1H), 4.45 – 4.34 (m, 1H), 3.59 (dd, *J* = 16.2, 6.6 Hz, 1H), 2.63 (d, *J* = 16.2 Hz, 1H), 0.78 (d, *J* = 6.9 Hz, 3H). ^{13}C NMR (151 MHz, $CDCl_3$) δ 154.0, 144.6, 142.3, 140.4, 138.4, 138.1, 136.3, 136.0, 133.5, 129.9, 127.7, 127.2, 127.1, 127.0, 126.7, 126.6, 126.2, 126.0, 125.2, 123.8, 123.4, 122.8, 42.3, 36.9, 20.3. HRMS (ESI Pos): for $[C_{25}H_{19}S_2]^+$ calcd. m/z = 383.0923, found 383.0923.

5. References

1 B. L. Feringa, *Angew. Chem. Int. Ed.*, 2017, **56**, 11060–11078.
2 S. Erbas-Cakmak, D. A. Leigh, C. T. McTernan and A. L. Nussbaumer, *Chem. Rev.*, 2015, **115**, 10081–10206.
3 B. L. Feringa, *Adv. Mater.*, 2020, **32**, 1906416.
4 T. van Leeuwen, A. S. Lubbe, P. Štacko, S. J. Wezenberg and B. L. Feringa, *Nat. Rev. Chem.*, 2017, **1**, 0096.
5 C. Pezzato, C. Cheng, J. F. Stoddart and R. D. Astumian, *Chem. Soc. Rev.*, 2017, **46**, 5491–5507.
6 D. Dattler, G. Fuks, J. Heiser, E. Moulin, A. Perrot, X. Yao and N. Giuseppone, *Chem. Rev.*, 2020, **120**, 310–433.
7 S. Kassem, T. van Leeuwen, A. S. Lubbe, M. R. Wilson, B. L. Feringa and D. A. Leigh, *Chem. Soc. Rev.*, 2017, **46**, 2592–2621.
8 A. S. Lubbe, C. L. G. Stähler and B. L. Feringa, in *Out-of-Equilibrium (Supra)molecular Systems and Materials*, eds. N. Giuseppone and A. Walther, Wiley-VCH GmbH., 2021, pp. 337–377.
9 A. Goel and V. Vogel, *Nat. Nanotechnol.*, 2008, **3**, 465–475.
10 Y. Asai, I. Kawagishi, R. E. Sockett and M. Homma, *J. Bacteriol.*, 1999, **181**, 6332–6338.
11 J. W. Canary, *Chem. Soc. Rev.*, 2009, **38**, 747–756.
12 B. L. Feringa and W. R. Browne, *Molecular Switches*, Wiley-VCH, Hoboken, USA, 2nd edn., 2011.
13 N. Xie, D. X. Zeng and Y. Chen, *J. Electroanal. Chem.*, 2007, **609**, 27–30.
14 H. Higuchi, E. Ohta, H. Kawai, K. Fujiwara, T. Tsuji and T. Suzuki, *J. Org. Chem.*, 2003, **68**, 6605–6610.
15 S. Zahn and J. W. Canary, *Science*, 2000, **288**, 1404–1407.

16 G. Beer, C. Niederalt, S. Grimme and J. Daub, *Angew. Chem. Int. Ed.*, 2000, **39**, 3252–3255.
17 D. J. Cárdenas, A. Livoreil and J. P. Sauvage, *J. Am. Chem. Soc.*, 1996, **118**, 11980–11981.
18 N. Armaroli, V. Balzani, J. P. Collin, P. Gaviña, J. P. Sauvage and B. Ventura, *J. Am. Chem. Soc.*, 1999, **121**, 4397–4408.
19 F. Durola and J. P. Sauvage, *Angew. Chem. Int. Ed.*, 2007, **46**, 3537–3540.
20 M. Asakawa, P. R. Ashton, V. Balzani, A. Credi, C. Hamers, G. Mattersteig, M. Montalti, A. N. Shipway, N. Spencer, J. F. Stoddart, M. S. Tolley, M. Venturi, A. J. P. White and D. J. Williams, *Angew. Chem. Int. Ed.*, 1998, **37**, 333–337.
21 G. Gescheidt, A. Lamprecht, J. Heinze, B. Schuler, M. Schmittel, S. Kiau and C. Rüchardt, *Helv. Chim. Acta*, 1992, **75**, 1607–1612.
22 A. Goulet-Hanssens, C. Rietze, E. Titov, L. Abdullahu, L. Grubert, P. Saalfrank and S. Hecht, *Chem*, 2018, **4**, 1740–1755.
23 A. Goulet-Hanssens, M. Utecht, D. Mutruc, E. Titov, J. Schwarz, L. Grubert, D. Bléger, P. Saalfrank and S. Hecht, *J. Am. Chem. Soc.*, 2017, **139**, 335–341.
24 T. Majima, S. Tojo, A. Ishida and S. Takamuku, *J. Org. Chem.*, 1996, **61**, 7793–7800.
25 T. Majima, S. Tojo, A. Ishida and S. Takamuku, *J. Phys. Chem.*, 1996, **100**, 13615–13623.
26 P. Mayorga-Burrezo, C. Sporer, J. A. De Sousa, N. Capra, K. Wurst, N. Crivillers, J. Veciana and C. Rovira, *Chem. Commun.*, 2020, **56**, 14211–14214.
27 M. Alemani, S. Selvanathan, F. Ample, M. V. Peters, K. H. Rieder, F. Moresco, C. Joachim, S. Hecht and L. Grill, *J. Phys. Chem. C*, 2008, **112**, 10509–10514.
28 M. Alemani, M. V. Peters, S. Hecht, K. H. Rieder, F. Moresco and L. Grill, *J. Am. Chem. Soc.*, 2006, **128**, 14446–14447.
29 T. Kudernac, N. Ruangsupapichat, M. Parschau, B. MacIá, N. Katsonis, S. R. Harutyunyan, K. H. Ernst and B. L. Feringa, *Nature*, 2011, **479**, 208–211.
30 W. R. Browne, M. M. Pollard, B. de Lange, A. Meetsma and B. L. Feringa, *J. Am. Chem. Soc.*, 2006, **128**, 12412–12413.
31 B. P. Corbet, M. B. S. Wonink and B. L. Feringa, *Chem. Commun.*, 2021, **57**, 7665–7668.
32 H. Logtenberg, J. Areephong, J. Bauer, A. Meetsma, B. L. Feringa and W. R. Browne, *ChemPhysChem*, 2016, 1895–1901.
33 J. Vicario, M. Walko, A. Meetsma and B. L. Feringa, *J. Am. Chem. Soc.*, 2006, **128**, 5127–5135.
34 J. Bauer, L. Hou, J. C. M. Kistemaker and B. L. Feringa, *J. Org. Chem.*, 2014, **79**, 4446–4455.
35 P. Štacko, J. C. M. Kistemaker and B. L. Feringa, *Chem. Eur. J.*, 2017, **23**, 6643–6653.
36 O. Ivashenko, H. Logtenberg, J. Areephong, A. C. Coleman, P. V. Wesenhagen, E. M. Geertsema, N. Heureux, B. L. Feringa, P. Rudolf and W. R. Browne, *J. Phys. Chem. C*, 2011, **115**, 22965–22975.
37 J. A. Ma and D. Cahard, *Chem. Rev.*, 2004, **104**, 6119–6146.
38 J. Baudoux and D. Cahard, *Org. React.*, 2008, **69**, 347–672.
39 A. K. Ghosh and B. Zajc, *Org. Lett.*, 2006, **8**, 1553–1556.
40 E. Differding and G. M. Rüegg, *Tetrahedron Lett.*, 1991, **32**, 3815–3818.

41 E. Differding and M. Wehrli, *Tetrahedron Lett.*, 1991, **32**, 3819–3822.
42 A. C. Coleman, J. Areephong, J. Vicario, A. Meetsma, W. R. Browne and B. L. Feringa, *Angew. Chem. Int. Ed.*, 2010, **49**, 6580–6584.
43 A. Cnossen, J. C. M. Kistemaker, T. Kojima and B. L. Feringa, *J. Org. Chem.*, 2014, **79**, 927–935.
44 N. Koumura, E. M. Geertsema, M. B. van Gelder, A. Meetsma and B. L. Feringa, *J. Am. Chem. Soc.*, 2002, **124**, 5037–5051.
45 D. O'Hagan, *Chem. Soc. Rev.*, 2008, **37**, 308–319.
46 C. Thiehoff, Y. P. Rey and R. Gilmour, *Isr. J. Chem.*, 2017, **57**, 92–100.
47 C. Thiehoff, M. C. Holland, C. Daniliuc, K. N. Houk and R. Gilmour, *Chem. Sci.*, 2015, **6**, 3565–3571.
48 C. Thiehoff, L. Schifferer, C. G. Daniliuc, N. Santschi and R. Gilmour, *J. Fluor. Chem.*, 2016, **182**, 121–126.
49 M. M. Pollard, A. Meetsma and B. L. Feringa, *Org. Biomol. Chem.*, 2008, **6**, 507–512.
50 M. M. Pollard, M. Klok, D. Pijper and B. L. Feringa, *Adv. Funct. Mater.*, 2007, **17**, 718–729.
51 M. Charton, *Top. Curr. Chem.*, 1983, **114**, 57–91.
52 V. Belot, D. Farran, M. Jean, M. Albalat, N. Vanthuyne and C. Roussel, *J. Org. Chem.*, 2017, **82**, 10188–10200.
53 H. Alper, C. Kwiatkowska, J.-F. Petrignani and F. Sibtain, *Tetrahedron Lett.*, 1986, **27**, 5449–5450.
54 M. Klok, N. Boyle, M. T. Pryce, A. Meetsma, W. R. Browne and B. L. Feringa, *J. Am. Chem. Soc.*, 2008, **130**, 10484–10485.
55 J. J. Snellenburg, S. Laptenok, R. Seger, K. M. Mullen and I. H. M. van Stokkum, *J. Stat. Softw.*, 2012, **49**, 1–22.
56 J. C. M. Kistemaker, S. F. Pizzolato, T. van Leeuwen, T. C. Pijper and B. L. Feringa, *Chem. Eur. J.*, 2016, **22**, 13478–13487.
57 T. Fernández Landaluce, G. London, M. M. Pollard, P. Rudolf and B. L. Feringa, *J. Org. Chem.*, 2010, **75**, 5323–5325.
58 O. Wong and R. H. McKeown, *J. Pharm. Sci.*, 1988, **77**, 926–932.

Chapter 3

Fast Synthesis and Redox Switching of Di- and Tetra-Substituted Bisthioxanthylidene Overcrowded Alkenes

A rapid and efficient method for the synthesis of overcrowded alkenes using (trimethylsilyl)diazomethane provides a range of substituted bisthioxanthylidenes. We show large conformational redox switching from folded to orthogonal states, which tolerates many substitution patterns. The facile access to bisthioxanthylidene switches with the potential for further functionalisation, in combination with the reliable redox chemistry, provides significant advantages to the design of electrochemically responsive systems.

Acknowledgement
I would like to thank Marco B. S. Wonink for his help with the electrochemistry of a part of the synthesised bisthioxanthylidene library and for discussions on the project.

Parts of this chapter have been published as: Brian P. Corbet, Marco B. S. Wonink, Ben L. Feringa, Fast Synthesis and Redox Switching of Di- and Tetra-substituted Bisthioxanthylidene Overcrowded Alkenes, *Chem. Commun.*, 2021, **57**, 7665-7668.

1. Introduction

Overcrowded alkenes[1,2] are an intriguing class of molecules that receives major attention and are particularly attractive in the design of soft actuators[3,4] and responsive materials.[5] Our group has a long-vested interest in overcrowded alkenes, for example, towards molecular motors[6–10] and switches, such as bistricyclic aromatic enes (BAEs).[11–18] These BAEs are a subset of overcrowded alkenes and include widely studied motifs, such as bifluorenylidenes[19], bis(thio-)xanthylidenes[20–22], bianthrones[23] and their derivatives (Figure 1a). For various structures in this class of molecules, fascinating photo-, thermo-, mechano-, and electro-chromic behaviour as well as dynamic stereochemistry has been demonstrated.[2,24–30] Previously, our group has demonstrated that bisthioxanthylidenes can be used as electrochromic conformational and luminescence switches, both in solution[17] and on surfaces.[18] Using electrochemical, thermal and photochemical stimuli, multiple states are individually addressable.[17] These properties provide attractive possibilities to design functional dynamic systems and responsive materials.

The characteristic conformational properties found in BAEs, mainly originate from the high steric hindrance around the overcrowded alkene unit.[2,24,31] There are two ways these molecules accommodate the overcrowding, which are: twisting around the central 9,9' double bond axis or folding of the tricyclic units. The twisting and folding can introduce helical chirality to these molecules and is the basis for the four main conformers observed in BAEs (Figure 1b). The *anti*- and *syn*-folded conformers alleviate strain by folding of the tricyclic units, which can lead to pyramidalisation of the central olefin carbon atoms. The *twisted* and *orthogonal* conformers have two planar tricyclic units and accommodate the overcrowding by rotation around the central double bond axis.

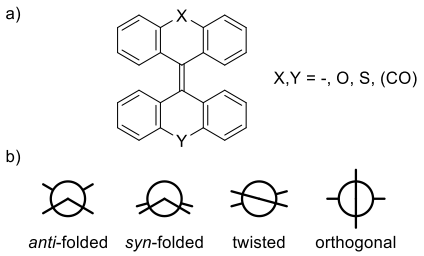

Figure 1. a) General structure of bistricyclic aromatic enes (BAEs). b) Schematic representation of the most common conformers of BAEs.

The *anti*-folded state is the most stable state for neutral bisthioxanthylidenes (Figure 1, X=Y=S). The strain caused by the

overcrowding around the central double bond is relieved by a significant folding of the thiopyran motif.[2] The *syn*-folded and the *twisted* state experience more strain because of a higher overlap between the two halves. Neutral *twisted* or *orthogonal* diradical states, with planar halves are possible, however, with significantly higher energies.[2] Our group previously demonstrated that, by photo-, electrochemical or thermal switching, higher energy conformers are accessible,[5,17] of which the neutral states will rapidly undergo thermal isomerisation to the favoured *anti*-folded state. We further showed that a stable, *orthogonal* state is accessible by oxidation towards a dicationic state with increased single bond character for the central C–C bond and two planar halves.[17]

In the synthesis of overcrowded alkenes (Scheme 1), the most challenging reaction is generally the formation of the overcrowded C=C double bond and only a relatively small number of transformations are suitable. Bisthioxanthylidenes are commonly obtained via a Barton–Kellogg synthesis,[11,32,33] where a diazo compound and a thioketone are used to form olefins via an episulfide intermediate (Scheme 1a). The aforementioned diazo compound is obtained from oxidation of a hydrazone, which in turn is frequently obtained starting from the corresponding thioketone. Long reaction times of typically 12–16 h are required for each step: the hydrazone formation, coupling and desulfurisation. Furthermore, the handling of the often very delicate diazo compound is necessary. Faster and easier synthesis routes, such as the one discussed in this work, can contribute to the study of libraries of compounds and serve as an important addition to the toolbox for incorporation of bisthioxanthylidenes as switches in responsive materials.

Here we present an alternative, very facile synthesis (Scheme 1a) of a variety of substituted bisthioxanthylidenes and their electrochemistry and redox switching (Scheme 1b). By demonstrating a simple, fast synthesis route of substrates with functional handles, in combination with the robust electrochemistry and the intriguing switching modes of bisthioxanthylidenes, we expect that these switches will facilitate the development of multi-responsive materials and complex dynamic molecular systems.

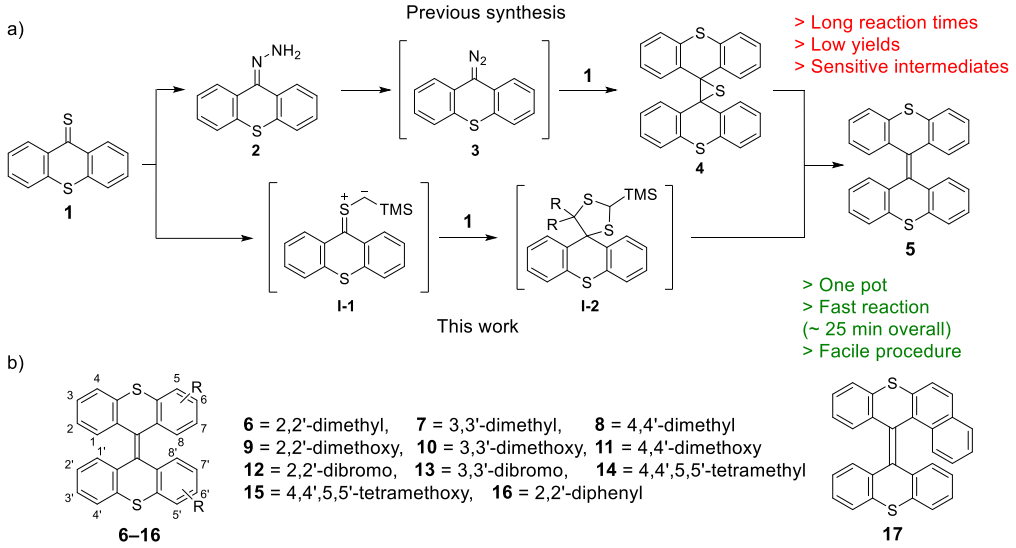

Scheme 1. a) Commonly used previous synthesis route (upper) and novel synthesis route (lower) introduced here, to access bisthioxanthylidenes. b) Schematic overview of bisthioxanthylidenes (**6–17**) studied.

2. Results & Discussion

2.1 Synthesis

Taken inspiration from the recent work of Mlostoń and co-workers,[34,35] we investigated the use of (trimethylsilyl)-diazomethane ($TMSCHN_2$) for the synthesis of bisthioxanthylidenes via dimerisation of thioketones. The dimerisation reaction cascade likely proceeds via a 1,3-dipolar cycloaddition of $TMSCHN_2$ with thioketone **1**, whereupon nitrogen exclusion provides a sulfur ylide (Scheme 1a, **I-1**). This ylide reacts in another 1,3-dipolar cycloaddition with a second equivalent of thioketone **1** leading to a 5-membered dithiane (**I-2**). The addition of tetrabutyl ammonium fluoride (TBAF) leads to the deprotection of the silyl group, the elimination of methanedithioate (CHS_2^-) and the formation of the overcrowded alkene **5**.[34,35] By optimisation of the reaction conditions for dimerisation we developed a fast (~25 min) and highly efficient method for sterically demanding bisthioxanthylidene formation. One equivalent of the thioketone is treated with $TMSCHN_2$ at -78 °C. No conversion to the sulfonium ylide is observed at this temperature and the reaction mixture is immediately allowed to warm up to room temperature. The conversion of the strongly coloured thioketone **1** can be easily monitored by TLC analysis or simple observation of the colour change. A second equivalent of thioketone was converted within a few minutes after addition. TBAF addition leads to full

conversion towards the overcrowded alkene within 5 min. The synthesis of bisthioxanthylidenes from two distinct thioketones is possible. However, this results in a mixture with the homocoupled products (see Section 4.6). The overall time for the complete, one-pot sequence from thioketone to overcrowded olefin is approximately 25 min.

Thioketones **18–28** could be obtained by thionation of corresponding thioxanthones using P_2S_5 and were submitted to the dimerisation conditions immediately after purification. The dimerisation reactions show moderate to excellent isolated yields (Scheme 2), while all conversions proceed rapidly and efficiently to give BAEs 6–16 as a mixture of *E*/*Z*-isomers. It should be noted that the purification of poorly soluble compounds by chromatographic methods is likely the reason for the most significant loss for some compounds showing lower isolated yields. The dimerisation reactions were mostly performed on a 0.18–1.26 mmol scale (see Section 4.3).

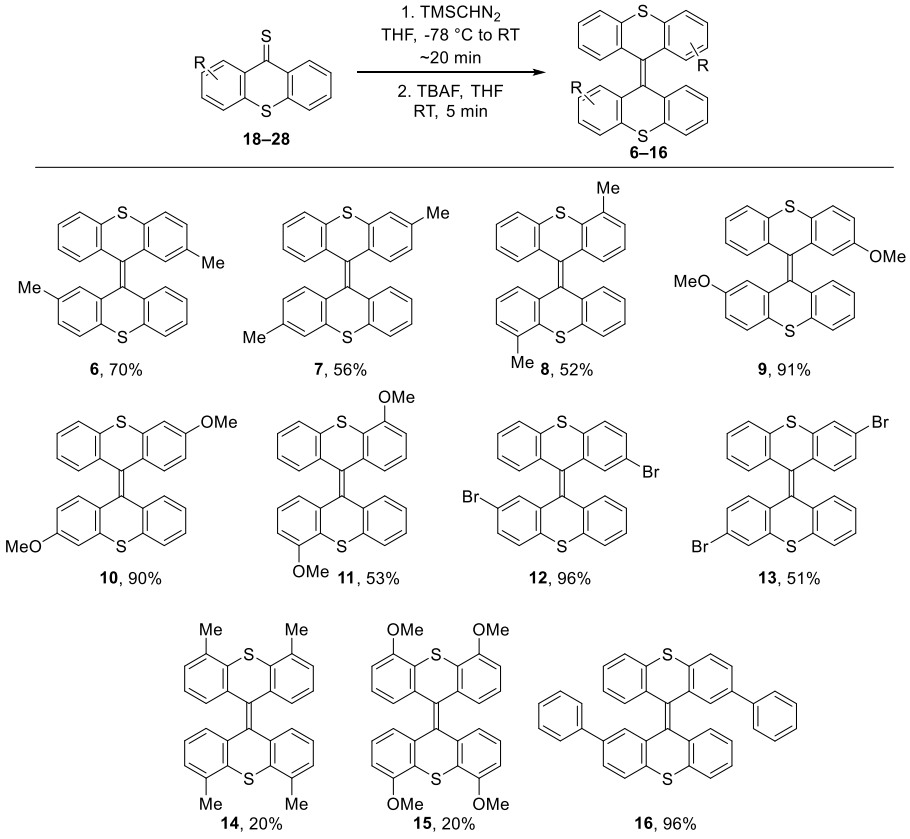

Scheme 2. Scope of the dimerisation reaction. Compounds **6** and **9** are known in literature,[17] compounds **7**, **8**, **10–16** are novel compounds. For unsymmetrically substituted products only the *E*-isomer is shown for clarity.

In order to investigate the influence of substitution patterns for bisthioxanthylidenes on electrochemical switching, we synthesised the methyl and methoxy substituted analogues **6–11**, substituted at the 2,2'-, 3,3'- and 4,4'-positions. The new method was again highly efficient for the synthesis of these compounds and especially methoxy substituted 9 and 10 were obtained in excellent yields. Two bromo substituted bisthioxanthylidenes **12** and **13** were prepared, not only to investigate the substituent effect on switching behaviour, but in particular to introduce synthetic handles for the further functionalisation of these switches or the incorporation in more complex systems. Starting from unsymmetrically substituted thioketones, the bisthioxanthylidene products were obtained as *E*/*Z*-mixtures with 50:50 up to 72:28 ratios (see Section 4.3). The applicability of this method is underlined by the tolerance for various substitution patterns. Further, the methoxy groups also provide a convenient functional handle for further derivatisation. The method is also applicable for tetrasubstituted bisthioxanthylidenes, as observed for **14** and **15**, although, for these bisthioxanthylidenes, impurities which could not be removed by flash column chromatography were present. In these cases, simple washing steps using Et_2O provided the corresponding products with excellent purity.

For many substrates, after treatment with $TMSCHN_2$, the observation of thioketone conversion by colour change only occurred after a significant time during warm up to room temperature. This prompted a number of attempts with a few substrates at a higher starting temperature. By using the simple procedure with a salt ice bath, where a temperature of -15 °C is reached, and subsequent warming up to room temperature, products **6**, **9** and **29** (Scheme 3) could be synthesised without the observation of any undesired reactivity or degradation of compounds.

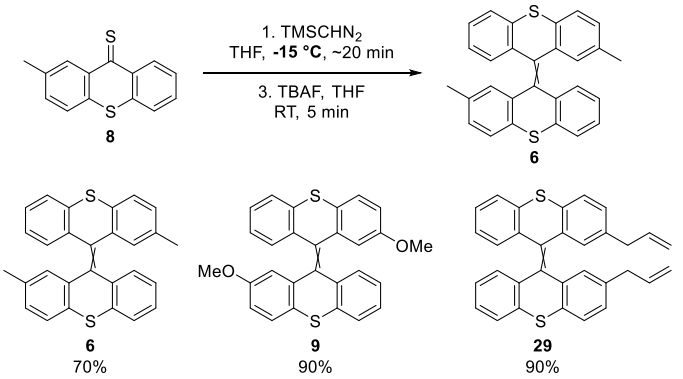

Scheme 3. Bisthioxanthylidenes obtained with a starting temperature of -15 °C.

A number of related thioketones were submitted to a similar dimerisation procedure to show unexpected results. Seven membered thioketone **30** showed insufficient conversion at low temperatures and the reaction mixture was heated to 40 °C. This only yielded a single major product after purification, which was not the overcrowded alkene, but rather exocyclic olefin **31** (Scheme 4). For another hindered thioketone, under the same reaction conditions, an exocyclic olefin **32** has been observed as well. The exact mechanism of this reaction is unknown and further research would be required to use this reaction as a methodology for exocyclic olefination. There is a possibility to form these products via a Barton–Kellogg reaction and spontaneous reaction of the formed episulfide towards an olefin.

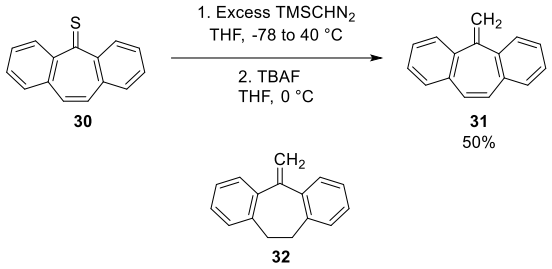

Scheme 4. Sterically hindered thioketones that led to exocyclic olefins.

The coupling protocol to access sterically demanding bisthioxanthylidenes presented here is a remarkably facile and fast alternative method compared to the previously used Barton–Kellogg reactions. With an efficient method for rapid access to these materials established and a library of compounds (Schemes 1b and 2, **6–17**) in hand, we proceeded to investigate their electrochemical properties.

2.2 Electrochemistry

From cyclic voltammetry (Figure 2b, see Section 4.7 for cyclic voltammograms of **6–17**) we observe a current at $E_{p,a}$ = 1.15 V vs. saturated calomel electrode (SCE) in the forward, oxidative direction of **10**. As demonstrated in our previous work,[17] **10** is in its *anti*-folded state and a conformational isomerisation to the *orthogonal* dication $\mathbf{10}^{2+}$ occurs upon oxidation, removing overall two electrons. The conformational change within the molecule from the *anti*-folded state with a central double bond proceeds towards an *orthogonal* state with a central single bond. In the reverse direction, the reduction of $\mathbf{10}^{2+}$ is observed at $E_{p,c}$ = 0.25 V vs. SCE, where the *orthogonal* $\mathbf{10}^{2+}$ accepts two electrons. This initially leads to a *twisted* state,[18] which converts relatively quickly on the timescale of the electrochemical experiment towards the thermodynamically favourable

anti-folded state. A small oxidation signal belonging to the *twisted* state can be observed at 0.34 V vs. SCE. The significant hysteresis between the main oxidation and reduction signals is caused by the considerable geometrical differences of the *anti*-folded and *orthogonal* states. Additional to the different redox response, this geometrical difference aids to explain the differences for the thermal and optical properties.[17]

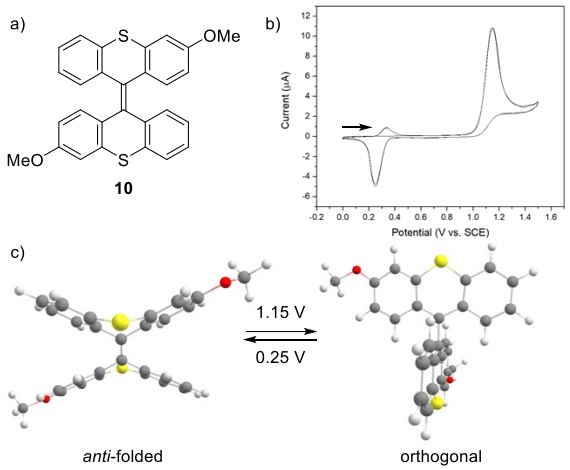

Figure 2. a) Structure of **10**. b) Cyclic voltammogram of **10** (1.0 mM), GC, Pt wire, SCE, CH_2Cl_2, scan speed 10 mV s^{-1}, $TBAPF_6$ (0.1 M). c) Illustration of the conformational switching, optimised geometry structures obtained from DFT calculations at B3LYP/6-31G** level of theory.

From the observed redox potentials for the synthesised library of compounds (Table 1), we can see that the electrochemistry of bisthioxanthylidenes is robust and tolerates several substituents and substitution patterns. The presence of electron donating substituents, either in linear or cross conjugated arrangement with respect to the central olefin, does not lead to a significant difference in redox potentials. The higher electron density of the methoxy substituted bisthioxanthylidenes (**9–11**) has a small but measurable effect, resulting in a more facile oxidation by stabilisation of the dicationic state.

As expected, the bromo-substituted bisthioxanthylidenes (**12**, **13**) show a significantly higher oxidation potential of 1.40 and 1.39 V vs SCE, respectively, while still observing the expected geometrical switching. Compound **12** shows the expected redox behaviour, only shifted towards more positive potentials, with a hysteresis comparable to the rest of the compounds in the library. However, 3,3'-dibromo-bisthioxanthylidene (**13**) shows two closely spaced, significantly smaller reduction signals. This is indicative of a chemical reaction occurring at the dicationic state. We

hypothesise that this could be either an oligomerisation reaction or nucleophilic attack by water. In **13**, the bromine substituents are conjugated in a *para* position to the central olefinic bond, which is a plausible explanation for the increased reactivity compared to its regioisomer **12**.

Table 1. Peak potentials from cyclic voltammetry[a] for oxidation and reduction.

	$E_{p,a}$[b] (V vs. SCE)	$E_{p,c}$[b] (V vs. SCE)	Hysteresis (V)
6	1.22	0.34	0.88
7	1.28	0.38	0.90
8	1.28	0.38	0.90
9	1.17	0.33	0.84
10	1.15	0.25	0.90
11	1.24	0.40	0.84
12	1.40	0.56	0.84
13[c]	1.39	0.47[d]	0.92[d]
14[e]	1.25	0.34	0.89
15[e]	1.16	0.31	0.85
16	1.26	0.45	0.81
17	1.29	0.46	0.83

Footnotes: a) **6–17** (1.0 mM), CH_2Cl_2, $TBAPF_6$ (0.1 M), GC, Pt wire, SCE, 10 mV s^{-1}, room temperature, diffusion limited conditions. b) $E_{p,a}$ = anodic peak potential; $E_{p,c}$ = cathodic peak potential. c) For **13** a different electrochemical response is observed (see text). d) The first observed wave was selected (see Section 4.7). e) Measured as saturated solution because of limited solubility.

The tetrasubstituted substrates **14** and **15** show a slight shift towards less positive potentials compared to the disubstituted substrates **8** and **11** with a comparable substitution pattern. Both tetrasubstituted bisthioxanthylidenes show a significantly lower solubility, but the number of substituents does not show a significant effect on the electrochemical switching. The presence of aromatic substituents, i.e. diphenyl bisthioxanthylidene (**16**), does not interfere with the desired electrochemical switching, with peak potentials at 1.26 and 0.45 V vs. SCE. The hysteresis for **16** (0.81 V) is again similar to the hysteresis observed for other substituted bisthioxanthylidenes (Table 1). Finally, the extension of the aromatic core in the non-symmetric 1,2-benzo-compound **17** (Scheme 1b) results in the expected electrochemical switching.

2.3 Chemical redox switching

The dicationic and neutral states of bisthioxanthylidenes can be addressed by electrochemical as well as chemical means. Under ambient conditions in the presence of non-dry solvents, compound **6** dissolved in CD_3CN (Figure 3a) was readily oxidised by addition of an excess of solid ceric

ammonium nitrate (Figure 3b), leading to a highly selective conversion towards the dicationic $\mathbf{6}^{2+}$ with a considerable downfield shift for all signals. Subsequent reduction by addition of an excess of solid cobaltocene restores the initial spectrum corresponding to the neutral, folded structure of **6** (Figure 3c), demonstrating the robust chemical switching behaviour of bisthioxanthylidenes.

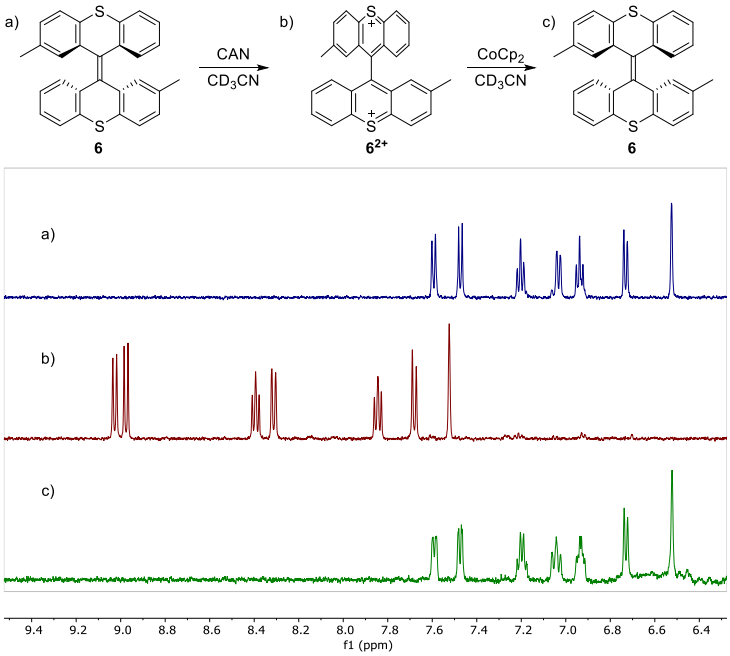

Figure 3. Chemical redox switching. ^{1}H-NMR spectroscopy (500 MHz, CD_3CN) of a) isomerically enriched **6**. b) $\mathbf{6}^{2+}$ obtained by oxidation with ceric ammonium nitrate. c) **6**, in an equal isomeric ratio, recovered by reduction with cobaltocene. For clarity only the *E*-isomer of **6** is shown.

3. Conclusions & Outlook

We have presented here a novel, efficient and rapid synthesis method for bisthioxanthylidenes, allowing for various substituent patterns and different regioisomers of these highly overcrowded alkenes. The scope of bisthioxanthylidenes investigated in this study shows that the electrochemical switching is robust and tolerates various substituents. The geometrically different neutral, *anti*-folded states and dicationic, *orthogonal* states are readily addressable both by electrochemical and chemical means. As now easily accessible, reliable and functionalisable switches that can be addressed by multiple stimuli, these bisthioxanthylidenes have great potential for their use in molecular switching in, for example, electrochromic responsive materials.

4. Experimental

4.1 General comments

For general information on chemicals, NMR spectroscopy, high-resolution mass spectrometry, cyclic voltammetry and DFT calculations, see Chapter 2.

In this chapter, all CVs were recorded with a scan speed of 0.010 Vs^{-1} at room temperature with tetrabutylammonium hexafluorophosphate (0.1 M) as supporting electrolyte in CH_2Cl_2, unless otherwise stated.

4.2 General synthetic methods

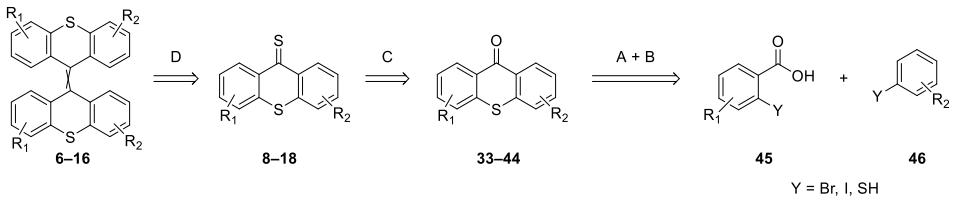

General method A – Ullmann thioether synthesis
In a pressure tube, the appropriate 2-halogenated benzoic acid **45** (1.00 equiv.), the appropriate benzene thiol **46** (1.05 equiv.), K_2CO_3 (3 equiv.) and Cu powder (5%) were suspended in DMF (0.3 M). The reaction mixture was degassed with Ar by bubbling for 15 min and the tube was closed. The reaction mixture was heated at reflux for 16 h. Next, the mixture was allowed to cool to room temperature and was diluted with H_2O. Aqueous HCl (6 M) was added to precipitate the thioether-benzoic acid product, which was subsequently filtered off and used without further purification.

General method B – Friedel Crafts acylation
The appropriate thioether-benzoic acid was added portion wise to stirring concentrated sulfuric acid. The reaction mixture was stirred at room temperature for 16 h or 50 °C for 4 h. The reaction mixture was carefully quenched by pouring it into an ice/water mixture. The product was extracted with CH_2Cl_2 and washed with saturated NaCl (aq) solution. The thioxanthone products were purified by flash column chromatography (silica gel, EtOAc/*n*-pentane or CH_2Cl_2/*n*-pentane).

General method C – Thionation
The appropriate thioxanthone **33–44** (1.0 equiv.) and P_2S_5 (2.0 equiv.) were dissolved in toluene (0.1 M) and the mixture was heated at reflux until full conversion of the ketone **33–44** (approximately 3 h). The crude reaction

mixture was filtered over a short pad of silica and flushed with CH_2Cl_2. Volatiles were removed under reduced pressure and the product was purified by flash column chromatography (silica gel, EtOAc/*n*-pentane or CH_2Cl_2/*n*-pentane) and used directly for the dimerisation procedure.

General method D - Dimerisation
The appropriate thioketone **8–18** (1.0 equiv.) was dissolved in dry THF (0.05 M). 0.5 equivalent of the thioketone solution was added to a separate Schlenk flask. The mixture was cooled to -78 °C and $TMSCHN_2$ (0.55 equiv., 2.0 M in Et_2O) was added. Immediately after addition, the mixture was allowed to warm up to room temperature. The typical thioketone colour fades and gas evolution can sometimes be observed. When the colour change is complete, the remaining thioketone solution is added and the mixture was stirred at room temperature for 10 min. There should be no remaining thioketone colour in the reaction mixture; full conversion of the thioketone was additionally confirmed by thin-layer chromatographic analysis. Tetrabutylammonium fluoride (2.0 equiv., 1.0 M in THF) was added to the mixture, followed by stirring at room temperature for 5 min. Volatiles were removed under reduced pressure and the product was purified by flash column chromatography (silica gel, CH_2Cl_2/*n*-pentane in ratios 1:50 to 1:1). If necessary, the products were triturated with cold *n*-pentane.

4.3 Data for bisthioxanthylidenes

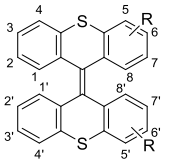

6–16

6 = 2,2'-dimethyl, **7** = 3,3'-dimethyl, **8** = 4,4'-dimethyl
9 = 2,2'-dimethoxy, **10** = 3,3'-dimethoxy, **11** = 4,4'-dimethoxy
12 = 2,2'-dibromo, **13** = 3,3'-dibromo, **14** = 4,4',5,5'-tetramethyl
15 = 4,4',5,5'-tetramethoxy, **16** = 2,2'-diphenyl

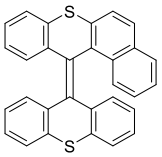

17

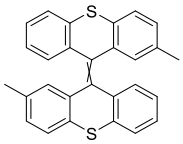

2,2'-dimethyl-9,9'-bisthioxanthylidene (**6**). Obtained as a mixture of *E*/*Z* isomers via general method D (Rf = 0.48, 15% CH_2Cl_2/*n*-pentane) on a 1.26 mmol scale as a white solid in 70% yield (183 mg, 0.44 mmol), 61:39 major/minor ratio. ^{1}H NMR (600 MHz, $CDCl_3$) δ 7.54 – 7.51 (m, $2H_{maj}$ + $2H_{min}$), 7.43 – 7.39 (m, $2H_{maj}$ + $2H_{min}$), 7.14 – 7.09 (m, $2H_{maj}$ + $2H_{min}$), 6.98 – 6.93 (m, $2H_{maj}$ + $2H_{min}$), 6.92 – 6.87 (m, $2H_{maj}$ + $2H_{min}$), 6.82 – 6.79 (m, $2H_{maj}$ + $2H_{min}$), 6.61 – 6.57 (m, $2H_{maj}$ + $2H_{min}$), 2.02 (s, $6H_{maj}$), 2.01 (s, $6H_{min}$). ^{13}C NMR (151 MHz, $CDCl_3$) δ 136.3, 136.2, 136.0, 135.9, 135.9, 135.8, 135.6,

135.4, 133.6, 132.2, 130.6, 130.6, 130.0, 130.0, 127.7, 127.7, 127.2, 127.1, 126.9, 126.8, 126.8, 126.7, 125.8, 125.5, 21.0, 20.9. HRMS (ESI Pos) for $[C_{28}H_{20}S_2]$+ calcd. m/z = 420.1001, found 420.0997.

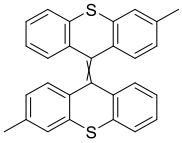

3,3'-dimethyl-9,9'-bisthioxanthylidene (**7**) Obtained as a mixture of *E*/*Z* isomers via general method D (Rf = 0.37, 15% CH_2Cl_2/*n*-pentane) on a 1.07 mmol scale as a white solid in 56% yield (127 mg, 0.30 mmol), 72:28 major/minor ratio. ^{1}H NMR (600 MHz, $CDCl_3$) δ 7.51 (d, *J* = 7.8 Hz, $2H_{maj}$ + $2H_{min}$), 7.35 (s, $2H_{maj}$ + $2H_{min}$), 7.13 – 7.07 (m, $2H_{maj}$ + $2H_{min}$), 6.93 – 6.82 (m, $2H_{maj}$ + $4H_{min}$), 6.81 – 6.77 (m, $2H_{maj}$), 6.74 (d, *J* = 1.4 Hz, $4H_{maj}$), 6.70 (dd, *J* = 8.3, 7.9 Hz, $4H_{min}$), 2.30 (s, $6H_{maj}$), 2.29 (s, $6H_{min}$). ^{13}C NMR, major isomer (101 MHz, $CDCl_3$) δ 136.7, 136.5, 135.8, 135.5, 133.5, 133.2, 130.1, 129.7, 127.7, 127.2, 127.0, 126.7, 125.7, 21.3. HRMS (ESI Pos) for $[C_{28}H_{20}S_2]$ calcd. m/z = 420.1001, found 420.0993.

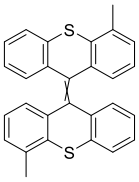

4,4'-dimethyl-9,9'-bisthioxanthylidene (**8**) Obtained as a mixture of *E*/*Z* isomers via general method D (Rf = 0.44, 15% CH_2Cl_2/*n*-pentane) on a 0.77 mmol scale as a pale brown solid in 52% yield (84 mg, 0.20 mmol), *E*/*Z*-isomers are non-distinguishable by ^{1}H-NMR spectroscopy, a number of ^{13}C signals do appear as two separate, overlapping signals. ^{1}H NMR (400 MHz, $CDCl_3$) δ 7.55 (dd, *J* = 7.8, 3.4 Hz, 2H), 7.16 – 7.08 (m, 2H), 7.04 – 6.96 (m, 2H), 6.94 – 6.86 (m, 2H), 6.85 – 6.75 (m, 4H), 6.65 (dd, *J* = 11.4, 7.7 Hz, 2H), 2.51 (s, 6H). ^{13}C NMR (101 MHz, $CDCl_3$) δ 136.4, 135.9, 135.7, 135. 6, 135.2, 134.1, 129.9, 128.0, 127.7, 127.4, 126.7, 125.9, 125.5, 20.8. HRMS (ESI Pos) for $[C_{28}H_{20}S_2]^+$ calcd. m/z = 420.1001, found 420.0996.

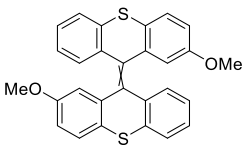

2,2'-dimethoxy-9,9'-bisthioxanthylidene (**9**) Obtained as a mixture of *E*/*Z* isomers via general method D (Rf = 0.17, 15% CH_2Cl_2/*n*-pentane) on a 1.16 mmol scale as a yellow solid in 91% yield (240 mg, 0.53 mmol), 59:41

major/minor ratio. ^{1}H NMR (400 MHz, $CDCl_3$) δ 7.56 – 7.51 (m, $2H_{maj}$ + $2H_{min}$), 7.45 – 7.39 (m, $2H_{maj}$ + $2H_{min}$), 7.17 – 7.10 (m, $2H_{maj}$ + $2H_{min}$), 6.99 – 6.86 (m, $2H_{maj}$ + $4H_{min}$), 6.81 (dd, *J* = 7.8, 1.4 Hz, $2H_{maj}$), 6.78 – 6.70 (m, $2H_{maj}$ + $2H_{min}$), 6.40 (d, *J* = 2.7 Hz, $2H_{maj}$), 6.33 (d, *J* = 2.7 Hz, $2H_{min}$), 3.39 (s, $6H_{maj}$), 3.35 (s, $6H_{min}$). ^{13}C NMR (151 MHz, $CDCl_3$) δ 158.1, 158.0, 137.2, 137.1, 136.3, 136.2, 135.9, 135.8, 133.8, 130.1, 129.9, 128.1, 128.1, 127.2, 127.2, 126.9, 126.9, 126.8, 126.7, 125.8, 125.8, 115.2, 115.2, 114.2, 113.9, 55.4, 55.2. HRMS (ESI Pos) for $[C_{28}H_{20}O_2S_2]^+$ calcd. m/z = 452.0899, found 452.0891.

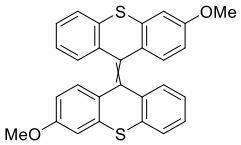

3,3'-dimethoxy-9,9'-bisthioxanthylidene (**10**) Obtained as a mixture of *E*/*Z* isomers via general method D (Rf = 0.24, 15% CH_2Cl_2/*n*-pentane) on a 0.18 mmol scale as a pale-yellow solid in 90% yield (37 mg, 0.08 mmol), 51:49 major/minor ratio. ^{1}H NMR (600 MHz, $CDCl_3$) δ 7.51 (d, *J* = 7.8 Hz, $2H_{maj}$ + $2H_{min}$), 7.14 – 7.08 (m, $2H_{maj}$ + $2H_{min}$), 7.07 – 7.03 (m, $2H_{maj}$ + $2H_{min}$), 6.94 (t, *J* = 7.5 Hz, $2H_{maj}$), 6.91 – 6.84 (m, $2H_{maj}$ + $2H_{min}$), 6.80 – 6.76 (m, $4H_{min}$), 6.70 (d, *J* = 8.6 Hz, $2H_{maj}$), 6.52 (dd, *J* = 8.6, 2.6 Hz, $2H_{min}$), 6.47 (dd, *J* = 8.6, 2.6 Hz, $2H_{maj}$), 3.79 (s, $6H_{min}$), 3.79 (s, $6H_{maj}$). ^{13}C NMR (151 MHz, $CDCl_3$) δ 158.3, 158.2, 137.1, 137.0, 136.8, 136.8, 135.5, 135.4, 132.5, 132.5, 131.1, 131.0, 130.1, 130.0, 128.9, 128.9, 127.2, 127.2, 126.7, 126.6, 125.9, 125.8, 55.5 (2C). HRMS (ESI Pos) for $[C_{28}H_{20}O_2S_2]^+$ calcd. m/z = 452.0899, found 452.0893.

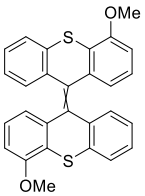

4,4'-dimethoxy-9,9'-bisthioxanthylidene (**11**) Obtained as a mixture of *E*/*Z* isomers via general method D (Rf = 0.24, 15% CH_2Cl_2/*n*-pentane) on a 0.30 mmol scale as a pale-yellow solid in 53% yield (36 mg, 0.08 mmol), *E*/*Z*-isomers are non-distinguishable by ^{1}H-NMR spectroscopy. ^{1}H NMR (600 MHz, $CDCl_3$) δ 7.57 (ddd, *J* = 7.8, 4.4, 1.2 Hz, $2H_{maj}$ + $2H_{min}$), 7.12 (dd, *J* = 7.5, 7.5 Hz, $2H_{maj}$ + $2H_{min}$), 6.93 – 6.85 (m, $4H_{maj}$ + $4H_{min}$), 6.81 (d, *J* = 7.9 Hz, $2H_{maj}$ + $2H_{min}$), 6.70 (d, *J* = 8.0 Hz, $2H_{maj}$ + $2H_{min}$), 6.45 (ddd, *J* = 7.8, 4.2, 1.1 Hz, $2H_{maj}$ + $2H_{min}$), 3.97 (s, $6H_{maj}$ + $6H_{min}$). ^{13}C NMR (151 MHz, $CDCl_3$) δ 155.8, 155.7, 137.2, 137.1, 136.1, 136.0, 135.6, 135.5, 133.5 (2C), 129.9, 129.9, 127.4, 127.4, 126.8, 126.8, 126.3, 126.3, 125.9, 125.8, 124.2, 124.1, 122.6, 122.5, 108.3 (2C), 56.2 (2C). HRMS (ESI Pos) for $[C_{28}H_{20}O_2S_2]^+$ calcd. m/z = 452.0899, found 452.0894.

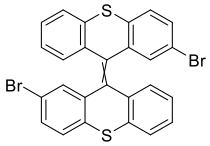

2,2'-dibromo-9,9'-bisthioxanthylidene (**12**) Obtained as a mixture of *E*/*Z* isomers via general method D (Rf = 0.57, 15% CH_2Cl_2/*n*-pentane) on a 0.49 mmol scale as an off-white solid in 96% yield (130 mg, 0.24 mmol), 56:44 major/minor ratio. ^{1}H NMR (600 MHz, $CDCl_3$) δ 7.57 – 7.51 (m, $2H_{maj}$ + $2H_{min}$), 7.44 – 7.38 (m, $2H_{maj}$ + $2H_{min}$), 7.33 (dd, *J* = 8.3, 2.1 Hz, $2H_{maj}$), 7.27 – 7.25 (m, $2H_{min}$), 7.21 (d, *J* = 7.4 Hz, $2H_{min}$), 7.16 (d, *J* = 7.4 Hz, $2H_{maj}$), 7.01 (d, *J* = 7.6 Hz, $2H_{min}$), 6.93 (d, *J* = 7.8 Hz, $2H_{maj}$), 6.89 (d, *J* = 2.1 Hz, $2H_{maj}$), 6.87 (d, *J* = 2.1 Hz, $2H_{min}$), 6.81 – 6.79 (m, $2H_{maj}$), 6.79 – 6.78 (m, $2H_{min}$). ^{13}C NMR signals of the separate isomers are non-distinguishable. ^{13}C NMR (101 MHz, $CDCl_3$) δ 137.5 (2C), 137.0 (2C), 135.3, 135.3, 135.1, 134.8, 134.8, 134.7, 133.2 (2C), 132.6, 132.5, 130.1, 130.0, 129.9, 129.8, 128.5, 128.5, 127.6, 127.4, 127.4, 127.3, 126.2, 126.2, 119.6. HRMS (ESI Pos): for $[C_{26}H_{14}Br_2S_2]^+$ calcd. m/z = 549.8878, found 549.8860.

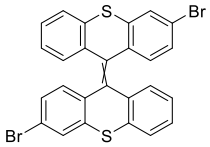

3,3'-dibromo-9,9'-bisthioxanthylidene (**13**) Obtained as a mixture of *E*/*Z* isomers via general method D (Rf = 0.60, 15% CH_2Cl_2/*n*-pentane) on a 0.29 mmol scale as a yellow solid in 51% yield (40 mg, 0.07 mmol), 50:50 ratio, labelled as isomer 1 and isomer 2. ^{1}H NMR (400 MHz, $CDCl_3$) δ 7.72 – 7.68 (m, $2H_{isomer1}$ + $2H_{isomer2}$), 7.56 – 7.51 (m, $2H_{isomer1}$ + $2H_{isomer2}$), 7.21 – 7.12 (m, $2H_{isomer1}$ + $2H_{isomer2}$), 7.09 (dd, *J* = 8.3, 2.0 Hz, $2H_{isomer1}$), 7.03 (dd, *J* = 8.3, 2.0 Hz, $2H_{isomer2}$), 6.98 (ddd, *J* = 7.6, 7.6, 1.2 Hz, $2H_{isomer1}$), 6.93 (ddd, *J* = 7.6, 7.6, 1.2 Hz, $2H_{isomer2}$), 6.84 – 6.76 (m, $2H_{isomer1}$ + $2H_{isomer2}$), 6.70 – 6.62 (m, $2H_{isomer1}$ + $2H_{isomer2}$). ^{13}C NMR signals of the separate isomers are non-distinguishable. ^{13}C NMR (101 MHz, $CDCl_3$) δ 138.0, 138.0, 135.6, 135.5, 135.1, 135.1, 135.0, 134.8, 133.2 (2C), 131.1, 131.0, 130.1, 130.0 (2C), 129.9, 129.3, 129.1, 127.5, 127.4, 127.3, 127.3, 126.5, 126.3, 120.8, 120.8. HRMS (ESI Pos): for $[C_{26}H_{14}Br_2S_2]^+$ calcd. m/z = 549.8878, found 549.8862.

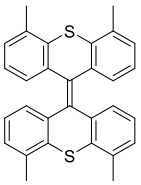

4,4',5,5'-tetramethyl-9,9'-bisthioxanthylidene (**14**) Obtained via general method D on a 0.30 mmol scale, purified by flash column chromatography (silica gel, CH_2Cl_2/Toluene, gradient 0:1 to 1:1) and trituration from Et_2O to obtain the title product as a white solid in 20% yield (27 mg, 0.06 mmol), ^{1}H NMR (600 MHz, $CDCl_3$) δ 7.00 (d, *J* = 7.4 Hz, 4H), 6.81 (dd, *J* = 7.6, 7.6 Hz, 4H), 6.63 (d, *J* = 7.8 Hz, 4H), 2.54 (s, 12r Not sufficiently soluble for ^{13}C NMR. HRMS (ESI Pos): for $[C_{30}H_{24}S_2]^+$ calcd. m/z = 448.1314, found 448.1311.

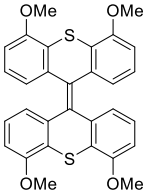

4,4',5,5'-tetramethoxy-9,9'-bisthioxanthylidene (**15**) Obtained via general method on a 0.35 mmol scale, purified by flash column chromatography (silica gel, CH_2Cl_2/Toluene, gradient 0:1 to 1:1) and trituration from Et_2O as a pale-yellow solid in 20% yield (18 mg, 0.04 mmol), ^{1}H NMR (600 MHz, $CDCl_3$) δ 6.86 (dd, *J* = 7.9, 7.9 Hz, 4H), 6.67 (dd, *J* = 8.1, 1.1 Hz, 4H), 6.44 – 6.40 (m, 4H), 3.95 (s, 12H). Not sufficiently soluble for ^{13}C NMR. HRMS (ESI Pos): for $[C_{30}H_{24}O_4S_2]^+$ calcd. m/z = 512.1111, found 512.1103.

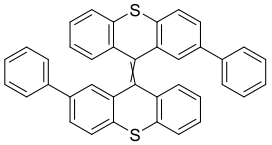

2,2'-diphenyl-9,9'-bisthioxanthylidene (**16**) Obtained as a mixture of *E*/*Z* isomers via general method D on a 0.84 mmol scale as a white solid in 96% yield (219 mg, 0.40 mmol), 60:40 major/minor ratio. ^{1}H NMR (600 MHz, $CDCl_3$) δ 7.66 (d, *J* = 8.1 Hz, $2H_{maj}$), 7.65 – 7.63 (m, $2H_{min}$), 7.61 (d, *J* = 8.1 Hz, $2H_{min}$), 7.58 – 7.56 (m, $2H_{maj}$), 7.40 – 7.36 (m, $2H_{maj}$ + $2H_{min}$), 7.31 – 7.27 (m, $2H_{maj}$ + $2H_{min}$), 7.24 – 7.18 (m, $4H_{maj}$ + $4H_{min}$), 7.16 (ddd, *J* = 7.8, 7.2, 1.4 Hz, $4H_{min}$), 7.12 (d, *J* = 1.9 Hz, $2H_{maj}$), 7.08 (d, *J* = 1.9 Hz, $2H_{min}$), 7.05 – 7.02 (m, $4H_{min}$), 7.02 – 6.99 (m, $4H_{maj}$), 6.99 – 6.92 (m, $4H_{maj}$ + $2H_{min}$), 6.89 – 6.86 (m, $2H_{maj}$). ^{13}C NMR (151 MHz, $CDCl_3$) δ 140.50, 140.49, 139.51, 139.02, 136.25, 136.12, 135.89, 135.83, 135.79, 135.63, 134.72, 134.57, 133.85, 133.82, 130.08, 129.99, 129.06, 128.79, 128.70, 128.62, 127.66, 127.51, 127.45,

127.31, 127.21, 127.05, 127.02, 126.96, 126.16, 125.99, 125.88, 125.83. HRMS (ESI Pos) for $[C_{38}H_{25}S_2]^+$ calcd. m/z = 545.1392, found 545.1385 and for $[C_{38}H_{24}S_2]^+$ calcd. m/z = 544.1314, found 544.1299.

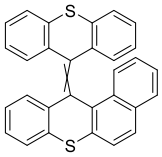

12-(9H-thioxanthen-9-ylidene)-12H-benzo[a]thioxanthene (**17**) (9H-thioxanthen-9-ylidene)hydrazine (152 mg, 0.67 mmol) was dissolved in 5 mL dry CH_2Cl_2, cooled to 0 °C and MnO_2 (289 mg, 3.33 mmol) was added. After full conversion (30 min, confirmed by TLC) the mixture was filtered over a pad of silica gel under N_2 flow and flushed with 5 mL dry CH_2Cl_2. The diazo solution was added to a solution of 12H-benzo[a]thioxanthene-12-thione (152 mg, 0.55 mmol) in 5 mL dry CH_2Cl_2 and the mixture was stirred for 16 h at room temperature. The solvent was removed under reduced pressure, the residue was dissolved in 8 mL dry toluene and tris(dimethylamino)phosphine (0.24 mL, 1.32 mmol) was added and the mixture was heated at reflux for 16 h. Volatiles were removed under reduced pressure and the product was purified by flash column chromatography using silica gel and CH_2Cl_2/*n*-pentane (1:9) as eluent. The product was obtained as a white solid in 23% yield (55 mg, 0.12 mmol). ^{1}H NMR (400 MHz, $CDCl_3$) δ 7.71 (d, *J* = 8.5 Hz, 1H), 7.69 – 7.60 (m, 4H), 7.57 (dd, *J* = 7.7, 0.7 Hz, 1H), 7.41 – 7.36 (m, 1H), 7.21 – 7.10 (m, 3H), 7.07 – 6.97 (m, 3H), 6.91 (td, *J* = 7.6, 1.2 Hz, 1H), 6.84 – 6.74 (m, 2H), 6.45 – 6.36 (m, 2H). ^{13}C NMR (151 MHz, $CDCl_3$) δ 137.3, 136.8, 136.3, 136.1, 135.5, 134.8, 134.7, 134.4, 132.5, 131.8, 131.7, 130.2, 129.4, 129.2, 128.6, 127.7, 127.4, 127.1, 126.9, 126.9, 126.9, 126.7, 126.6, 126.3, 126.2, 125.8, 125.5, 125.2, 125.1, 125.0. HRMS (ESI Pos) for $[C_{30}H_{18}S]^+$ calcd. m/z = 442.0844, found m/z = 442.0837.

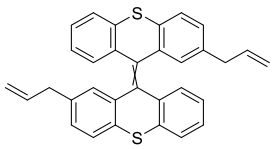

2,2'-diallyl-bisthioxanthylidene (**29**). Thioketone preparation: 2-allyl-9H-thioxanthene-9-one was dissolved in toluene (17 mL) and Lawesson's reagent (727 mg, mmol, 1.05 equiv.) was added to the mixture, which was subsequently stirred at reflux for 45 min. The mixture was allowed to cool down to room temperature and the product was purified by flash column chromatography (silica, CH_2Cl_2/*n*-pentane, 10%).

Dimerisation: The freshly prepared thioketone was dissolved in dry THF (17 mL) and divided into two equal portions. One portion was cooled to -15 °C and $TMSCHN_2$ (mL, 2.0 M in Et_2O, 0.55 equiv.) was added. Immediately after addition, the mixture was allowed to warm up to room temperature. After full conversion of the thioketone, another portion of 2-allyl-9H-thioxanthene-9-thione (mg, mmol. equiv.) is added and the mixture was stirred at room temperature for 10 min. Tetrabutylammonium fluoride (2.0 equiv., 1.0 M in THF) was added to the mixture and followed by stirring at room temperature for 5 min. Volatiles were removed under reduced pressure and the product was purified by flash column chromatography (silica gel, CH_2Cl_2/*n*-pentane in ratios 8%). The product was obtained as an *E*/*Z*-mixture in an unknown ratio, as an off-white solid in 90% yield (364 mg, 0.77 mmol). ^{1}H NMR (600 MHz, $CDCl_3$) δ 7.53 (ddd, J = 7.9, 2.8, 1.2 Hz, 2H), 7.45 (d, J = 8.0 Hz, 2H), 7.14 – 7.10 (m, 2H), 6.99 – 6.94 (m, 2H), 6.91 – 6.87 (m, 2H), 6.83 – 6.78 (m, 2H), 6.62 (dd, J = 6.1, 1.9 Hz, 2H), 5.63 – 5.52 (m, 2H), 4.91 – 4.83 (m, 4H), 3.10 – 2.96 (m, 4H). ^{13}C NMR (151 MHz, $CDCl_3$) δ 140.0, 137.9, 136.9, 136.9, 136.1, 136.1, 136.1, 136.0, 135.9, 135.8, 133.6, 133.6, 133.1, 133.1, 130.2, 130.1, 129.9, 129.9, 127.3, 127.2, 127.2, 127.2, 127.1, 127.0, 126.8, 126.7, 125.8, 125.8, 116.0, 116.0, 39.8, 39.7.

4.4 Data for thioxanthones

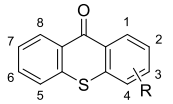

33–43

33 = 2-methyl, **34** = 3-methyl, **35** = 4-methyl
36 = 2-methoxy, **37** = 3-methoxy, **38** = 4-methoxy
39 = 2-bromo, **40** = 3-bromo, **41** = 4,5-dimethyl
42 = 4,5-dimethoxy, **43** = 2-phenyl

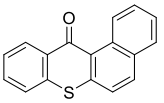

44

All spectroscopic data of known compounds was in agreement with literature. **33**[37], **34**[38], **35**[39], **36**[40], **37**[40], **38**[37], **39**[41], **40**[42], **42**[43], **44**[41].

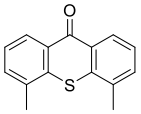

4,5-dimethylthioxanthone (**41**) Obtained via general method A and B on a 4.95 mmol scale as a white solid in 39% yield over 2 steps (464 mg, 1.93 mmol). ^{1}H NMR (400 MHz, $CDCl_3$) δ 8.51 (d, J = 8.1 Hz, 2H), 7.51 (d, J = 7.3 Hz, 2H), 7.42 (dd, J = 7.7, 7.7 Hz, 2H), 2.59 (s, 6H). ^{13}C NMR (101 MHz, $CDCl_3$) δ 181.1, 136.2, 134.4, 133.6, 129.3, 127.7, 125.9, 19.7. HRMS (ESI Pos) for $[C_{15}H_{13}OS]^+$ calcd. m/z = 241.0682, found m/z = 241.0682.

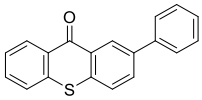

2-phenylthioxanthone (**43**) A sealed tube was charged with 2-bromothioxanthone (**39**, 407 mg, 1.4 mmol, 1.0 equiv.), $Pd(PPh_3)_4$ (81 mg, 0.07 mmol, 0.05 equiv.), K_2CO_3 (580 mg, 4.2 mmol, 3.0 equiv.), phenylboronic acid (190 mg, 1.6 mmol, 1.1 equiv.) and a mixture of toluene:ethanol:water, 5:3:1 (14 mL, 0.1 M). N_2 was bubbled through the solution for 10 min and the tube was sealed. The reaction mixture was heated at 130 °C for 16 h. The reaction mixture was allowed to cool to room temperature, taken up in CH_2Cl_2 and washed with water and saturated NaCl (aq) and dried over $MgSO_4$. Volatiles were removed under reduced pressure and the product was purified by flash column chromatography (silica gel, CH_2Cl_2/*n*-pentane, 1:9) and obtained as a yellow solid in 86% yield (348 mg, 1.21 mmol). ^{1}H NMR (400 MHz, $CDCl_3$) δ 8.88 (d, *J* = 2.1 Hz, 1H), 8.68 – 8.63 (m, 1H), 7.89 (dd, *J* = 8.4, 2.2 Hz, 1H), 7.74 – 7.69 (m, 2H), 7.69 – 7.65 (m, 1H), 7.65 – 7.58 (m, 2H), 7.54 – 7.46 (m, 3H), 7.43 – 7.37 (m, 1H). ^{13}C NMR (101 MHz, $CDCl_3$) δ 180.1, 139.7, 139.5, 137.3, 136.2, 132.5, 131.2, 130.1, 129.6, 129.4, 129.2, 128.0, 128.0, 127.3, 126.7, 126.5, 126.2. HRMS (APCI Pos) for $[C_{19}H_{13}OS]^+$ calcd. m/z = 298.06816, found m/z = 289.06938.

4.5 Data for dicationic species

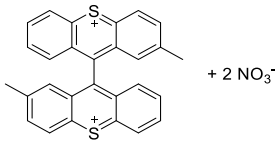

2,2'-dimethyl-[9,9'-bithioxanthene]-10,10'-diium nitrate (**6^{2+}**). Obtained by oxidation of **6** in CD_3CN with an excess of ceric ammonium nitrate. ^{1}H NMR (500 MHz, CD_3CN) δ 9.03 (d, *J* = 8.6 Hz, 2H), 8.98 (d, *J* = 8.8 Hz, 2H), 8.39 (dd, *J* = 7.8, 7.7 Hz, 2H), 8.35 – 8.27 (m, 2H), 7.84 (dd, *J* = 8.7, 7.5 Hz, 2H), 7.68 (d, *J* = 8.8 Hz, 2H), 7.52 (s, 2H), 2.35 (s, 6H). HRMS (ESI Pos) for $[C_{28}H_{20}S_2]^{2+}$ calcd. m/z = 210.04977, found m/z = 210.04972.

4.6 Coupling of two distinct thioketones

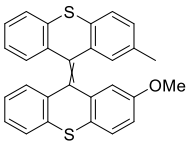

2-methyl-2'-methoxy bisthioxanthylidene (**47**). 2-methoxythioxanthene-thione (30 mg, 1.0 equiv.) was dissolved in THF (1.5 mL) and cooled to -78 °C. $TMSCHN_2$ (60 µL, 1.05 equiv.) was added and the mixture was allowed to slowly warm up to room temperature. When the colour of the thioketone had faded, a THF (1.5 mL) solution of 2-methylthioxanthene-thione (28 mg, 1.0 equiv.) was added to the mixture. After the colour of the second thioketone had faded, TBAF (1.0 M in Et_2O, 0.20 mL, 2.0 equiv.) was added and the mixture was stirred at room temperature for 5 min. Volatiles were removed under reduced pressure and the product was purified by flash column chromatography (silica, CH_2Cl_2/*n*-pentane). The product was obtained as an off-white solid in 9% yield (5.0 mg, 0.01 mmol). The product was obtained as an *E*/*Z*-mixture in 53:47 ratio (major/minor). ^{1}H NMR (600 MHz, $CDCl_3$) δ 7.55 – 7.51 (m, $2H_{maj}$ + $2H_{min}$), 7.45 – 7.38 (m, $2H_{maj}$ + $2H_{min}$), 7.16 – 7.09 (m, $2H_{maj}$ + $2H_{min}$), 6.98 – 6.93 (m, $3H_{maj}$), 6.93 – 6.86 (m, $1H_{maj}$ + $3H_{min}$), 6.82 – 6.78 (m, $2H_{maj}$ + $1H_{min}$), 6.73 (ddd, *J* = 11.7, 8.5, 2.7 Hz, $2H_{min}$), 6.66 (s, $1H_{maj}$), 6.59 (s, $1H_{min}$), 6.32 (dd, *J* = 8.4, 2.7 Hz, $1H_{maj}$ + $1H_{min}$), 3.35 (s, $3H_{maj}$), 3.34 (s, $3H_{min}$), 2.05 (s, $3H_{maj}$), 2.01 (s, $3H_{min}$). ^{13}C NMR (151 MHz, $CDCl_3$) δ 158.0, 157.9, 137.3, 137.1, 136.2, 136.2, 136.2, 136.1, 136.0, 136.0, 135.9, 135.8, 135.8, 135.8, 135.7, 135.7, 133.8, 133.8, 133.7, 133.6, 132.3, 132.1, 130.8, 130.5, 130.1, 130.0, 130.0, 129.9, 128.1, 128.0, 127.8, 127.8, 127.2, 127.2, 127.2, 127.1, 126.9, 126.9, 126.9, 126.9, 126.8, 126.8, 126.8, 126.8, 125.9, 125.8, 125.8, 125.5, 115.1, 115.1, 114.0, 114.0, 55.3, 55.2, 21.0, 21.0. HRMS (ESI Pos): for $[C_{28}H_{20}OS]^+$ calcd. m/z = 436.0950, found m/z = 436.0954.

From this reaction, **6** was obtained in 24% isolated yield and **9** was obtained in 42% isolated yield.

4.7 Seven membered ring compounds

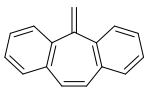

5-methylene-5H-dibenzo[a,d][7]annulene (**31**). To a solution of 5H-dibenzo[a,d][7]annulene-5-thione (42 mg, 0.19 mmol, 0.5 equiv.) in THF (2.5 mL) at -78 °C was added $TMSCHN_2$ (0.10 mL, ~2.0 M, 0.20 mmol, 0.53 equiv.) and the mixture was allowed to warm up to room temperature. Some fading

of the deep green colour was observed. Another portion of 5H-dibenzo[a,d][7]annulene-5-thione (42 mg, 0.19 mmol, 0.5 equiv.) in THF (2.5 mL) was added and the mixture was stirred at room temperature for 30 min. Additional $TMSCHN_2$ (0.1 mL, ~2.0 M, 0.2 mmol, 0.53 equiv.) was added and the reaction mixture was stirred at 40 °C until the thioketone colour faded to a pale-yellow. TLC analysis (silica, CH_2Cl_2/*n*-pentane, 10%) showed full conversion of the starting material and the mixture was cooled to 0 °C and TBAF (0.7 mL, 1.0 M, 0.70 mmol, 1.8 equiv.) was added to the mixture. Volatiles were removed under reduced pressure and the product was purified by flash column chromatography (silica, CH_2Cl_2/*n*-pentane, 10%). The product was further crystallised from *n*-pentane and obtained as a white solid in 50% yield (39 mg, 0.19 mmol). ^{1}H NMR (400 MHz, $CDCl_3$) δ 7.46 – 7.27 (m, 8H), 6.86 (s, 2H), 5.29 (s, 2H). ^{13}C NMR (101 MHz, $CDCl_3$) δ 151.0, 141.0, 134.1, 131.4, 128.9, 128.8, 128.2, 127.6, 120.6. Compound data is in accordance with literature.[44]

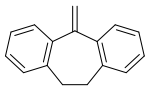

5-methylene-10,11-dihydro-5H-dibenzo[a,d][7]annulene (**32**). Obtained using the same method for **31**, starting from 10,11-dihydro-5H-dibenzo[a,d][7]annulene-5-thione. ^{1}H NMR (400 MHz, $CDCl_3$) δ 7.35 (dd, *J* = 7.2, 1.8 Hz, 2H), 7.23 – 7.15 (m, 4H), 7.12 (dd, *J* = 6.9, 2.0 Hz, 2H), 5.42 (s, 2H), 3.15 (s, 4H). ^{13}C NMR (101 MHz, $CDCl_3$) δ 152.0, 141.3, 138.5, 129.0, 128.3, 127.8, 126.3, 117.6, 33.4. Compound data is in accordance with literature.[45]

4.8 Electrochemistry

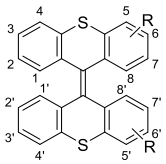

6–16

6 = 2,2'-dimethyl, **7** = 3,3'-dimethyl, **8** = 4,4'-dimethyl
9 = 2,2'-dimethoxy, **10** = 3,3'-dimethoxy, **11** = 4,4'-dimethoxy
12 = 2,2'-dibromo, **13** = 3,3'-dibromo, **14** = 4,4',5,5'-tetramethyl
15 = 4,4',5,5'-tetramethoxy, **16** = 2,2'-diphenyl

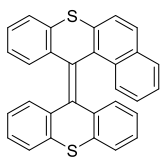

17

Cyclic voltammograms of **6–17**. Glassy carbon working electrode, Pt wire counter electrode, SCE reference electrode. 1.0 mM **16–17** in CH_2Cl_2 with 0.1 M $TBAPF_6$ as supporting electrolyte. Measured at room temperature under diffusion limited conditions.

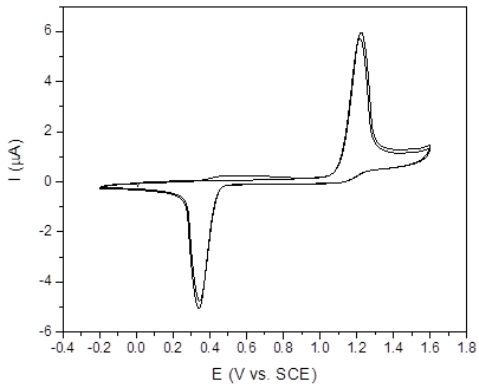
I (μA)
E (V vs. SCE)

6

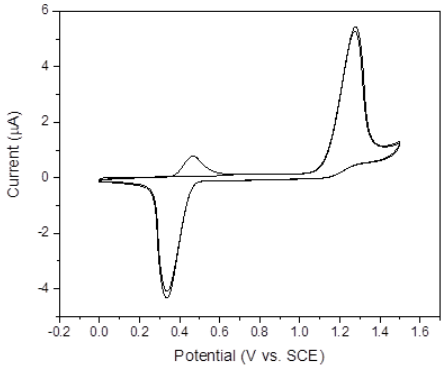
Current (μA)
Potential (V vs. SCE)

7

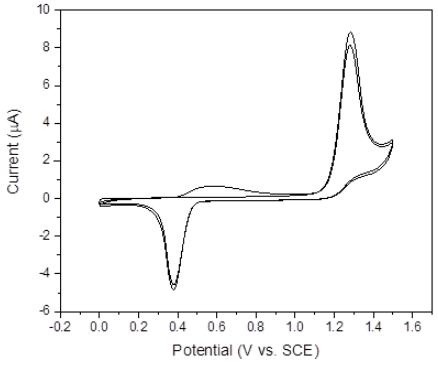
Current (μA)
Potential (V vs. SCE)

8

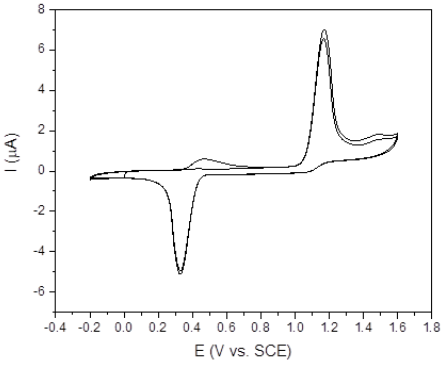
I (μA)
E (V vs. SCE)

9

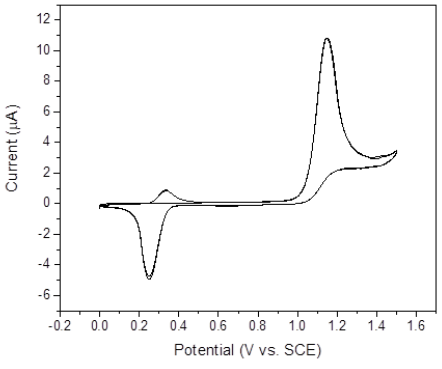
Current (μA)
Potential (V vs. SCE)

10

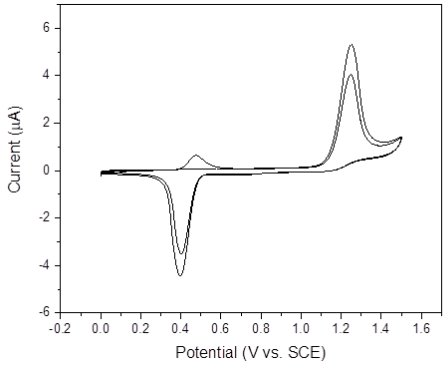
Current (μA)
Potential (V vs. SCE)

11

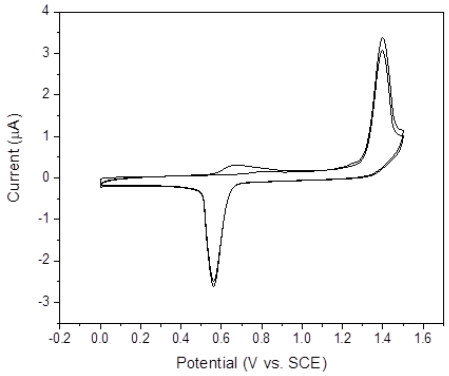

12

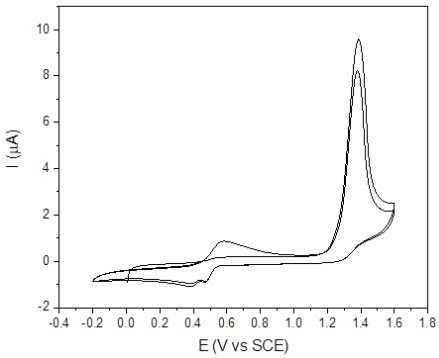

13

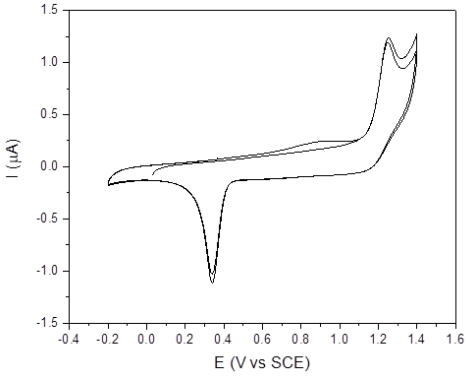

14

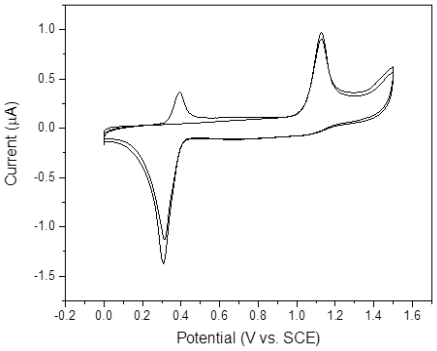

15

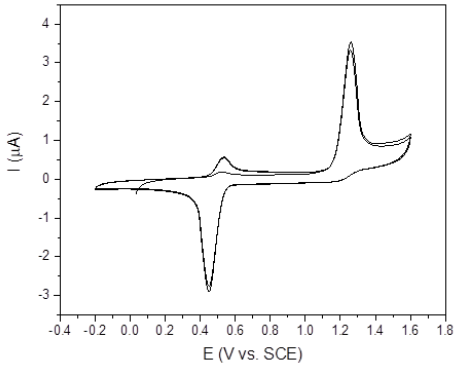

16

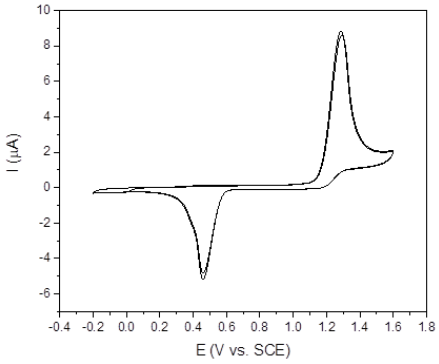

17

5. References

1 B. L. Feringa and W. R. Browne, *Molecular Switches*, Wiley-VCH, Hoboken, USA, 2nd edn., 2011.
2 P. U. Biedermann, J. J. Stezowski and I. Agranat, *Eur. J. Org. Chem.*, 2001, 15–34.
3 J. Chen, F. K. C. Leung, M. C. A. Stuart, T. Kajitani, T. Fukushima, E. van der Giessen and B. L. Feringa, *Nat. Chem.*, 2018, **10**, 132–138.
4 F. K. C. Leung, T. van den Enk, T. Kajitani, J. Chen, M. C. A. Stuart, J. Kuipers, T. Fukushima and B. L. Feringa, *J. Am. Chem. Soc.*, 2018, **140**, 17724–17733.
5 J. Cheng, P. Štacko, P. Rudolf, R. Y. N. Gengler and B. L. Feringa, *Angew. Chem. Int. Ed.*, 2017, **56**, 291–296.
6 B. L. Feringa, *Angew. Chem. Int. Ed.*, 2017, **56**, 11060–11078.
7 S. Kassem, T. van Leeuwen, A. S. Lubbe, M. R. Wilson, B. L. Feringa and D. A. Leigh, *Chem. Soc. Rev.*, 2017, **46**, 2592–2621.
8 D. Roke, S. J. Wezenberg and B. L. Feringa, *Proc. Natl. Acad. Sci. U.S.A.*, 2018, **115**, 9423–9431.
9 J. C. M. Kistemaker, A. S. Lubbe and B. L. Feringa, *Mater. Chem. Front.*, 2021, **5**, 2900–2906.
10 A. S. Lubbe, C. L. G. Stähler and B. L. Feringa, in *Out-of-Equilibrium (Supra)molecular Systems and Materials*, eds. N. Giuseppone and A. Walther, Wiley-VCH GmbH., 2021, pp. 337–377.
11 W. F. Jager, B. de Lange, A. M. Schoevaars, F. van Bolhuis and B. L. Feringa, *Tetrahedron: Asymmetry*, 1993, **4**, 1481–1497.
12 B. L. Feringa, W. F. Jager and B. de Lange, *Tetrahedron Lett.*, 1992, **33**, 2887–2890.
13 E. M. Geertsema, R. Hoen, A. Meetsma and B. L. Feringa, *Eur. J. Org. Chem.*, 2006, 3596–3605.
14 E. M. Geertsema, A. M. Schoevaars, A. Meetsma and B. L. Feringa, *Org. Biomol. Chem.*, 2006, **4**, 4101–4112.
15 P. M. Erne, P. Štacko, D. J. van Dijken, J. Chen, M. C. A. Stuart and B. L. Feringa, *Chem. Commun.*, 2016, **52**, 11697–11700.
16 A. C. Coleman, J. M. Beierle, M. C. A. Stuart, B. Maciá, G. Caroli, J. T. Mika, D. J. van Dijken, J. Chen, W. R. Browne and B. L. Feringa, *Nat. Nanotechnol.*, 2011, **6**, 547–552.
17 W. R. Browne, M. M. Pollard, B. de Lange, A. Meetsma and B. L. Feringa, *J. Am. Chem. Soc.*, 2006, **128**, 12412–12413.
18 O. Ivashenko, H. Logtenberg, J. Areephong, A. C. Coleman, P. V. Wesenhagen, E. M. Geertsema, N. Heureux, B. L. Feringa, P. Rudolf and W. R. Browne, *J. Phys. Chem. C*, 2011, **115**, 22965–22975.
19 N. A. Bailey and S. E. Hull, *Acta Cryst.*, 1978, 3289–3295.
20 J. F. D. Mills and S. C. Nyburg, *J. Chem. Soc.*, 1963, 308–321.
21 R. Korenstein, K. A. Muszkat and E. Fischer, *J. Photochem.*, 1976, **5**, 345–353.
22 G. Sánchez-Sanz, I. Alkorta and J. Elguero, *Tetrahedron*, 2011, **67**, 7316–7320.
23 D. H. Evans and R. W. Busch, *J. Am. Chem. Soc.*, 1982, **104**, 5057–5062.

24 A. Levy, P. U. Biedermann, S. Cohen and I. Agranat, *J. Chem. Soc. Perkin Trans. 2*, 2001, 2329–2341.

25 T. Matsue, D. G. Williams and D. H. Evans, *J. Electroanal. Chem.*, 1987, **233**, 63–76.

26 X. Yin, J. Z. Low, K. J. Fallon, D. W. Paley and L. M. Campos, *Chem. Sci.*, 2019, **10**, 10733–10739.

27 Y. Ishigaki, T. Hashimoto, K. Sugawara, S. Suzuki and T. Suzuki, *Angew. Chem. Int. Ed.*, 2020, **59**, 6581–6584.

28 Y. Matsuo, Y. Wang, H. Ueno, T. Nakagawa and H. Okada, *Angew. Chem. Int. Ed.*, 2019, **58**, 8762–8767.

29 G. Kortüm, *Angew. Chem.*, 1958, **70**, 14–20.

30 E. M. Geertsema, A. Meetsma and B. L. Feringa, *Angew. Chem. Int. Ed.*, 1999, **38**, 2738–2741.

31 P. U. Biedermann, I. Agranat and J. J. Stezowski, *Chem. Commun.*, 2001, **2**, 954–955.

32 A. Cnossen, J. C. M. Kistemaker, T. Kojima and B. L. Feringa, *J. Org. Chem.*, 2014, **79**, 927–935.

33 D. J. van Dijken, J. Chen, M. C. A. Stuart, L. Hou and B. L. Feringa, *J. Am. Chem. Soc.*, 2016, **138**, 660–669.

34 G. Mlostoń, R. Hamera-Fałdyga and H. Heimgartner, *J. Sulfur Chem.*, 2018, **39**, 267–278.

35 G. Mlostoń, P. Pipiak, R. Hamera-Fałdyga and H. Heimgartner, *Beilstein J. Org. Chem.*, 2017, **13**, 1900–1906.

36 Gaussian 16, Rev B.01, M. J. Frisch, G. W. Trucks, H. B. Schlegel, G. E. Scuseria, M. A. Robb, J. R. Cheeseman, G. Scalmani, V. Barone, G. A. Petersson, H. Nakatsuji, *et al.*, Gaussian, Inc. Wallingford, CA, 2016.

37 J. Li, C. Jin and W. Su, *Heterocycles*, 2011, **83**, 855–866.

38 J. Zhao and R. C. Larock, *J. Org. Chem.*, 2007, **72**, 583–588.

39 E. Filippatos, A. Papadaki-Valiraki, C. Roussakis and J.-F. Verbist, *Arch. Pharm.*, 1993, **326**, 451–456.

40 S. Khan, P. L. Bernad, V. A. Korshun, E. M. Southern and M. S. Shchepinov, *Synlett*, 2005, 2453–2456.

41 Z. Shi, S. Chen, Q. Xiao and D. Yin, *J. Org. Chem.*, 2021, **86**, 3334–3343.

42 X. Wei, Y. Chen, R. Duan, J. Liu, R. Wang, Y. Liu, Z. Li, Y. Yi, Y. Yamada-Takamura, P. Wang and Y. Wang, *J. Mater. Chem. C*, 2017, **5**, 12077–12084.

43 M. M. Pollard, M. K. J. ter Wiel, R. A. van Delden, J. Vicario, N. Koumura, C. R. van den Brom, A. Meetsma and B. L. Feringa, *Chem. Eur. J.*, 2008, **14**, 11610–11622.

44 M. D. Banciu, C. Costea, C. Draghici, A. Banciu, D. Mihaiescu and D. Ciuculescu, *J. Anal. Appl. Pyrolysis*, 2003, **67**, 359–368.

45 G. A. Molander and E. D. Dowdy, *J. Org. Chem.*, 1999, **64**, 6515–6517.

Chapter 4

Three-State Switching of Extended Bisthioxanthylidenes

Two molecular switches, based on bridged bisthioxanthylidenes, were developed utilising thermal, photochemical and electrochemical stimuli. The conformers involved with these switches are investigated by DFT calculations and based on experimental evidence and the theoretical investigations we can explain the switching behaviour of these structures. An anthracenyl-bridged switch is kinetically trapped because of the high steric hindrance of the central motif and can be reliably switched between an orthogonal dicationic state, an orthogonal diradical state and a closed-shell folded state. Furthermore, a phenyl-bridged switch has a thermal equilibrium at room temperature and can be observed, as a neutral compound, in both a folded and orthogonal state, as well as in a dicationic orthogonal state. The combined computational and experimental data provide us with a better insight into the switching of overcrowded alkenes and the studied compounds have a great potential for application in molecular machines or organic electronics.

Acknowledgement
I would like to thank Marco Wonink for his contributions on the synthesis, electrochemistry and NMR experiments presented in this chapter and I would like to thank Stefano Crespi for fruitful discussions on computational chemistry.

Parts of this chapter have been accepted for publication as: Marco B.S. Wonink, Brian P. Corbet, Artem A. Kulago, Gregory B. Boursalian, Bas de Bruin, Edwin Otten, Wesley R. Browne, and Ben L. Feringa, *Three-State Switching of an Anthracene Extended Bisthiaxanthylidene with a Highly Stable Diradical State*, *J. Am. Chem. Soc.,* 2021, **143**, 18020–18028.

1. Introduction

In recent years, molecular switches with various redox- and conformational states, addressed by external stimuli such as electricity, light and/or heat have attracted tremendous attention.[1,2,3] A multitude of properties, such as magnetic, optical, and biological activity can be affected and controlled.[4,5,6,7] These types of switches have a potential for application in, for example, memory devices, sensors or molecular machines.[3,8–10] Overcrowded alkenes, in particular bistricyclic aromatic enylidenes (BAEs), light-driven molecular motors (see also Chapter 1 of this thesis) and bisthioxanthylidene switches (see also Chapter 3 of this thesis) developed in our group are key examples of these switchable molecular systems.[10]

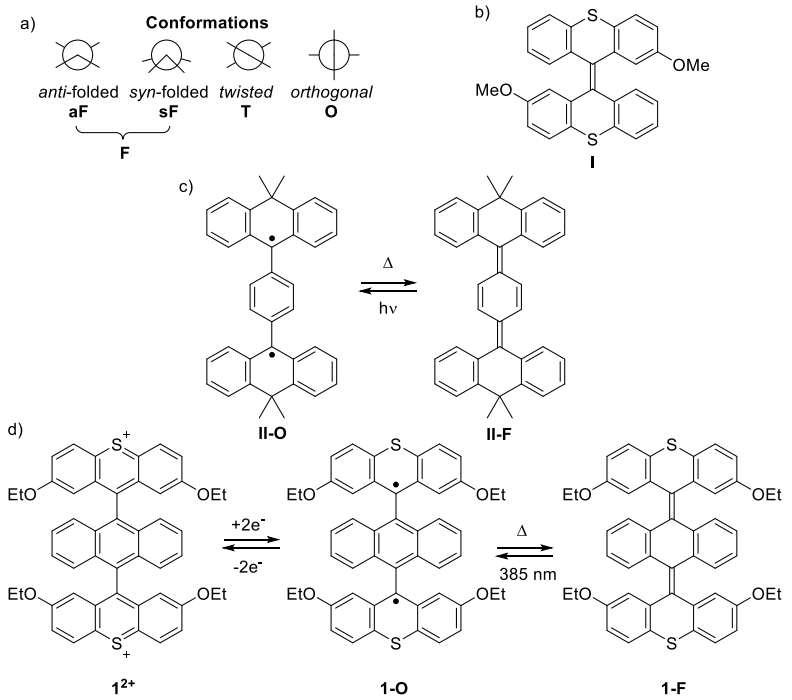

Figure 1. a) Conformations of BAEs. b) Bisthioxanthylidene switch used in our previous work.[6,11] c) Dihydro-dimethyl-anthryl-based switch by Kubo and co-workers.[12] d) This work on aromatically extended bisthioxanthylidene switches.

Fundamentally, a molecular switch requires multiple, addressable states.[13] In the case of BAEs, the steric hindrance in the fjord region plays a key role in the observation of different isomers.[14] A number of distinct conformations of BAEs are schematically described in Figure 1a, where the steric hindrance is accommodated by folding or twisting of the two halves into an *anti*-folded (**aF**), *syn*-folded (**sF**), twisted (**T**) or orthogonal (**O**) state.

Bisthioxanthylidenes (Figure 1b) undergo conformational changes induced by either electricity or light[6,11,15] and, upon oxidation, could be isolated as a dicationic state with nearly orthogonal (**O**) upper and lower tricyclic aromatic moieties.[6] More recently, an aromatically extended BAE, based on the 9,10-dihydro-10,10-dimethyl-9-anthryl motif, developed by Kubo and co-workers,[12] was used to demonstrate conformational changes induced by heat or light (Figure 1c). A switchable interconversion between a neutral closed-shell (**II-F**) and triplet open-shell diradical (**II-O**) state was observed which affected the redox properties of these compounds.

The stability of organic radical compounds is, in general, controlled by steric effects, delocalisation of spin density, and aromatic stabilisation.[16–19] Many stable diradical organic molecules have aromatic bridging motifs, where the closed-shell state has a quinoidal character.[17,18,20,21] For diradicals and diradicaloids, switching between the open and closed-shell states is possible. Depending on the activation barrier for interconversion, the diradical states can be in thermal equilibrium with the closed-shell states or there can be a multitude of thermally stable or metastable states.[12,22–24] Stable organic radical compounds can be used in applications such as photovoltaic devices or organic field-effect transistors and are promising for the future development of molecular switches and optoelectronically active materials.[24,25]

In our ongoing research into responsive systems, we sought to develop switchable molecules with a stable diradical state. Anthracenyl-bridged bisthioxanthylidene **1** (Figure 2) contains two overcrowded alkene motifs, leading to distinct and addressable conformational isomers. As an analogue of bisthioxanthylidenes, molecule **1** was envisioned as a stable redox switch, aided by the two polarizable sulfur atoms.[6,26] The quinoidal or aromatic central bridging part was anticipated to be a motif leading to stable organic radical compounds. To further investigate the influence of the steric crowding around the central overcrowded double bonds on the conformational switching properties, phenyl-bridged switch **2** (Figure 2) was used as an additional target in this study. Initial investigations by Artem Kulago into the synthesis, electro- and photochemistry of these compounds showed promising results,[27] which prompted the continued research into extended bisthioxanthylidenes.

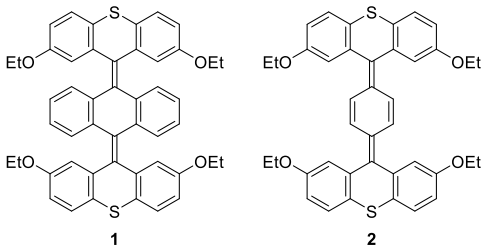

Figure 2. The target anthracenyl- (**1**) and phenyl-bridged (**2**) bisthioxanthylidenes used in this chapter.

In this chapter we will discuss the conformational switching determined by computational methods and the relevant electrochemical and thermal switching. For a detailed discussion about the synthesis, EPR spectroscopy, X-ray crystallography and photochemical switching, the reader is referred to Refs 28, 29.

2. Results & Discussion

In parallel with our experimental study, we performed a computational study into our target molecules **1** and **2** (Figure 2) using DFT calculations at B3LYP/6-31G** level of theory. This commonly used method[30–32] was chosen as it often provides reliably usable results and does not have a severe computational cost. Compared to other considered functionals (ωB97X-D and B3LYP-D3) and more extensive basis sets (def2-TZVP), the B3LYP/6-31G** level of theory provided the best method for our analysis in terms of both accuracy and computing time. For further details on the other levels of theory, see Section 4.2.

2.1 Computational studies of anthracenyl-bridged bisthioxanthylidene

The DFT computational investigation (B3LYP/6-31G**) of the different possible conformers of **1** showed that the most stable conformation is a doubly *anti*-folded (**1-F**) structure for the neutral molecule (Figure 3, Table 1). This structure is reminiscent of the bisthioxanthylidenes (see Chapter 3), but due to the additional central quinoidal folded anthracenyl bridge there are two *anti*-folded conformations across the double bonds, resulting in the outer thioxanthene motifs being folded in the same direction.

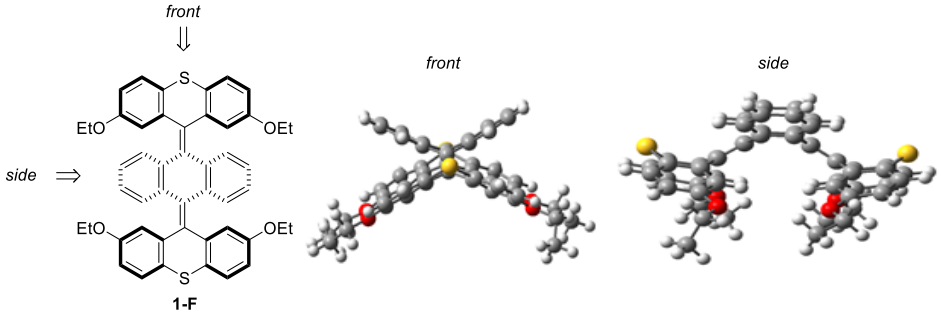

Figure 3. Overview of the geometry of the thermodynamic minimum energy structure **1-F**. The *front* and *side* views are indicated, which are used in this way throughout this chapter.

A ring flip in either the upper or lower thioxanthene motif would lead to a singly *syn*-folded (**1-asF**) and a doubly *syn*-folded (**1-ssF**) structure (Figure 4). Both of the optimised geometries correspond to a local minimum energy. The degree of folding in the anthracenyl motif or the thioxanthene motifs is not significantly different from the degree of folding in the *anti*-folded state (**1-F**, Figure 3). However, the orientation of many groups is changed greatly. The ethoxy groups that were pointing outwards in **1-F** are more directed towards other parts within the molecule. Furthermore, the sulfur atoms in the *syn*-folded rings, with respect to the central bridging unit, are pointed more inwardly, leading to a stronger influence of the electron density around sulfur on the overall intramolecular forces.

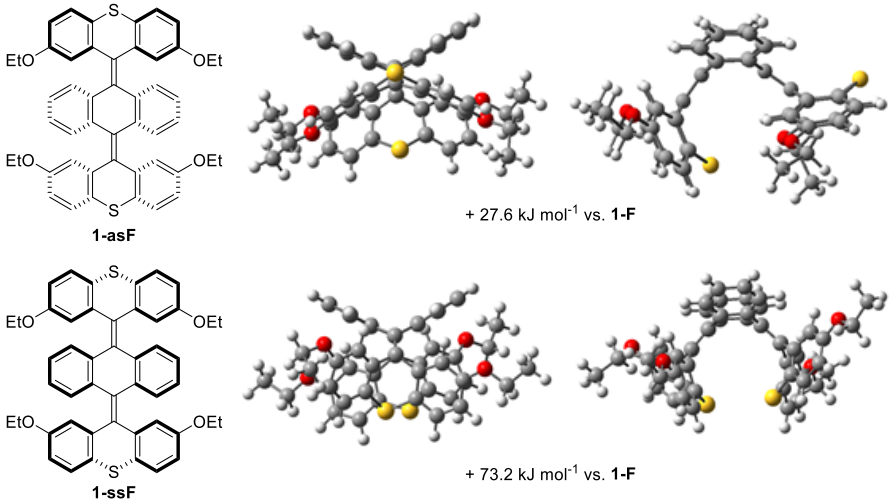

Figure 4. Overview of the geometries for the *anti-syn* and *syn-syn* folded structural isomers of **1**.

The described combination of steric and electronic factors leads to an increase in energy and thus a decrease in stability. The energies are

increased, relative to the global minimum of **1-F**, with 27.6 kJ mol^{-1} and 73.2 kJ mol^{-1} for **1-asF** and **1-ssF**, respectively (Table 1). This significant increase makes it unlikely that any *syn*-folded geometry will be involved under experimental conditions.

Table 1. Relative energies of neutral conformers of **1**.

Structure	Relative energy [kJ mol^{-1}]
Double *anti* **1-F**	0.0
Anti-syn **1-asF**	27.6
Syn-syn **1-ssF**	73.2
Orthogonal (closed shell) **1-O$_{cs}$**	79.0
Orthogonal (open shell) **1-O**	2.9

The orthogonal geometry has the outer thioxanthene motifs twisted away from the central anthracenyl bridge, reducing steric hindrance. In this geometry, a closed-shell system **1-O$_{cs}$** shows elongated C–C bonds between bridge and outer halves and dihedral angles of approximately 82°. Decreasing the dihedral angle from 82° gradually increases the energy of the system and no other local minima have been observed with planarised thioxanthene motifs. Increased double bond character destabilises the overall energy of the structure, because of the high amount of steric strain caused by the anthracenyl bridge.

Using a broken symmetry approach, thus allowing for open-shell systems, **1-O** could be found as a singlet diradical species (**1-O(s)**, Figures 5 and 6). The geometry of this is virtually identical to **1-O$_{cs}$**, but is significantly lower in energy (ΔE = 76.1 kJ mol^{-1}).

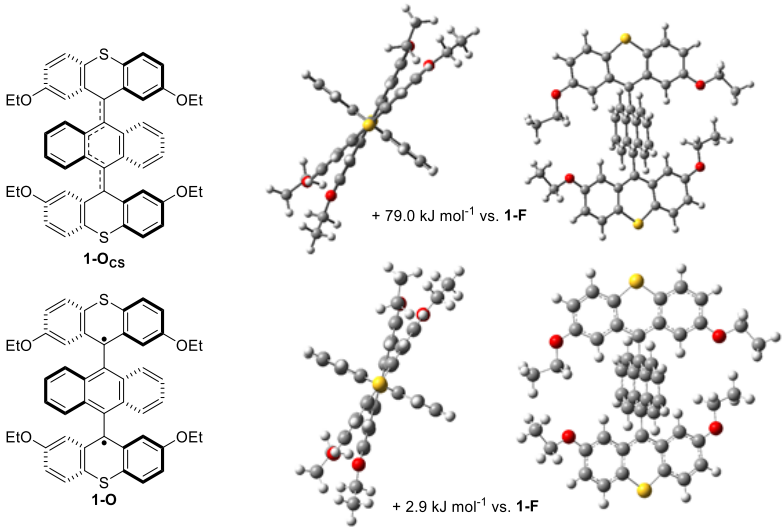

Figure 5. Conformations of the closed and open shell structures of **1-O**.

Mulliken spin analysis (Figure 6) shows that the spin density is high on the carbon atoms connected to the anthracenyl bridge. The thioxanthene parts are the major contributors for the spin density, whereas the central bridge has low to no population of spin density at all, resulting in a separation of the radicals.

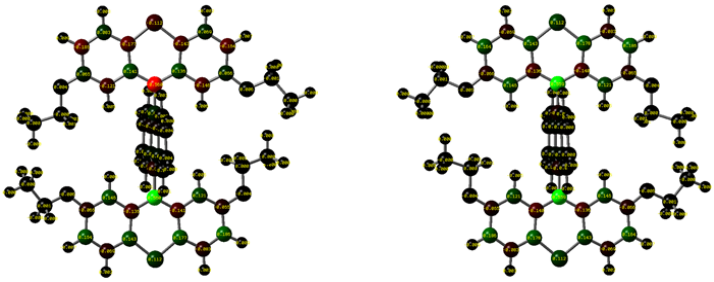

Figure 6. Mulliken spin population analysis of **1-O(s)** and **1-O(t)**.

Calculation of the triplet state of the diradical species (**1-O(t)**) showed a very similar picture to the singlet diradical species with a slightly higher energy (ΔE_{ST} = 0.059 kJ mol^{-1}) after Yamaguchi spin decontamination[33] and zero-point energy corrections. This energy difference would correspond to a 51:49 distribution of **1-O(s)**:**1-O(t)** at 293 K. However, it is important to note that the energy differences are smaller than the expected error margins, so the only conclusion we can derive is that the energy levels are nearly identical.

The dicationic molecule $\mathbf{1}^{2+}$ (Figure 7), which is important for the redox switching, has a highly similar conformation to **1-O** and the global minimum for this molecule is found with this orthogonal geometry. No other minimum energy structures were found for the dicationic molecules. Mulliken charge distribution in $\mathbf{1}^{2+}$ indicated a high charge localisation on the sulfur atoms, as was expected.[6,11]

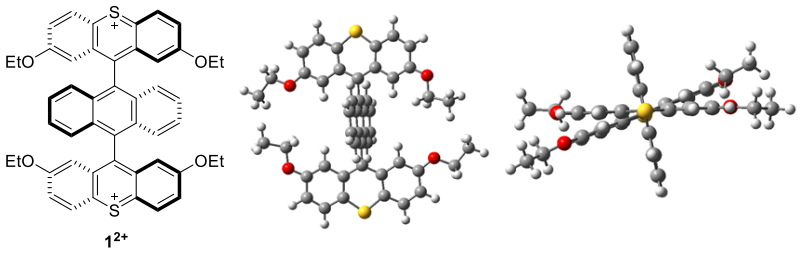

Figure 7. Optimised geometry of dicationic, orthogonal $\mathbf{1}^{2+}$.

The calculated interconversion barrier between the orthogonal and folded states of compound **1** (Figure 8) shows that the stable diradical state and the closed-shell, folded state of the molecule have a high barrier for interconversion (128.1 kJ mol^{-1}) leading towards the slightly more stable folded state (**1-F**). The transition state (**TS1**) is an overall bent structure where a degree of folding is already present. The consequences of this high barrier for the switching are further discussed in section 2.3.

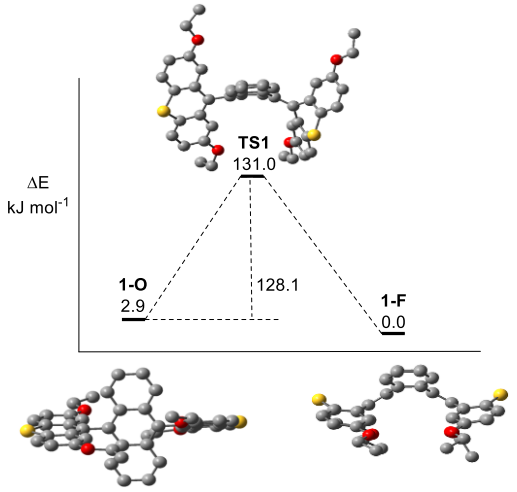

Figure 8. Schematic and graphic representation of the thermal isomerisation pathway for the neutral conformers between the planarised, orthogonal and folded structures of **1**. Hydrogen atoms are omitted for clarity.

2.2 Computational studies of phenyl-bridged bisthioxanthylidene

For the different conformers of **2** (Figures 9, 10), the steric hindrance is significantly lower compared to the conformers of **1** (Figures 3–5). From the optimisation of the expected geometries, we observed that phenyl-bridged **2** has a folded structure as its global minimum. This orientation has an almost planar phenyl bridge and the outer thioxanthene rings are in a *syn*-folded conformation towards one another (Figure 9). As with **1**, the sulfur atoms are pointed in the same direction, however, there is no significant folding in the bridging unit. The lower amount of steric hindrance results in smaller relative energy differences between the conformers.

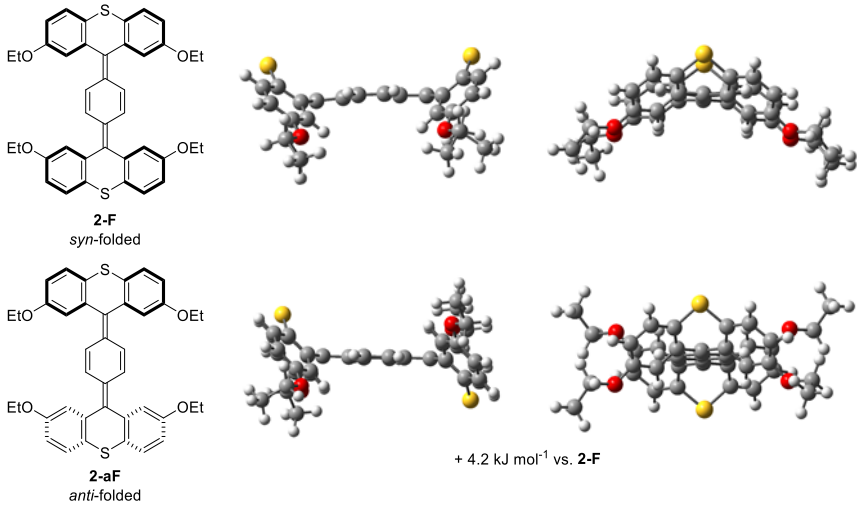

Figure 9. Optimised geometries of the folded conformers of **2**.

An alternative folding to the global minimum (**2-F**) is the accessible conformer **2-aF** (Figure 9) that is slightly higher in energy (4.2 kJ mol^{-1}, Table 2). With the small phenyl bridge, the central ring is no longer involved in the folding for stabilisation and accommodation of the steric hindrance, due to the overcrowding around the central double bonds. Consequently, there are only two folded conformers. The energy difference between *syn*- and *anti*-folded states is much less pronounced than that in the anthracenyl-bridged case.

Table 2. Relative energies of neutral conformers of **2**.

Structure	Relative energy [kJ mol^{-1}]
Syn **2-F**	0.0
Anti **2-aF**	4.2
Twisted **2-T**	58.2
Orthogonal **2-O**	1.7

Again, similar to **1**, geometries with planar outer thioxanthylidene motifs are found as local minima. In contrast, now two distinct structures can be identified with a twisted and orthogonal orientation **2-T** and **2-O**, respectively (Figure 10). Their most notable geometrical differences being the C–C bond length between the phenyl and thioxanthylidene motifs (1.45 Å for **2-T** and 1.49 Å for **2-O**) and the dihedral angles (51° for **2-T** and 77° for **2-O**). This means that with a relatively low steric hindrance from the bridging phenyl unit, it is possible to obtain a local minimum structure that is a closed-shell state with increased double bond character, while maintaining a planarised geometry for all rings in the molecule. For a closed-shell system, the increase of the dihedral angle from **2-T** towards an orthogonal conformer correlated with an increase of the energy of the system and no local minimum could be found with a larger dihedral angle than 51°.

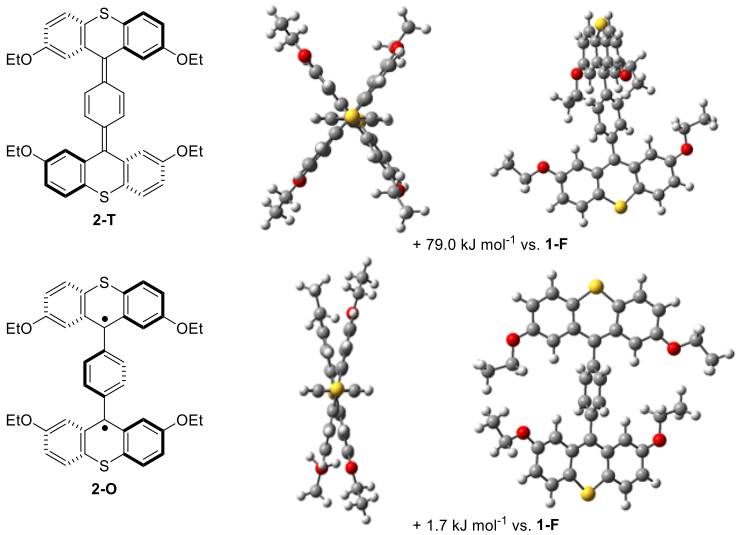

Figure 10. Optimised geometries of the planarised conformers of **2**.

At a much lower energy than the twisted conformer **2-T**, the open-shell diradical **2-O** was found as another local minimum. For **2-O**, the singlet–triplet gap after zero-point energy and Yamaguchi spin decontamination corrections[33] was ΔE_{ST} = 0.607 kJ mol^{-1} with a slightly higher energy triplet state. This energy difference would correspond to a 56:44 distribution of **2-O(s)**:**2-O(t)** at 293 K. Again, it is important to note that the energy differences are small. From the near degeneracy of the singlet and triplet state we can expected that both state could be populated. The Mulliken spin population analysis (Figure 11) shows that the diradical character is mostly found on the carbon atoms at the position next to the bridging unit. As found in comparable molecules, the central aromatic bridging unit is the leading cause for the separation and stability of the diradical species.[17,18,20,21]

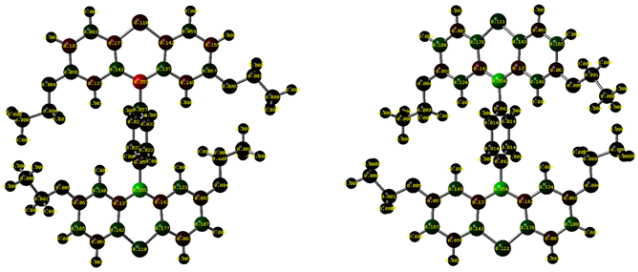

Figure 11. Mulliken spin population analysis of **1-O(s)** and **1-O(t)**.

The dicationic molecule $\mathbf{2}^{2+}$ (Figure 12) has a conformation akin to **2-O** (Figure 11) and anthracenyl-bridged $\mathbf{1}^{2+}$ (Figure 7). This geometry is found as the global minimum energy structure and the charge distribution is significantly high on the sulfur atoms, in line with expectations.

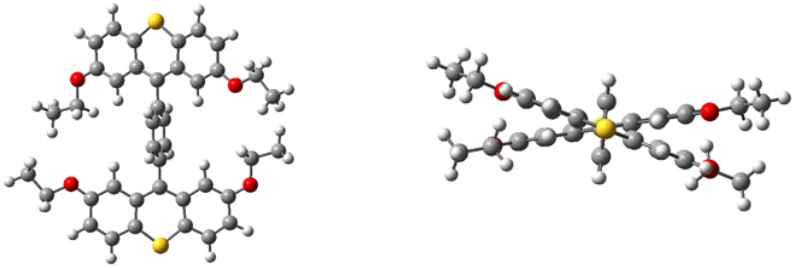

Figure 12. Optimised geometry of the dicationic structure $\mathbf{2}^{2+}$.

In order to investigate the twist-fold isomerisation pathway for the phenyl bridged bisthioxanthylidene, a 2D potential energy surface (PES) was constructed by a scan of the two dihedral angles $\theta 1$ and $\theta 2$ (Figure 13),

allowing for open-shell structures with a singlet multiplicity. This resulted in a caldera shaped PES with global minima around dihedral angles of $\theta 1 \approx \theta 2 \approx 0°$ or 180° and a plateau area with roughly equal energy around dihedral angles $\theta 1 \approx \theta 2 \approx 90°$. The **2-O(s)** conformer, found in the centre of this plot has flexibility for rotation around the central C–C bonds towards a number of nearly isoenergetic conformations (central blue valley). Moving outwards, there are a number of dihedral angle combinations that are higher in energy (red regions). Finally, the four corners of the plotted shape represent the folded structure **2-F** (Figure 9) as the energetic minima of the plot.

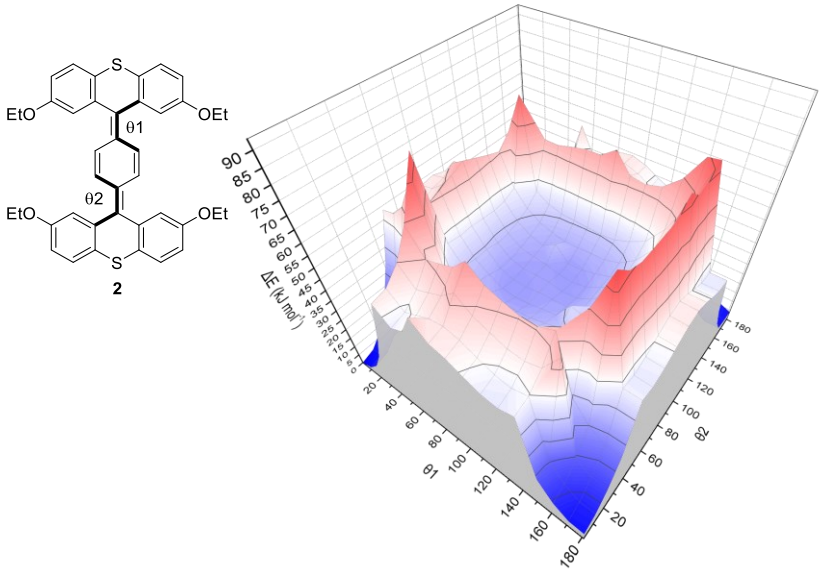

Figure 13. Potential energy surface plot from 2D scan of dihedral angles of **2** ($\theta 1$, $\theta 2$). For the numerical energy values see Section 4.3.

By probing the possible pathways for twist-fold isomerisation, using the constructed PES, we see that there are many points on the graph that could be a transition state for the **2-O(s)** to **2-F** transformation with a highly similar energy barrier. This means that there are many comparable reaction coordinates through which this isomerisation can occur with an analogous reaction profile. Four saddle points on the "caldera edge" were selected as starting points for further computational investigation. These saddle points have a nearly identical energy and each transition would result in the same folded structure. In this chapter, one transition state is chosen for clarity and the represented **TS2** (Figure 14) has dihedral angles of $\theta 1 = 121.3°$ and $\theta 2 = 34.7°$.

The low calculated barrier for the isomerisation process between **2-O** and **2-F**, via **TS2** ($\Delta E^{\ddagger}$ = 39.7 kJ mol^{-1}, Figure 14) is in accordance with experimental observations. As with the previously described twist-fold isomerisation of **1** (via **TS1**, Figure 8), **TS2** is partially folded and partially planar. A notable amount of flexibility of different conformers is allowed, compared to the anthracenyl-bridge **1**, because of the small size of the phenyl-bridge. The low barrier and relative energy differences between **2-O** and **2-F** (Figure 14) can explain the shape of the cyclic voltammogram (Section 2.3, Figure 17), where a relatively fast thermal equilibrium process occurs and both the orthogonal and folded structures are present in solution, which is discussed in more detail in Section 2.3.

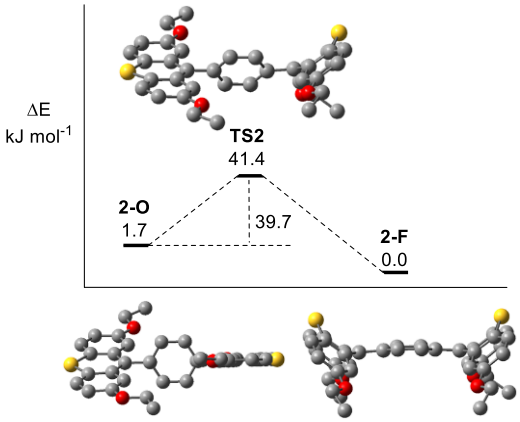

Figure 14. Schematic and graphic representation of the thermal isomerisation pathway for the neutral conformers between the planarised and folded structures of **2**. Hydrogen atoms are omitted for clarity.

2.3 Electrochemistry and thermal switching

The target compounds used in the experimental analysis (Figure 15), were synthesised by Marco Wonink. For a full discussion on the synthesis, X-ray crystallography, EPR spectroscopy, the reader is referred to Refs 28, 29.

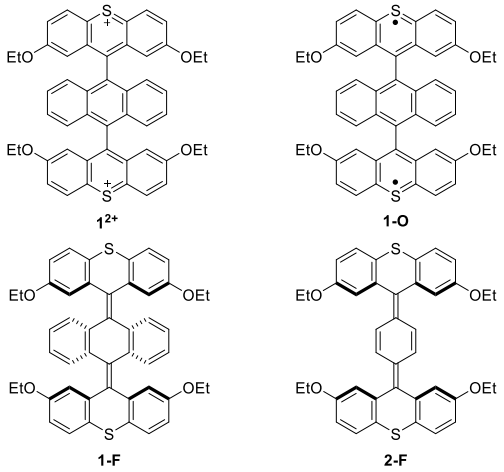

Figure 15. Synthesised targets **1²⁺**, **1-O**, **1-F** and **2-F**.

Variable temperature (VT) ^{1}H NMR studies on the paramagnetic compound **1-O** showed broad residual solvent signals in the initial spectrum at room temperature (Figure 16a). Signals from **1-O** were not observed, probably due to the extent of broadening resulting in the exclusive observation of a baseline. This broadening is caused by the presence of paramagnetic species and rotation around the central C–C bond axes. Increasing the temperature to 100 °C, resulted in sharper, more resolved signals (Figure 16e), assigned to the structure of **1-F**. Cooling back to 25 °C shows persistence of these signals (Figure 16f), consistent with a high activation barrier for interconversion between **1-F** and **1-O** and kinetic trapping of both species. Full conversion towards **1-F** was achieved by maintaining a temperature of 100 °C for 40 h, when the ^{1}H-NMR spectrum at 25 °C showed highly resolved signals, indicative of the full conversion of the paramagnetic compound **1-O**.

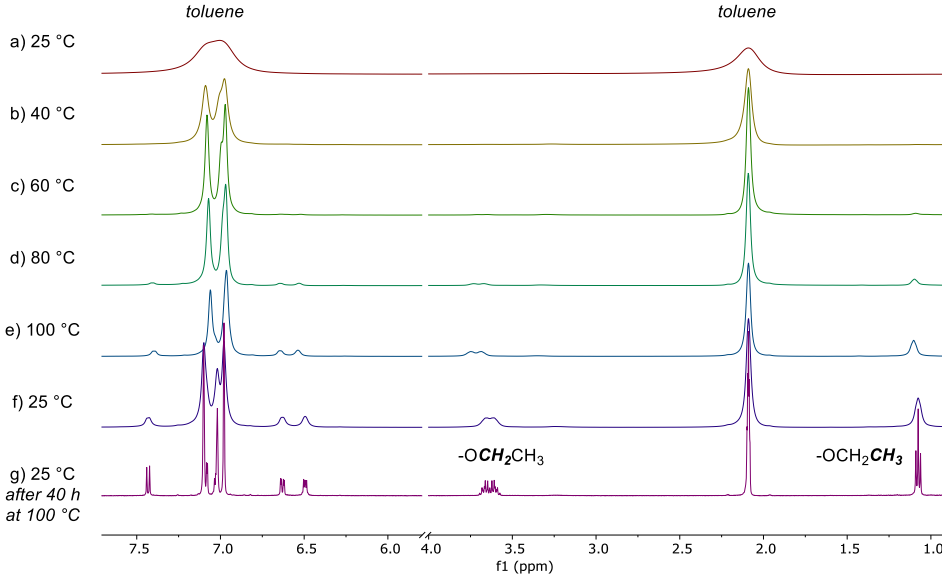

Figure 16. VT-^{1}H NMR (500 MHz, toluene-d8) spectra of the neutral, orthogonal **1-O**. a) – e) Incrementally increased temperature from 25 to 100 °C; f) subsequent return to 25 °C; g) **1-F**, measured at 25 °C after full thermal conversion of **1-O** after 40 h at 100 °C.

Cyclic voltammetry (CV) of $\mathbf{1}^{2+}$ in CH_2Cl_2 shows two closely spaced waves around -0.42 V vs. Fc/Fc^+ (Figure 17). In contrast to non-bridged bisthioxanthylidenes (see Chapter 3), these redox events are split because of a stabilisation of the radical cation by delocalisation of the SOMO over the entire molecule.[34] This causes the second reduction of $\mathbf{1}^{1+\cdot}$ towards **1-O** to occur at a more negative potential.

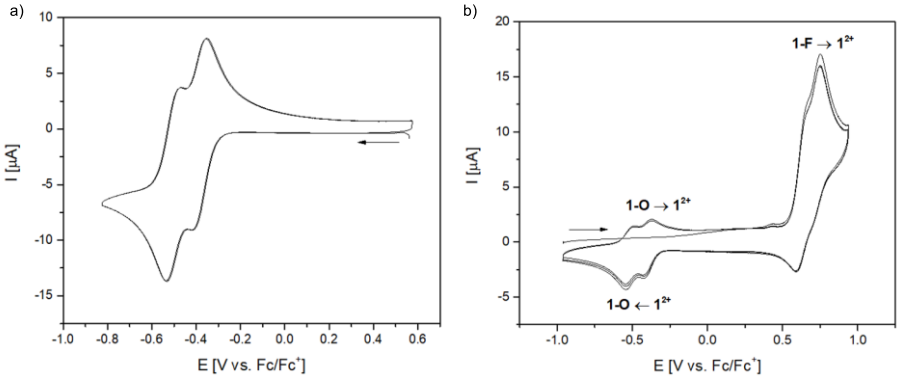

Figure 17. a) CV of $\mathbf{1}^{2+}$ (0.5 mM, CH_2Cl_2, RT, 0.1 V s^{-1}). b) CV of **1-F** (0.5 mM, CH_2Cl_2, RT, 0.1 V s^{-1}).

The reversibility of these waves indicates that the structures of $\mathbf{1}^{2+}$ and **1-O** are of a similar nature, which fits with our hypothesis that the reduction of $\mathbf{1}^{2+}$ leads to the diradical state **1-O** without any significant conformational changes. DFT calculations indicated that **1-O** is a local minimum (Figure 8, ΔE = 2.9 kJ mol^{-1} relative to **1-F**), kinetically trapped with a high barrier ($\Delta E^{\ddagger}$ = 128.1 kJ mol^{-1}) for isomerisation at room temperature towards the global minimum **1-F**. The high barrier for isomerisation is the result of the high steric hindrance in the fjord region in the double folded molecule **1-F** and the requirement for multiple "ring slips" to interconvert between folded and orthogonal states. The oxidation of **1-F** (Figure 17b) occurs at a markedly higher potential ($E_{p,a}$ = 0.71 V vs. Fc/Fc^{+}) than the oxidation of **1-O**. After this oxidation of the folded state, the dicationic $\mathbf{1}^{2+}$ is formed, with increased single bond character and a strongly favourable orthogonal state. Indeed, that the reduction of $\mathbf{1}^{2+}$ leads to the formation of **1-O**, is confirmed in the second oxidative sweep where the oxidation of **1-O** to $\mathbf{1}^{2+}$ is now observed. In summary, the data is in accordance with the expected conformational change upon redox switching.[12,35]

DFT calculations indicated that the thermal isomerisation behaviour of **2** is markedly different than that of **1**. From the observed experimental data, the electrochemical switching of **2** is in accordance with computational results. As seen in Figure 18a, cyclic voltammetry of **2-F** at room temperature and a high scan speed (blue) shows a broad oxidation wave and a relatively sharp reduction wave. Decreasing the scan speed (red and black) shows less broadening of the oxidation signal with a peak potential closer to the corresponding reduction. This is indicative of an equilibrium process, which is fast on the timescale of the electrochemical measurement.[23,36,37] At room temperature, the closed-shell, folded **2-F** is in a thermal equilibrium with the open-shell, diradical, orthogonal **2-O**. The observed oxidation corresponds to the oxidation of **2-O**, which has a similar geometry to $\mathbf{2}^{2+}$, which is the resulting structure after oxidation, whereas the oxidation of **2-F** is expected at a higher potential.

At -50 °C (Figure 18b), the CV shows a lack of oxidation current in the range of -0.35 – -0.10 V vs. Fc/Fc^{+}, but rather shows a peak current at 0.14 V vs. Fc/Fc^{+}. This hysteresis is consistent with the oxidation of **2-F**, having a significantly different structure than both **2-O** and $\mathbf{2}^{2+}$ and therefore a different oxidation potential. In accordance with the computational results, at low temperature the global minimum energy structure of **2-F** is present, but in contrast to the room temperature measurements, there is no noticeable amount of the **2-O** state present to be oxidised at lower potentials. Indeed, at a higher potential, **2-F** gets oxidised to $\mathbf{2}^{2+}$, which then quickly

adopts an orthogonal geometry. Subsequently, $\mathbf{2}^{2+}$ is reduced in the return sweep, at the same potential as observed at room temperature.

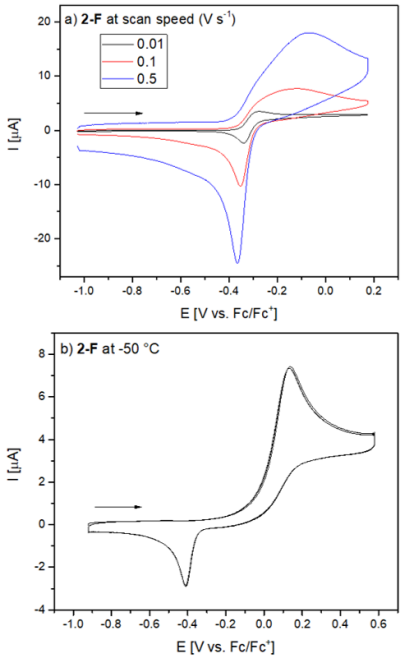

Figure 18. a) CV of **2-F** at different scan speeds (0.5 mM, CH_2Cl_2, RT). b) CV of **2-F** at -50 °C (0.5 mM, CH_2Cl_2, 0.1 V s^{-1}).

By VT-^{1}H NMR spectroscopy, starting from **2-F** at 25 °C, we observe a slight downfield shift and broadening of the signals upon increasing the temperature (Figure 19a–g), caused by the increased population of the paramagnetic diradical state. Returning to 25 °C (Figure 19h) immediately restored the initial spectrum and no kinetic trapping is observed for **2**, consistent with a low interconversion barrier. Both the electrochemical and thermal investigations by NMR spectroscopy corroborate the switching behaviour, described by the computational study.

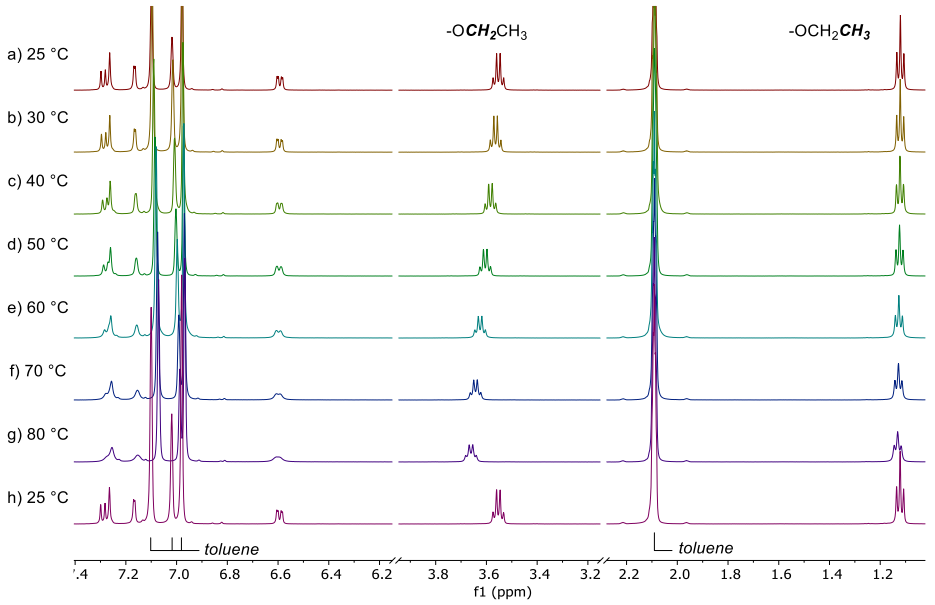

Figure 19. VT-^{1}H NMR (500 MHz, toluene-d8) spectra of the neutral, folded **2-F**. a) – g) incrementally increased temperature from 25 to 80 °C and h) subsequent return to 25 °C.

3. Conclusions & Outlook

The anthracenyl- and phenyl-bridged bisthioxanthylidenes **1** and **2** show that a number of conformational isomers are individually addressable. The steric hindrance in these overcrowded alkenes is crucial for the stability and observability of specific conformers. The isomers representing the orthogonal states of $\mathbf{1}^{2+}$ and $\mathbf{2}^{2+}$ can be reduced to the geometrically similar diradicals **1-O** and **2-O**, respectively. Where **1-O** is a kinetically trapped diradical species, the diradical **2-O** readily isomerises to the global minimum energy structure of the closed-shell, folded **2-F**. The anthracenyl-bridged closed shell isomer **1-F** is accessible at high temperatures and **1-O** can be fully converted. We can conclude that the steric factors of the bridging unit in our switches are of tremendous influence on the multistability of our molecular switches. Especially the robust redox switching between the dicationic $\mathbf{1}^{2+}$, stable diradical **1-O** and the subsequent thermal switching to **1-F** is a fascinating discovery and can be used as a starting point for further development of electrochemically switchable molecules or multi-stimuli responsive materials.

4. Experimental

4.1 General comments

For general information on chemicals and NMR spectroscopy, see Chapter 2. For details on the synthesis and characterisation of compounds, the reader is referred to Refs 28 and 29.

In this chapter, DFT calculations were carried out using the Gaussian 16 Rev. B.01 software package.[38] All stationary point optimisations were confirmed by the absence of imaginary frequencies, all transition state optimisations were confirmed with having only one imaginary frequency, corresponding to the transformation of investigation. The geometries of the open shell diradical species were obtained using the broken symmetry (BS)-DFT approach. The energies of these structures were corrected from spin contamination applying the method of Yamaguchi.[33] All the energies mentioned in the main text are obtained by summing the electronic energies with the zero-point vibrational energies. VT-NMR studies in anhydrous and deoxygenated toluene were performed on a Varian Unity Plus 500 NMR spectrometer. Cyclic voltammograms were recorded using a three-electrode setup on a CHI600C (CH Instruments) or a VSP-300 Potentiostat/Galvanostat (Biologic Science Instruments) using an Ag/AgCl wire as pseudo-reference electrode (RE), glassy carbon (3 mm diameter) disc working electrode (WE), and a platinum wire as counter electrode (CE). The working electrode was polished with aluminium oxide on a microcloth pad before every experiment. All cyclic voltammograms were recorded at room temperature, with scan rate 0.1 V s^{-1}, unless otherwise stated, under an argon atmosphere using dry, degassed CH_2Cl_2 and 0.1 M tetrabutyl ammonium hexafluorophosphate ($TBAPF_6$) as electrolyte with a substrate concentration of 0.5 mM. All cyclic voltammograms were calibrated by the addition of ferrocene at the end of the experiment as an internal reference.

4.2 Selection of the level of theory for the DFT calculations

The conformers involved in the thermal and electrochemical switching were optimised at the B3LYP/6-31G**, B3LYP-D3/6-31G** and ωB97X-D/def2-SVP levels of theory. The energies of the optimised structures were further calculated with the more extensive basis set def2-TZVP. The electronic energies, including the zero-point energy and Yamaguchi's spin decontamination corrections[33] are presented in Table 3. B3LYP/6-31G** was chosen as it is an often used method with low computational cost and often reliable results. Long-range interactions were considered and the ωB97X-D, which includes Grimme's D2 dispersion

model[39] and the B3LYP-D3 functionals were used for the optimisation and energy calculations. Def2-TZVP was used as a more extensive basis set compared to 6-31G**.

The experimental data on compounds **1** and **2** shows that the folded structures **1-F** and **2-F** are the most stable structures and that the diradical states are accessible with a high barrier for **1** and a low barrier for **2**.[28] The experimental data further shows that, for the orthogonal states, the triplet state is slightly lower in energy than the singlet state (0.092 kJ mol^{-1} by EPR).[28]

The computed data shows that the singlet and triplet energies for all the orthogonal states are nearly identical. The accuracy of the numbers obtained in this method are consistent with a small singlet-triplet gap.

Interestingly, the better performance, when compared to the experimental results, comes from the simpler, commonly used B3LYP/6-31G** level of theory. These discrepancies are possibly coming from the different characteristics of the functionals used to model the broken symmetry solution. It is known in the literature that the amount of exact exchange and the presence of empirical dispersion can alter the thermochemistry in diradicals, obtained using DFT calculations.[40]

Table 3. Energies of the conformers relative to the folded structures in kJ mol^{-1}, including correction for spin contamination using Yamaguchi's approximation and zero-point energy.

	b3lyp [b] /6-31g**	b3lyp /def2-tzvp //b3lyp /6-31g**	b3lyp-d3 /6-31g**	b3lyp-d3 /def2-tzvp //b3lyp-d3 /6-31g**	ωb97xd /def2-svp	ωb97xd /def2-tzvp //ωb97xd /def2svp
1-O(s)	2.9	0.4	4.4	2.7	20.5	27.3
1-O(t)	2.9	0.4	4.4	2.7	20.5	27.3
TS1	131.0	132.6	110.5	112.3	122.9[a]	121.3[a]
1-F	0.0	0.0	0.0	0.0	0.0	0.0
2-O(s)	1.7	-2.1	-12.9	-13.5	-28.9	-18.3
2-O(t)	2.5	-2.1	-12.4	-13.0	-29.1	-18.4
TS2	41.4	74.5	44.2	43.6	59.4	62.2
2-F	0.0	0.0	0.0	0.0	0.0	0.0

Footnotes: a) Using the geometry obtained by b3lyp-d3/6-31g**, as the optimisation using the ωb97xd functional did not provide convergence to the correct transition state. b) The values used in this chapter are highlighted in green.

4.3 Energies of 2D PES of 2

Table 4. Energies (kJ mol^{-1}) of the 2D PES of 2 constructed along the two dihedral angles $\theta 1$ and $\theta 2$ in ° at B3LYP/3-21G level of theory using a broken-symmetry approach.

$\theta 1$ / $\theta 2$	1	11	21	31	41	51	61	71	81	91
1	0.000	1.907	7.978	18.480	33.641	53.428	47.120	50.103	52.852	53.786
11	1.911	3.688	9.573	19.892	34.934	54.661	48.504	51.343	54.100	55.123
21	7.982	9.576	15.275	25.437	40.347	59.914	52.858	55.408	57.975	62.995
31	18.489	19.897	25.441	35.457	50.154	69.516	59.988	61.892	63.998	66.144
41	33.650	34.946	40.355	50.154	64.614	83.757	47.124	46.239	46.477	45.864
51	53.444	54.668	59.909	69.506	83.749	43.546	40.067	38.964	39.086	37.786
61	47.030	48.412	52.785	59.871	47.126	40.072	36.335	35.030	33.376	33.436
71	50.028	51.266	55.303	61.786	46.227	38.954	35.030	31.947	31.335	32.033
81	60.080	54.042	57.921	63.951	46.478	39.077	33.389	31.342	31.346	32.404
91	53.813	55.147	62.770	69.447	45.908	37.846	33.483	32.072	32.411	32.401
101	52.290	53.820	57.981	64.463	45.485	38.174	34.495	33.453	32.850	31.602
111	49.251	50.918	55.444	62.327	46.099	39.508	36.170	34.438	33.046	32.082
121	46.549	48.362	53.159	60.677	48.233	41.849	38.255	42.903	35.279	35.308
131	45.697	47.533	52.623	60.741	52.203	45.947	42.650	41.137	40.956	40.686
141	47.722	49.513	54.830	63.539	59.225	53.436	50.498	49.551	49.394	48.789
151	17.903	20.786	64.058	38.558	70.463	64.975	62.392	61.852	61.758	61.356
161	9.119	12.000	18.870	29.866	85.993	81.055	78.991	78.974	79.145	78.975
171	4.386	7.239	14.069	25.071	47.435	46.245	47.863	50.864	53.435	53.988
181	3.991	6.781	13.565	24.550	47.366	46.086	47.639	50.662	53.349	54.037

Table 4 continued.

θ1 / θ2	101	111	121	131	141	151	161	171	181
1	52.213	49.135	46.409	45.586	30.246	17.921	9.122	4.384	3.993
11	58.414	50.814	48.228	48.342	33.122	20.803	12.009	7.248	6.783
21	58.935	55.347	53.054	54.964	39.894	27.638	18.876	14.087	13.577
31	64.182	62.232	60.565	65.593	50.720	38.587	29.893	25.082	24.558
41	45.411	46.001	48.114	79.995	65.492	53.590	44.991	40.286	39.798
51	38.095	39.417	41.729	45.808	63.611	55.926	49.711	46.193	57.964
61	34.432	36.064	38.117	42.529	63.556	56.787	51.077	47.817	47.609
71	33.428	34.349	36.323	41.038	64.961	59.076	53.885	50.834	50.650
81	32.782	37.993	35.188	40.882	66.252	61.057	56.255	53.478	53.355
91	31.551	32.081	35.217	40.535	66.349	61.348	56.707	54.071	54.106
101	31.075	32.486	35.763	40.222	70.342	59.601	54.783	52.133	52.302
111	32.515	34.022	36.072	40.920	63.336	57.068	51.802	48.976	49.189
121	35.801	36.099	37.944	43.200	62.594	55.433	49.625	46.525	46.723
131	40.638	40.794	42.397	46.542	64.207	56.149	49.738	46.275	46.372
141	49.092	49.076	50.406	54.236	69.388	60.412	53.332	49.422	49.341
151	61.947	61.730	62.795	66.290	78.907	69.071	64.951	24.668	24.553
161	83.482	79.297	80.054	83.177	29.817	17.676	9.336	13.718	13.507
171	52.011	48.840	46.367	46.100	25.813	13.609	5.207	6.818	6.511
181	52.190	49.057	46.570	46.203	26.312	14.028	5.527	4.277	3.909

5. References

1 M. Baroncini, S. Silvi and A. Credi, *Chem. Rev.*, 2020, **120**, 200–268.
2 M. M. Russew and S. Hecht, *Adv. Mater.*, 2010, **22**, 3348–3360.
3 B. L. Feringa and W. R. Browne, *Molecular Switches*, Wiley-VCH, Hoboken, USA, 2nd edn., 2011.
4 N. Kida, M. Hikita, I. Kashima, M. Okubo, M. Itoi, M. Enomoto, K. Kato, M. Takata and N. Kojima, *J. Am. Chem. Soc.*, 2009, **131**, 212–220.
5 H. Li, J. O. Jeppesen, E. Levillain and J. Becher, *Chem. Commun.*, 2003, **3**, 846–847.
6 W. R. Browne, M. M. Pollard, B. de Lange, A. Meetsma and B. L. Feringa, *J. Am. Chem. Soc.*, 2006, **128**, 12412–12413.
7 W. Szymanski, J. M. Beierle, H. A. V. Kistemaker, W. A. Velema and B. L. Feringa, *Chem. Rev.*, 2013, **113**, 6114–6178.
8 A. Coskun, J. M. Spruell, G. Barin, W. R. Dichtel, A. H. Flood, Y. Y. Botros and J. F. Stoddart, *Chem. Soc. Rev.*, 2012, **41**, 4827–4859.
9 J. C. M. Kistemaker, A. S. Lubbe and B. L. Feringa, *Mater. Chem. Front.*, 2021, **5**, 2900–2906.
10 S. Kassem, T. van Leeuwen, A. S. Lubbe, M. R. Wilson, B. L. Feringa and D. A. Leigh, *Chem. Soc. Rev.*, 2017, **46**, 2592–2621.
11 B. P. Corbet, M. B. S. Wonink and B. L. Feringa, *Chem. Commun.*, 2021, **57**, 7665–7668.
12 T. Nishiuchi, R. Ito, E. Stratmann and T. Kubo, *J. Org. Chem.*, 2020, **85**, 179–186.
13 B. L. Feringa, R. A. van Delden, N. Koumura and E. M. Geertsema, *Chem. Rev.*, 2000, **100**, 1789–1816.
14 P. U. Biedermann, J. J. Stezowski and I. Agranat, *Eur. J. Org. Chem.*, 2001, 15–34.
15 J. Cheng, P. Štacko, P. Rudolf, R. Y. N. Gengler and B. L. Feringa, *Angew. Chem. Int. Ed.*, 2017, **56**, 291–296.
16 B. Tang, J. Zhao, J. F. Xu and X. Zhang, *Chem. Sci.*, 2020, **11**, 1192–1204.
17 Z. Zeng, Y. M. Sung, N. Bao, D. Tan, R. Lee, J. L. Zafra, B. S. Lee, M. Ishida, J. Ding, J. T. López Navarrete *et al.*, *J. Am. Chem. Soc.*, 2012, **134**, 14513–14525.
18 M. Abe, *Chem. Rev.*, 2013, **113**, 7011–7088.
19 T. Nishiuchi, R. Ito, A. Takada, Y. Yasuda, T. Nagata, E. Stratmann and T. Kubo, *Chem. Asian J.*, 2019, **14**, 1830–1836.
20 T. Kubo, A. Shimizu, M. Sakamoto, M. Uruichi, K. Yakushi, M. Nakano, D. Shiomi, K. Sato, T. Takui, Y. Morita and K. Nakasuji, *Angew. Chem. Int. Ed.*, 2005, **44**, 6564–6568.
21 W. W. Porter, T. P. Vaid and A. L. Rheingold, *J. Am. Chem. Soc.*, 2005, **127**, 16559–16566.
22 X. Yin, J. Z. Low, K. J. Fallon, D. W. Paley and L. M. Campos, *Chem. Sci.*, 2019, **10**, 10733–10739.
23 Y. Ishigaki, T. Hashimoto, K. Sugawara, S. Suzuki and T. Suzuki, *Angew. Chem. Int. Ed.*, 2020, **59**, 6581–6584.

24 G. E. Rudebusch, J. L. Zafra, K. Jorner, K. Fukuda, J. L. Marshall, I. Arrechea-Marcos, G. L. Espejo, R. Ponce Ortiz, C. J. Gómez-García, L. N. Zakharov, M. Nakano, H. Ottosson, J. Casado and M. M. Haley, *Nat. Chem.*, 2016, **8**, 753–759.
25 X. Hu, W. Wang, D. Wang and Y. Zheng, *J. Mater. Chem. C*, 2018, **6**, 11232–11242.
26 Y. Ishigaki, Y. Hayashi and T. Suzuki, *J. Am. Chem. Soc.*, 2019, **141**, 18293–18300.
27 A. A. Kulago, PhD Thesis, Rijksuniversiteit Groningen, 2011.
28 M. B. S. Wonink, B. P. Corbet, A. A. Kulago, G. B. Boursalian, B. de Bruin, E. Otten, W. R. Browne and B. L. Feringa, *J. Am. Chem. Soc,* 2021, **143**, 18020–18028.
29 M. B. S. Wonink, PhD Thesis, Rijksuniversiteit Groningen, 2022.
30 J. Tirado-Rives and W. L. Jorgensen, *J. Chem. Theory Comput.*, 2008, **4**, 297–306.
31 S. F. Sousa, P. A. Fernandes and M. J. Ramos, *J. Phys. Chem. A*, 2007, **111**, 10439–10452.
32 T. van Leeuwen, J. Pol, D. Roke, S. J. Wezenberg and B. L. Feringa, *Org. Lett.*, 2017, **19**, 1402–1405.
33 K. Yamaguchi, H. Fukui and T. Fueno, *Chem. Lett.*, 1986, **15**, 625–628.
34 W. R. Browne, J. J. D. de Jong, T. Kudernac, M. Walko, L. N. Lucas, K. Uchida, J. H. van Esch and B. L. Feringa, *Chem. Eur. J.*, 2005, **11**, 6414–6429.
35 B. A. Olsen and D. H. Evans, *J. Am. Chem. Soc.*, 1981, **103**, 839–843.
36 S. F. Nelsen, L. Echegoyen and D. H. Evans, *J. Am. Chem. Soc.*, 1975, **97**, 3530–3532.
37 S. F. Nelsen, L. Echegoyen, E. L. Clennan, D. H. Evans and D. A. Corrigan, *J. Am. Chem. Soc.*, 1977, **99**, 1130–1134.
38 Gaussian 16, Rev. B.01, M. J. Frisch, G. W. Trucks, H. B. Schlegel, G. E. Scuseria, M. A. Robb, J. R. Cheeseman, G. Scalmani, V. Barone, G. A. Petersson, H. Nakatsuji, *et al.*, Gaussian, Inc., Wallingford, CA, 2016.
39 J. Da Chai and M. Head-Gordon, *Phys. Chem. Chem. Phys.*, 2008, **10**, 6615–6620.
40 D. López-Carballeira and F. Ruipérez, *J. Mol. Model.*, 2016, **22**, 76.

Chapter 5

Modulating Conformational Redox Switching Using Pyridyl-Functionalised Bisthioxanthylidenes

Two bisthioxanthylidene switches, functionalised with alkyl linkers and pyridyl ligands are developed in order to modify the conformational switching by electrochemical stimuli using metal complexation. The design of the switches is based on DFT calculations and considerations on various linker lengths, resulting in a linker of three methylene units. The target switches could be synthesised via late-stage functionalisation of a bisallyl bisthioxanthylidene core and the switches were investigated using UV-vis spectroscopy, fluorescence spectroscopy and cyclic voltammetry. These spectroscopic and electrochemical studies elucidate the metal complexations and, in the case of iron complexes, show the quenching of the bisthioxanthylidene luminescence and a modified redox switching. Upon oxidation and reduction of a Fe-Terpy functionalised switch, a previously unobserved species in electrochemical modulation of redox-states of bisthioxanthylidenes is found, likely to be a twist-folded structure.

Acknowledgement
I would like to thank Jorn Steen for useful discussions on electrochemistry and I would like to thank Wesley Browne for fruitful discussions on the project in general.

1. Introduction

Molecular motion is a fascinating concept in nanoscience that is not only important in biological processes,[1,2] but has sprouted an entire field of study towards the development of artificial molecular switches, motors and machines.[3–10] Many of these artificial molecular machines make use of coordination chemistry.[11,12] A wide scope of intramolecular interactions, mechanically interlocked molecules[13] and metal-ligand interactions have been shown to be versatile structures and principles, and such key motifs have been applied for motion at the molecular scale.[4,14]

Our group has had a particular interest in the bisthioxanthylidene scaffold (see also Chapters 3 and 4 of this thesis).[15–17] As a previously developed example in this line of research, biscrownether bisthioxanthylidene **1** (Figure 1) has been developed, combining an overcrowded alkene with coordinating crown ether groups.[18] The core overcrowded alkene switch was functionalised with crown ethers of different sizes and the complexation with sodium and potassium ions was studied. Furthermore, the folded structure of the molecule dictates the helicity of the crown ethers, which could be resolved as stable enantiomers.

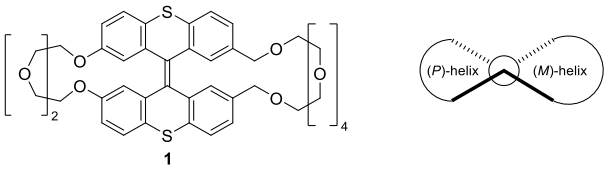

Figure 1. Bisthioxanthylidene biscrown ether.[18]

A landmark example of a mechanically interlocked catenane molecular switch, using Cu-coordination chemistry was developed by Sauvage and co-workers (Figure 2).[19] The Cu-redox chemistry dictates the orientation of the interlocked rings. The Cu^{I} species prefers a four-coordinated complex with two Bpy (2,2'-bipyridyl) motifs (top left), whereas the oxidised Cu^{II} species prefers the five-coordinated complex with one Bpy and one Terpy (2,2':6',2''-terpyridine) ligand (bottom right).

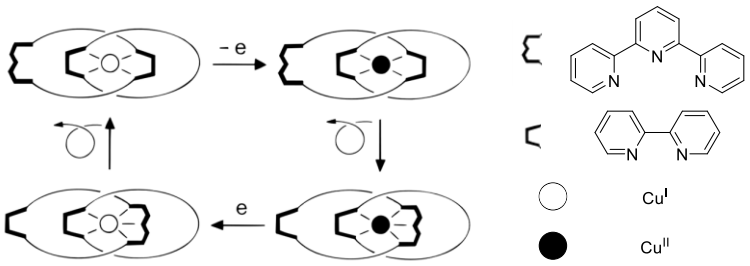

Figure 2. Schematic overview of the Cu^{I}/Cu^{II}, Bpy/Terpy catenane switch. Figure adapted with permission from Ref 19, copyright ACS.

Rotary molecular motion around an axis has been investigated to operate with light (see Chapter 1 of this thesis), electric potential (see Chapter 2 of this thesis) and by chemical reactions.[20,21] One example of a chemically driven motor uses selective orthogonal deprotection and lactone formation to drive unidirectional rotational motion around a biaryl axis (Scheme 1a).[20] Starting from **2a**, lactone ring opening and allyl protection (step A) leads to enantiomerically stable **2b**. The key step for the lactone ring opening is the initial asymmetric reduction using (*S*)-2-methyl-CBS-oxazaborolidine forming a phenol and an alcohol, followed by allylation of the phenol and oxidation of the intermediate primary alcohol. PMB deprotection and lactone formation (step B) leads to the effectively 180° rotated upper aryl ring in **2c**. Lactone hydrolysis and PMB protection (step C), followed by allyl deprotection and lactone formation (step D) finishes the full rotation around the biaryl axis. Another example of chemically driven, rotary motion utilises palladium coordination chemistry (Scheme 1b).[21] Here a number of chiral Pd-species can be specifically addressed by selective CH activation (step A) and oxidative insertion (step D). The energetically preferred stereoisomers of the Pd-species (steps B and E) provide a directional driving force to the molecule. Such chemically driven motors show that by using a specific selected sequence of events it is possible to drive motion clockwise or counter clockwise at the molecular scale.

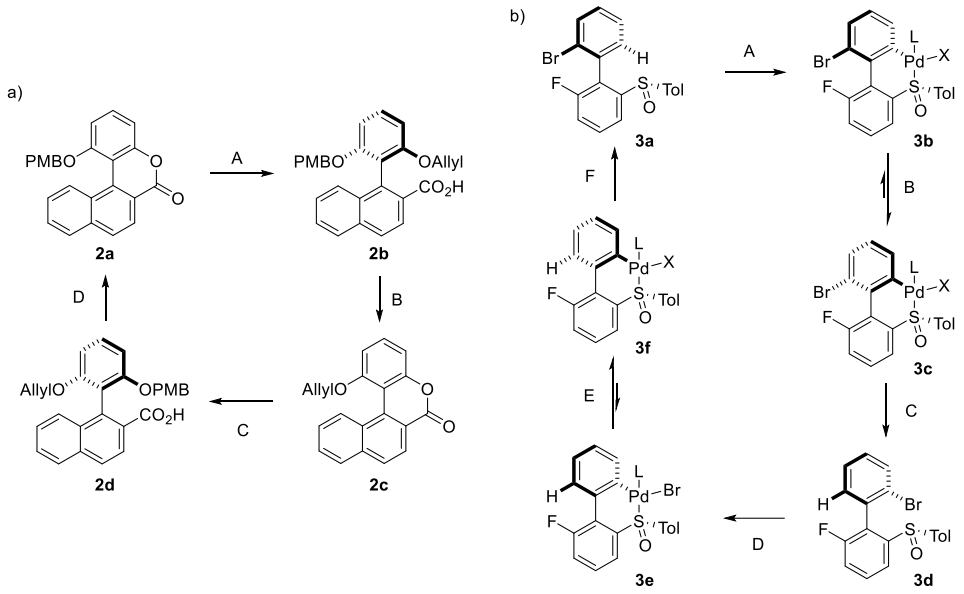

Scheme 1. Chemically driven molecular motors.

To further develop the chemistry of our bisthioxanthylidene redox switches, we envisioned the use of metal-coordinating ligands, linked to a bisthioxanthylidene core (Scheme 2) to modulate the behaviour of the switch. This configuration could provide directed switching between the *E*- and *Z*-isomers. In the proposed design presented here, the redox switching of the non-coordinated bisthioxanthylidenes (***Z*-4**, $\mathbf{4}^{2+}$ and ***E*-4**) has no preference for either ***E*-4** or ***Z*-4**, with free rotation in the dicationic $\mathbf{4}^{2+}$. Complexation of a metal could provide a bias for ***Z*-4[M]** over ***E*-4[M]** by a preference for a *Z*-twisted dicationic complex $\mathbf{4}^{2+}$**[M]**. Consequently, the reduction of $\mathbf{4}^{2+}$**[M]** would result in a *Z*-enriched mixture. In order to demonstrate the proposed electrochemical switching, the *E*- and *Z*-isomers need to be clearly distinguishable and a reversible metal complexation needs to be developed. Important to note it the potential formation of supramolecular oligomers, especially for the *E*-isomers. As a 1:1 monomeric complex with metals is unlikely with short linkers, there is a possibility for the formation of 1:1 dimeric complexes or oligomers. The formation of supramolecular oligomers is dependent on the concentration and the binding properties of the ligands to the metals.[22] With the introduction of chiral elements in the core or the metal-ligand coordination, unidirectional electrochemically driven rotary motion might be feasible.

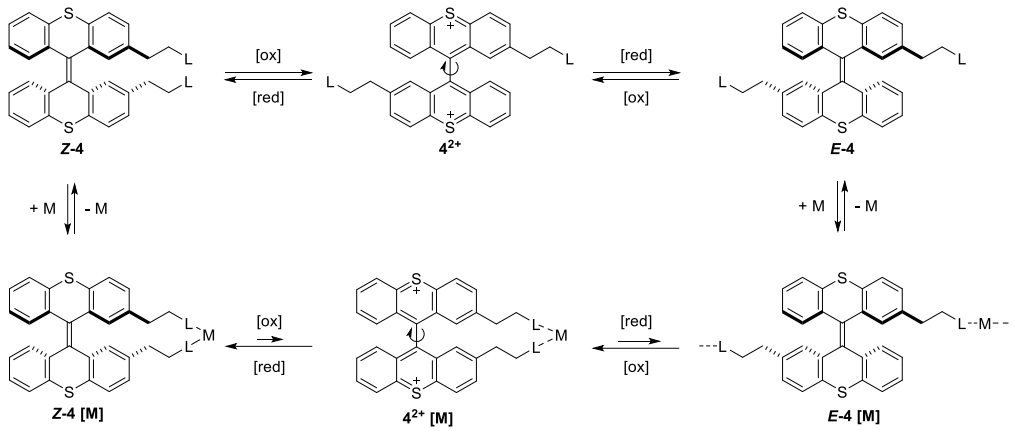

Scheme 2. Schematic switching diagram of a ligand-functionalised bisthioxanthylidene.

The interaction of the functionalised switches does not necessarily have to be limited to the pyridine-metal interactions discussed in this chapter, but could be further developed using other interactions. Many potential non-covalent interactions could be investigated inspired by the different interactions studied in the field of coordination chemistry, such as phenanthroline or phosphorus ligands, crown ethers, sulfide bridges, hydrogen bonds or Coulombic interactions.

Aside from the potential for influencing the direction of redox switching, the ligands can be used as handles to influence the properties of these switches, as bisthioxanthylidenes themselves have interesting electrochemical and luminescence switching properties.[16,23] Vice versa, the bisthioxanthylidene switch can be used to influence the properties of a metal complex, via either electrochemical or photochemical stimuli.

In the present study we developed prototype switches in order to investigate the mutual influence of two redox- and photoactive functional motifs of a ligand-functionalised bisthioxanthylidene system. We envisioned to find a suitable switch-linker-ligand combination with metal complexation that can be used to modify the previously developed redox behaviour, which is an important first step towards control over electrochemically driven molecular motion.

2. Results & Discussion

2.1 Computational chemistry

The initial design of our functionalised bisthioxanthylidene switches features a common bisthioxanthylidene core, alkyl linkers and pyridyl ligands (Scheme 2, Figure 3). Terpy and Bpy were chosen as common, strong binding, metal coordinating ligands.[24,25] To aid with a specific target design, the influence of the linker length on the bisthioxanthylidene core geometry was investigated by DFT calculations. For the non-exhaustive computational study Bpy-ligands and Zn^{2+} metal centres were used. The calculations were performed with B3LYP/6-31G** level of theory for the organic parts of the molecule, using an effective core potential with a LanL2DZ basis set for the Zn centre.

From the computational studies on the neutral switches with linker lengths of two, three, four or five methylene units (Figure 3) we can observe that the Bpy ligands can coordinate to a metal centre without distorted geometries and with Zn–N distances of 2.06 – 2.07 Å (Figure 3). In contrast, the linker length has an observed effect on the geometry of the bisthioxanthylidene parts. In the case of a linker length of three, four or five methylene units (Figure 3b, c and d, respectively) the angle from the folding of the halves (A1 and A2) is in the range of 66 – 70°. However, the switch with a linker length of two methylene units has an A1 angle of 85°, indicating that the geometry of the switch is significantly influenced by the proximity of the Bpy-metal complex.

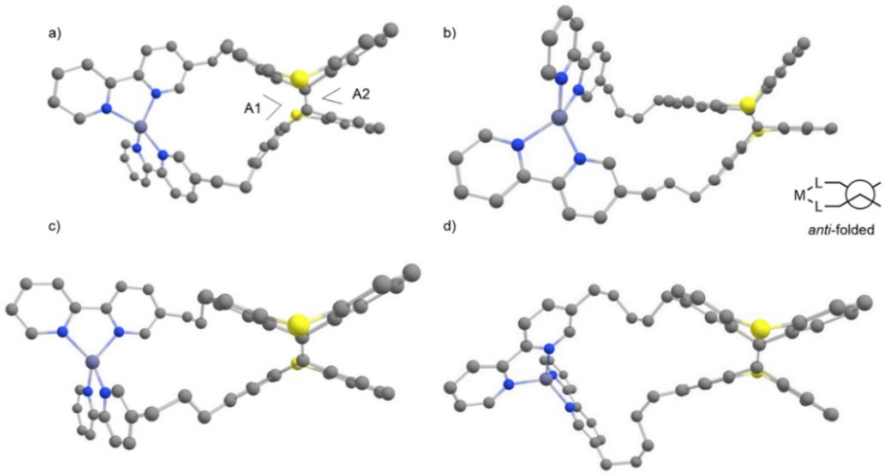

Figure 3. Optimised geometries of bisthioxanthylidenes with methylene linkers and Bpy ligands coordinated to a Zn^{2+} centre (B3LYP/6-31G**, ECP LanL2DZ for Zn). Methylene linker sizes of: a) 2 units, b) 3 units, c) 4 units, d), 5 units. Hydrogens omitted for clarity.

For the all of the investigated oxidised switches with a dicationic bisthioxanthylidene core, the linker length does not significantly influence the geometry of the Bpy-metal complex (Figure 4). The Zn–N distances are in the range of 2.07 – 2.09 Å and the dihedral angles for the switch (θ1 and θ2) are in the range of 76 – 85°. This indicates that there is a deviation from the commonly found orthogonal state of bisthioxanthylidene dications (for more detailed information, see Chapter 3 of this thesis) towards a twisted geometry with smaller dihedral angles. The relatively wide range of dihedral angles is caused by the facile flexibility due to partial rotation around the central axis. Nevertheless, there is a bias for more acute angles towards the linked ligands.

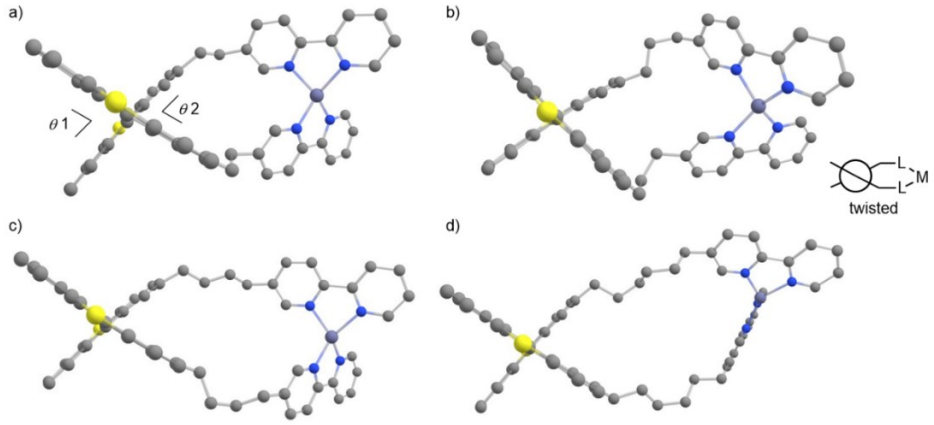

Figure 4. Optimised geometries of the dicationic state of bisthioxanthylidenes with methylene linkers and Bpy ligands coordinated to a Zn^{2+} centre (B3LYP/6-31G**, ECP LanL2DZ for Zn). Methylene linker sizes of: a) 2 units, b) 3 units, c) 4 units, d), 5 units. Hydrogen atoms omitted for clarity.

As a result of these computational investigations, we found that linker lengths of three methylene units or more provides sufficient flexibility so that the metal-coordination site and the redox-switching site do not lead to major distortion of the respective geometries. A linker length of three methylene units would ensure that only the *Z*-bisthioxanthylidene can form a monomeric complex, while avoiding steric distortion.

2.2 Synthesis

The DFT calculations indicated that a linker between the electrochemically switchable bisthioxanthylidene core and the metal coordinating ligands of three methylene units would be a good target. This linker length of three methylene units could be accessible by allylation and subsequently

utilisation of the terminal olefin in a cross-coupling reaction or other olefin functionalisation.

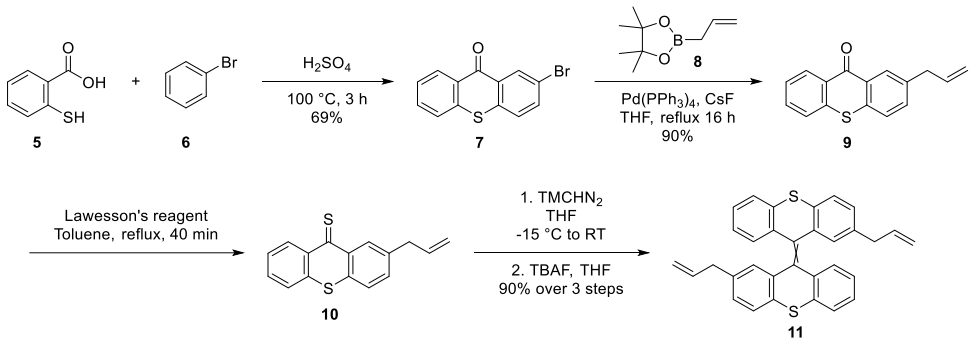

5 6 7 9 10 11

Scheme 3. Synthesis of the bisallyl-functionalised bisthioxanthylidene core.

The core is synthesised in a similar method to other bisthioxanthylidenes discussed in Chapter 3 of this thesis. 2-Bromo-thioxanthone (**7**) was prepared by reaction of thiosalicylic acid (**5**) and bromobenzene (**6**) in sulfuric acid in 69% yield (Scheme 1). Bromide **7** can be converted into a bisthioxanthylidene (see Chapter 3). However, in the current route towards **11**, it was chosen to perform the allylation at an early stage. This allylation was performed by Suzuki cross-coupling with commercially available allyl boronic acid pinacol ester **8** and the allylated ketone **9** was obtained in excellent yield. Ketone **9** was subsequently thionated with Lawesson's reagent, thioketone **10** was purified by flash column chromatography and immediately used in the following step. This dimerisation procedure provides a clean method towards bisthioxanthylidenes and was highly successful in the case of bis-allyl bisthioxanthylidene **11** with 90% yield over the final three steps.

The required target ligand for Bpy-functionalisation could be synthesised via a Stille coupling using 2,5-dibromo pyridine (**12**) and 2-stannyl pyridine **13** (Scheme 4) and Bpy-bromide **14** was obtained in a good yield.[26]

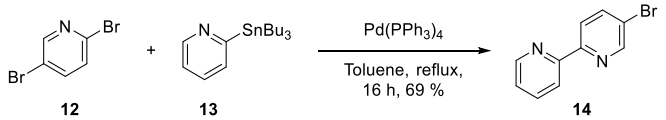

12 13 14

Scheme 4. Synthesis of the target Bpy-bromide.

The required target for Terpy-functionalisation requires a few more steps. Firstly, 2,6-dibromo pyridine (**15**) was used in a Stille coupling to form Bpy-bromide **16**. For the next cross-coupling, **12** was metalated by slow addition of *n*-BuLi in toluene. Solvent polarity has a strong effect on the

directing capabilities of the pyridine nitrogen atom[27] and an apolar solvent is required to obtain the desired **17** preferentially. However, the optimal outcome of the reaction was a 3:1 ratio of **17** and **18**. Slower *n*-BuLi addition times up to 45 min did not improve the obtained product ratio. Furthermore, modifying the reaction via an organomagnesium species using *i*-PrMgCl, which had the potential to show better directing properties, did not improve the ratio of **17**:**18**. As separation attempts of **17** and **18** were unsuccessful, the synthesis was continued using a mixture of regioisomers.

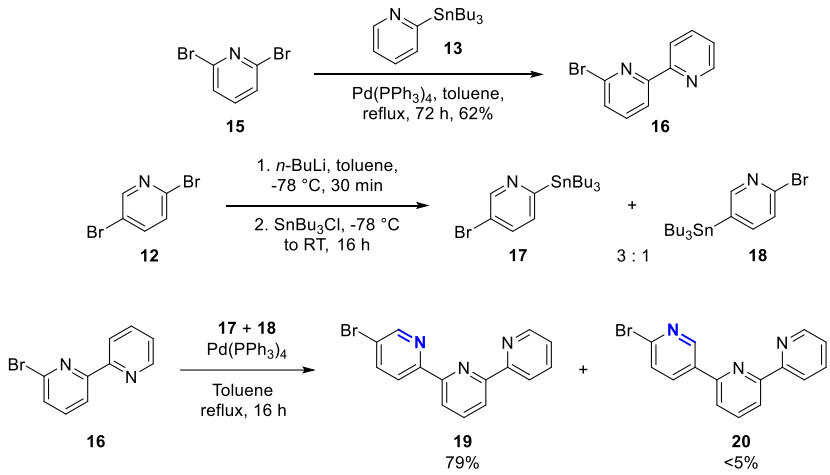

Scheme 5. Synthesis of target Terpy-bromide **19**.

With this mixture of **17** and **18**, there is a possibility to form regioisomeric products **19** and **20** in the subsequent coupling, with the only difference being the position of a pyridine nitrogen atom (highlighted in blue, Scheme 5). We observed that only one major product was obtained after the reaction. Distinguishing which of the regioisomeric products **19** and **20** is formed, is most easily done by ^{13}C NMR spectroscopy (Figure 4), focussing on the *C*Br signal. By simulation of the ^{13}C NMR spectra,[28] the chemical shift of the *C*Br for **19** is estimated to be 121.3 ppm, where for **20** the *C*Br signal is estimated to be 140.2 ppm. Most of the other simulated signals are in close proximity and would therefore be less practical for distinguishing these molecules. Indeed, from the experimental ^{13}C NMR spectrum of the major product, we observe a quaternary signal at 121.3 ppm assigned to the indicated *C*Br atom, whereas no quaternary carbon signal is observed in the 140 ppm region. The lack of any significant amount of the formation of **20** suggests that the Stille coupling between **16** and **18**, compared to the Stille coupling between **16** and **17**, is much slower or more unlikely to occur under these reaction conditions.

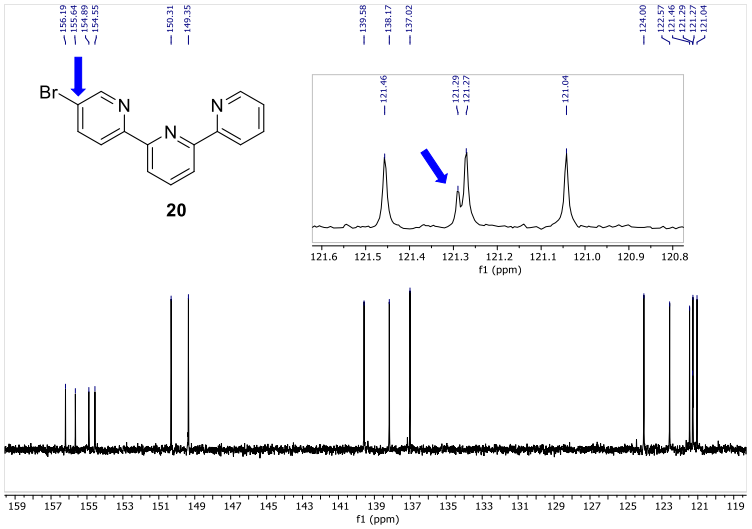

Figure 4. ^{13}C NMR (151 MHz, $CDCl_3$) of **20**. The blue arrow indicates the *C*Br signal.

With the target bisthioxanthylidene and ligands in hand, the next step in the synthesis was the functionalisation of the core with the prepared ligands. Initial attempts to functionalise a thioxanthone at an earlier stage in the synthesis had proven to be unsuccessful (Scheme 6). 9-Borabicyclo[3.3.1]nonane (9-BBN) was used for the hydroboration of the terminal olefin functionality of **9**, as a commonly used borane source for the coupling of primary alkyl-sp^3 moieties with aryl halides.[29] Unfortunately, this coupling did not show any conversion to the desired product **21**. TLC analysis showed full conversion of starting material **9**, indicating that reaction other than the required reaction occurs, either from the starting material or any of the formed intermediates.

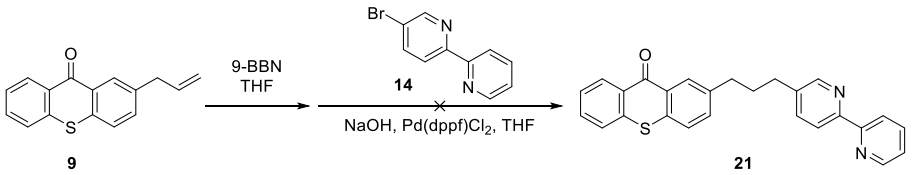

Scheme 6. Unsuccessful functionalisation of ketone **2** with 5-bromo-2,2'-bipyridine.

The synthesis of the target compounds was successfully achieved by cross-coupling of a bis-borylated bisthioxanthylidene, generated *in situ* from bis-allyl **11**. Again, 9-BBN was chosen for hydroboration of the terminal olefin motifs, followed by Suzuki cross-coupling. An excess of 9-BBN as THF solution at room temperature was found to be the optimal condition for coupling. The progress of this reaction was carefully followed by TLC

analysis as it was found that extended reaction times for the hydroboration led to the formation of unwanted side products.

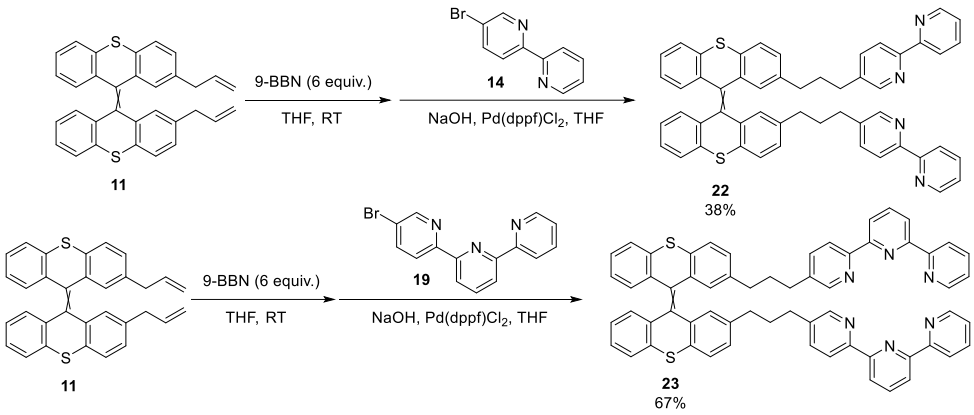

Scheme 7. Ligand functionalisation of bisthioxanthylidene **11** via Suzuki cross-coupling.

With these conditions, the targets **22** and **23** could be synthesised in 38 and 67% yield, respectively, and were characterised by NMR spectroscopy and high resolution mass spectrometry. For these targets it is important to note that careful handling is advised. Contact with metals that can coordinate to the ligands should be avoided and the transfer of solids was done using glass instruments. Purification was performed by flash column chromatography with basic silica and alumina and solvents were prepared by filtration over basic alumina. The *E*- and *Z*-isomers of **22** and **23** were not distinguishable by UV-vis or ^{1}H-NMR spectroscopy and the switches were obtained in an unknown ratio of stereoisomers.

2.3 Electrochemistry

With the target compounds in hand, the first step was to investigate the influence of the ligands on the electrochemical switching of the bisthioxanthylidene core. From cyclic voltammetry of Bpy-functionalised compound **22** (Figure 5) we observe that the common response for bisthioxanthylidenes (see also Chapter 3 of this thesis) is present without much deviation. An oxidation wave is observed at $E_{p,a}$ = 1.31 V vs. SCE without corresponding reduction and a reduction wave is observed at $E_{p,c}$ = 0.32 V vs. SCE. For comparison, 2,2'-dimethyl-bisthioxanthylidene has peak currents of $E_{p,a}$ = 1.22 and $E_{p,c}$ = 0.34 V vs. SCE.[15] The significant hysteresis between the oxidation and reduction (0.99 V) is larger, partially due to a higher scan speed, but is still comparable to other substituted bisthioxanthylidenes.[15]

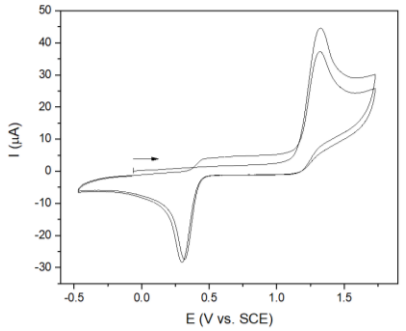

Figure 5. Cyclic voltammogram of Bpy-functionalised bisthioxanthylidene **22** (1.0 mM), CH_2Cl_2, $TBAPF_6$ (0.1 M), 100 mV s^{-1}, diffusion limited conditions.

Cyclic voltammetry of Terpy-functionalised bisthioxanthylidene **23** shows a similar picture (Figure 6). In CH_2Cl_2, under diffusion limited conditions, an oxidation is observed at $E_{p,a}$ = 1.26 V vs. SCE and the corresponding reduction is observed at $E_{p,c}$ = 0.40 V vs. SCE. This provides a hysteresis of 0.86 V, again similar to other substituted bisthioxanthylidenes. From the CVs of **22** and **23** it shows that the functionalisation of the electrochemically switchable core with pyridyl-ligands with alkyl linkers does not interfere with the redox processes commonly found with bisthioxanthylidenes.[15–17]

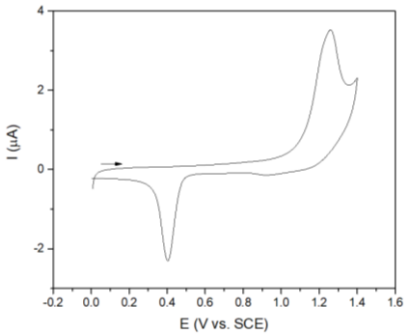

Figure 6. Cyclic voltammogram of Terpy-functionalised bisthioxanthylidene **23** (~0.5 mM), CH_2Cl_2 (filtered over basic alumina), $TBAPF_6$ (0.1 M), diffusion limited conditions, 10 mV s^{-1}.

2.4 Metal complexes

For further analysis of the pyridyl-ligand functionalised bisthioxanthylidenes, metal complexes of the Terpy-functionalised switch **23** with either Zn or Fe (Scheme 8) were analysed by absorption and fluorescence spectroscopy as well as cyclic voltammetry.

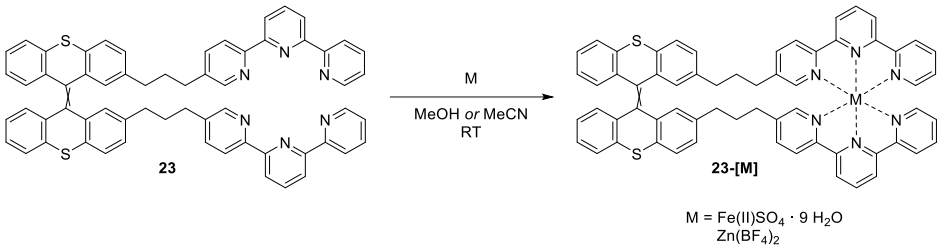

Scheme 8. Metal complexations of **23** to **23-[Fe^{II}]** and **23-[Zn^{II}]**.

By UV-vis spectroscopy we observed, as expected, the spectrum of **23** to be a straightforward combination of the absorption spectra of a bisthioxanthylidene[16] and a Terpy ligand (see section 4.3) with the highest absorption tailing towards 380 nm. Upon incremental addition of $Zn^{II}(BF_4)_2$ we see a decreasing band centred around 280 nm and two increasing bands at 326 nm and 340 nm (Figure 7). These two increased absorption bands at 326 nm and 340 nm are typical for the absorption of a Zn^{II}-$Terpy_2$ complex (see Section 4.3). Upon zinc addition, an isosbestic point can be observed until the ratio approaches 1:1, where a small deviation can be observed to higher wavelengths.

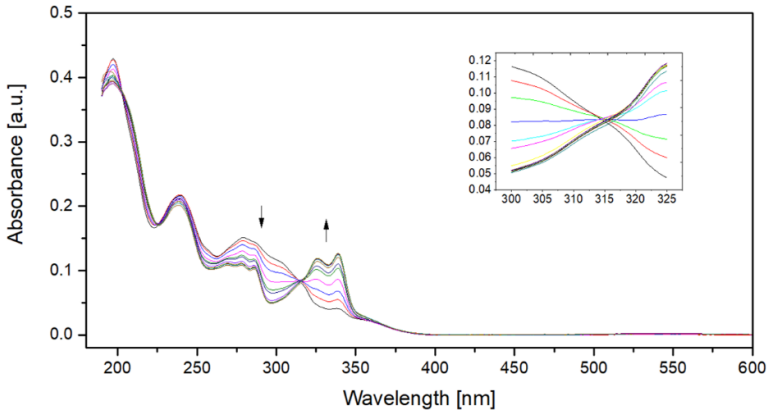

Figure 7. UV-vis absorption spectra of **23** ($2.4 \cdot 10^{-6}$ M in MeCN) with increasing amounts of $Zn^{II}(BF_4)_2$ in MeCN to **23-[Zn^{II}]**.

The addition of $Fe^{II}SO_4$ to **23** in MeOH (Figure 8) shows decreasing bands at 238 and 281 nm and increasing bands at 324 and 552 nm. The 552 nm band is a typical absorption band observed for Fe-Terpy complexes (see Section 4.3) and at sufficient concentrations, the solution turns noticeably purple. The addition of Fe^{II} to the switch shows a clear isosbestic point (see inset).

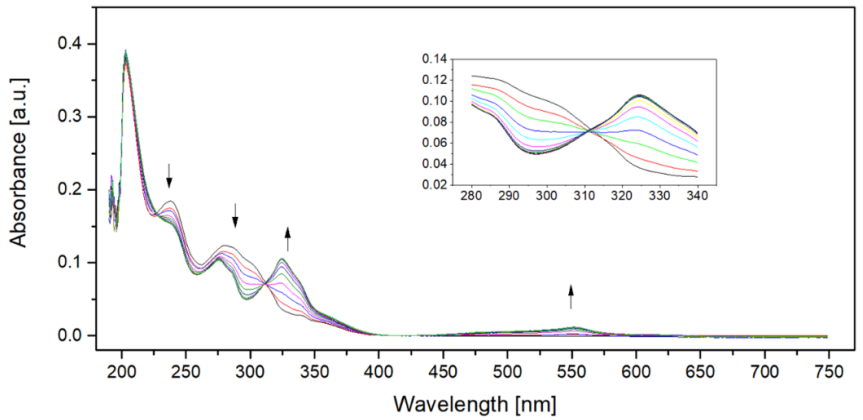

Figure 8. UV-vis absorption spectra of **23** ($2.4 \cdot 10^{-6}$ M in MeOH) with increasing amounts of $Fe^{II}SO_4$ in MeOH to **23-[Fe^{II}]**.

From the absorption spectroscopy experiments we can see that the complexation of the switch with metals is fast and shows the expected shifts for the formation of Terpy-M complexes. The complexation appears to be mostly a single process, suggesting that, at these concentrations, reactions such as supramolecular oligomerisation do not occur to a large degree. The formation of a 1:1 dimeric complex cannot be excluded from this data.

The formation of Fe complexes with our fluorescent bisthioxanthylidene core[16] prompted us to investigate the fluorescence quenching within **23-[Fe^{II}]**. Indeed, when we add $Fe^{II}SO_4$ to a solution of switch **23** ($1.2 \cdot 10^{-6}$ M in MeOH) we observe that the typical blue fluorescence of a bisthioxanthylidene is quenched. This shows that the formed iron-Terpy complex quenches the excited state energy of the bisthioxanthylidene in a non-radiative fashion. The alkyl linkers prevent conjugation between the bisthioxanthylidene and the metal complex. Therefore, the mechanism of quenching is likely a proximity based energy-transfer process.[30,31]

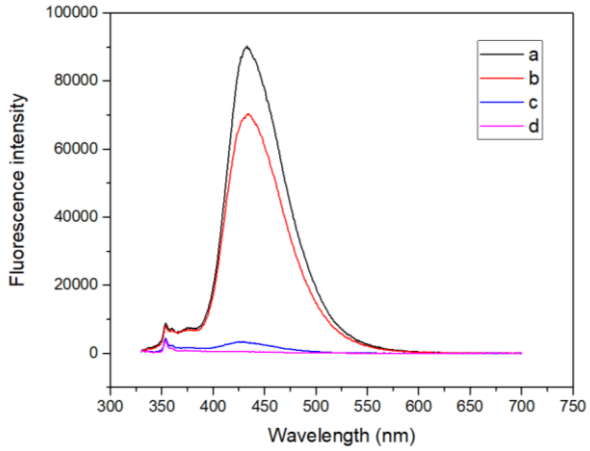

Figure 9. Emission spectra at $\lambda_{ex.}$ = 320 nm of: a) **23** ($1.2 \cdot 10^{-6}$ M) in MeOH; b) After addition of 0.5 equiv. $Fe^{II}SO_4 \cdot 9\ H_2O$ in MeOH; c) after addition of 4.5 equiv. $Fe^{II}SO_4 \cdot 9\ H_2O$ in MeOH; d) After addition of 10 equiv. $Fe^{II}SO_4 \cdot 9\ H_2O$ in MeOH.

In addition to the optical studies into the switch-metal complexes we performed electrochemical experiments using cyclic voltammetry of the Terpy-functionalised switch **23** and the formation of Zinc and Iron complexes. Figure 10a shows the cyclic voltammogram of switch **23** in MeCN with peak potentials at $E_{p,a}$ = 1.25 V vs. SCE and $E_{p,c}$ = 0.35 V vs. SCE. By addition of $Zn(BF_4)_2$ the zinc-complex is formed. However, there is no major change to the CV, the same waves are observed, albeit at a reduced intensity.

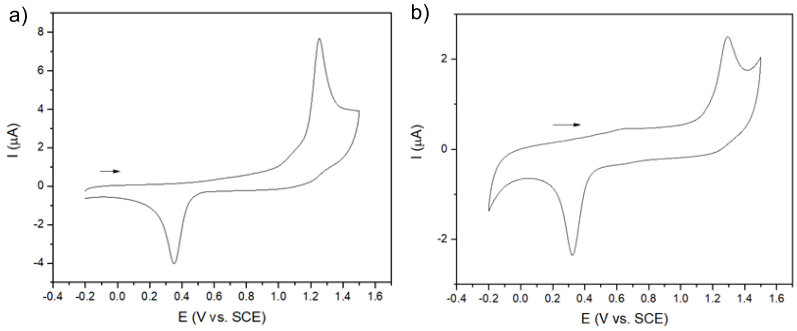

Figure 10. CV in MeCN, $TBAPF_6$, diffusion limited, at scan speed 20 mV s^{-1} of: a) **23**; b) **23-[Zn^{II}]**.

From cyclic voltammetry of the iron complex of **23** (Figure 11) we observe a much stronger effect of metal complexes, where four major waves are observed in the first cycle. The first wave (A) at 1.14 V vs. SCE is the $Fe^{II} \rightarrow Fe^{III}$ oxidation of a hexacoordinate Terpy-Fe species.[32] The second wave (B) at 1.33 V vs. SCE corresponds to the oxidation of the folded, core bisthioxanthylidene to its dicationic state. In the reverse sweep, no

reduction wave of the folded dicationic bisthioxanthylidene core is observed, as it is expected to have undergone the commonly observed transformation towards the orthogonal state. The first observed reduction (C) at 1.06 V vs. SCE is the reduction of the iron redox couple ($Fe^{III} \rightarrow Fe^{II}$)[32] related to wave A. At 0.30 V vs. SCE the reduction of the orthogonal bisthioxanthylidene motif can be observed (D). This concludes the first cycle, which appears to be a combination of the expected redox events for both the bisthioxanthylidene core and the Terpy-Fe complex separately. However, in the second cycle a new oxidation (E) is observed at 1.07 V vs. SCE, which partially overlaps with the iron oxidation (F). In combination with the decrease of B it is likely that E corresponds to the oxidation of the bisthioxanthylidene core motif of a newly formed species. The third cycle does not deviate strongly from the second, where only a slight increase of E and slight decrease of B is observed, as the previously oxidised species is mostly converted towards the newly formed species.

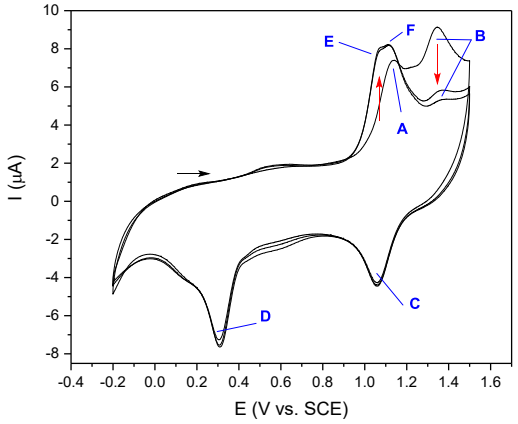

Figure 11. CV of **23-[Fe^{II}]** in MeCN, $TBAPF_6$, diffusion limited, 100 mV s^{-1}. The red arrows indicate the increase or decrease of the indicated wave with subsequent sweeps.

A possible explanation for the newly found electrochemical switching is the formation of a new geometrical shape. However, further in-depth experiments would be necessary to prove the geometry of the observed species, for example, spectroelectrochemical measurements or the isolation and characterisation of intermediates isolated after bulk electrochemical experiments. A proposed explanation for the observed electrochemistry is presented here.

Before metal complexation, there is a mixture of the *E*- and *Z*-isomers of switch **23** in an unknown ratio. Upon complexation at UV-vis concentrations (Figure 8) we did not observe the formation of multiple distinct species.

From CV we also do not observe any different species in the first cycle, nor do we observe separate oxidations, originating from a difference between ***E*-23-[Fe]** and ***Z*-23-[Fe]**.

Taking the *Z*-bisthioxanthylidene Fe^{II} complex as a starting point (Figure 12, **I**), the first oxidation (A) would lead to an Fe^{III} species (**II**). The subsequent bisthioxanthylidene oxidation would lead to the short lived, folded **III**, which is expected to rapidly form the most stable geometry for bisthioxanthylidenes in species **IV**, which finishes the first oxidative scan.

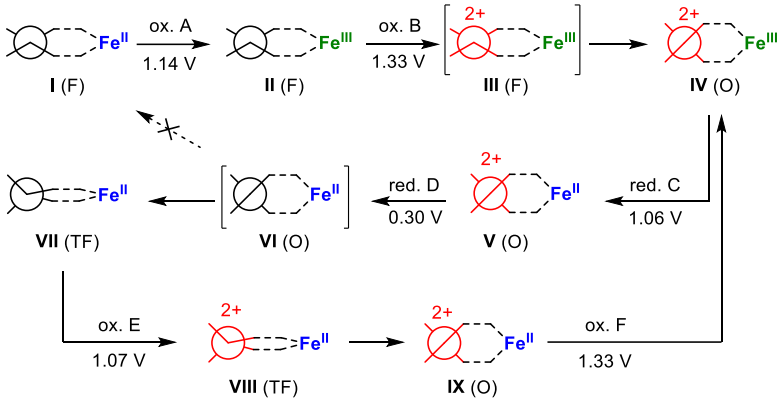

Figure 12. Schematic overview of the proposed switching mechanism observed for **23-[Fe]**. The geometrical state of the bisthioxanthylidene part is indicated in parentheses (F = folded, O = orthogonal, TF = twist-fold). Colour indications: black = neutral bisthioxanthylidene, red = dicationic bisthioxanthylidene, blue = Fe^{II}, green = Fe^{III}.

The first encountered reduction (C) leads to an Fe^{II} species, without reduction of the more stable, orthogonal dicationic bisthioxanthylidene (**V**). Reduction of the core (D) leads initially to the unfavourably oriented **VI**. Here the formed Fe-Terpy complex is likely of influence to the folding and relative stability of the geometries of the bisthioxanthylidene part. In other bisthioxanthylidene redox switches, a species such as **VI** would rapidly reorient towards the most stable folded structure. This commonly is the *anti*-folded structure, meaning for **23-[Fe]** the formation of structure **I**. However, from the decrease of oxidation B, originating from this folded structure we can deduce that this does not occur. Instead, the formation of a previously unknown species takes place, which we hypothesise is a twist-folded state (**VII**). The small wave observed in the second oxidation sweep around 0.55 V vs. SCE could be attributed to the formation of a small amount of the twisted form. The oxidation of this new twist-folded state (1.07 V vs. SCE) occurs at an intermediate potential between the oxidation of the twisted (0.55 V vs. SCE) and the folded state (1.33 V vs. SCE). Subsequently, the oxidation of the Fe^{II}-Terpy complex occurs (F) at a similar to the initial

Fe^{II}-Terpy oxidation (B), resulting in the previously mentioned species **IV**, which is confirmed by the observed reduction in the second reduction sweep.

From cyclic voltammetry we can conclude that the formation of the Zn complex does not have a significant influence on the geometrical redox switching of bisthioxanthylidenes. The formation of the Fe complex has a stronger influence and a novel species can be observed. The strong influence of Fe compared to Zn probably involves the stronger binding of Fe to Terpy.[33,34] The binding of Zn might be too dynamic to have a significant influence in a similar manner to Fe. The formation of the Fe complex likely prevents the reorientation of the orthogonal state towards the *anti*-folded state.

3. Conclusions & Outlook

Two bisthioxanthylidene redox switches have been developed with alkyl linkers and Bpy and Terpy ligands. The typical redox properties of these switches are not inhibited by the presence of these ligands. Metal complexes with Zn and Fe show that the Fe complexes of the Terpy-functionalised switch shows fluorescence quenching and a novel pathway in the redox switching. Hereby a new geometric shape, most likely a twist-fold state, is involved after the first redox cycle.

We can conclude that the formation of metal complexes can change the redox switching. However, in order to control the directionality of this switching, we require the ability to distinguish the various proposed isomers. A desymmetrisation of the switch could provide a handle to distinguish *E*- and *Z*-isomers. Extensive spectroelectrochemical measurements or the isolation of intermediates could shed more light on the intriguing switching process. Nevertheless, this study demonstrates the possibility of influencing the conformational switching of a redox switch by an external complexation event.

4. Experimental

4.1 General comments

For general information on chemicals, NMR spectroscopy, high-resolution mass spectrometry, cyclic voltammetry and DFT calculations, see Chapter 2.

4.2 Synthesis and characterisation of compounds

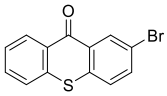

2-bromo-9H-thioxanthen-9-one (**7**). Thiosalicylic acid (**5**, 2.0 g, 13 mmol, 1.0 equiv.) and bromobenzene (**6**, 5.3 mL, 50 mmol, 3.8 equiv.) were added to 20 mL conc. H_2SO_4 and the mixture was stirred at 100 °C for 3 h. After allowing the reaction mixture cool down to room temperature, it was carefully poured onto an ice/water mixture. The mixture was filtered and the residue washed with water. The product was purified by hot filtration using THF with the product present in the filtrate. The product was obtained as a yellow solid in 69% yield (2.62 g, 9.0 mmol). ^{1}H NMR (400 MHz, $CDCl_3$) δ 8.73 (d, *J* = 2.2 Hz, 1H), 8.60 (dd, *J* = 8.2, 1.5 Hz, 1H), 7.70 (dd, *J* = 8.6, 2.2 Hz, 1H), 7.64 (ddd, *J* = 8.3, 7.0, 1.5 Hz, 1H), 7.57 (dd, *J* = 8.1, 1.4 Hz, 1H), 7.50 (ddd, *J* = 8.2, 7.0, 1.3 Hz, 1H), 7.45 (d, *J* = 8.6 Hz, 1H). ^{13}C NMR (101 MHz, $CDCl_3$) δ 178.9, 137.0, 136.2, 135.4, 132.7, 132.6, 130.6, 130.2, 129.0, 127.7, 126.8, 126.2, 120.4. Compound data in accordance with literature.[35]

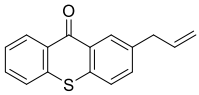

2-allyl-9H-thioxanthen-9-one (**9**). 2-Bromo-9H-thioxanthen-9-one (**7**, 300 mg, 1.03 mmol, 1.0 equiv.), $Pd(PPh_3)_4$ (84 mg, 0.07 mmol, 0.07 equiv.) and CsF (620 mg, 4.08 mmol, 4.0 equiv.) were dissolved in dry THF (16 mL, 0.07 M). Allylboronic acid pinacol ester (**8**, 0.30 mL, 1.55 mmol, 1.5 equiv.) was added and the mixture was heated at reflux for 16 h. Water was added and the product was extracted with CH_2Cl_2, the combined organic phase was washed with brine and dried over $MgSO_4$. The product was purified by flash column chromatography (silica, EtOAc/*n*-pentane, 5%) and obtained as a pale-yellow solid in 90% yield (235 mg, 0.93 mmol). ^{1}H NMR (400 MHz, $CDCl_3$) δ 8.60 (dd, *J* = 8.1, 1.5 Hz, 1H), 8.43 (d, *J* = 2.0 Hz, 1H), 7.62 – 7.51 (m, 2H), 7.51 – 7.40 (m, 3H), 6.04 – 5.94 (m, 1H), 5.16 – 5.10 (m, 2H), 3.51 (d, *J* = 6.8 Hz, 2H). ^{13}C NMR (101 MHz, $CDCl_3$) δ 180.0, 138.7, 137.4, 136.6, 135.0, 133.2, 132.2, 130.0, 129.5, 129.3, 129.3, 126.3, 126.2, 126.1, 116.8, 39.9. HRMS (ESI Pos): for $[C_{16}H_{13}OS]^+$ calcd. m/z = 253.0682, found 253.0680.

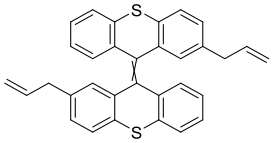

2,2'-diallyl-bisthioxanthylidene (**11**). Thioketone preparation: 2-allyl-9H-thioxanthene-9-one (**9**, 428 mg, 1.7 mmol, 1.0 equiv.) was dissolved in toluene (17 mL, 0.1 M) and Lawesson's reagent (727 mg, 1.78 mmol, 1.05 equiv.) was added to the mixture, which was subsequently heated at reflux for 45 min. The mixture was allowed to cool down to room temperature and thioketone **10** was purified by flash column chromatography (silica, CH_2Cl_2/*n*-pentane, 10%).

Dimerisation: The freshly prepared thioketone (**10**) was dissolved in dry THF (17 mL) and divided into two equal portions. One portion was cooled to -15 °C and $TMSCHN_2$ (0.47 mL, 2.0 M in Et_2O, 0.94 mmol, 0.55 equiv.) was added. Immediately after addition, the mixture was allowed to warm up to room temperature. After full conversion of the thioketone, the remaining portion of 2-allyl-9H-thioxanthene-9-thione was added and the mixture was stirred at room temperature for 10 min. Tetrabutylammonium fluoride (1.7 mL, 1.0 M in THF, 1.7 mmol, 1.0 equiv.) was added to the mixture, followed by stirring at room temperature for 5 min. Volatiles were removed under reduced pressure and the product was purified by flash column chromatography (silica, CH_2Cl_2/*n*-pentane, 8%). The product was obtained as an *E*/*Z*-mixture in an unknown ratio, as an off-white solid in 90% yield over 2 steps (364 mg, 0.77 mmol). ^{1}H NMR (600 MHz, $CDCl_3$) δ 7.53 (ddd, *J* = 7.9, 2.8, 1.2 Hz, 2H), 7.45 (d, *J* = 8.0 Hz, 2H), 7.14 – 7.10 (m, 2H), 6.99 – 6.94 (m, 2H), 6.91 – 6.87 (m, 2H), 6.83 – 6.78 (m, 2H), 6.62 (dd, *J* = 6.1, 1.9 Hz, 2H), 5.63 – 5.52 (m, 2H), 4.91 – 4.83 (m, 4H), 3.10 – 2.96 (m, 4H). ^{13}C NMR (151 MHz, $CDCl_3$) δ 140.0, 137.9, 136.9, 136.9, 136.1, 136.1, 136.1, 136.0, 135.9, 135.8, 133.6, 133.6, 133.1, 133.1, 130.2, 130.1, 129.9, 129.9, 127.3, 127.2, 127.2, 127.2, 127.1, 127.0, 126.8, 126.7, 125.8, 125.8, 116.0, 116.0, 39.8, 39.7. HRMS (APCI Pos): for $[C_{32}H_{25}S_2]^+$, calcd. m/z = 473.1392, found 473.1377.

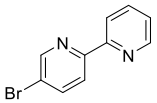

5-bromo-2,2'-bipyridine (**14**). 2-(Tributylstannyl)-pyridine (**13**, 0.88 mL, 2.72 mmol, 1.0 equiv.), 2,5-dibromopyridine (**12**, 711 mg, 3.00 mmol, 1.1 equiv.) and $Pd(PPh_3)_4$ (40 mg, 0.02 mmol, 0.01 equiv.) were dissolved in dry toluene (8 mL). The mixture was degassed by bubbling Ar for 15 min and subsequently heated at reflux for 40 h. After cooling down to room temperature, the mixture was filtered over a glass frit. The product was extracted by 1.0 M HCl (aq) and washed with CH_2Cl_2. $NaHCO_3$ was added to

the aqueous phase until pH > 7 and the product was extracted by CH_2Cl_2. The product was purified by flash column chromatography (silica, EtOAc/*n*-pentane, 15% + 1% NEt_3) and obtained as a white solid in 69% yield (440 mg, 1.87 mmol,). ^{1}H NMR (500 MHz, $CDCl_3$) δ 8.72 (dd, *J* = 2.3, 0.8 Hz, 1H), 8.66 (ddd, *J* = 4.8, 1.8, 0.9 Hz, 1H), 8.36 (ddd, *J* = 8.0, 1.1, 1.1 Hz, 1H), 8.31 (dd, *J* = 8.5, 0.7 Hz, 1H), 7.93 (dd, *J* = 8.5, 2.4 Hz, 1H), 7.81 (ddd, *J* = 7.8, 7.8, 1.8 Hz, 1H), 7.32 (ddd, *J* = 7.6, 4.8, 1.2 Hz, 1H). ^{13}C NMR (126 MHz, $CDCl_3$) δ 155.3, 154.8, 150.3, 149.4, 139.6, 137.1, 124.1, 122.5, 121.3, 121.1. HRMS (ESI Pos): for $[C_{10}H_8BrN_2]^+$ calcd. m/z = 236.9845, found m/z = 236.9840.

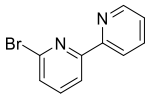

6-bromo-2,2'-bipyridine (**16**). 2,6-Dibromopyridine (**15**, 1255 mg, 5.29 mmol, 1.01 equiv.) and $Pd(PPh_3)_4$ (62 mg, 0.05 mmol, 1.0 mol%) were dissolved in toluene (27 mL, 0.2 M). 2-(tributylstannyl)-pyridine (**13**, 1.68 mL, 5.25 mmol, 1.0 equiv.) was added to the mixture which was subsequently heated at reflux for 72 h. The reaction was allowed to cool to room temperature the product was extracted with 1 M HCl (aq) and the aqueous phase was washed with CH_2Cl_2. The acidic phase was neutralised with $NaHCO_3$ and the product was extracted with CH_2Cl_2. The combined organic phases were dried over Na_2SO_4 and volatiles were removed under reduced pressure. The product was purified by flash column chromatography (silica, MeOH/CH_2Cl_2, 0–5%) and obtained as a white solid in 62% yield (766 mg, 3.26 mmol). ^{1}H NMR (500 MHz, $CDCl_3$) δ 8.66 (ddd, *J* = 4.8, 1.8, 0.9 Hz, 1H), 8.40 (ddd, J = 8.1, 1.1, 1.1 Hz, 1H), 8.38 (dd, *J* = 7.8, 0.9 Hz, 1H), 7.82 (ddd, *J* = 7.8, 7.8, 1.8 Hz, 1H), 7.67 (dd, *J* = 7.8, 7.8 Hz, 1H), 7.49 (dd, *J* = 7.8, 0.9 Hz, 1H), 7.32 (ddd, *J* = 7.5, 4.8, 1.2 Hz, 1H). ^{13}C NMR (126 MHz, $CDCl_3$) δ 157.5, 154.7, 149.4, 141.7, 139.4, 137.2, 128.1, 124.4, 121.6, 119.9. HRMS (ESI Pos): for $[C_{10}H_8BrN_2]^+$, calcd. m/z = 236.9845, found 236.9842. Compound data is in accordance with literature.[36]

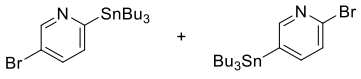

17 **18**

5-bromo-2-(tributylstannyl)pyridine (**17**). 2,5-Dibromopyridine (400 mg, 1.69 mmol, 1.0 equiv.) was dissolved in toluene (17 mL, 0.1 M) and the mixture was cooled down to -78 °C. *n*-Butyllithium (1.6 M in hexanes, 1.11 mL, 1.78 mmol. 1.05 equiv.) was added dropwise over 40 min to the cold mixture which was then stirred at -78 °C for 30 min. Tributyltin chloride (0.48 mL, 1.78 mmol, 1.05 equiv.) was added and the mixture was kept at that temperature for 30 min after which it was allowed to warm to room temperature and stirred for an additional 16 h. The reaction was quenched

with methanol and the mixture filtered over a pad of basic alumina. The product (**17**) and its regioisomer (**18**) were obtained in a 3:1 ratio. The crude mixture was used for further reaction without additional purification. ^{1}H NMR (400 MHz, $CDCl_3$) δ 8.81 (dd, *J* = 2.5, 0.8 Hz, 1H), 7.63 (dd, *J* = 7.9, 2.4 Hz, 1H), 7.29 (dd, *J* = 7.9, 0.8 Hz, 1H), 1.58 – 1.40 (m, 6H), 1.37 – 1.25 (m, 6H), 1.15 – 1.08 (m, 6H), 0.92 – 0.84 (m, 9H).

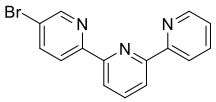

5-bromo-2,2':6',2''-terpyridine (**19**). 6-Bromo-2,2'-bipyridine (**16**, 370 mg, 1.57 mmol, 1.2 equiv.), $Pd(PPh_3)_4$ (90 mg, 0.08 mmol, 0.06 equiv.) and the crude 5-bromo-2-(tributylstannyl)pyridine mixture (**17**+**18**, 1.27 mmol, 1.0 equiv.) were dissolved in toluene (16 mL, 0.08 M) and the mixture was heated at reflux for 16 h. After cooling down to room temperature, the mixture was extracted three times with 1.0 M HCl (aq) and the aqueous phase was washed with EtOAc. Na_2CO_3 was added to the aqueous phase until pH > 7 and the product was extracted with EtOAc. The combined organic phases were washed with brine, dried over Na_2SO_4 and volatiles were removed under reduced pressure. The product was purified by flash column chromatography (silica, EtOH/EtOAc/*n*-pentane, 1:4:50 to 1:4:10 + 1% NEt_3) and precipitation from *n*-heptane. The product was obtained as an off-white solid in 79% yield (314 mg, 1.01 mmol). ^{1}H NMR (600 MHz, $CDCl_3$) δ 8.74 (d, *J* = 2.3 Hz, 1H), 8.71 (d, *J* = 4.8 Hz, 1H), 8.58 (d, *J* = 7.9 Hz, 1H), 8.53 (d, *J* = 8.5 Hz, 1H), 8.47 (d, 1H), 8.42 (d, *J* = 7.8 Hz, 1H), 7.99 – 7.93 (m, 2H), 7.86 (ddd, *J* = 7.7, 1.8 Hz, 1H), 7.36 – 7.32 (m, 1H). ^{13}C NMR (151 MHz, $CDCl_3$) δ 156.2, 155.6, 154.9, 154.6, 150.3, 149.4, 139.6, 138.2, 137.0, 124.0, 122.6, 121.5, 121.3, 121.3, 121.0. HRMS (ESI Pos): for $[C_{15}H_{11}BrN_3]^+$ calcd. m/z = 312.0131, found m/z = 312.0130.

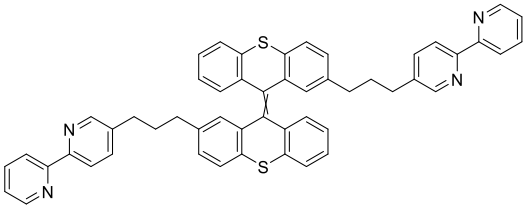

2,2'-bis(3-([2,2'-bipyridin]-5-yl)propyl)-9,9'-bithioxanthenylidene (**22**). 2,2'-Diallyl-bisthioxanthylidene (**11**, 100 mg, 0.21 mmol, 1.0 equiv.) was dissolved in THF (2.5 mL, 0.08 M). 9-BBN (0.5 M in THF, 2.5 mL, 1.25 mmol, 6.0 equiv.) was added and the mixture was stirred at room temperature until full conversion of the starting material (TLC). The freshly prepared hydroboration product was then transferred to a solution of 5-bromo-2,2'-bipyridine (**14**, 199 mg, 0.85 mmol, 4.0 equiv.) and $Pd(dppf)Cl_2$

(16 mg, 0.022 mmol, 0.1 equiv.) in THF (2.5 mL, 0.34 M) which was degassed by bubbling Ar for > 15 min. This mixture was heated at reflux for 16 h. The reaction mixture was allowed to cool to room temperature and volatiles were removed under reduced pressure. The product was purified by repeated flash column chromatography (silica, MeOH/CH_2Cl_2, 0 – 10%, + 2% NEt_3) and obtained as a yellow solid in 38% yield (63 mg, 0.08 mmol). ^{1}H NMR (600 MHz, $CDCl_3$) δ 9.01 – 8.94 (m, 3H), 8.89 – 8.84 (m, 6H), 8.67 – 8.60 (m, 2H), 8.23 – 8.16 (m, 3H), 7.99 – 7.93 (m, 3H), 7.68 – 7.60 (m, 1H), 7.55 (dd, *J* = 7.4 Hz, 1H), 7.48 (d, *J* = 7.9 Hz, 1H), 7.23 – 7.15 (m, 1H), 7.12 – 7.01 (m, 2H), 6.97 – 6.93 (m, 2H), 6.90 – 6.84 (m, 1H), 6.82 (dd, *J* = 7.8, 1.5 Hz, 1H), 6.64 (d, *J* = 1.8 Hz, 1H), 2.62 (t, *J* = 8.0 Hz, 4H), 2.50 – 2.27 (m, 4H), 1.76 – 1.64 (m, 4H). HRMS (ESI Pos): for $[C_{52}H_{40}N_4S_2]^+$ calcd. m/z = 784.2671, found m/z = 784.2700.

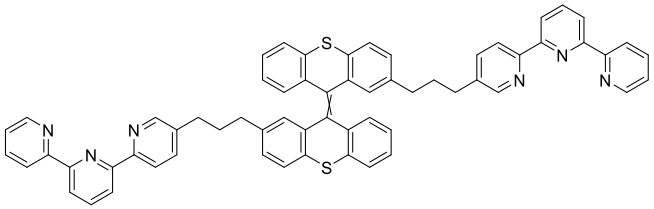

2,2'-bis(3-([2,2':6',2''-terpyridin]-5-yl)propyl)-9,9'-bithioxanthenylidene (**23**). 2,2'-Diallyl-bisthioxanthylidene (**11**, 75 mg, 0.16 mmol, 1.0 equiv.) was dissolved in THF (2.0 mL, 0.08 M) and 9-BBN (0.5 M in THF, 1.89 mL, 0.95 mmol, 5.9 equiv.) was added and the mixture was stirred at room temperature until full conversion of the starting material (TLC, MeOH/CH_2Cl_2, 10%) after approximately 10 min. The freshly prepared hydroboration product was transferred to a solution of 5-bromo-2,2':6',2''-terpyridine (**19**, 75 mg, 0.47 mmol, equiv.) and Pd(dppf)Cl_2 (12 mg, 0.016 mmol, 0.1 equiv.) in THF (3 mL, 0.16 M), which was degassed by bubbling Ar for > 15 min. The combined mixture was heated at reflux for 16 h. The reaction mixture was allowed to cool to room temperature and volatiles were removed under reduced pressure. The product was purified by flash column chromatography (silica, EtOH/EtOAc/*n*-pentane, 0:75:25 to 16:63:21) and obtained as an off-white solid in 67% yield (103 mg, 0.11 mmol). ^{1}H NMR (500 MHz, C_6D_6) δ 8.83 – 8.77 (m, 5H), 8.75 (d, *J* = 8.0 Hz, 2H), 8.61 – 8.56 (m, 2H), 8.52 (d, *J* = 2.3 Hz, 2H), 7.50 – 7.37 (m, 6H), 7.37 – 7.30 (m, 3H), 7.26 (dd, *J* = 8.1, 2.3 Hz, 2H), 7.03 – 6.96 (m, 2H), 6.86 (d, *J* = 1.8 Hz, 2H), 6.81 – 6.72 (m, 4H), 6.71 – 6.65 (m, 2H), 6.63 – 6.54 (m, 2H), 2.18 – 2.00 (m, 8H), 1.40 – 1.32 (m, 4H). HRMS (ESI Pos): for $[C_{62}H_{47}N_6S_2]^+$ calcd. m/z = 939.3298, found 939.3278.

4.3 Additional UV-vis spectroscopy

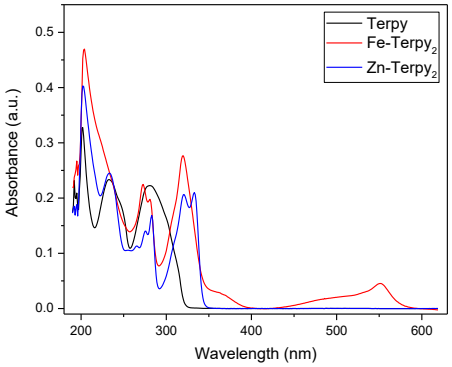

Figure 13. UV-vis absorption spectra of Terpy, [Fe^{II}]-$Terpy_2$ and [Zn^{II}]-$Terpy_2$ in MeOH (1.0 μM).

5. References

1 X. Zhao, K. Gentile, F. Mohajerani and A. Sen, *Acc. Chem. Res.*, 2018, **51**, 2373–2381.

2 R. D. Vale and R. A. Milligan, *Science*, 2000, **288**, 88–95.

3 J. C. M. Kistemaker, A. S. Lubbe and B. L. Feringa, *Mater. Chem. Front.*, 2021, **5**, 2900–2906.

4 M. Baroncini, S. Silvi and A. Credi, *Chem. Rev.*, 2020, **120**, 200–268.

5 S. Kassem, T. van Leeuwen, A. S. Lubbe, M. R. Wilson, B. L. Feringa and D. A. Leigh, *Chem. Soc. Rev.*, 2017, **46**, 2592–2621.

6 J. P. Sauvage, *Angew. Chem. Int. Ed.*, 2017, **56**, 11080–11093.

7 J. F. Stoddart, *Angew. Chem. Int. Ed.*, 2017, **56**, 11094–11125.

8 I. Aprahamian, *ACS Cent. Sci.*, 2020, **6**, 347–358.

9 M. Baroncini, L. Casimiro, C. de Vet, J. Groppi, S. Silvi and A. Credi, *ChemistryOpen*, 2018, **7**, 169–179.

10 C. Pezzato, C. Cheng, J. F. Stoddart and R. D. Astumian, *Chem. Soc. Rev.*, 2017, **46**, 5491–5507.

11 B. Taghavi Shahraki, S. Maghsoudi, Y. Fatahi, N. Rabiee, S. Bahadorikhalili, R. Dinarvand, M. Bagherzadeh and F. Verpoort, *Coord. Chem. Rev.*, 2020, **423**, 213484.

12 M. N. Tasbas, E. Sahin and S. Erbas-Cakmak, *Coord. Chem. Rev.*, 2021, **443**, 214039.

13 C. J. Burns and J. Fraser Stoddart, Eds., *The Nature of the Mechanical Bond: From Molecules to Machine*, John Wiley & Sons, Hoboken, NJ, USA, 2016.

14 L. Zhang, V. Marcos and D. A. Leigh, *Proc. Natl. Acad. Sci. U.S.A.*, 2018, **115**, 9397–9404.

15 B. P. Corbet, M. B. S. Wonink and B. L. Feringa, *Chem. Commun.*, 2021, **57**, 7665–7668.

16 W. R. Browne, M. M. Pollard, B. de Lange, A. Meetsma and B. L. Feringa, *J. Am. Chem. Soc.*, 2006, **128**, 12412–12413.
17 W. F. Jager, B. de Lange, A. M. Schoevaars, F. van Bolhuis and B. L. Feringa, *Tetrahedron: Asymmetry*, 1993, **4**, 1481–1497.
18 E. M. Geertsema, A. M. Schoevaars, A. Meetsma and B. L. Feringa, *Org. Biomol. Chem.*, 2006, **4**, 4101–4112.
19 A. Livoreil, J. P. Sauvage, N. Armaroli, V. Balzani, L. Flamigni and B. Ventura, *J. Am. Chem. Soc.*, 1997, **119**, 12114–12124.
20 S. P. Fletcher, F. Dumur, M. M. Pollard and B. L. Feringa, *Science*, 2005, **310**, 80–82.
21 B. S. L. Collins, J. C. M. Kistemaker, E. Otten and B. L. Feringa, *Nat. Chem.*, 2016, **8**, 860–866.
22 T. F. A. de Greef, M. M. J. Smulders, M. Wolffs, A. P. H. J. Schenning, R. P. Sijbesma and E. W. Meijer, *Chem. Rev.*, 2009, **109**, 5687–5754.
23 O. Ivashenko, H. Logtenberg, J. Areephong, A. C. Coleman, P. V. Wesenhagen, E. M. Geertsema, N. Heureux, B. L. Feringa, P. Rudolf and W. R. Browne, *J. Phys. Chem. C*, 2011, **115**, 22965–22975.
24 R. D. Hancock, *Chem. Soc. Rev.*, 2013, **42**, 1500–1524.
25 E. C. Constable, *Chem. Soc. Rev.*, 2007, **36**, 246–253.
26 A. Boulay, C. Deraeve, L. Vander Elst, N. Leygue, O. Maury, S. Laurent, R. N. Muller, B. Mestre-Voegtlé and C. Picard, *Inorg. Chem.*, 2015, 54, 1414–1425.
27 X. Wang, P. Rabbat, P. O'Shea, R. Tillyer, E. J. J. Grabowski and P. J. Reider, *Tetrahedron Lett.*, 2000, **41**, 4335–4338.
28 A. M. Castillo, L. Patiny and J. Wist, *J. Magn. Reson.*, 2011, **209**, 123–130.
29 S. R. Chemler, D. Trauner and S. J. Danishefsky, *Angew. Chem. Int. Ed*, 2001, **40**, 4544–4568.
30 Y. Luo, K. Barthelmes, M. Wächtler, A. Winter, U. S. Schubert and B. Dietzek, *Chem. Eur. J.*, 2017, **23**, 4917–4922.
31 F. Laquai, Y.-S. Park, J.-J. Kim and T. Basché, *Marcomol. Rapid Commun.* 2009, **30**, 1203–1231.
32 J. Conradie and K. G. von Eschwege, *Data in Brief*, 2020, **31**, 105754.
33 J. Lee, H. H. Moon, K. Paeng and C. Song, *Polymers*, 2018, **10**, 1173.
34 Y. Zhang, J. R. Vallin, J. K. Sahoo, F. Gao, B. W. Boudouris, M. J. Webber and W. A. Phillip, *ACS Cent. Sci.*, 2018, **4**, 1697–1707.
35 Z. Shi, S. Chen, Q. Xiao and D. Yin, *J. Org. Chem.*, 2021, **86**, 3334–3343.
36 B. D. Heuberger, D. Shin and C. Switzer, *Org. Lett.*, 2008, **10**, 1091–1094.

Chapter 6

Computational and Experimental Studies of *N,N'*-Substituted Isoindigos and Related Structural Variants

Isoindigo is of interest for its use as a potential drug core structure and for the development of organic photovoltaic materials. The facile synthesis and functionalisation, together with a broad absorption of visible light, makes it a useful compound in applications such as bulk heterojunction organic photovoltaics. Here we present new insights into the substituent effects of N-functionalised isoindigos, developing a reliable and fast in silico screening approach of a library of compounds. Using experimental UV-Vis and electrochemical data increased the accuracy of the TD-DFT method employed. This procedure allowed us to accurately predict the optical and electrochemical properties of N-functionalised isoindigos and the elucidation of the relationship between substituent effects and electronic properties. Additionally, a number of structural variants of isoindigo are investigated.

Acknowledgement
I would like to thank Ferdinand Kiss for his significant contributions to the synthesis of *N*,*N*'-isoindigos, and his contributions to the DFT calculations, Emmanuel Vrionakis for contributions to the synthesis of *N*,*N*'-isoindigos, Dr. Nadja Simeth and Dr. Stefano Crespi for their general contributions to the project. Furthermore, I would like to thank Daniel Döllerer for the synthesis of the demethylated structural variant in section 2.5.

Parts of this chapter have been published as: *Predicting the Substituent Effects in the Optical and Electrochemical Properties of N,N'-substituted Isoindigos*, Ferdinand L. Kiss, Brian P. Corbet, Nadja A. Simeth, Ben L. Feringa, Stefano Crespi, *Photochem. Photobiol. Sci.*, 2021, **20**, 927–938.

1. Introduction

Isoindigo was first synthesised in 1842[1] and initially identified with the name "indin" (Figure 1a).[2] This structure belongs to the indigoid family of compounds, together with indigo itself, indirubin and thioindigo. Similarly, to indirubin scaffolds,[3] isoindigo and its derivatives became attractive to the pharmaceutical industry. For example, *N*-substituted isoindigos have found use in leukaemia treatment under the commercial names Natura and Meisoindigo (Figure 1b).[3–5] Other molecules based on the same motif showed promising activity against different tumour strains under *in vitro* conditions.[3,6] Indigo- and thioindigo- compounds[7] are widely employed as dyes in the textile industry,[8] as photosensitisers,[9,10] and are studied regarding their photophysical and photochromic properties.[11–15] In more recent research efforts it was demonstrated that isoindigo is highly suitable for organic photovoltaics (OPVs)[16] and optoelectronics.[16–20] The facile synthesis and derivatisation of isoindigo are beneficial for the efficient incorporation in numerous applications. Several 6,6'-substituted isoindigo derivatives are reported as p-type donors in donor–acceptor–donor (DAD) materials and conjugated polymers due to their electron deficiency.[4,17] Installing substituents at the lactam nitrogen is largely unexplored for such applications.[4] Only a limited selection of *N*-alkylations is reported to overcome solubility issues in isoindigo OPV research.[4] At the same time, aromatic substituents at the nitrogen are rare and only found in a few bio-active isoindigos.[3,6]

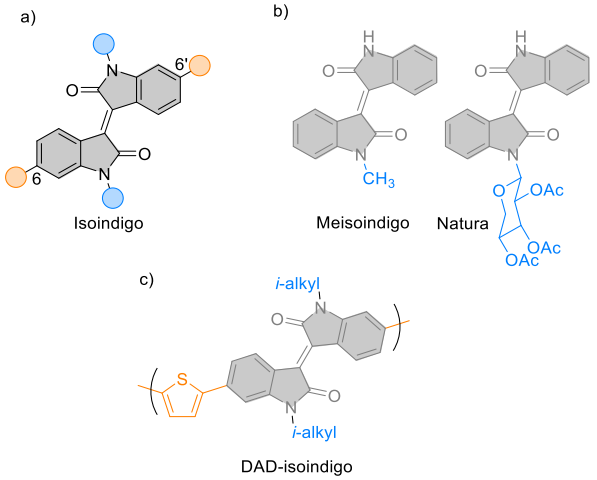

Figure 1. a) Isoindigo with the 6,6'- and *N*,*N*'-substitution at positions highlighted in orange and blue, respectively. b) Bioactive *N*-substituted isoindigos Meisoindigo (left) and Natura (right), which are used in cancer treatment. c) A 6,6'-substitution pattern, used as a handle to obtain DAD-materials. The exemplary structure is one of the initial proposed OPV-polymers.[16]

Isoindigo absorbs light in the visible region (3900 M^{-1} cm^{-1} in DMSO at 490 nm[18]) tailing in the near-infrared (NIR).[18,21,22] Consequently, the molecule holds great potential for high conversion efficiency in photochemical processes using visible light. Furthermore, isoindigos are stable towards photobleaching,[23] a property attributable to an ultrafast singlet fission pathway, occurring after excitation.[24] In a thiophene-functionalised isoindigo derivative it was demonstrated that this sub-ns event leads to efficient triplet pair separation in solid films, while in solution it leads to the radiationless deactivation of the excited state, recovering the starting material at the ground state.[24]

The introduction of substituents onto the isoindigo core structure allows tuning its UV-Vis absorption profile.[5,25] The π-system of isoindigos can be easily extended at the 6,6'-position (Figure 1a, orange). Substituents at the lactam nitrogens (Figure 1a, blue), such as alkyl chains, prevent π-π stacking and lead to increased solubility of isoindigo derivatives.[17] To the best of our knowledge, the influence of *N*,*N*'-substituents on the optical and electronic properties of isoindigos have not been systematically studied, so far. Functionalisation on the lactam nitrogen is synthetically straightforward and provides an additional handle for tuning the electronic properties of the core structure. A reliable prediction tool is crucial to efficiently judge the outcome of a synthetic modification and facilitate effective, rational design for specific optoelectronic applications.

Computational chemistry provides valuable methods to predict the properties of a compound, supporting the development of new molecules, drugs and materials.[26,27] To apply quantum mechanical calculations to a library of compounds, the availability of a fast and accurate method is a key requirement. In this context, density functional theory (DFT) is known as the "workhorse" of current theoretical studies in chemistry and physics.[28,29] However, DFT methods often vary in their performances,[30,31] making the choice of the proper functional for a specific application of utmost importance.[29,32] Besides various attempts to categorise functionals by accuracy in a hierarchy as in the Perdew "Jacob's ladder",[33] extensive benchmarks are needed to identify the functional best suited for a specific use.

Here, we present a library of 50 isoindigo derivatives focusing on the *N*,*N*'-functionalisation pattern. The library was explored computationally, utilising an extensively benchmarked method to obtain insights into the substitution effects on the optical and electronic properties of isoindigo. Additionally, we synthesised a limited subset of selected isoindigo derivatives to experimentally validate the accuracy and reliability of the

computational methods. Furthermore, a number of structural variants of isoindigo were synthesised to gain further insights into their electronic properties. Koopmans' theorem was applied to provide an understanding of the electrochemical properties based on computational and experimental data. The presented computational methodology serves as a predictive tool and can consequently pave the way for the rational design of isoindigos as chromophores in material sciences and organic photovoltaics.

2. Results & Discussion

2.1 Design and synthesis

We explored a library of functionalised isoindigo derivatives employing substituents with varying electronic and steric demand to rationalise their effect on the properties of the chromophore (Figure 2). The focus was towards the less explored *N*,*N*'-functionalisation over the 6,6'-substitution of isoindigo. We selected 4-methoxyphenyl as electron-donor and 4-nitrophenyl, 4-trifluoromethylphenyl, 4-fluorobenzyl and benzonitrile as electron-acceptor units, respectively, while the unsubstituted phenyl group serves as a reference. Additionally, *t*-butyl-acetyl and *t*-butyloxycarbonyl were selected for their different steric demand and electronic character. Permutation of the aforementioned *N*,*N*'-substituents resulted in a library of 45 derivatives (Figure 2, blue, **1–45**). *N*-propyl- and *N*,*N*'-bis-propyl substituted derivatives were included, to serve as a reference for the commonly used alkylated isoindigo derivatives in the OPV research (Figure 2, blue, **46–47**). For comparison, we included a nitrile group as electron-poor and a methoxy group as electron-rich substituents on the more frequently used 6,6'-position, providing three additional derivatives (Figure 2, orange, 48–50). Compounds **25**, **27**, **30**, **31**, **35**, **36**, **45**, **46** and **47** (Figure 2, grey boxes) were synthesised to reference our library.

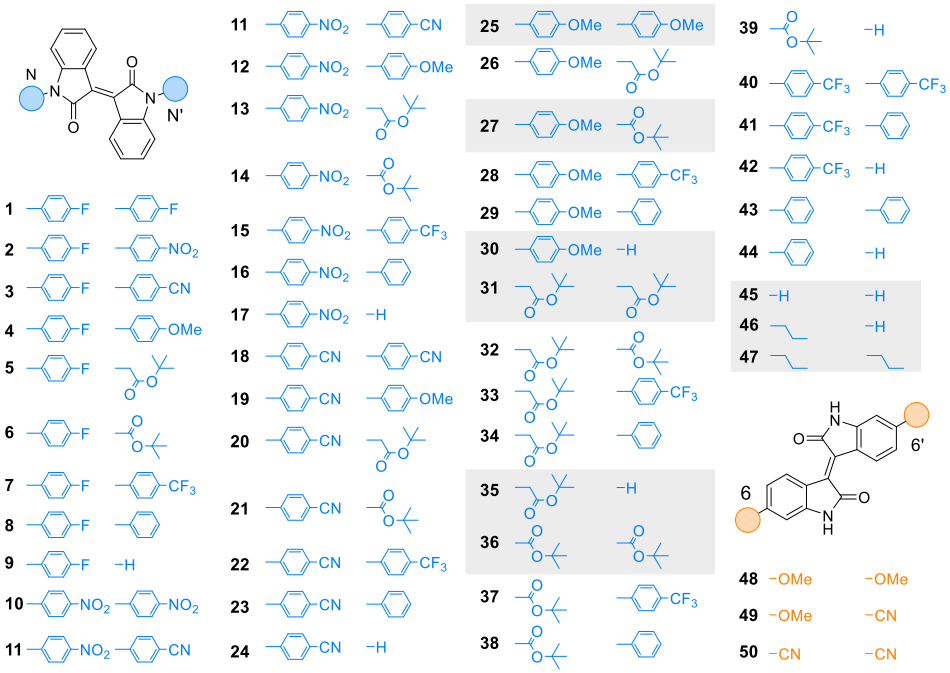

Figure 2. Library of the isoindigo compounds used in this study. Blue indicates the *N,N'*-substituted isoindigos, orange indicates the 6-6'-substituted isoindigos. The grey boxes highlight the synthesised structures for the computational studies.

2.2 Benchmark study

We benchmarked several functionals and basis sets to find the best-suited time-dependent DFT method (TD-DFT) to analyse the optical properties of the isoindigo library efficiently. The absorption spectra and the solvatochromism of unfunctionalised isoindigo **45** served as reference for the benchmarking, of which the geometry was optimised at the ωB97XD/def2-TZVP level of theory with the applicable electron-density based solvent model (SMD). The solvatochromism[34] of λ_{max} in different solvents (toluene, MeOH, $CHCl_3$, MeCN) relative to DMSO was computed at different levels of theory with the respective SMD solvent model[35] using 25 computed states. These results were compared with the experimental results (Figure 3). The average error of the solvatochromism (defined as "Avg.-Error" in Figure 3), the average of the absolute deviations of λ_{max} in the chosen solvents from experimental results (Abs.-Error), as well as the difference between the highest and lowest error of the solvatochromism (Error-range) and the lowest and highest error of the solvatochromism (Min.-Error and Max.-Error), were used to select the best suited functional. Furthermore, the calculation wall time was used to compare the efficiency of the calculation methods, defined as "CalcTime" (For computational and

hardware details, see section 4.1). We aimed for the lowest errors (Avg.-Error, Abs.-Error, Min.-Error and Max.-Error), a uniform description in all solvents (small Error-range) and a computationally efficient method (short CalcTime).

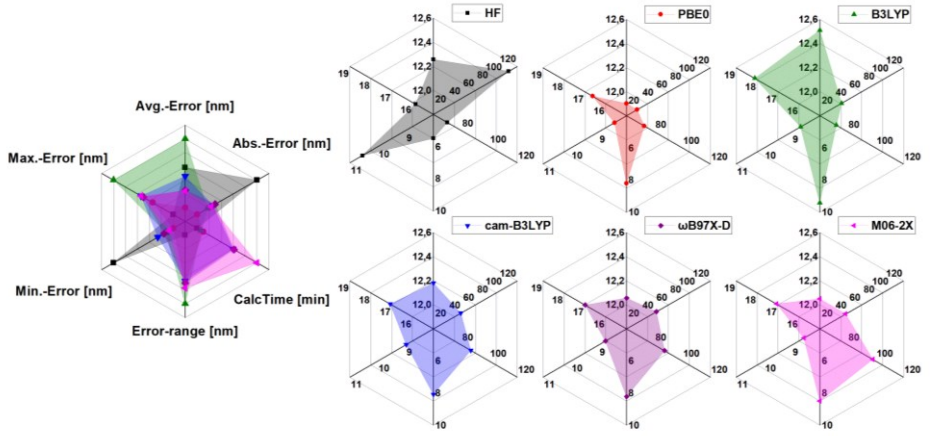

Figure 3. Benchmarks of the error of the change of λ_{max} in different solvents (toluene, methanol, chloroform, acetonitrile) relative to DMSO (Avg.-Error) computed at the TD-HF level and at a selected number of TD-DFT functionals with the respective SMD solvent model and 25 computed states versus experimental results. Other parameters used are the absolute deviation of λ_{max} in the chosen solvents from experimental results (Abs.-Error), the computing wall time (CalcTime), the difference between the highest and lowest relative error (Error-range) and the lowest and highest relative error (Min.-Error and Max.-Error), respectively.

Our study gave the TD-PBE0/cc-pVDZ level of theory[36,37] as the best-suited method for the simulations of the UV-Vis spectra of the library. The general applicability regarding excitation energies of TD-PBE0 in intramolecular excited state charge-transfer (CT), as the one observed in isoindigo, was demonstrated earlier,[22,30,38] even though in some cases TD-PBE0 has shown limitations in describing the CT character of the excitations.[38] In our case, visual inspection of the orbital contribution to the lower excited states confirmed a limited effect of the functional on the nature and order of the states. Furthermore, the PBE0 functional showed a low calculation time in combination with low errors in the photochromism. After selection of the functional, additional benchmarking of the basis set was done with the same parameters (Table 1), which resulted in the cc-pVDZ basis set as the optimal basis set. With the information on optimal functional and basis set, we extended the computational analysis to the full library of *N*,*N*'-substituted isoindigo derivatives using the PBE0/cc-pVDZ level of theory.

Table 1. Benchmark of basis sets using the PBE0 functional with the optimal basis set (cc-pVDZ) highlighted in bold.

	def2-TZVP	**aug-cc-pVDZ**	**cc-pVDZ**	**cc-pVTZ**	**6-311+ G(2d,p)**	**6-311++ G(2d,p)**
Avg.-Error [nm]	-12.10	-12.27	**-11.59**	-12.13	-12.33	-12.33
Abs.-Error [nm]	15.53	18.18	**6.37**	13.33	18.87	18.89
Error-Range [nm]	9.61	9.23	**8.81**	9.09	9.25	9.25
Min-Error [nm]	-8.02	-8.45	**-7.7**	-8.34	-8.53	-8.53
Max-Error [nm]	-17.63	-17.68	**-16.51**	-17.43	-17.78	-17.78

2.3 Optical Properties

Our calculations revealed that all derivatives show the expected $S_0 \rightarrow S_1$ π-π* vertical excitation (between 480 nm and 530 nm in MeOH). This transition occurs with different probabilities, determined by their oscillator strength (*f*). The second vertical transition to the S_2 has, in most cases, a low oscillator strength, known as a dark state. This finding is in accordance with previous calculations on isoindigos.[5] Introducing different substituents on the lactam nitrogen influences the position of λ_{max} and the oscillator strength of the respective transition. For instance, an isoindigo with two Boc-groups (**36**) has an unusually high oscillator strength of 0.3019 to the S_1. In contrast, the asymmetrically substituted isoindigos with only one Boc unit show a bright π-π* $S_0 \rightarrow S_2$ transition. For example, isoindigo **27** with a higher probability (*f* = 0.1733 in toluene) than the excitation to the S_1 (*f* = 0.1051 in toluene).

Table 2. Comparison of experimental and theoretical (TD-BPE0/cc-pVDZ level of theory) optical and electrochemical properties and exciton binding energy.

#	Solvent	λ_{max} [nm]		Oscillator strength (*f*)	$E_{1/2}$ [V vs. Fc/Fc^+]	Exciton binding energy (calc.) [eV]
		Exp.	Calc.			
25	Toluene	508	508	0.1422		
	MeCN	503	508	0.1366	-1.12[a]	4.30
	MeOH	512	526	0.0932		
27[b]	Toluene	400	449	0.1733		
	MeCN	396	451	0.1655	-1.01[a]	4.18
	MeOH	402	459	0.2239		
30	Toluene	484	492	0.1748		
	MeCN	485	497	0.1496	-1.13	4.30
	MeOH	494	504	0.1650		
31	Toluene	485	490	0.1999		
	MeCN	482	493	0.1712	-1.11	4.69
	MeOH	483	497	0.1740		
35	Toluene	487	486	0.1995		
	MeCN	483	490	0.1783	-1.15[a]	4.64
	MeOH	482	497	0.1821		
36	Toluene	474	487	0.3019		
	MeCN	472	487	0.2727	-0.90	4.82
45	Toluene	484	482	0.3967		
	MeCN	478	487	0.1884	-1.16[a]	4.74
	MeOH	481	496	0.1870		
46	Toluene	489	496	0.1492		
	MeCN	483	501	0.1286	-1.19	4.63
	MeOH	485	509	0.1256		
47	Toluene	493	501	0.1594		
	MeCN	493	507	0.1361	-1.20	4.56
	MeOH	495	515	0.1330		

Footnotes: a) Determined from computational results, corrected by the parametrisation scheme described below. b) λ_{max} as S_0-S_2 transition band, since the S_0-S_1 transition does not build up to a local maximum, leading to a formal increased error.

While the π-π* transitions in most derivatives were not apparent to be charge transfer (CT) states from natural transition orbital analysis, the special case of **27** showed three consecutive bright and marked CT states (e.g. the $S_0 \rightarrow S_1$ transition in Figure 4). This could be of interest for optoelectronic applications, as several excitations and thus a broader spectral range would lead to productive charge separation.

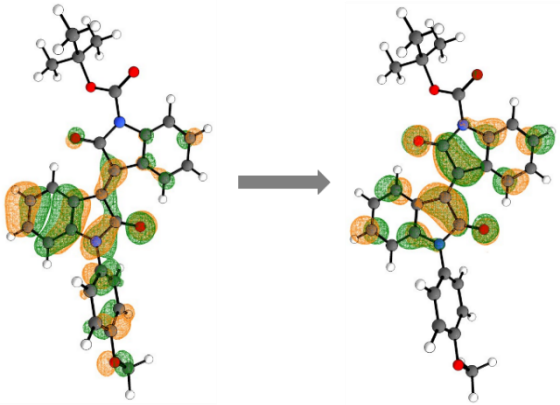

Figure 4. Natural transition orbitals of **27** for the $S_0 \rightarrow S_1$ transition of **27**.

A push-pull configuration as in **12** (4-methoxyphenyl and 4-nitrophenyl substituents), results in the most bathochromically shifted λ_{max} of the library (530 nm compared to 481 nm of the unsubstituted isoindigo **45**). All derivatives containing an anisole substituent show an additional aromatic contribution to the frontier orbitals, whereas other substitution patterns show frontier orbitals that are primarily centred on both oxindole halves. While a push-pull substitution pattern on the nitrogens induced a substantial bathochromic shift of λ_{max}, the calculations indicated less marked substituent effects at the 6,6'-position. Specifically, **48** (6,6'-bis-OMe) has the highest oscillator strength (f = 0.3967) of the 6,6'-derivatives but the lowest λ_{max} at 467 nm in toluene. By replacing the two electron-donating methoxy moieties by either one or two nitrile substituents, λ_{max} increases with simultaneously decreasing f with 49 (f = 0.3421 at 479 nm in toluene) and **50** (f = 0.2404 at 484 nm in toluene). These findings emphasise the challenging balance of absorptivity and electronic transition maximum in the design of new isoindigo chromophores.

The synthesised isoindigo derivatives were characterised regarding their UV-Vis absorption spectra. As an example, the experimental and predicted spectra of **27** and **36** are depicted in Figure 5 (For the other spectra see Section 4.4). The experimental properties of all isoindigo-derivatives, in the respective solvents, are in good accordance with the calculated results (Figure 5) and are summarised in Table 2.

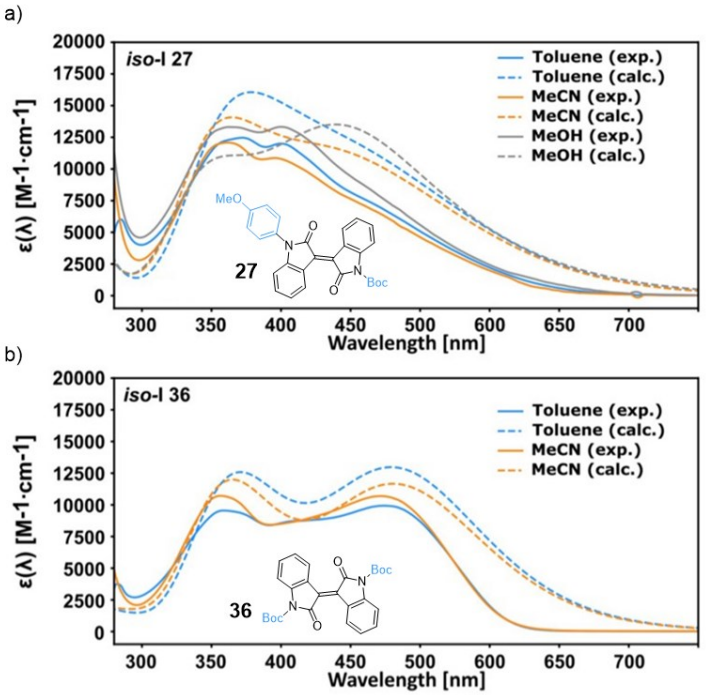

Figure 5. Experimental (solid lines) and calculated spectra (dashed lines) of a) **27** and b) **36**.

The $S_0 \rightarrow S_1$ transition at ca. 475 nm in **27** does not correspond to a local maximum in both calculated and experimental spectra, therefore the $S_0 \rightarrow S_2$ excitation band is used as a reference. Isoindigo **36** has the highest attenuation coefficient for the π-π* transition (ε = 10695 M^{-1} cm^{-1} in MeCN), which was accurately predicted in the TD-DFT model. The remaining derivatives show high and distinct attenuation coefficients with broad absorption bands ranging up to ca. 600 nm.

To understand the substituent effects on the nature of the electronic transition, we proceeded to analyse the library using transition density matrices (TDMs). This treatment allows accessing the electron and the hole distribution in the excited state and identifying their delocalisation.[39] In this way the electronic excitation processes such as CT can be visualised,[39] which is of direct relevance in optoelectronic materials.[5,40,41] We divided each compound into fragments to facilitate the interpretation of the results (Figure 6a). The choice of the fragments allows us to ascribe the off-diagonal elements in the TDMs to CT and diagonal elements to local excitations. We used the Multiwfn software to analyse the TDMs and the exciton binding energies.[42] Inspecting the TDMs, we can assign four major transition behaviours to the first excited state. Symmetric and asymmetric TDMs, which can be further categorised by the presence of solely inductive or

additional mesomeric effects. In symmetric TDMs, both the electron and the hole share a similar distribution around the central double bond, spreading on both oxindole halves of the molecule. On the contrary, asymmetric TDMs have a hole located on one half of the structure. The electron for all $S_0 \rightarrow S_1$ TDMs is localised on fragments 3 and 4 (Figure 6a).

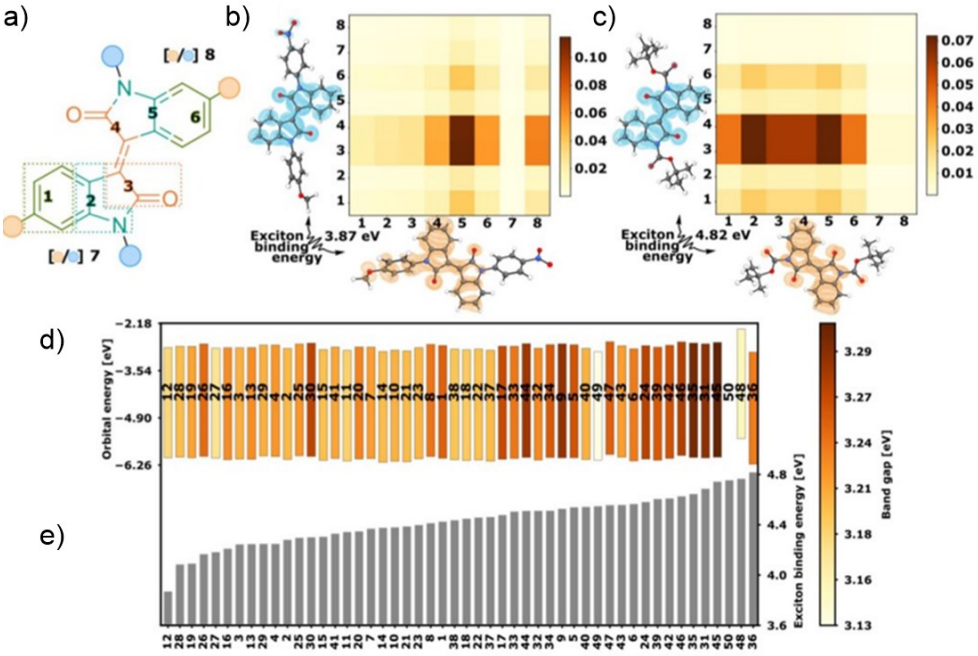

Figure 6. a) Fragments used to visualise an analyse the transition density matrices (TDMs). b) Asymmetric TDM of **12**. c) More symmetrical TDM of **36**. d) Orbital energies of the library where the lower end of the coloured bars denotes E_{HOMO}, the upper end of the coloured bars denotes E_{LUMO} and the colour denotes the resulting bandgap. Note: E_{HOMO} and E_{LUMO} of 50 is out of range with -0.558 eV and 0.928 eV. e) Exciton binding energies of the library.

The presence of electron-donating and -withdrawing groups interacting with the hole is the origin of the asymmetry in the TDMs. The donation of electron density to the hole via mesomeric effects by an electron donating moiety distorts the hole location. In this case, the TDM can be categorised as mesomerically influenced, rather than indirectly affected by only inductive effects. As can be observed in the strongly mesomeric polarised TDM of **12** (Figure 6b) with a *p*-nitrophenyl and a *p*-anisole *N*-substituent. The mesomeric contribution to the TDM is highly dependent on the polarity difference induced by the *N*,*N*'-substituents. The strong polarisation induced by the anisole and nitrophenyl substitution, and the mesomeric effects in **12** lead to a significant hole-density at the *N*,*N*'-substituents. In contrast, the unpolarised, bis-anisole substituted **25** shows barely any hole-density at the position of the substituent.[43] The findings related to the enhanced resonance

between the hole density and the anisole in **12** are in contrast to other examples where the rotation of the phenyl ring prevented an effective overlap, a trend encountered in 6,6'-substituted patterns.[5,17] The inductively dominated TDM of **36** (Figure 6c) shows no localisation of the hole on either of the specific oxindole-halves, nor does it show any significant TDM-elements on the substituents.

The known methodological limitation of the analysis of the excited state character and the excitation process[44,45] can be observed from the electron and hole-densities in Figures 6b and 6c. The CT is not always apparent from electron-hole or natural transition orbital analysis alone. This is due to the poorly defined localisation of the electron density around electron-donating and -withdrawing groups.[38] The TDM analysis, however, aided the identification of the CT and the substitution effects.

Next, we focused on the exciton binding energies, which represent the Coulomb attraction between the exciton quasiparticles (electron and hole). It is a measure for the separability of the exciton in free charges and is directly related to the generation of an effective current in optoelectronics.[41] The strong polarisation and the mesomeric effects in **12** significantly lower the exciton binding energy to 3.87 eV, compared to 4.82 eV in the symmetric **36** (Figures 6b, 6c and 6e). Analysing the HOMO and LUMO energies (E_{HOMO} and E_{LUMO}) provides further information on the effects of the *N*,*N*'-substitution on the electronic structure properties (Figure 6d). The bandgaps (E_{HOMO}-E_{LUMO}) of the *N*,*N*'-library varied by a range of 0.136 eV, with a maximum of 3.309 eV in the unsubstituted **45** and a minimum of 3.173 eV in **26**. Investigation of the bandgap and the exciton binding energy reveals evidence of a direct correlation between the two: for *N*,*N*'-substituted isoindigos, the bandgap increases with rising exciton binding energy (Figure 5d, and 5e), whereas some derivatives are outliers in this trend (e.g. **26**, **30**, **40**). These findings indicate that the exciton binding energy correlates to the bandgap of the *N*,*N*'-library, specifically. The 6,6'-substituted isoindigo derivatives **48–50** are outliers in this series. Isoindigo **49** shows the second smallest bandgap of the library (3.13 eV) while being positioned in the upper third of the library regarding the exciton binding energy. Additionally, **50** shows the lowest bandgap in the series (0.371 eV), but is characterised by the third-highest exciton binding energy of 4.75 eV. These examples, combined with the above-mentioned variation in the E_{HOMO} and E_{LUMO}, emphasise further that 6,6'-substitution patterns cannot be categorised following the same trend observed for *N*,*N*'-substituted isoindigo derivatives.

2.4 Electrochemical properties

According to Koopmans' theorem,[46] E_{HOMO} and E_{LUMO} can be approximated to the ionisation potential (IP) and electron affinity (EA), respectively (Figure 7).

In our study, we decided to utilise the linear dependency of the EA and the reduction potential combined with Koopmans' theorem to apply a parameterisation method on the computed values. We derived the E_{LUMO}s from experimental reduction potentials ($E_{LUMO}^{exp.}$) of a small sub-library of compounds, that we use to parametrise the complete dataset of E_{LUMO}s obtained computationally ($E_{LUMO}^{calc.}$). This approach is extensively described in the literature.[5,47–51] We derived $E_{LUMO}^{exp.}$s from the reduction half-wave potential ($E_{1/2}$) versus Fc/Fc^+, obtained by cyclic voltammetry in acetonitrile, by applying eq. 1, using the value of 5.1 eV vs vacuum for ferrocene.[48]

$$E_{LUMO}^{exp.} = -(E_{1/2}^{red.} + 5.1)\ [\text{eV}] \qquad eq.\,1$$

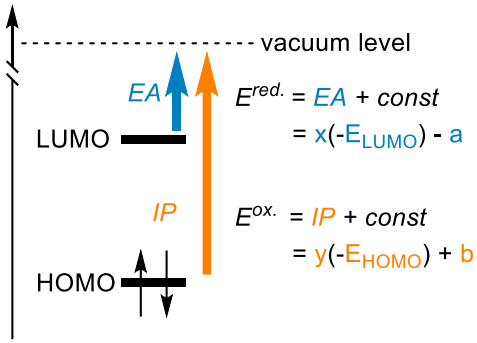

Figure 7. E_{HOMO} and E_{LUMO} can be approximated to electron affinities (EA) and ionisation potential (IP). The reduction and oxidation potentials can be obtained from the EA and IP.

An example of the isoindigos i.e., **36**, that was studied by experimental cyclic voltammetry is shown in Figure 8. Starting from positive potential in the negative potential direction we observe two reversible reductions to the anion and dianionic species, respectively. Using the first reduction potential and the relation of the internal reference to the vacuum level (eq. 1), we could obtain experimental information about the LUMO energy levels of a set of isoindigos.

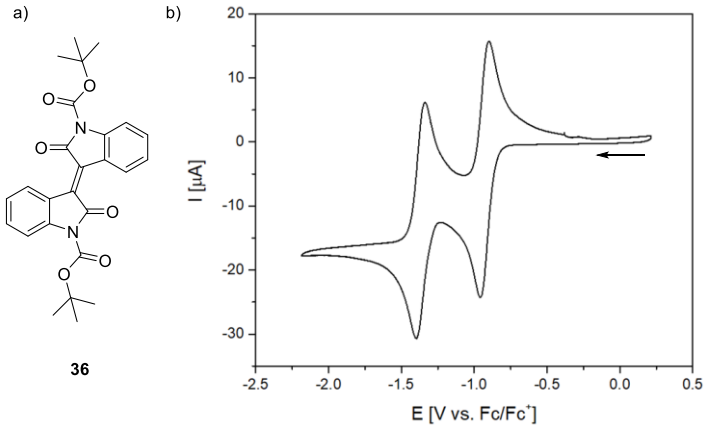

Figure 8. a) Structure of bis-Boc-*N*-Isoindigo **36**. b) Cyclic voltammetry of **36**.

The experimental values were plotted against the theoretical ones and the parameters of the relation between $E_{LUMO}^{exp.}$ and $E_{LUMO}^{calc.}$ were obtained by linear regression (Figure 9). Applying eq. 1, we inferred the parametrisation coefficients (cf. *x* and *a* in Figure 7) to correct the calculated results via eq. 2 to better analyse the reduction potentials in the library.

$$eq.2 \qquad E_{1/2}^{red.} = -(0.9595\, E_{LUMO}^{calc.} - 1.3245) - 5.1)\ [\text{V vs. Fc}/Fc^{+}]$$

A correlation between *N,N'*-substitution pattern and the E_{LUMO} is observed. The *N,N'*-substituted isoindigo derivatives show more stable LUMOs (lower energy relative to the vacuum level) with electron-withdrawing groups and more destabilised ones by introducing electron-donating groups. Contrary to the considerations taken concerning the TDMs and the exciton binding energy, we do not observe a significant difference from inductive or mesomeric effects. Applying Koopmans' theorem, these findings were used to obtain an accurate prediction of the reduction potentials. Electron-withdrawing groups increase (**36**, $E_{1/2}$(param./exp.) = -0.89 V/-0.90 V), while weakly electron-donating groups decrease the reduction potentials (**47**, $E_{1/2}$(param./exp.) = -1.20 V/-1.18V). While the electron-donating bis-anisole substituted isoindigo **25** shows a higher reduction potential ($E_{1/2}$(param.) = -1.12 V) and thus seems to oppose the trend, the push-pull configurations support the findings, as their reduction potentials range is in between the pull-pull and push-push configurations (e.g. $E_{1/2}$(param.) = -1.02 V, -1.06 V and -1.06 V for **12**, **19** and **28**).

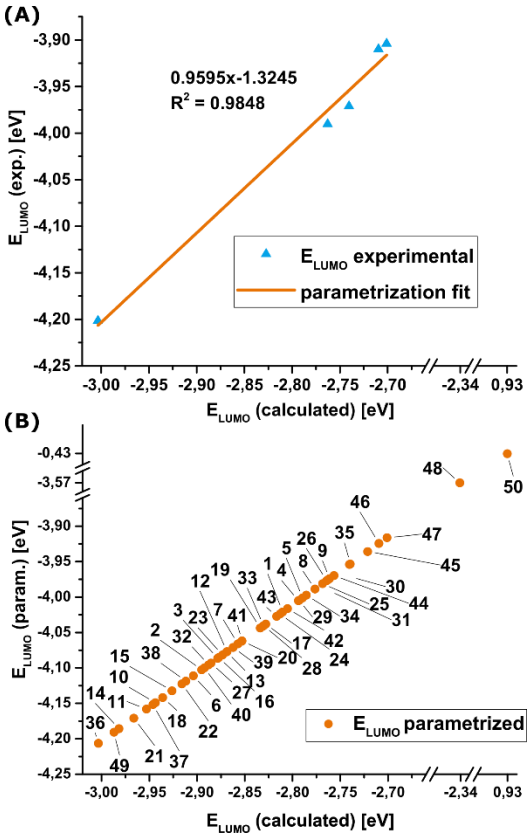

Figure 9. a) Parametrisation of the calculated E_{LUMO}s with an experimental subset of isoindigo derivatives. b) Application of the parametrisation to the isoindigo library. The 6,6'-substitution pattern (**48–50**) does not follow the same trend as the *N,N*'-substitution pattern regarding the E_{LUMO} (see discussion in the text) and is only included here for a general overview.

As the reduction potential is directly linked to the open-circuit voltage of photovoltaics,[41] the method, presented here could aid the design of enhanced photovoltaic materials.

2.5 Related structural variants of isoindigo

Compound **53**, a structural variant of the previously shown isoindigos with a dimethyl functionality instead of a carbonyl was synthesised to further probe the electrochemical and photochemical properties of isoindigos (Scheme 1). Compound **53**, provided by Daniel Döllerer, was obtained via a Knoevenagel condensation of **51** and **52**.

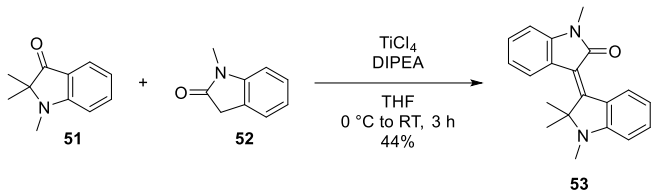

Scheme 1. Synthesis of **53**.

The CV of **53** shows an interesting difference to the electrochemistry of the related isoindigos. In the reductive direction, a reversible redox wave is observed (Figure 10a and b) at $E_{1/2}$ = -1.46 V vs. Ag/AgCl, highly similar to the first redox signal observed in isoindigos (e.g. Figure 8b). The second reduction at $E_{p,c}$ = -2.0 V vs. Ag/AgCl is markedly different without a corresponding oxidation. In the case of **53**, in the oxidative direction, a new oxidation is observed at a much higher potential (-0.4 V vs. Ag/AgCl). This could mean that either a chemical reaction, such as hydration, took place or that there is a significant change within the molecule itself. Both of the amide functionalities of the isoindigos seem to be crucial for the electrochemical reversibility of the second reduction.

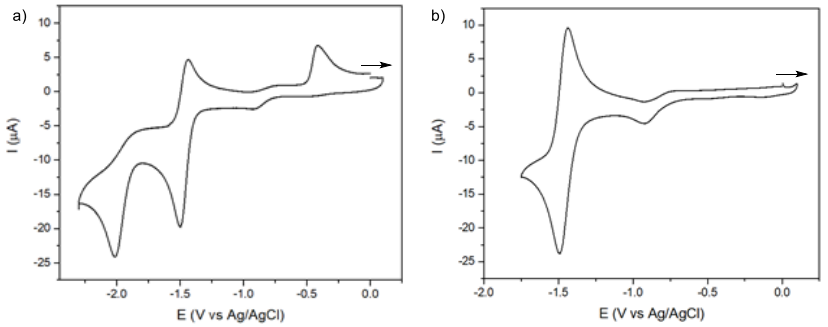

Figure 10. CV of **53** with: a) measured between -2.2 and 0.1 V vs. Ag/AgCl and b) between -1.7 and 0.2 V vs. Ag/AgCl. Note: the signal around -0.9 V vs. Ag/AgCl is from a small amount of oxygen left in solution.

Expanding further on the isoindigo scaffold, a novel, indanone-bridged variant (**57**, Scheme 2) was synthesised via a double condensation reaction under acidic conditions from *N*-propylated isatin (**55**).

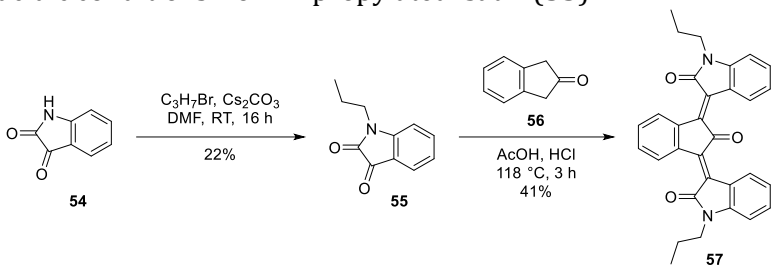

Scheme 2. Synthesis of **57**.

From the CV of **57** (Figure 11) we observe in the reductive direction that there are 4 major reduction signals (Figure 11a, labelled A, C, D, E) and one minor reduction (B). A, C and D are electrochemically reversible signals and E is irreversible, where, potentially, the species formed after reduction undergoes a chemical reaction. Alternatively, a significant geometrical change could cause the irreversibility of this compound. The small, irreversible oxidation signal (F) is present at -0.6 V vs. Fc/Fc^+ which is only observed after the reduction at A (Figure 11b). This signal F is dependent on the scan rate, where a higher scan rate increases the relative current intensity (Figure 11c). The B and B' signals observed at a lower scan speed are not observed at higher scan speeds. The nature of the species that is oxidised at F is unknown. The relatively simple molecule **57** shows an high number of reliable and reproducible redox events in the reductive direction and seems able to accommodate a high charge denstiy.

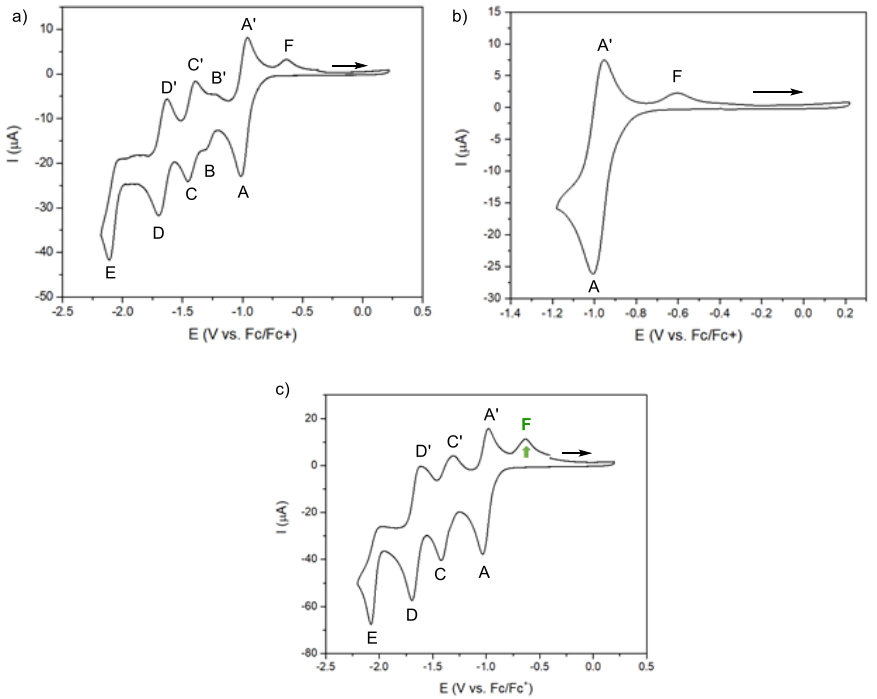

Figure 11. Cyclic voltammetry of **57** at a) scan rate = 100 mV s^{-1}. b) scan rate = 100 mV s^{-1}, different potential range. c) scan rate = 200 mV s^{-1}.

3. Conclusions & Outlook

In this work, we conducted a detailed investigation into the substitution effects on the *N,N'*-site of isoindigo, providing an alternative for optical and electronic tuning to the already well-studied 6,6'-position.[17] To achieve a comprehensive study of a broad range of substituents, a combination of computational and experimental methods on a library of molecules was applied and a subset of these molecules was synthesised to allow for parametrisation.

TD-PBE0/cc-pVDZ emerged as the best-suited method to simulate the experimental properties of isoindigo, reaching a good agreement between the simulated and calculated ones. Based on the computational data, we discovered trends relating the optical properties to the substitution patterns and obtained important information on the absorption wavelengths, the extinction coefficients and the influence of substituents on bright or dark states.

The analysis of the excitation behaviour by TDMs elucidated the difference between symmetric and asymmetric hole distributions, and inductive and

resonance contributions to the hole-density. In mesomeric push-pull TDMs we observed a significant contribution of anisole moieties to the hole-density, in contrast to related 6,6'-substituted isoindigos.

The analysis of the exciton binding energy showed that strongly polarised derivatives have lower exciton binding energies, and we discovered a relation in the *N,N*'-library between the bandgap and the exciton binding energy. A lower bandgap correlates with a lower Coulomb attraction between the electron and the hole, while this trend does not hold for the 6,6'-substitution patterns.

From electrochemical data of a limited subset of synthesised targets and a parametrisation method for E_{LUMO}, we developed a method for prediction of the reduction potentials of the library of *N*,*N*'-substituted isoindigos. We could enhance the prediction by discovering trends[52] towards the accurate calculation of electrochemical properties. The data elucidated a relationship between electron-donating (e.g. propyl) and -withdrawing (e.g. Boc) groups to decrease and increase the reduction potential in the *N,N*'-substitution patterns, respectively. This approach shows potential to be useful for rational design and library screening of similar compounds.

The structural variant of isoindigo, where an amide functionality is exchanged for a dimethylamine functionality, shows a markedly different electrochemical response for the second reduction. Furthermore, an indanone-bridged isoindigo variant was developed with a significantly high number of reduction events, resulting in a high charge density that could be of interest for application in organic electronics.

In conclusion, we successfully elucidated several *N,N*'-substitution effects in isoindigo, which shows potential for more extensive use in material sciences. Taking 27 as an example, the three consecutive CT states, in combination with a low exciton binding energy of 4.18 eV, and a low bandgap could enable broad spectral operating OPV-materials. We expect that this study will foster more detailed research on the electronic structure of substituted isoindigos. Additionally, we see major potential in the use of *N,N*'-substitution for optical and electronic tuning in cases where the 6,6'-site is already occupied.[53]

4. Experimental

4.1 General comments

For general information on chemicals, NMR spectroscopy, high-resolution mass spectrometry, cyclic voltammetry and DFT calculations, see Chapter 2.

In this chapter, dry solvents were collected from a Pure Solve MD5 solvent dispenser from Demaco, an MBraun SPS-800 solvent purification system, or by drying for 48 h over 3 Å molecular sieves. All CVs were recorded at room temperature, a scan speed 0.1 V/s under an argon atmosphere in acetonitrile, degassed by bubbling argon (>2 min prior to measurement) and tetrabutylammonium hexafluorophosphate (0.1 M) as supporting electrolyte. All isoindigo CVs were referenced to added ferrocene as internal reference.

Calculations were performed with the Gaussian16 software[54] on the Peregrine high performance computing cluster on computation nodes with two Intel Xeon E5 2680v3 or two Intel Xeon E5 2680v4 CPUs in a shared memory architecture connected by a 56 Gbps Infiniband network. Eight cores and 8 GB memory were used for each job. The isoindigo library was constructed by a preliminary molecular mechanics geometry optimisation on a set of 100 conformers and a single point calculation at the PM7 level of theory using the MOPAC2012 software.[55] The structures were further optimised in the gas phase and in different solvents (DMSO, MeCN, $CHCl_3$, Toluene, MeOH), using SMD solvent models,[35] at the ωB97X-D/def2-TZVP level of theory. Vibrational frequency analysis confirmed that the geometries were minimum energy states. Imaginary vibrational frequencies that corresponded to the *t*-butyl rotation were ignored if the optimisation criteria of the Gaussian16 software were met. After optimisation, the UV-Vis spectra of all molecules were simulated using TD-DFT calculations at the PBE0/cc-pVDC level of theory with the respective SMD-model over 25 states.

Further extensive details about the computational study, such as the geometries of the optimised structures, a full list of frontier orbitals, vertical excitation properties and transition density matrices can be found in the supplementary information of the published work related to this chapter.[43]

4.2 Synthesis and characterisation of compounds

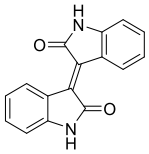

(*E*)-[3,3'-biindolinylidene]-2,2'-dione (**45**). Isatin (414 mg, 2.81 mmol, 1.03 equiv.) and 2-oxindole (364 mg, 2.73 mmol, 1.00 equiv.) were dissolved in glacial acetic acid (4.0 mL) and 4 drops of conc. HCl were added. The solution was stirred at 120 °C for 16 h and slowly cooled to room temperature. The precipitate was filtered off and rinsed with water and pentane. The solids were dried in vacuo yielding the title compound (556 mg, 2.10 mmol, 77%) as a dark violet powder. ^{1}H NMR (400 MHz, DMSO-d_6) δ = 10.88 (s, 1H), 9.06 (dd, *J* = 8.1, 1.2 Hz, 1H), 7.34 (ddd, *J* = 7.6, 7.6, 1.2 Hz, 1H), 6.96 (ddd, *J* = 7.8, 7.8, 1.2 Hz, 1H), 6.84 (d, *J* = 7.5 Hz, 1H). HRMS (ESI Pos): for $[C_{16}H_{11}N_2O_2]^+$ calcd. m/z = 263.0815, found m/z = 263.0819. Compound data is in accordance with literature.[56]

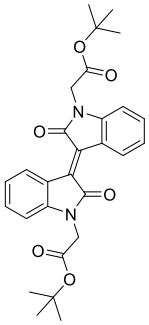

Di-tert-butyl 2,2'-(2,2'-dioxo-[3,3'-biindolinylidene]-1,1'-diyl)(*E*)-diacetate (**31**). Isoindigo (**45**, 72 mg, 0.27 mmol, 1.00 equiv.), Cs_2CO_3 (222 mg, 0.68 mmol, 2.50 equiv.), DMF (360 µL) and tert-butyl 2-bromoacetate (0.24 mL, 1.64 mmol, 6.00 equiv.) were added to a sealed tube and the mixture was stirred at room temperature for 15 h. The resulting mixture was diluted with EtOAc, washed twice with H_2O and the aqueous layer was extracted twice with CH_2Cl_2. The combined organic layers were dried over Na_2SO_4 and subsequently concentrated under reduced pressure. The product was purified by flash column chromatography (silica, EtOAc/Petroleum ether 40-60, 25%) and dried under vacuum. The product was obtained as a red solid in 53% yield (70 mg, 0.14 mmol). ^{1}H NMR (400 MHz, $CDCl_3$) δ = 9.20 (d, *J* = 8.0 Hz, 2H), 7.35 (dd, *J* = 7.7, 7.7 Hz, 2H), 7.07 (dd, *J* = 7.8, 7.8 Hz, 2H), 6.68 (d, *J* = 7.8 Hz, 2H), 4.46 (s, 4H), 1.46 (s, 18H). ^{13}C NMR (101 MHz, $CDCl_3$) δ = 166.7, 148.6, 144.3, 132.6, 130.3, 122.8, 121.8, 107.9,

82.9, 77.5, 77.16, 76.8, 42.3, 28.2. HRMS (ESI Pos): for $[C_{28}H_{30}N_2O_6Na]^+$ calcd. m/z = 513.1996, found m/z = 513.1983.

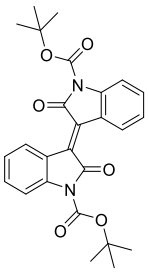

Di-tert-butyl (*E*)-2,2'-dioxo-[3,3'-biindolinylidene]-1,1'-dicarboxylate (**36**). To a solution of di-tert-butyl dicarbonate (410 mg, 1.88 mmol, 1.95 equiv.) in THF (1.0 mL) was added isoindigo (**45**, 255 mg, 0.96 mmol, 1.0 equiv.) in THF (17 mL) dropwise over 30 min at room temperature. DMAP (23.5 mg, 0.193 mmol, 0.20 equiv.) was added and the mixture was stirred at room temperature for 18 h. The volatiles were evaporated at 75 °C and the solid residue was diluted in EtOAc and washed with 1 M NH_4Cl (aq) solution twice. The product was extracted from the aqueous layer with CH_2Cl_2 and dried over Na_2SO_4. Volatiles were removed under reduced pressure and the product was dried under vacuum. No further purification was required and the product was obtained as a red solid in 84% yield (376 mg, 0.81 mmol). ^{1}H NMR (400 MHz, $CDCl_3$) δ = 8.96 (dd, *J* = 8.2, 1.3 Hz, 2H), 7.81 (d, *J* = 8.3 Hz, 2H), 7.43 (ddd, *J* = 8.5, 7.5, 1.3 Hz, 2H), 7.17 (ddd, *J* = 8.4, 7.5, 1.2 Hz, 2H), 1.68 (s, 18H). Compound data is in accordance with literature.[57]

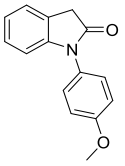

1-(4-methoxyphenyl)indolin-2-one (**58**). Oxindole (488 mg, 3.67 mmol, 1.20 equiv.), 4-iodoanisol (715 mg, 3.06 mmol, 1.00 equiv.), K_2CO_3 (844 mg, 6.11 mmol, 2.00 equiv.) and CuI (29 mg, 0.15 mmol, 0.05 equiv.) were added to a crimp top vial under N_2 atmosphere. Dry 1,4-dioxane (3.0 mL) and 1,2-dimethylethylenediamine (0.05 mL, 0.46 mmol, 0.15 equiv.) were added and the reaction mixture which was subsequently stirred for 22 h at 110 °C. The reaction mixture was allowed to cool to room temperature under continuous stirring. The crude mixture was filtered through a plug of silica gel and washed with EtOAc. The filtrate was concentrated under reduced and the product was purified by flash column chromatography (silica, EtOAc/Petroleum ether 40-60, 20–40%). The product was obtained as a white solid in 12% yield (85 mg, 0.354 mmol). ^{1}H NMR (400 MHz $CDCl_3$) δ =

7.34 – 7.28 (m, 3H), 7.20 (ddd, J = 7.8, 7.8, 1.1 Hz, 1H), 7.09 – 7.02 (m, 3H), 6.73 (d, J = 7.9 Hz, 1H), 3.86 (s, 3H), 3.70 (s, 2H). ^{13}C NMR (101 MHz, $CDCl_3$) δ = 174.9, 159.3, 145.8, 128.1, 127.9, 127.2, 124.7, 124.4, 122.8, 115.1, 109.4, 55.7, 36.1. Compound data is in accordance with literature.[58]

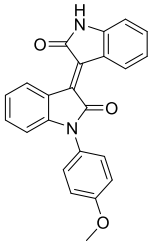

(*E*)-1-(4-methoxyphenyl)-[3,3'-biindolinylidene]-2,2'-dione (**30**). Isatin (22 mg, 0.15 mmol, 1.4 equiv.) and 1-(4-methoxyphenyl)indolin-2-one (**58**, 25 mg, 0.1 mmol, 1.0 equiv.) were dissolved in glacial acetic acid (0.2 mL) and 2 drops of conc. HCl (aq) were added. The solution was stirred at 120 °C for 2 h turning dark red. The reaction mixture was diluted with EtOAc and washed with water, dried over Na_2SO_4 and volatiles were removed under reduced pressure. The product was purified by flash column chromatography (silica, EtOAc/Petroleum ether 40-60, 25%) and obtained as a red solid in 43% yield. (17 mg, 0.05 mmol). ^{1}H NMR (400 MHz, $CDCl_3$) δ = 9.18 (d, J = 4.9 Hz, 1H), 9.16 (d, *J* = 5.2 Hz, 1H), 7.54 – 7.52 (m, 2H), 7.38 – 7.27 (m, 3H), 7.13 – 7.04 (m, 3H), 7.00 (ddd, *J* = 7.9, 7.5, 1.2 Hz, 1H), 6.81 (d, *J* = 8.2 Hz, 1H), 6.68 (d, *J* = 8.3 Hz, 1H), 3.88 (s, 3H). ^{13}C NMR (101 MHz, $CDCl_3$) δ = 132.8, 132.6, 130.6, 130.0, 128.6, 122.9, 122.6, 115.2, 109.3, 109.2, 77.5, 77.2, 76.8, 55.7. HRMS (ESI Pos): for $[C_{23}H_{17}N_2O_3]^+$ calcd. m/z = 369.1234, found m/z = 369.1231.

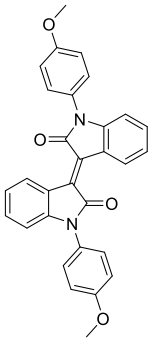

During the aforementioned synthesis of (*E*)-1-(4-methoxyphenyl)-[3,3'-biindolinylidene]-2,2'-dione (**30**), homocoupling of 1-(4-methoxyphenyl)indolin-2-one occurred and (*E*)-1,1'-bis(4-methoxyphenyl)-[3,3'-biindolinylidene]-2,2'-dione (**25**) was obtained as a red solid in 4% yield (3 mg, 0.01 mmol). ^{1}H NMR (400 MHz, $CDCl_3$) δ = 9.22

(d, *J* = 8.1 Hz, 2H), 7.41 – 7.32 (m, 4H), 7.29 (dd, *J* = 7.7, 1.2 Hz, 2H), 7.10 – 7.06 (m, 4H), 7.03 (ddd, *J* = 7.9, 7.9, 1.2 Hz, 2H), 6.69 (d, *J* = 7.6 Hz, 2H), 3.88 (s, 6H). HRMS (ESI Pos): for $[C_{30}H_{23}N_2O_4]^+$ calcd. m/z = 475.1652, found m/z = 475.1638.

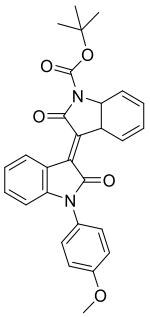

Tert-butyl(*E*)-1'-(4-methoxyphenyl)-2,2'-dioxo-[3,3'-biindolinylidene] -1-carboxylate (**27**). (*E*)-1-(4-methoxyphenyl)-[3,3'-biindolinylidene]-2,2'-dione (**30**, 2.0 mg, 0.005 mmol, 1.0 equiv.) and di-tert-butyl dicarbonate (4.0 mg, 0.02 mmol, 4.0 equiv.) were dissolved in 1.0 mL THF. One crumble of 4-dimethylaminopyridine was added and the mixture was stirred at room temperature for 4 h. Volatiles were removed under reduced pressure at 75 °C. The mixture was diluted with EtOAc and washed with 1.0 M NH_4Cl (aq). The aqueous layer was extracted with CH_2Cl_2 and the combined organic layers were dried over Na_2SO_4. The product was dried under vacuum and obtained as a red solid in ~68% yield (1.8 mg, 0.004 mmol). ^{1}H NMR (600 MHz, C_6D_6) δ 9.60 (dd, *J* = 8.2, 1.3 Hz, 1H), 9.33 (dd, *J* = 8.0, 1.2 Hz, 1H), 8.12 (dd, *J* = 8.2, 1.1 Hz, 1H), 7.10 – 7.01 (m, 3H), 6.97 – 6.88 (m, 2H), 6.85 (ddd, *J* = 7.9, 7.7, 1.3 Hz, 1H), 6.77 – 6.71 (m, 2H), 6.45 (dd, *J* = 7.7, 1.2 Hz, 1H), 3.25 (s, 3H), 1.51 (s, 9H). HRMS (ESI Pos): [M-H_2+Na]$^+$, for $[C_{28}H_{24}N_2O_5Na]^+$, m/z calcd. 491.15774, found 491.15671.

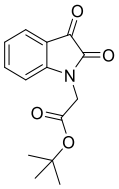

Tert-butyl 2-(2,3-dioxoindolin-1-yl)acetate (**59**). Isatin (505 mg, 3.43 mmol, 1.00 equiv.), Cs_2CO_3 (2.35 g, 7.21 mmol, 2.10 equiv.), DMF (2.0 mL) and tert-butyl bromoacetate (2.0 mL, 13.7 mmol, 4.00 equiv.) were added to a sealed vial and the mixture was stirred at room temperature for 15 h. The resulting mixture was diluted with EtOAc, washed with H_2O and the aqueous layer was re-extracted with EtOAc. The combined organic layers were dried over Na_2SO_4 and the product was purified by flash column chromatography

(silica, EtOAc/Petroleum ether 40-60, 50%). The product was obtained as a dark orange solid in 76% yield (685 mg, 2.62 mmol). ^{1}H NMR (400 MHz, $CDCl_3$) δ = 7.64 (ddd, *J* = 7.4, 1.4, 0.6 Hz, 1H), 7.59 (ddd, J = 7.8, 7.8, 1.3 Hz, 1H), 7.15 (dd, *J* = 7.6, 7.6 Hz, 1H), 6.77 (d, *J* = 8.0 Hz, 1H), 4.39 (s, 2H), 1.46 (s, 9H). ^{13}C NMR (101 MHz, $CDCl_3$) δ = 182.8, 165.9, 158.2, 150.7, 138.5, 125.7, 124.2, 117.8, 110.3, 83.6, 77.5, 77.2, 76.8, 42.2, 28.1. HRMS (ESI Pos): for $[C_{14}H_{15}NO_4Na]^+$ calcd. m/z = 284.0893, found m/z = 284.0899.

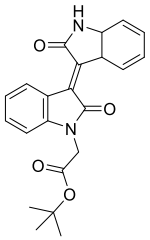

Tert-butyl (*E*)-2-(2,2'-dioxo-[3,3'-biindolinylidene]-1-yl)acetate (**35**). Tert-butyl 2-(2,3-dioxoindolin-1-yl)acetate (**59**, 44 mg, 0.17 mmol, 1.0 equiv.) and 2-oxindole (22 mg, 0.17 mmol, 1.0 equiv.) were dissolved in glacial acetic acid (1.0 mL) and 2 drops of HCl were added. The mixture was stirred at reflux temperature for 4.5 h and subsequently for 16 h at room temperature. The reaction mixture was filtered and the residue was washed with water, *n*-pentane and carefully with EtOAc. The product was dried under vacuum and obtained as a red solid. ^{1}H NMR (400 MHz, DMSO-d_6) δ 10.94 (s, 1H), 9.15 – 9.08 (m, 1H), 9.02 (d, *J* = 8.0 Hz, 1H), 7.41 (ddd, *J* = 7.7, 7.7, 1.2 Hz, 1H), 7.36 (ddd, *J* = 7.6, 7.6, 1.2 Hz, 1H), 7.10 – 7.02 (m, 2H), 6.97 (dd, *J* = 7.8, 7.8 Hz, 1H), 6.85 (dd, *J* = 7.9, 1.1 Hz, 1H), 4.58 (s, 2H), 3.32 (s, 9H). ^{13}C NMR (101 MHz, DMSO-d_6) δ = 169.2, 168.8, 167.4, 144.4, 144.1, 134.2, 133.1, 132.5, 131.6, 129.4, 129.1, 121.9, 121.6, 121.2, 120.8, 109.7, 108.7, 41.2, 40.2, 40.0, 39.9, 39.7, 39.5, 39.3, 39.1, 38.9.

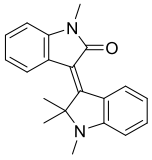

(*E*)-1,1',2',2'-tetramethyl-[3,3'-biindolinylidene]-2-one (**55**). Obtained via Knoevenagel condensation of 1,2,2-trimethylindolin-3-one and 1-methylindolin-2-on. ^{1}H NMR (600 MHz, $CDCl_3$) δ 8.01 (bs, 1H), 8.03 (d, *J* = 8.2 Hz, 1H), 7.32 – 7.28 (m, 1H), 7.17 (dd, *J* = 7.6, 7.6 Hz, 1H), 6.91 (dd, *J* = 7.7, 7.7 Hz, 1H), 6.80 (d, *J* = 7.8 Hz, 1H), 6.61 (dd, *J* = 7.5, 7.5 Hz, 1H), 6.54 (d, *J* = 8.2 Hz, 1H), 3.27 (s, 3H), 2.83 (s, 3H), 1.80 (s, 6H). ^{13}C NMR (151 MHz, $CDCl_3$) δ 167.6, 164.0, 156.9, 142.2, 134.9, 127.9, 127.4, 123.7, 123.2, 121.5, 120.8, 116.6, 116.2, 108.2, 107.7, 28.0, 26.0, 19.8. HRMS (ESI Pos): for

$[C_{20}H_{20}N_2O]^+$ calcd. m/z = 305.1648, found m/z = 305.1650. Provided by Daniel Döllerer.

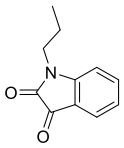

1-Propylindoline-2,3-dione (**56**). Isatin (560 mg, 3.8 mmol, 1.0 equiv.), Cs_2CO_3 (200 mg, 0.61 mmol, 0.16 equiv.) and 1-bromopropane (1.4 mL, 15 mmol, 4.0 equiv.) were dissolved in 1.0 mL DMF and the mixture was stirred at room temperature for 16 h. The resulting mixture was diluted with EtOAc, washed three times with water and the aqueous layer was back-extracted once with EtOAc. The combined organic layers were dried over $MgSO_4$ and concentrated under reduced pressure. The product was purified by flash column chromatography (silica, EtOAc/*n*-pentane, 20–50%) and obtained as an orange solid in 22% yield. (157 mg, 0.83 mmol). ^{1}H NMR (600 MHz, $CDCl_3$) δ 7.63 – 7.50 (m, 2H), 7.11 (dd, *J* = 7.5 Hz, 1H), 6.90 (d, *J* = 7.9 Hz, 1H), 3.69 (t, *J* = 6.6 Hz, 2H), 1.79 – 1.70 (m, 2H), 1.00 (t, *J* = 7.4 Hz, 3H). ^{13}C NMR (151 MHz, $CDCl_3$) δ 183.8, 158.3, 151.3, 138.4, 125.6, 123.7, 117.7, 110.3, 42.0, 20.8, 11.5. Compound data is in accordance with literature.[59]

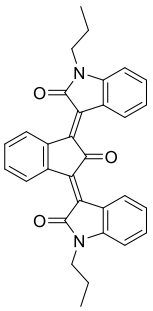

3,3'-((1E,3E)-2-oxo-1H-indene-1,3(2H)-diylidene)bis(1-propylindolin-2-one) (**57**). 1-Propylindoline-2,3-dione (56, 62 mg, 0.33 mmol, 1.0 equiv.) and 2-indanone (22 mg, 0.16 mmol, 0.5 equiv.)were dissolved in glacial acetic acid (1.5 mL) with 2 drops of conc. HCl. The mixture was stirred while heated at reflux for 3 h. After cooling to room temperature, water was added to the mixture and the mixture was extracted with EtOAc, washed with water and dried over $MgSO_4$. The product was purified by flash column chromatography (silica, EtOAc/*n*-pentane, 25-50%) and obtained as a dark red solid in 41% yield. (65 mg, 0.14 mmol). ^{1}H NMR (600 MHz, $CDCl_3$) δ 9.02 – 8.93 (m, 2H), 8.86 (d, *J* = 7.9 Hz, 2H), 7.55 – 7.49 (m, 2H), 7.40 – 7.34 (m, 2H), 7.15 – 7.08 (m, 2H), 6.82 (d, *J* = 7.8 Hz, 2H), 3.75 (t, *J* = 7.4 Hz, 4H), 1.78 – 1.72 (m, 4H), 1.00 (t, *J* = 7.4 Hz, 6H). ^{13}C NMR (151 MHz, $CDCl_3$) δ 194.7, 167.7, 144.6, 140.8, 138.4, 131.8, 131.3, 129.2, 129.1, 127.7, 122.3, 122.1,

108.2, 41.8, 21.0, 11.6. HRMS (ESI Pos): for $[C_{31}H_{28}N_2O_3Na]^+$ calcd. m/z = 497.1836, found 497.1825.

4.3 Electrochemistry

Cyclic voltammetry used in this chapter, but not shown in the main text is shown here:

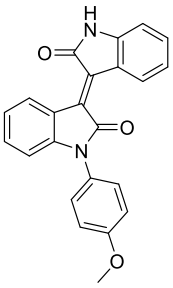

30

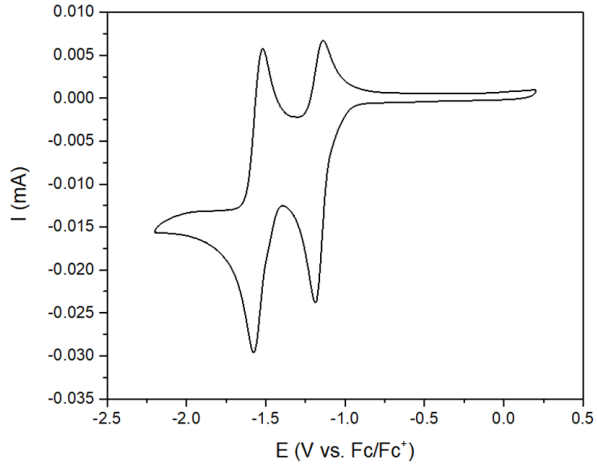

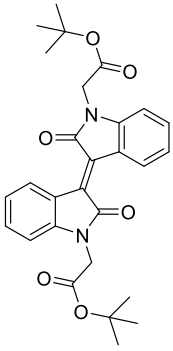

31

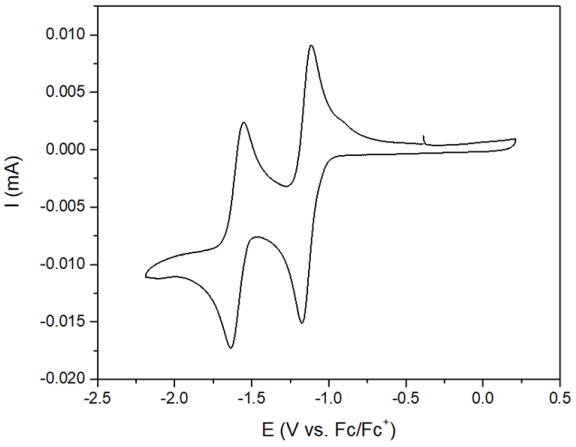

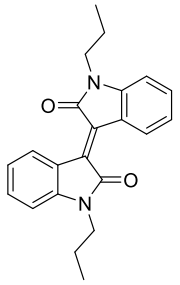

46

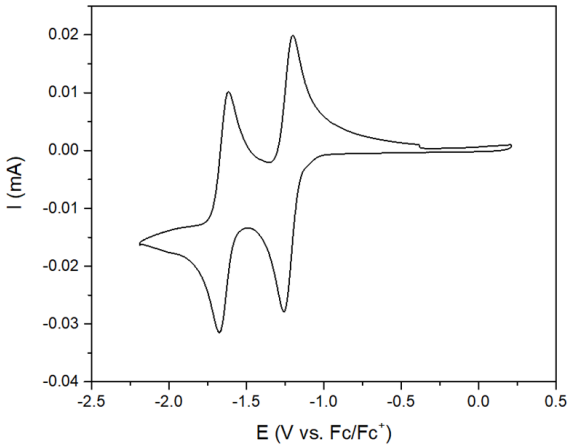

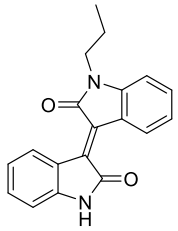

47

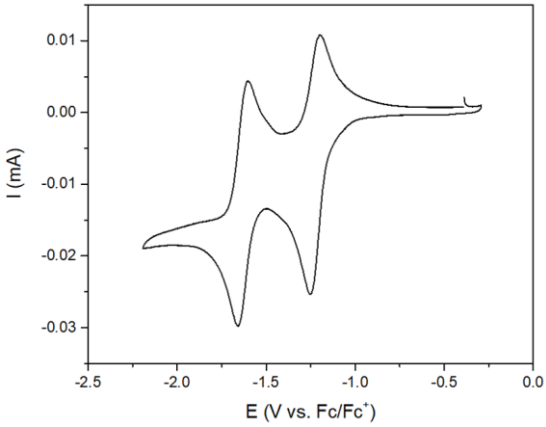

Table 3. Parametrisation of E_{LUMO} and corresponding reduction half-wave potentials ($E_{1/2}$)

Compound	E_{LUMO} [Ha]	E_{LUMO} [eV]	$E_{LUMO\ param.}$ [eV]	$E_{1/2}$ [V] according to eq. 1
1	-0.10328	-2.81	-4.02	-1.08
2	-0.10640	-2.90	-4.10	-1.00
3	-0.10578	-2.88	-4.09	-1.01
4	-0.10267	-2.79	-4.01	-1.09
5	-0.10251	-2.79	-4.00	-1.10
6	-0.10672	-2.90	-4.11	-0.99
7	-0.10500	-2.86	-4.07	-1.03
8	-0.10203	-2.78	-3.99	-1.11
9	-0.10148	-2.76	-3.97	-1.13
10	-0.10818	-2.94	-4.15	-0.95

11	-0.10852	-2.95	-4.16	-0.94
12	-0.10542	-2.87	-4.08	-1.02
13	-0.10543	-2.87	-4.08	-1.02
14	-0.10958	-2.98	-4.19	-0.91
15	-0.10754	-2.93	-4.13	-0.97
16	-0.10574	-2.88	-4.09	-1.01
17	-0.10393	-2.83	-4.04	-1.06
18	-0.10790	-2.94	-4.14	-0.96
19	-0.10414	-2.83	-4.04	-1.06
20	-0.10484	-2.85	-4.06	-1.04
21	-0.10901	-2.97	-4.17	-0.93
22	-0.10716	-2.92	-4.12	-0.98
23	-0.10560	-2.87	-4.08	-1.02
24	-0.10338	-2.81	-4.02	-1.08
25	-0.10174	-2.77	-3.98	-1.12
26	-0.10158	-2.76	-3.98	-1.12
27	-0.10604	-2.89	-4.09	-1.01
28	-0.10403	-2.83	-4.04	-1.06
29	-0.10264	-2.79	-4.00	-1.10
30	-0.10071	-2.74	-3.95	-1.15
31	-0.10153	-2.76	-3.98	-1.12
32	-0.10613	-2.89	-4.10	-1.00
33	-0.10401	-2.83	-4.04	-1.06
34	-0.10237	-2.79	-4.00	-1.10
35	-0.10068	-2.74	-3.95	-1.15
36	-0.11037	-3.00	-4.21	-0.89
37	-0.10827	-2.95	-4.15	-0.95
38	-0.10701	-2.91	-4.12	-0.98
39	-0.10519	-2.86	-4.07	-1.03
40	-0.10629	-2.89	-4.10	-1.00
41	-0.10486	-2.85	-4.06	-1.04
42	-0.10309	-2.81	-4.02	-1.08
43	-0.10351	-2.82	-4.03	-1.07
44	-0.10130	-2.76	-3.97	-1.13
45	-0.10001	-2.72	-3.94	-1.16
46	-0.09957	-2.71	-3.92	-1.18

47	-0.09926	-2.70	-3.92	-1.18
48	-0.08606	-2.34	-3.57	-1.53
49	-0.10977	-2.99	-4.19	-0.91
50	0.03411	0.93	-0.43	-4.67

4.4 UV-Vis spectroscopy

UV-Vis spectra of a number of isoindigos from the library in MeCN at the indicated concentrations (grey lines) and . Included is the molar attenuation coefficient (ε) in M^{-1} cm^{-1} determined at the absorption maximum for the first transition around 510 nm, except for **27**, where the absorption maximum of the next transition (λ = 396 nm) was used.

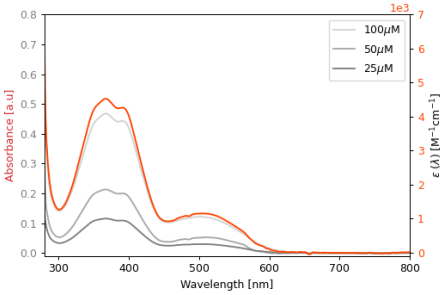

25, ε = 1250

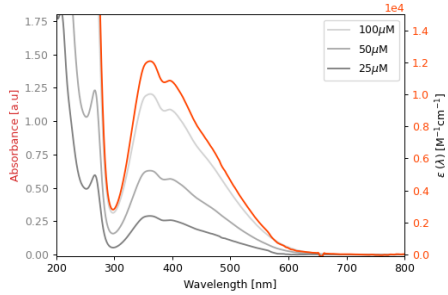

27, ε $_{(\lambda = 396\ nm)}$ = 10865

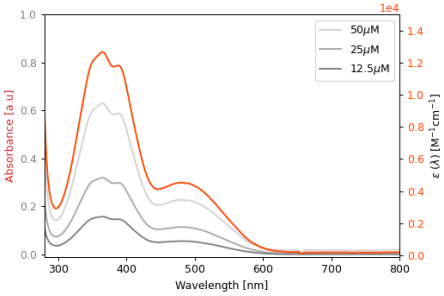

30, ε = 5277

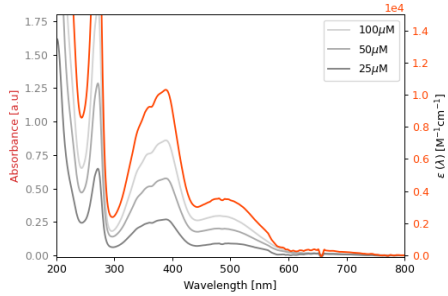

31, ε = 3501

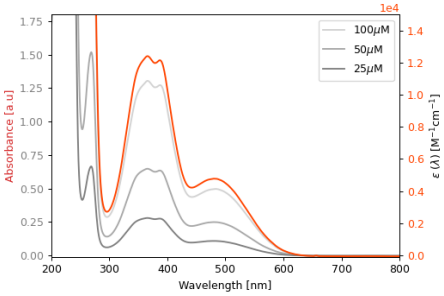

35, ε = 4773

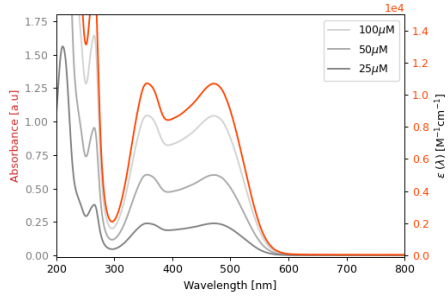

36, ε = 10695

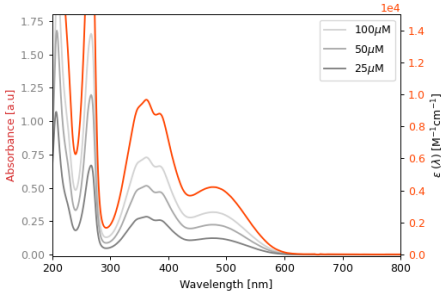

45, ε = 4208

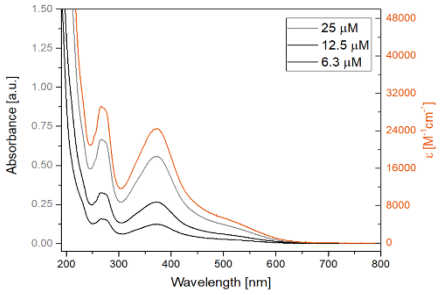

57, ε = 24367

5. References

1 Laurent, *J. für Prakt. Chemie*, 1842, **26**, 123–125.
2 L. Sander, *Ber. Dtsch. Chem. Ges.*, 1925, **58,** 820–824.
3 X. K. Wee, W. K. Yeo, B. Zhang, V. B. C. Tan, K. M. Lim, T. E. Tay and M. L. Go, *Bioorg. Med. Chem.*, 2009, **17**, 7562–7571.
4 A. V. Bogdanov, L. I. Musin and V. F. Mironov, *Arkivoc*, 2015, **2015**, 362–392.
5 L. A. Estrada, R. Stalder, K. A. Abboud, C. Risko, J. L. Brédas and J. R. Reynolds, *Macromolecules*, 2013, **46**, 8832–8844.
6 P. Zhao, Y. Li, G. Gao, S. Wang, Y. Yan, X. Zhan, Z. Liu, Z. Mao, S. Chen and L. Wang, *Eur. J. Med. Chem.*, 2014, **86**, 165–174.
7 P. Friedländer, *Ber. Dtsch. Chem. Ges.*, 1906, **39**, 1060–1066.
8 E. Steingruber, in *Ullmann's Encyclopedia of Industrial Chemistry*, Wiley-VCH Verlag GmbH & Co. KGaA, Weinheim, Germany, 2000.
9 M. Hosseinnezhad, S. Moradian and K. Gharanjig, *Dyes and Pigments*, 2015, **123**, 147–153.
10 A. K. Rajan and L. Cindrella, *Opt. Mater.*, 2019, **88**, 39–47.
11 C. Petermayer, S. Thumser, F. Kink, P. Mayer and H. Dube, *J. Am. Chem. Soc.*, 2017, **139**, 15060–15067.
12 A. Gerwien, P. Mayer and H. Dube, *Nat. Commun.*, 2019, **10**, 4449.
13 A. Gerwien, T. Reinhardt, P. Mayer and H. Dube, *Org. Lett.*, 2018, **20**, 232–235.
14 A. Sailer, F. Ermer, Y. Kraus, F. H. Lutter, C. Donau, M. Bremerich, J. Ahlfeld and O. Thorn-Seshold, *ChemBioChem*, 2019, **20**, 1305–1314.
15 S. Wiedbrauk and H. Dube, *Tetrahedron Lett.*, 2015, **56**, 4266–4274.
16 R. Stalder, J. Mei and J. R. Reynolds, *Macromolecules*, 2010, **43**, 8348–8352.
17 N. M. Randell and T. L. Kelly, *Chem. Rec.*, 2019, **19**, 973–988.
18 S. Luňák, P. Horáková and A. Lyčka, *Dyes and Pigments*, 2010, **85**, 171–176.
19 J. Huang, Z. Chen, Z. Mao, D. Gao, C. Wei, Z. Lin, H. Li, L. Wang, W. Zhang and G. Yu, *Adv. Electron. Mater.*, 2017, **3**, 1700078.
20 G. Zhang, Y. Fu, Z. Xie and Q. Zhang, *Macromolecules*, 2011, **44**, 1414–1420.
21 D. Wang, W. Ying, X. Zhang, Y. Hu, W. Wu and J. Hua, *Dyes and Pigments*, 2015, **112**, 327–334.

22 E. A. Perpète, J. Preat, J. M. André and D. Jacquemin, *J. Phys. Chem. A*, 2006, **110**, 5629–5635.
23 M. U. Munshi, J. Martens, G. Berden and J. Oomens, *J. Phys. Chem. A*, 2019, **123**, 8226–8233.
24 L. Wang, S. Bai, Y. Wu, Y. Liu, J. Yao and H. Fu, *Angew. Chem. Int. Ed.*, 2020, **59**, 2003–2007.
25 Y. Rout, V. Chauhan and R. Misra, *J. Org. Chem.*, 2020, **85**, 4611–4618.
26 C. N. Cavasotto, M. G. Aucar and N. S. Adler, *Int. J. Quantum Chem.*, 2019, **119**, e25678.
27 L.-Q. Chen, L.-D. Chen, S. V. Kalinin, G. Klimeck, S. K. Kumar, J. Neugebauer and I. Terasaki, *NPJ Comput. Mater.*, 2015, **1**, 15007.
28 P. Geerlings and F. de Proft, *Phys. Chem. Chem. Phys.*, 2008, **10**, 3028–3042.
29 S. Mai, A. J. Atkins, F. Plasser and L. González, *J. Chem. Theory Comput.*, 2019, **15**, 3470–3480.
30 A. D. Laurent and D. Jacquemin, *Int. J. Quantum Chem.*, 2013, **113**, 2019–2039.
31 S. S. Leang, F. Zahariev and M. S. Gordon, *J. Chem. Phys.*, 2012, **136**, 104101.
32 T. Ohto, M. Dodia, J. Xu, S. Imoto, F. Tang, F. Zysk, T. D. Kühne, Y. Shigeta, M. Bonn, X. Wu and Y. Nagata, *J. Phys. Chem. Lett.*, 2019, **10**, 4914–4919.
33 J. P. Perdew, in *AIP Conference Proceedings*, AIP Publishing, 2003, vol. 577, pp. 1–20.
34 A. Marini, A. Muñoz-Losa, A. Biancardi and B. Mennucci, *J. Phys. Chem. B*, 2010, **114**, 17128–17135.
35 A. V. Marenich, C. J. Cramer and D. G. Truhlar, *J. Phys. Chem. B*, 2009, **113**, 6378–6396.
36 C. Adamo and V. Barone, *J. Chem. Phys.*, 1999, **110**, 6158–6170.
37 T. H. Dunning, *J. Chem. Phys.*, 1989, **90**, 1007–1023.
38 B. Demoulin, M. M. T. El-Tahawy, A. Nenov, M. Garavelli and T. Le Bahers, *Theor. Chem. Acc.*, 2016, **135**, 96.
39 Y. Li and C. A. Ullrich, *Chem. Phys.*, 2011, **391**, 157–163.
40 H. Sun, D. Liu, T. Wang, P. Li, C. N. Bridgmohan, W. Li, T. Lu, W. Hu, L. Wang and X. Zhou, *Org. Electron.*, 2018, **61**, 35–45.
41 H.-W. Li, Z. Guan, Y. Cheng, T. Lui, Q. Yang, C.-S. Lee, S. Chen and S.-W. Tsang, *Adv. Electron. Mater.*, 2016, **2**, 1600200.
42 T. Lu and F. Chen, *J. Comput. Chem.*, 2012, **33**, 580–592.
43 F. L. Kiss, B. P. Corbet, N. A. Simeth, B. L. Feringa and S. Crespi, *Photochem. Photobiol. Sci.*, 2021, **20**, 927–938.
44 X. Mu, J. Wang and M. Sun, *J. Phys. Chem. C*, 2019, **123**, 14132–14143.
45 Y. Dawei, Z. Xiaojuan, W. Zhiming, Y. Bing, M. Yuguang and P. Yuyu, *RSC Adv.*, 2018, **8**, 27979–27987.
46 T. Koopmans, *Physica*, 1934, **1**, 104–113.
47 C. G. Zhan, J. A. Nichols and D. A. Dixon, *J. Phys. Chem. A*, 2003, **107**, 4184–4195.
48 C. M. Cardona, W. Li, A. E. Kaifer, D. Stockdale and G. C. Bazan, *Adv. Mater.*, 2011, **23**, 2367–2371.
49 V. V. Pavlishchuk and A. W. Addison, *Inorganica Chim. Acta*, 2000, **298**, 97–102.

50 L. S. Albuquerque, J. J. R. Arias, B. P. Santos, M. de F. V. Marques and S. N. Monteiro, *J. Mater. Res. Technol.*, 2020, **9**, 7975–7988.

51 L. Leonat, G. Sbârcea and I. V. Brânzoi, *U.P.B. Sci. Bull., Ser. B*, 2013, **75**, 112–118.

52 M. Karakawa, T. Nagai, K. Adachi, Y. Ie and Y. Aso, *RSC Adv.*, 2017, **7**, 7122–7129.

53 P. Liesfeld, Y. Garmshausen, S. Budzak, J. Becker, A. Dallmann, D. Jacquemin and S. Hecht, *Angew. Chem. Int. Ed.*, 2020, **59**, 19352–19358.

54 Gaussian 16, Rev. B.01, M. J. Frisch, G. W. Trucks, H. B. Schlegel, G. E. Scuseria, M. A. Robb, J. R. Cheeseman, G. Scalmani, V. Barone, G. A. Petersson, H. Nakatsuji, *et al.*, Gaussian, Inc., Wallingford, CA, 2016.

55 MOPAC2012, J. J. P. Stewart, 2012, http://openmopac.net.

56 X. Yao, T. Wang and Z. Zhang, *Eur. J. Org. Chem.*, 2018, 4475–4478.

57 B. M. Trost and M. Osipov, *Angew. Chem. Int. Ed.*, 2013, **52**, 9176–9181.

58 R. A. Altman, A. M. Hyde, X. Huang and S. L. Buchwald, *J. Am. Chem. Soc.*, 2008, **130**, 9613–9620.

59 A. D. Mamuye, S. Monticelli, L. Castoldi, W. Holzer and V. Pace, *Green Chem.*, 2015, **17**, 4194–4197.

Chapter 7

Helical Chirality-Controlled Rotational Molecular Motion

Four overcrowded alkenes, containing a fluorenyl-helicene motif, were studied as targets for the development of unidirectional rotational molecular motors controlled exclusively by helical chirality. These structures are promising candidates for new molecular switches and motors and have potential applications as electrochemical switches. By DFT and spin-flip TD-DFT calculations we investigated the enantiomeric stability of the methyl-fluorenyl-helicene motif and found an acceptably high barrier for helix inversion. Computational studies confirm that the target compounds are promising as switches and motors, but further extensive studies are required for a full understanding of the photochemical and thermal switching processes. In addition to these theoretical studies, a helically chiral ketone was synthesised as an important building block for the target molecules. A number of strategies for the synthesis of the target overcrowded alkenes have been attempted and further routes are discussed.

Acknowledgements
I would like to thank Rutger Schim van der Loeff and Dr. Romain Costil for their contributions to the synthesis discussed in this chapter. I would further like to thank Dr. Stefano Crespi for fruitful discussions about computational chemistry.

1. Introduction

Overcrowded alkenes are a class of molecules with a myriad of fascinating properties.[1–3] Our group has a long-vested interest in overcrowded alkene-based molecular switches and motors,[4–8] which has led to an ongoing search for novel structures and the investigation of new scaffolds to study their switching properties. The application of such switches is discussed in the previous chapters.

Since the establishments of the unidirectional photochemically-driven molecular rotary motors,[9,10] our group has been investigating different motor scaffolds and different methods to drive unidirectional rotation.[4,11] The various generations of molecular motors notably have a different number of stereogenic centres (see also Chapter 1). Unidirectional rotation of overcrowded alkenes usually relies on the chirality and (pseudo)axial- or (pseudo)equatorial orientation of a stereogenic alkyl group. The important fundamental step of thermal helix inversion (THI), governing the overall speed of rotation, is based on the inversion of helical chirality of the overcrowded alkene. For the further development of new motor structures, we envisioned to use a helically chiral rotor for overcrowded alkene-based rotary motion.

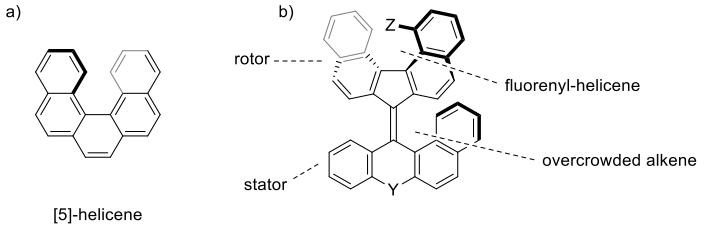

Figure 1. a) [5]-Helicene. b) General example of a fluorenyl-helicene rotor overcrowded alkene.

One of the most widely studied compounds with helical chirality is the class of helicenes (Figure 1a).[12–16] A chain of *ortho*-fused aromatic rings cannot adopt a planar geometry due to steric strain, which in turn leads to their helical shape. Helicenes (Figure 1a) and helicene-like structures can be used as a chiral motif in a molecule with exclusively sp^2-hybridised carbon atoms. The helical geometrical implications of such structures lead to a distortion of the conjugated π-system. This results in many fascinating optoelectronic effects.[12–16] The configurational stability of helicenes depends on the barrier for interconversion of the helix. For example, for [5]-helicene this barrier is $\Delta E^{\ddagger}_{isom.}$ = 102.1 kJ mol^{-1}.[17] In combination with an overcrowded alkene, a motif such as a helicene or a structural variant (e.g. Figure 1b) could provide a step towards a new class of motors.

The structure in Figure 1b is reminiscent of a previously developed molecular motor with an extended aromatic core,[18] but notably does not have a stereogenic methyl substituent. The enantiomeric stability of the helicene motif is important for the switching of these molecules. If substituent Z (Figure 1b) does not enforce a fixed helical shape, the interconversion between helical stereoisomers is likely to occur at room temperature. With a small barrier for this interconversion, a paddling motion of the helicene motif could be driven by rotary movement of the opposing half. There are ongoing studies into this paddling motion with similar molecular scaffolds in our group. This chapter will focus on stable helical motifs to control rotary motion.

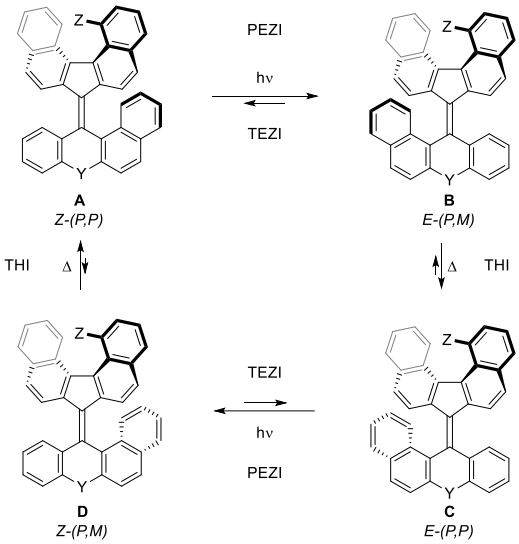

Scheme 1. Fundamental steps of the unidirectional rotation with an exclusively helically chiral overcrowded alkene. PEZI = photochemical *E*/*Z*-isomerisation, TEZI = thermal *E*/*Z*-isomerisation, THI = thermal helix inversion.

The envisioned unidirectional rotation in helical chirality-controlled molecular motion is expected to follow similar steps to previously developed molecular motors. From the thermodynamically most stable state (Scheme 1, **A**), a photochemical *E*/*Z*-isomerisation occurs, resulting in a higher energy *metastable* state **B**. Because of the interaction between the lower half and the upper half, the photoisomerisation product has increased strain within the molecule. From this *metastable* state, a THI can occur to alleviate this strain, resulting in more stable state **C** with the two halves rotated 180° with respect to each other. Repetition of the photochemical *E*/*Z*-isomerisation towards **D** and subsequent THI will result in the original stable state **A**, completing the 360°, unidirectional rotation.

The proposed design requires that the helical chirality of the upper half is retained at the temperature required for the thermal helix inversion. Furthermore, the interaction between the two halves has to provide a sufficient driving force and directionality for the THI. This means that the potential for the molecule to be used as motor is a matter of a difference in energy between the diastereomeric structures. With these design principles in mind, we envisioned overcrowded alkenes **1–4** (Figure 2) as good candidates to study the helical chirality controlled unidirectional rotation.

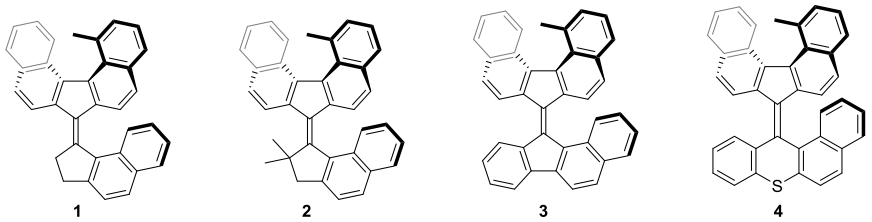

Figure 2. Target overcrowded alkenes **1–4**.

A methyl group in the fluorenyl-helicene motif was chosen in the design of the target molecules as it was expected to be synthetically accessible, provide a good handle for analysis by NMR spectroscopy and would likely provide a stable helical configuration, compared to the thermal helix inversion steps.[19] Furthermore, in contrast to common molecular motors, the designed targets **2**, **3** and **4** have no allylic hydrogen. In previous research into the development of electrochemically driven molecular motors (see also Chapter 2), the allylic hydrogen was found to be prone to deprotonation upon oxidation, leading to side reactions and as a result, molecular rotation was not feasible. Therefore, targets **2**, **3** and **4** are also compounds of interest for redox-driven switching and potentially electrochemically driven rotational motion.

The goal of this project is to investigate fluorenyl-helicene based overcrowded alkenes by computational and experimental methods. We wanted to investigate the photochemical and electrochemical properties of this new scaffold and develop new switches and a unidirectional rotary motor controlled exclusively by helical chirality.

2. Results & Discussion

2.1 Helix inversion of the fluorenyl-helicene motif

The steric hindrance in the fluorenyl-helicene motif has an influence on its enantiomeric stability. Using this motif to drive unidirectional motion would require the rotor helix inversion to be outside the energy range of other thermal steps occurring during rotation. Therefore, we first investigated the thermal helix inversion of the target methyl-fluorenyl-helicene motif (Figure 2) using DFT calculations.

The *Z*-(*P*,*M*) isomer of **1** has two helically chiral motifs (Figure 3): one formed by the fluorenyl-helicene motif (Figure 3, indicated red) and one formed by the helical structure at the central olefinic bond (Figure 3, indicated blue). Indeed, there are two helix inversion processes possible, one inverting the helicity of the rotor and stator halves and one inverting the helicity of the fluorenyl-helicene motif. Figure 3 shows a calculated reaction pathway for helix inversion of the fluorenyl-helicene part.

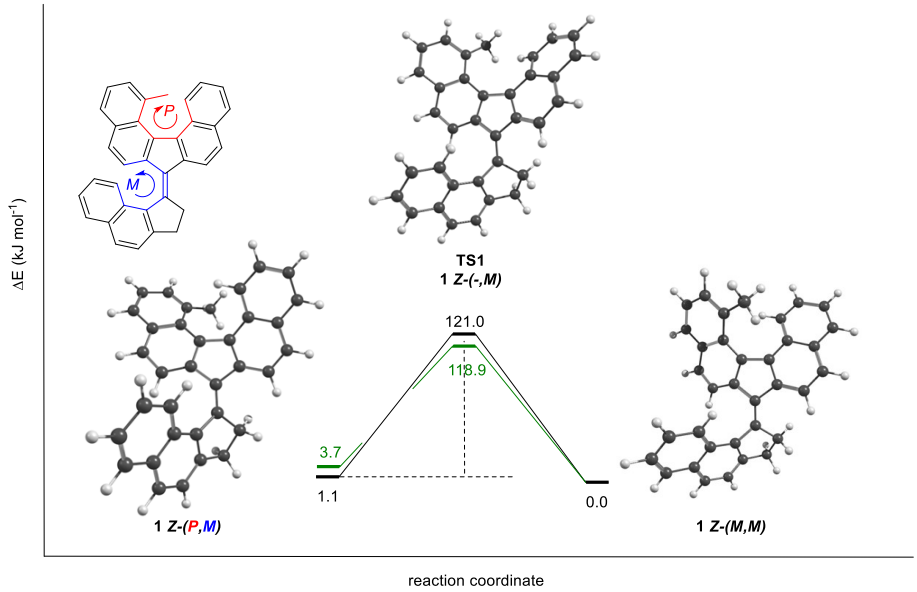

Figure 3. Helix inversion of the fluorenyl-helicene motif in **1** (black) and **2** (green).

At the B3LYP/6-31G** level of theory, the geometries and energies for the helical inversion mechanism through a more symmetrical, planarised transition state were calculated and the relative energy towards the most stable conformer in this example is 121.0 kJ mol^{-1} (barrier for isomerisation: $\Delta E^{\ddagger}_{\mathbf{1}\ Z\text{-}(P,M) \rightarrow \mathbf{1}\ Z\text{-}(M,M)}$ = 119.9 kJ mol^{-1}). This is significantly higher than most

thermal helix inversion barriers for second generation molecular motors with two five-membered rings.[20] With different opposing halves there could be an influence on the helix inversion of the fluorenyl-helicene. However, using the more bulky dimethylated analogue **2**, a highly similar transition state energy level (118.9 kJ mol^{-1}) was observed, which means that the lower half only has a small effect on the fluorenyl-helicene helix inversion.

As there are two helical chiral elements present, the inversion of chirality at the fluorenyl-helicene part leads to another stereoisomer with a different energy. Therefore, the ratio of the relative stability of the *P*- and *M*-helical fluorenyl-helicene will depend on the other stereochemical elements, i.e. the stator-rotor helicity and the *E*/*Z*-isomers. Indeed, all stereoisomers will have different energies dependent on the various intramolecular interactions. The helicity of the fluorenyl-helicene motif will differently influence the four stereoisomers expected in the rotation cycle.

2.2 Computational investigations on switching and rotation

Computational investigations were continued by studying the potential for unidirectional rotation. Using DFT calculations at the B3LYP/6-31G** level of theory[21,22] and spin-flip TD-DFT ("SFDFT") calculations at BHandHLYP/Def2-SVP level of theory[23] we determined the relative stability of the ground state stereoisomers and the transition states of the envisioned thermal helix inversion (THI) and thermal *E*/*Z*-isomerisation (TEZI) steps.

The **1 *E*-(*P*,*M*)** isomer (Scheme 2) was observed as the most stable isomer, based on DFT calculations. This structure could be isomerised via a photochemical *E*/*Z*-isomerisation (PEZI1) to **1 *Z*-(*P*,*P*)**, a stereoisomer only slightly higher in energy by 2.3 kJ mol^{-1}. Ordinarily with molecular motors, this state would be of a significantly higher energy and function as a *metastable* state.[24] However, in this case all stereoisomers have relatively similar energy levels. THI from the **1 *Z*-(*P*,*P*)** state results in **1 *Z*-(*P*,*M*)**, which is slightly higher in energy, meaning the backwards reaction for THI is slightly more favoured. As the energy levels are not much separated it is likely that this energy profile would lead to a mixture of **1 *Z*-(*P*,*P*)** and **1 *Z*-(*P*,*M*)**. The newly obtained **1 *Z*-(*P*,*M*)** can be converted to **1 *E*-(*P*,*P*)** via PEZI2, which finally after THI2 could return to the original stereoisomer completing the full rotation. This last step has a more favourable energy profile for forward rotation with a larger difference in energy between **1 *E*-(*P*,*P*)** and **1 *E*-(*P*,*M*)** (ΔE = 5.0 kJ mol^{-1}) than was the case for THI1 (ΔE = -1.1 kJ mol^{-1}).

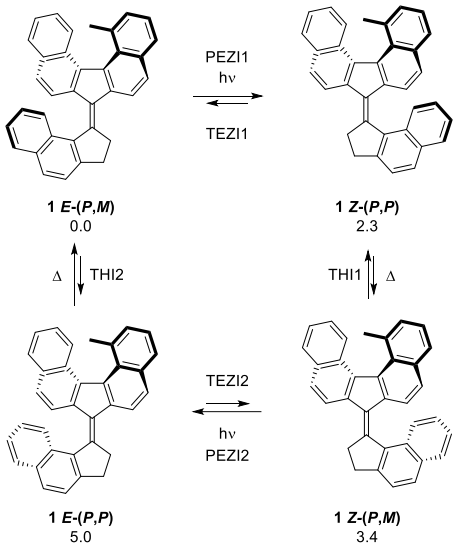

Scheme 2. Ground state stereoisomers of **1** involved in the switching steps with energy levels indicated in kJ mol^{-1} from DFT calculations (B3LYP/6-31G**).

All geometries of the stereoisomers of the targets **1–4** (Figure 2) were optimised and the thermal interconversions between them were investigated. The energy levels, relative to the lowest observed energy for each molecule, resulting from the DFT calculations (B3LYP/6-31G**) and the results of the SFDFT calculations (BHandHLYP/Def2-SVP), of target compounds **1–4** are presented in Tables 1a, 1b and Figure 4. The geometry of the ground state isomers and the transition states were optimised using DFT calculations using at the B3LYP/6-31G** level of theory. This method generally provides useful, reliable information on the energy levels of molecular motor stereoisomers and thermal helix inversion processes.[20-22,25,26] Further computational investigations using single point SFDFT calculations were added as a facile method that has provided useful information on molecular motors.[27] SFDFT has an advantage over the DFT method used as it includes more exact exchange energies and has been found to describe open shell species more accurately.[28–30]

Table 1a. Energies from DFT (B3LYP/6-31G**) in kJ mol^{-1}.

	E-(*P*,*M*)	*Z*-(*P*,*P*)	*Z*-(*P*,*M*)	*E*-(*P*,*P*)	THI1	THI2	TEZI1	TEZI2
1	0.0	2.3	3.4	5.0	110.0	101.7	98.7	98.7
2	0.5	3.7	0.0	3.2	126.8	149.4	79.9	76.6
3	0.8	6.5	0.0	5.6	97.5	94.1	61.1	61.5
4	0.0	0.9	10.2	10.8	115.9	127.6	92.0	92.9

Table 1b. Energies from SFDFT (BHandHLYP/Def2-SVP) in kJ mol^{-1}.

	E-(*P*,*M*)	*Z*-(*P*,*P*)	*Z*-(*P*,*M*)	*E*-(*P*,*P*)	THI1	THI2	TEZI1	TEZI2
1	0.0	0.3	3.4	2.8	117.3	106.7	118.8	119.4
2	0.0	3.8	2.9	3.8	139.3	158.7	100.5	97.1
3	0.9	2.5	0.0	2.7	99.6	95.4	88.2	88.3
4	4.2	0.0	14.8	14.9	132.4	144.7	124.0	124.8

Footnote: THI1 is defined as the transition state between *Z*-(*P*,*P*) and *Z*-(*P*,*M*); THI2 as the transition state between *E*-(*P*,*P*) and *E*-(*P*,*M*); TEZI1 as the transition state between *E*-(*P*,*M*) and *Z*-(*P*,*P*); TEZI2 as the transition state between *Z*-(*P*,*M*) and *E*-(*P*,*P*) conforming to Scheme 2.

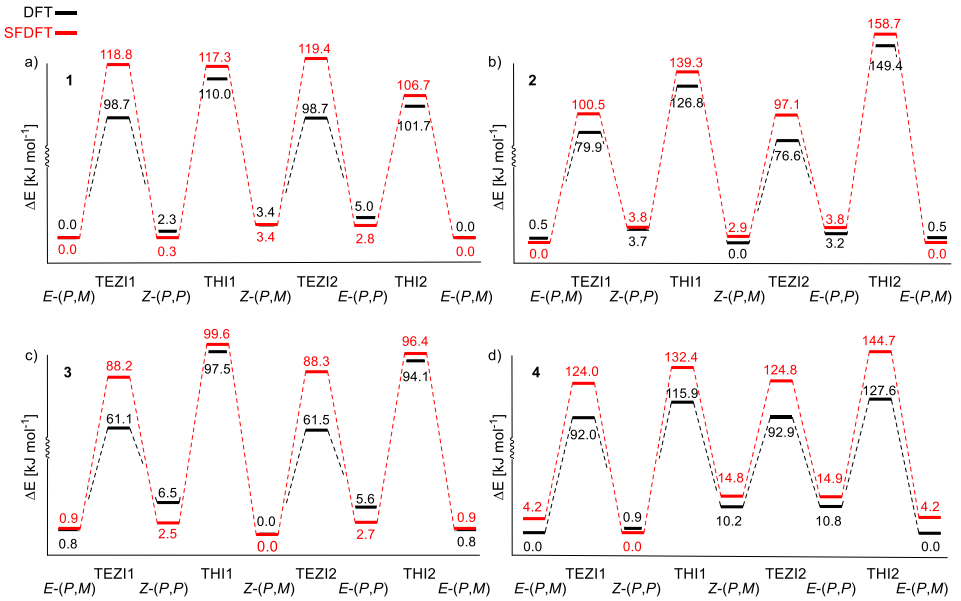

Figure 4. Energy diagram from the calculated results from Tables 1a and 1b using DFT (black) and SFDFT (red) of the ground and transition states of: a) **1**, b) **2**, c) **3** and d) **4**.

With the investigations into the thermal transitions, it has to be noted for the TEZI that the DFT method can be inaccurate due to the biradicaloid character of this reaction profile.[25] The SFDFT is a better method, but an extensive computational study on these molecules using multireference methods could provide still more reliable information on the TEZI energy levels. For ground state calculations and THIs, the method has shown to provide useful data.[20–22,25,26]

From the calculations we can observe that for the target compounds **1–3** the energy levels of the ground state stereoisomers are relatively close within the same energy range. For thioxanthene-based compound **4**, the energy landscape is significantly different with the *Z*-(*P*,*M*) and *E*-(*P*,*P*) isomers being higher in energy with the higher energy isomers having a slightly more pronounced folding in the thioxanthene motif and a slightly stronger twist of the fluorenyl-helicene.

The obtained data shows that the barriers for THI are relatively high compared to previously developed overcrowded alkene-based molecular rotary motors (see Chapter 1). The difference in THI energy levels between **1** and **2** illustrates that the introduction of the two methyl groups significantly increases the barrier for thermal helix inversion. However, the modification towards inclusion of a benzo-fused ring in compound **3** results in overall lower THI barriers. This is likely due to lowered flexibility, resulting in a twisted conformation. Compound **4**, with a six-membered sulfur containing ring, shows increased barriers compared to the case of compound **3** with a five-membered ring. The thioxanthene motif in compound **4**, leads to increased strain in the fjord-region. In contrast, the more facile folding of a sulfur-containing ring is a somewhat stabilising factor.[31]

The TEZI levels from SFDFT (Table 1b) show that for compound **1** the TEZI is at a higher level of energy than the THI, where for compounds **2–4** the TEZI energy levels are lower. All SFDFT TEZI levels are significantly higher than the DFT results, due to a better description of the biradicaloid transition state.[28–30] A lower TEZI energy level compared to THI energy level will result in a T-type molecular photoswitch[32] rather than a unidirectional molecular motor.[33] Such a photoswitch can convert in one direction photochemically and will convert back to the original state in a thermal step.

An overall energy profile for unidirectionality would require a significant bias in at least one THI step and that the thermal pathways in the opposing direction are less likely to occur. From the DFT results, compound **1** has a clear bias in the step from *E*-(*P*,*P*) to *E*-(*P*,*M*) (THI2) and compounds **2** and **3** have a bias in the same direction for both THI steps. From SFDFT compound **1** would have two THIs in opposing directions while both THIs for compounds **2** and **3** are in the same direction. Compound **4** does not show a favourable energy profile for directional rotation.

These calculations provide the insight that the energies of the ground state conformers do not differ significantly. The lack of a significantly destabilised

metastable state (see also Chapter 1) results in relatively high barriers for THI compared to previously known molecular motors.[24] Additionally, the ability to predict unidirectional rotation based on calculations is more difficult for these overcrowded alkenes. For a full understanding of the switching of these types of molecules, multireference method computational investigations and experimental studies are required.[34]

2.3 Synthesis

In parallel to the computational studies, synthetic routes towards the final overcrowded alkenes were explored. Experimental data of the target compounds using absorption, CD and NMR spectroscopy, as well as cyclic voltammetry studies would provide a great source of information for the understanding of the switching of purely helically chiral overcrowded olefins.

As is common with molecular motors, the final step in the envisioned synthesis of the fluorenyl-helicene motor is the synthesis of the central overcrowded olefin, which can be done via Barton-Kellogg synthesis (Scheme 3).[20,35,36] For this step, a thioketone and diazo compound are required and both can be obtained from the corresponding ketones. For our envisioned structures (Figure 2, **1–4**), helically chiral fluorenone **5** is required. The subsequent further disconnections in this retrosynthetic analysis were envisioned as a Friedel-Crafts cyclisation to form the central five-membered ring. Final disconnection of the C_{sp2}–C_{sp2} bond results in an aryl cross-coupling reaction between a peri-substituted naphthalene compound **7** and an *ortho* halogenated 2-naphthalene carboxylic acid **8**. Depending on the type of coupling, a protection group could be used for the carboxylic acid.

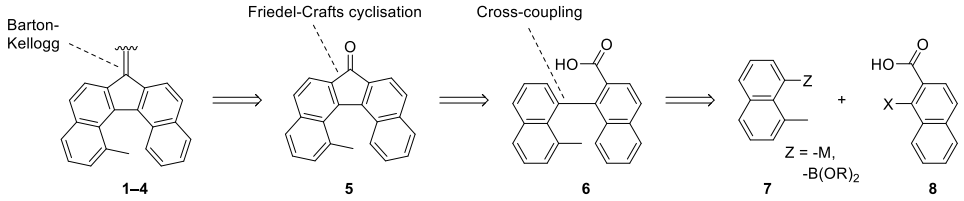

Scheme 3. Retrosynthetic analysis of the fluorenyl-helicene overcrowded alkene.

The first reaction performed was a Suzuki cross-coupling of an aryl boronic acid and an aryl halide (Scheme 3, Z = -$B(OH)_2$, X = Br). The required boronic acid **11** was synthesised by monomethylation of 1,8-dibromonaphthalene (Scheme 4). With MeLi and subsequent addition of MeI, monomethylated compound **10** could be obtained, albeit with a small amount of the dimethylated product present. This impurity was not successfully separated

from product **10** using conventional flash column chromatography, due to the apolar nature of both compounds **9** and **10**. However, for the subsequent steps, the dimethylated impurity is not of significant importance as it did not provide any issues going forward. The subsequent lithium-bromide exchange was performed with *n*-BuLi, followed by borylation using $B(OMe)_3$ and finally hydrolysis using aqueous HCl. Product **11** could be obtained in 48% yield (over 3 steps) and any remaining apolar impurities could be easily removed by trituration with *n*-pentane.

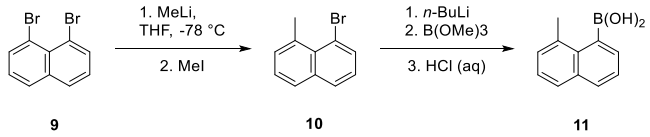

Scheme 4. Preparation of boronic acid **11**.

Initial investigations into the formation of the biaryl bond utilised a Suzuki cross-coupling of a methyl ester-functionalised bromonaphthalene **12** (Scheme 5). For catalyst systems, triaryl phosphine ligands (Conditions A-C), the dialkylbiaryl DavePhos and diphosphine ligand DPEPhos were used. K_2CO_3, CsF and K_3PO_4 were chosen as bases and several solvent systems were examined (see Scheme 5). Unfortunately, under these conditions, no conversion to the coupled product **13** was observed. The most prevalent reaction was the protodeborylation of **11**. Even at lower temperatures and extended reaction times up to 7 days (Conditions D and E), product **13** could not be observed. In a modified reaction, using aldehyde **14** instead of methyl ester **13**, the desired coupled product was also not obtained.

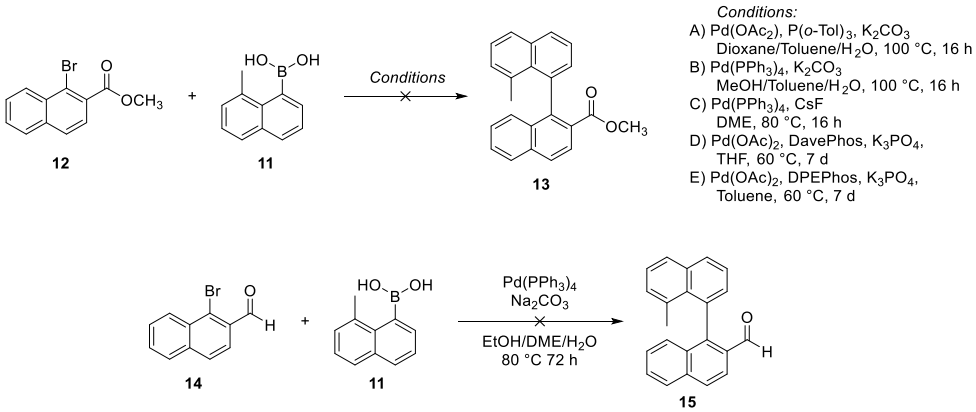

Scheme 5. Attempted biaryl palladium cross-couplings.

In a new strategy, a method utilising nucleophilic aromatic substitution (S_NAr) was attempted (Scheme 6) using naphthyl-lithium species **16** as a

nucleophile and a coupling partner with either a methoxy or fluoride leaving group (**17** and **18**, respectively), based upon reported methods in the literature.[37,38] With the S_NAr strategy, no conversion was observed, presumably because of the lack of nucleophilicity and consequent steric hindrance of **16**. Increased temperatures up to 80 °C, or the addition of a stoichiometric equivalent of 1,2-dimethoxyethane did not improve the outcome of the reaction.

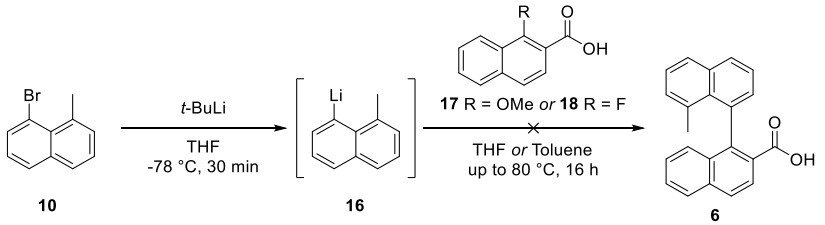

Scheme 6. Attempted S_NAr coupling.

Finally, a successful route for the synthesis of the biaryl intermediate **6** (Scheme 3) was found using a Suzuki cross-coupling reaction that utilises the improved reactivity of a partially saturated coupling partner (Scheme 7).

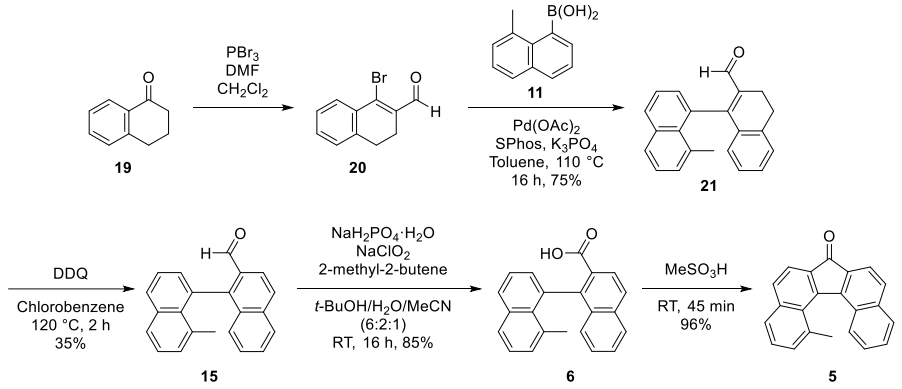

Scheme 7. Synthesis of fluorenyl helicene **5**.

Kellogg and co-workers reported a method for cross-coupling towards sterically hindered biaryls via coupling of such a partially saturated bromide and subsequent aromatisation of the coupled product.[39] From their work on a structure, comparable to compound **6**, it was found that the electron density and flexibility of the halide substrate seem to have a significant effect to the efficacy of the cross-coupling reaction. Taking inspiration from the work of Kellogg and co-workers, **19** was transformed to **20** in a Villsmeier-Haack reaction to yield a partially saturated coupling partner for boronic acid **11**.

The cross-coupling of boronic acid **11** and bromide **20** with $Pd(OAc)_2$ and SPhos resulted in the coupling product **21** in 75% yield. Compound **21** could be aromatised using DDQ, albeit in a low yield of 35% for **15**. A subsequent Pinnick oxidation provided the carboxylic acid **6** in a good yield. The target ketone **5** could be obtained in excellent yield via a Friedel-Crafts acylation with methyl sulfonic acid at room temperature.

When the cyclisation towards **5** was initially performed using methyl sulfonic acid at 110 °C, a significant amount of regioisomeric product **22** was obtained (Scheme 8). We hypothesise that under these conditions for Friedel-Crafts acylation it is plausible that intermediate **I-1** is formed by attack of the methylated carbon to the carboxylic acid moiety. The methyl group in this intermediate is nearly perpendicular to the naphthalene motif and adjacent to a position with significant carbocation character. This likely results in a good orbital overlap and therefore 1,2-methyl shift can readily occur to form **I-2**. Subsequent elimination of **I-2** results in **22**. Notably, the reaction performed at room temperature did not show any of the regioisomeric product and only the desired helicene fluorenone **5** was obtained.

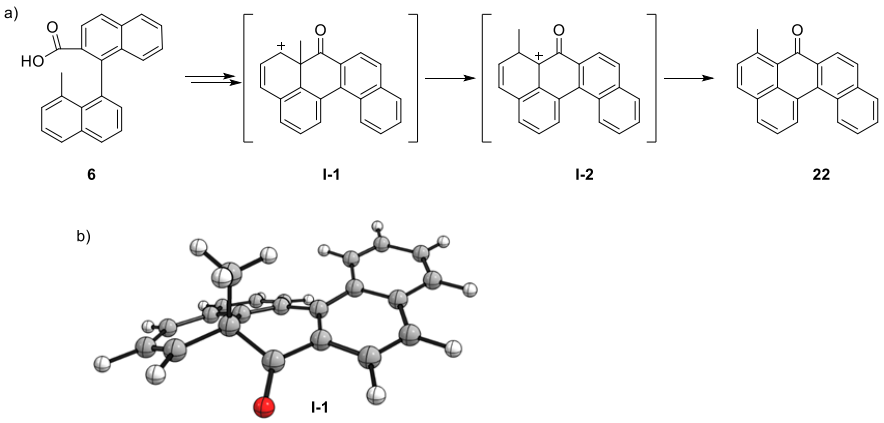

Scheme 8. a) A proposed mechanism for the Friedel-Crafts cyclisation and subsequent 1,2-methyl shift to form **22**. b) the calculated structure for cationic intermediate **I-1** at B3LYP/6-31G** level of theory.

With helicene-fluorenone **5** in hand, we proceeded to the synthesis of the overcrowded alkenes. The initial strategy was to use the helicene-fluorenone as a diazo compound in the Barton-Kellogg coupling. This step was envisioned to be performed via oxidation of the corresponding hydrazone **23**. To obtain **23**, ketone **5** was submitted to a number of conditions (Scheme 9) without successful conversion towards product **23**. The direct synthesis using hydrazine hydrate in a pressure tube did not show

conversion, even at temperatures up to 120 °C for 7 days using a stoichiometric amount of $Sc(OTf)_3$. An alternative method utilised tosylhydrazine (Scheme 9, condition C) to form the corresponding tosylhydrazone, which can undergo an elimination reaction[40,41] towards hydrazone **23**. Unfortunately, no conversion towards the tosylhydrazone was observed. The synthesis of the hydrazone of the non-methylated analogue had been successful under less harsh conditions,[18] which is indicative of the influence of the increased twisting of the five-membered ring leading to a significant decrease in reactivity.

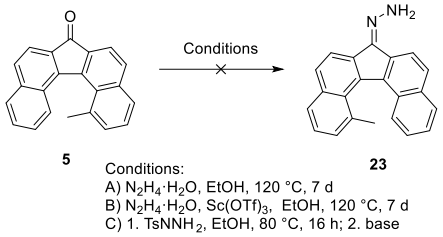

Scheme 9. Attempted conditions for synthesis of hydrazone **23**.

Subsequently in our strategy, we inverted the coupling partners for the Barton-Kellogg synthesis and proceeded with the thionation of fluorenone **5** (Scheme 10). Fluorenone thioketones are typically relatively unstable compounds, degrading over time. Therefore, such thioketones as **24** require synthesis shortly before use in the next reaction. The thioketone synthesis was done using Lawesson's reagent in toluene and could be monitored by TLC analysis.

The subsequent Barton-Kellogg coupling was attempted with diazo compounds **25** and **26** to synthesise overcrowded alkenes **1** and **4**, respectively. With diazo compound **25**, first a solvent system of DMF and THF was used at room temperature (A) where no conversion of the starting materials was observed. At an increased temperature of 60 °C (B), the reaction did not result in conversion towards the desired products and degradation of starting materials could be observed. With diazo compound **26**, using the same conditions, likewise resulted in no conversion at room temperature (A) and degradation at 60 °C (B). Changing the solvent to toluene provided a comparable outcome with no conversion at room temperature (C) and degradation at 60 °C (D). Based on a literature precedent using Rhodium catalysts for Barton-Kellogg couplings,[42] the Barton-Kellogg coupling in the presence of $Rh_2(OAc)_4$ was attempted (E). However, the Rhodium catalysed reaction at room temperature only led to degradation of the diazo compound.

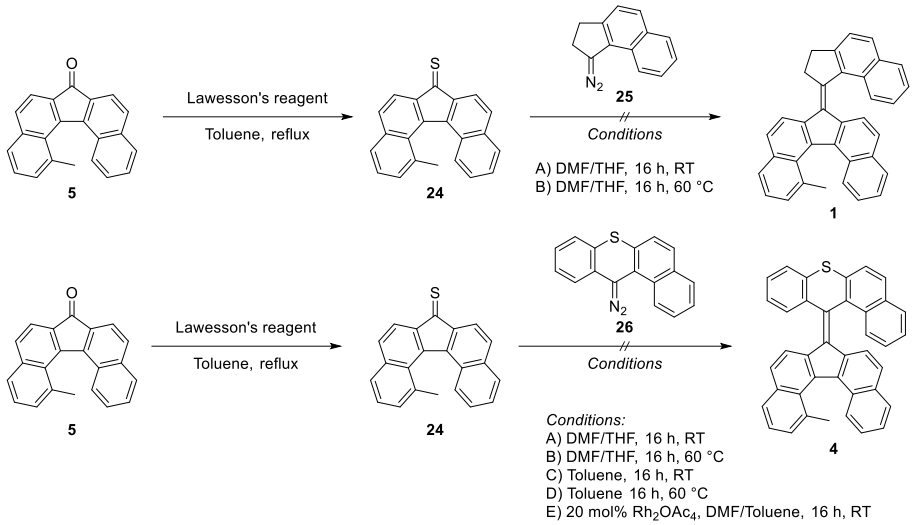

Scheme 10. Attempted Barton-Kellogg couplings of **17**.

From the unsuccessful Barton-Kellogg reactions and the hydrazone synthesis, it seems that the twisting in the fluorenyl-helicene motif has a significant effect of lowering the reactivity of the ketone or could be leading to decreased stability of reaction intermediates. Other reactions to synthesise overcrowded alkenes such as the $TMSCHN_2$ procedure[8] (see also Chapter 3) or crossed McMurry coupling[43,44] could be attempted, which should include further optimisation of these reactions to obtain a sufficient amount of the cross-coupled product.

3. Conclusions & Outlook

Four overcrowded alkene molecules with a fluorenyl-helicene motif have been designed in an ongoing investigation towards unidirectional molecular rotation solely based on helical chirality. These four targets contain a methylated fluorenyl-helicene motif which has relatively stable helical chirality ($\Delta E^{\ddagger} \sim 120$ kJ mol^{-1}), based on DFT calculations.

Further computational studies using DFT and spin-flip TD-DFT calculations showed that the ground state stereoisomers are relatively close to one another in energy levels. There are noticeable effects from the introduction of methyl group, benzo-fused rings and thiopyran motifs. The methyl groups increase thermal barriers, the benzo-fused ring decreases barriers and the thiopyran motif leads to a more complex overall energy profile. Overall, these effects are important for the future design of switches and motors based on the fluorenyl-helicene scaffold. From the obtained results we can conclude that the proposed targets are promising as switches and

potentially unidirectional rotational motors. For an accurate description of the barriers for thermal E/Z-isomerisation and unidirectionality, additional computational investigations are required, such as multireference methods.

Towards obtaining the final targets, there has been significant progress in the synthesis of the fluorenyl-helicene ketone as an important building block for the desired overcrowded alkenes. This required an unexpected approach via the coupling of a partially saturated compound and late stage aromatisation. The final ketone could be obtained successfully after ring-closing Friedel-Crafts reaction.

Unfortunately, the obtained helically chiral ketone has shown poor reactivity towards formation of overcrowded alkenes. The twisting caused by the methyl group is a likely reason for this altered reactivity. Other reactions such as a McMurry or $TMSCHN_2$ based coupling might be used to obtain the final target compounds.

In conclusion, the fluorenyl-helicene scaffold is a promising structure for the development of new photo- and electrochemical switches, but requires further investigation. We have provided information important to the development of future designs for switches and motors and showed a synthetic pathway for an important building block.

4. Experimental

4.1 General comments

For general information on chemicals, NMR spectroscopy, high-resolution mass spectrometry, cyclic voltammetry and DFT calculations, see Chapter 2.

In this chapter, DFT calculations were performed using the Gaussian 16 software[45] on the Peregrine High Performance Computing cluster. SF-DFT calculations were performed using the ORCA software package.[46] All energies are reported in kJ mol^{-1} and include the thermal corrections to the Gibbs free energy.

4.2 Synthesis and characterisation of compounds

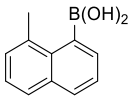

8-Methylnaphthalen-1-boronic acid (**11**). *Methylation*: 1,8-dibromonaphthalene (5.0 g, 17.5 mmol, 1.0 equiv.) was dissolved in THF (35 mL, 0.5 M) and cooled to 0 °C. MeLi (1.6 M in Et_2O, 11.5 mL, 18.4 mmol, 1.05 equiv.) was added dropwise over 30 min and the mixture was stirred for an additional 30 min at 0 °C and subsequently at room temperature for 16 h. The reaction was quenched with water, the organic and aqueous phases separated and the organic phase was washed with brine, dried over $MgSO_4$ and volatiles were removed under reduced pressure. The 1-bromo-8-methylnaphthalene intermediate was purified by flash column chromatography (silica, *n*-pentane) and obtained as a yellow solid with a 10% impurity of 1,8-dimethylnaphthalene, based on ^1H and ^{13}C NMR spectroscopic analysis.

Borylation: n-BuLi (1.6 M in hexanes, 12.5 mL, 20 mmol, 1.2 equiv.) was added over 15 min to a solution of 1-bromo-8-methylnaphthalene (3.7 g, 16.7 mmol, 1.0 equiv.) in dry THF (75 ml, 0.2 M) at -78 °C and the mixture was stirred at that temperature for 1 h. Trimethyl borate (5.6 mL, 50.2 mmol, 3 equiv.) was then added and the mixture was allowed to warm up to room temperature and stirred for 2 h. Aqueous HCl (1 M, 100 mL) was added and the mixture was stirred for 16 h. The mixture was extracted with Et_2O, the combined organic layers were washed with brine, dried over $MgSO_4$, and concentrated under reduced pressure. Filtration over a pad of silica (*n*-pentane/EtOAc, 1:1) followed by trituration with *n*-pentane yielded the product as a white solid in 48% yield (1.5 g, 8.1 mmol). ^1H NMR (400 MHz, $CDCl_3$) δ 7.87 (d, *J* = 8.1 Hz, 1H), 7.73 (d, *J* = 7.8 Hz, 1H), 7.61 (d, *J* = 6.7 Hz, 1H), 7.45 (dd, *J* = 7.4, 7.4 Hz, 1H), 7.42 – 7.33 (m, 2H), 4.67 (br. s, 2H), 2.80 (s, 3H). ^1H NMR (600 MHz, DMSO-*d6*) δ 8.27 (br. s, 2H), 7.85 (dd, *J* = 6.8, 2.8 Hz, 1H), 7.75 (br. d, *J* = 7.6 Hz, 1H), 7.47 – 7.42 (m, 2H), 7.37 (dd, *J* = 7.5, 7.5 Hz, 1H), 7.34 (d, *J* = 6.9 Hz, 1H), 2.74 (s, 3H). ^{13}C NMR (151 MHz, DMSO-*d6*) δ 135.3, 133.6, 133.4, 129.4, 128.4, 127.3, 127.0, 125.1, 124.6, 21.5. Compound data is in accordance with literature.[47]

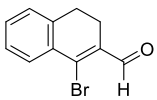

1-Bromo-3,4-dihydronaphthalene-2-carbaldehyde (**20**). At 0 °C, PBr_3 (11.7 mL, 125 mmol, 2.6 equiv.) was added to a mixture of DMF (11.2 mL, 144 mmol, 3.5 equiv.) and CH_2Cl_2 (200 mL) and the mixture was stirred at

0 °C for 2 h. A solution of α-tetralone (7.0 g, 47.9 mmol, 1.0 equiv.) in CH_2Cl_2 (38 mL, 1.3 M) was added to the Villsmeier reagent solution via a cannula and the mixture was subsequently heated at reflux for 16 h. The reaction was quenched by careful addition of water with vigorous stirring. The mixture was extracted with CH_2Cl_2, washed extensively with 5% LiCl (aq) solution, washed with brine and dried over $MgSO_4$. Volatiles were removed under reduced pressure and the product was obtained as a brown solid in 66% yield (7.5 g, 31.6 mmol). ^{1}H NMR(400 MHz, $CDCl_3$) δ = 10.26 (s, 1H), 7.94 – 7.85 (m, 1H), 7.40 –7.29 (m, 2H), 7.24 –7.15 (m, 1H), 2.84 (dd, *J* = 9.2, 6.8 Hz, 2H), 2.63 (dd, *J* = 9.3, 6.7 Hz, 2H). ^{13}C NMR (101 MHz, $CDCl_3$) δ 193.3, 139.2, 139.1, 134.7, 133.1, 131.5, 128.9, 127.7, 127.3, 27.3, 23.0. Compound data is in accordance with literature.[39]

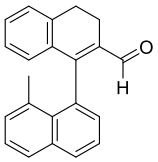

8'-Methyl-3,4-dihydro-[1,1'-binaphthalene]-2-carbaldehyde (**21**). 1-Bromo-3,4-dihydronaphthalene-2-carbaldehyde (**20**, 640 mg, 2.7 mmol, 1.0 equiv.) 8-methylnaphthalen-1-boronic acid (**11**, 603 mg, 3.2 mmol, 1.2 equiv.) K_2CO_3 (1.15 g, 5.4 mmol, 2.0 equiv.), $Pd(OAc)_2$ (30.3 mg, 0.13 mmol, 0.05 equiv.), and SPhos (133 mg, 0.32 mmol, 0.12 equiv.) were dissolved in toluene (degassed using freeze-pump-thaw under Ar, 13.5 mL, 0.2 M) under an Ar atmosphere. The mixture was heated at reflux for 22 h under a N_2 atmosphere. The reaction mixture was then diluted in Et_2O, washed with sat. $NaHCO_3$ (aq), brine, dried with $MgSO_4$, and volatiles were removed under reduced pressure. Purification by flash column chromatography (silica, *n*-pentane/Et_2O, 99:1 to 90:10) afforded the product as a yellow oil in 75% yield (605 mg, 2.0 mmol). ^{1}H NMR (400 MHz, $CDCl_3$): δ = 9.52 (s, 1H), 7.97 (dd, *J* = 8.2, 1.5 Hz, 1H), 7.87 – 7.80 (d, *J* = 8.2 Hz, 1H), 7.50 (dd, *J* = 8.2, 7.0 Hz, 1H), 7.41 (dd, *J* = 8.2, 7.0 Hz, 1H), 7.28 (m, 4H), 7.02 (td, *J* = 7.3, 2.0 Hz, 1H), 6.64 (d, *J* = 7.7, 1H), 3.02 (t, *J* = 8.1 Hz, 2H), 2.84 (dt, *J* = 16.4, 7.3 Hz, 1H), 2.72 (dt, *J* = 16.4, 8.9 Hz, 1H), 2.43 (s, 3H). ^{13}C NMR (101 MHz, $CDCl_3$): δ = 193.4, 157.1, 138.0, 136.5, 135.1, 134.8, 134.4, 132.5, 132.4, 130.8, 130.4, 130.4, 130.3, 128.5, 128.1, 127.9, 127.1, 126.1, 124.6, 27.4, 23.5, 20.3. HRMS (ESI Pos): for $[C_{22}H_{17}O]^+$ ($[M-H_2+H]^+$) calcd. m/z = 297.1274, found m/z = 298.1276.

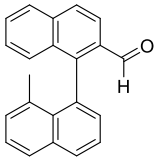

8'-Methyl-[1,1'-binaphthalene]-2-carbaldehyde (**15**). 8'-Methyl-3,4-dihydro-[1,1'-binaphthalene]-2-carbaldehyde (**21**, 179 mg, 0.60 mmol, 1.0 equiv.) and DDQ (408 mg, 1.8 mmol, 3.0 equiv.) were dissolved in chlorobenzene (2.4 ml, 0.25 M) under a N_2 atmosphere and the mixture was heated at 120 °C for 3 h. The mixture was filtered over Celite, rinsed with CH_2Cl_2, and volatiles were removed under reduced pressure. Purification by flash column chromatography (silica, *n*-pentane/Et_2O, 99:1 to 90:10) yielded the product as a white solid in 35% yield (62 mg, 0.21 mmol). ^{1}H NMR (400 MHz, $CDCl_3$): δ = 9.80 (d, *J* = 1.5 Hz, 1H), 8.22 – 7.86 (m, 6H), 7.68 – 7.47 (m, 3H), 7.47 – 7.35 (m, 2H), 7.20 (d, *J* = 7.1 Hz, 1H), 1.68 (s, 3H). ^{13}C NMR (151 MHz, $CDCl_3$) δ 192.7, 149.1, 135.8, 134.9, 134.9, 133.9, 132.6, 132.5, 132.0, 131.1, 130.4, 129.0, 128.5, 128.3, 128.1, 128.1, 127.3, 126.3, 125.2, 124.4, 122.0, 23.7. HRMS (APCI Pos): for $[C_{22}H_{17}O]^+$, calcd. m/z = 297.1274, found m/z = 297.1267.

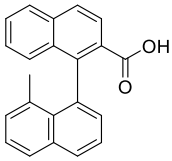

8'-Methyl-[1,1'-binaphthalene]-2-carboxylic acid (**6**). To a solution of 8'-methyl-[1,1'-binaphthalene]-2-carbaldehyde (**15**, 118 mg, 0.40 mmol, 1.0 equiv.) and 2-methyl-2-butene (0.42 mL, 4.0 mmol, 10 equiv.) in *t*-BuOH/THF/H_2O (2:1:1, 4.0 mL, 0.1 M) were added $NaH_2PO_4 \cdot 2H_2O$ (156 mg, 1.0 mmol, 2.5 equiv.) and $NaClO_2$ (80 wt% purity, 90 mg, 0.80 mmol, 2.0 equiv.), and the mixture was stirred for 18 h at room temperature. HCl (1 M, aq) was added and the aqueous layer was extracted with CH_2Cl_2. The combined organic layers were washed with brine, dried over $MgSO_4$, and concentrated under reduced pressure. The product was purified by flash column chromatography (silica, *n*-pentane/EtOAc, 9:1 to 1:1) and obtained as an off-white solid in 85% yield (106 mg, 0.34 mmol). ^{1}H NMR (400 MHz, $CDCl_3$) δ 8.01 (d, *J* = 8.7 Hz, 1H), 7.95 – 7.88 (m, 4H), 7.84 (d, *J* = 8.2 Hz, 1H), 7.52 (ddd, *J* = 8.1, 6.7, 1.2 Hz, 1H), 7.45 (dd, *J* = 8.2, 7.0 Hz, 1H), 7.38 (dd, *J* = 8.2, 7.0 Hz, 1H), 7.27 (ddd, *J* = 8.3, 6.1, 1.3 Hz, 2H), 7.17 – 7.10 (m, 3H), 1.68 (s, 3H). ^{13}C NMR (101 MHz, $CDCl_3$) δ = δ 172.4, 145.8, 136.4, 135.2, 134.8, 134.7, 134.0, 132.2, 129.5, 129.4, 128.6, 128.3, 128.0, 127.9, 127.9, 127.8, 127.0, 126.6, 126.0, 125.6, 124.6, 23.5. HRMS (ESI Neg): for $[C_{22}H_{15}O_2]^-$ calcd. m/z = 311.1078, found m/z = 311.1081.

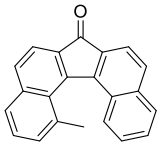

1-Methyl-7H-dibenzo[c,g]fluoren-7-one (**5**). 8'-Methyl-[1,1'-binaphthalene]-2-carboxylic acid (**6**, 77 mg, 0.25 mmol, 1 equiv.) was added to trifluoromethanesulfonic acid (2.5 ml, 0.1 M) at 0 °C and the mixture was stirred for 45 min at room temperature. The reaction mixture was then poured on aqueous NaOH (1 M, 50 mL), extracted with CH_2Cl_2 and the combined organic layers were washed with brine, dried with $MgSO_4$ and concentrated under reduced pressure. Filtration over a pad of silica, flushed with *n*-pentane/CH_2Cl_2 (1:1) provided the product as an orange solid in 96% yield (71 mg, 0.24 mmol). ^{1}H NMR (600 MHz, $CDCl_3$) δ 8.78 – 8.70 (m, 1H), 8.65 (d, *J* = 7.5 Hz, 1H), 8.53 (d, *J* = 8.6 Hz, 1H), 8.15 (d, *J* = 8.2 Hz, 1H), 8.04 (d, *J* = 8.0 Hz, 1H), 8.01 – 7.97 (m, 1H), 7.95 (d, *J* = 8.6 Hz, 1H), 7.72 (t, *J* = 7.8 Hz, 1H), 7.69 – 7.59 (m, 3H), 3.10 (s, 3H). ^{13}C NMR (151 MHz, $CDCl_3$) δ = 185.2, 145.9, 136.9, 135.4, 134.2, 131.8, 131.5, 131.2, 131.1, 130.0, 129.7, 129.0, 128.9, 128.5, 128.4, 127.7, 126.8, 126.6, 125.6, 124.9, 123.1, 25.7. HRMS (ESI Pos): for $[C_{22}H_{15}O]^+$ calcd. m/z = 295.1117, found m/z = 295.1119.

Note: isomeric product **22**, observed at high temperature Friedel-Crafts cyclisation (see text): ^{1}H NMR (400 MHz, $CDCl_3$) δ 8.78 – 8.70 (m, 1H), 8.65 (d, *J* = 7.5 Hz, 1H), 8.53 (d, *J* = 8.6 Hz, 1H), 8.15 (d, *J* = 8.2 Hz, 1H), 8.04 (dd, *J* = 8.0, 1.2 Hz, 1H), 8.01 – 7.97 (m, 1H), 7.95 (d, *J* = 8.6 Hz, 1H), 7.72 (dd, *J* = 7.8, 7.8 Hz, 1H), 7.69 – 7.59 (m, 3H), 3.10 (s, 3H). ^{13}C NMR (151 MHz, $CDCl_3$) δ 185.2, 145.9, 136.9, 135.4, 134.2, 131.8, 131.5, 131.2, 131.1, 130.1, 129.7, 129.0, 128.9, 128.5, 128.4, 127.7, 126.8, 126.6, 125.6, 124.9, 123.1, 24.7.

5. References

1 B. L. Feringa and W. R. Browne, *Molecular Switches*, Wiley-VCH, Hoboken, USA, 2nd edn., 2011.

2 D. H. Waldeck, *Chem. Rev.*, 1991, **91**, 415–436.

3 P. U. Biedermann and I. Agranat, *Top. Curr. Chem.*, 2014, **350**, 177–278.

4 S. Kassem, T. van Leeuwen, A. S. Lubbe, M. R. Wilson, B. L. Feringa and D. A. Leigh, *Chem. Soc. Rev.*, 2017, **46**, 2592–2621.

5 W. F. Jager, B. de Lange, A. M. Schoevaars, F. van Bolhuis and B. L. Feringa, *Tetrahedron: Asymmetry*, 1993, **4**, 1481–1497.

6 R. Costil, S. Crespi, L. Pfeifer and B. L. Feringa, *Chem. Eur. J.*, 2020, **26**, 7783–7787.

7 J. de Jong, B. L. Feringa and S. J. Wezenberg, *ChemPhysChem*, 2019, **20**, 3306–3310.

8 B. P. Corbet, M. B. S. Wonink and B. L. Feringa, *Chem. Commun.*, 2021, **57**, 7665–7668.

9 N. Koumura, R. W. J. Zijistra, R. A. van Delden, N. Harada and B. L. Feringa, *Nature*, 1999, **401**, 152–155.

10 B. L. Feringa, *Angew. Chem. Int. Ed.*, 2017, **56**, 11060–11078.

11 J. C. M. Kistemaker, A. S. Lubbe and B. L. Feringa, *Mater. Chem. Front.*, 2021, **5**, 2900–2906.

12 M. Jakubec and J. Storch, *J. Org. Chem.*, 2020, **85**, 13415–13428.

13 T. Mori, *Chem. Rev.*, 2021, **121**, 2373–2412.

14 M. Gingras, *Chem. Soc. Rev.*, 2013, **42**, 968–1006.

15 M. Gingras, G. Félix and R. Peresutti, *Chem. Soc. Rev.*, 2013, **42**, 1007–1050.

16 G. Gingras, *Chem. Soc. Rev.*, 2013, **42**, 1051–1095.

17 J. Barroso, J. L. Cabellos, S. Pan, F. Murillo, X. Zarate, M. A. Fernandez-Herrera and G. Merino, *Chem. Commun.*, 2017, **54**, 188–191.

18 T. Van Leeuwen, J. Pol, D. Roke, S. J. Wezenberg and B. L. Feringa, *Org. Lett.*, 2017, **19**, 1402–1405.

19 J. A. Thomann, MSc Thesis, Rijksuniversiteit Groningen, 2020.

20 J. Vicario, M. Walko, A. Meetsma and B. L. Feringa, *J. Am. Chem. Soc.*, 2006, **128**, 5127–5135.

21 A. D. Becke, *J. Chem. Phys.*, 1993, **98**, 5648–5652.

22 C. Lee, W. Yang and R. G. Parr, *Phys. Rev. B*, 1988, **37**, 785–789.

23 Y. Harabuchi, S. Maeda, T. Taketsugu, N. Minezawa and K. Morokuma, *J. Chem. Theory Comput.*, 2013, **9**, 4116–4123.

24 J. C. M. Kistemaker, S. F. Pizzolato, T. van Leeuwen, T. C. Pijper and B. L. Feringa, *Chem. Eur. J.*, 2016, **22**, 13478–13487.

25 J. C. M. Kistemaker, S. F. Pizzolato, T. van Leeuwen, T. C. Pijper and B. L. Feringa, *Chem. Eur. J.*, 2016, **22**, 13478–13487.

26 A. Cnossen, J. C. M. Kistemaker, T. Kojima and B. L. Feringa, *J. Org. Chem.*, 2014, **79**, 927–935.

27 Y. Li, F. Liu, B. Wang, Q. Su, W. Wang and K. Morokuma, *J. Chem. Phys.*, 2016, **145**, 244311.

28 Y. Shao, M. Head-Gordon and A. I. Krylov, *J. Chem. Phys.*, 2003, **118**, 4807–4818.

29 N. Minezawa and M. S. Gordon, *J. Phys. Chem. A*, 2011, **115**, 7901–7911.

30 L. V. Slipchenko and A. I. Krylov, *J. Chem. Phys.*, 2002, **117**, 4694–4708.

31 P. U. Biedermann, J. J. Stezowski and I. Agranat, *Eur. J. Org. Chem.*, 2001, 15–34.

32 H. Bouas-Laurent and H. Dürr, *Pure Appl. Chem.*, 2001, **73**, 639–665.

33 M. Klok, M. Walko, E. M. Geertsema, N. Ruangsupapichat, J. C. M. Kistemaker, A. Meetsma and B. L. Feringa, *Chem. Eur. J.*, 2008, **14**, 11183–11193.

34 A. Kazaryan, J. C. M. Kistemaker, L. V. Schäfer, W. R. Browne, B. L. Feringa and M. Filatov, *J. Phys. Chem. A*, 2010, **114**, 5058–5067.

35 N. Koumura, E. M. Geertsema, M. B. van Gelder, A. Meetsma and B. L. Feringa, *J. Am. Chem. Soc.*, 2002, **124**, 5037–5051.

36 M. K. J. ter Wiel, J. Vicario, S. G. Davey, A. Meetsma and B. L. Feringa, *Org. Biomol. Chem.*, 2005, **3**, 28–30.

37 T. T. T. Nguyen, H. Guyon, K. P. P. Nguyen, A. Boussonnière, J. Mortier and A. S. Castanet, *Eur. J. Org. Chem.*, 2020, 3829–3833.
38 R. Aissaoui, A. Nourry, A. Coquel, T. T. H. Dao, A. Derdour, J. J. Helesbeux, O. Duval, A. S. Castanet and J. Mortier, *J. Org. Chem.*, 2012, **77**, 718–724.
39 M. W. van der Meijden, T. Balandina, O. Ivasenko, S. De Feyter, K. Wurst and R. M. Kellogg, *Chem. Eur. J.*, 2016, **22**, 14633–14639.
40 T. Katsina, K. E. Papoulidou and A. L. Zografos, *Org. Lett.*, 2019, **21**, 8110–8115.
41 A. Krebs, W. Rüger, B. Ziegenhagen, M. Hebold, I. Hardtke, R. Müller, M. Schütz, M. Wietzke and M. Wilke, *Chem. Ber.*, 1984, **117**, 277–309.
42 T. A. Schmidt and C. Sparr, *Angew. Chem. Int. Ed.*, 2021, **60**, 23911–23916.
43 J. E. McMurry, *Chem. Rev.*, 1989, **89**, 1513–1524.
44 X. F. Duan, J. Zeng, J. W. Lü and Z. Bin Zhang, *Synthesis*, 2007, 713–718.
45 Gaussian 16, Rev B.01, M. J. Frisch, G. W. Trucks, H. B. Schlegel, G. E. Scuseria, M. A. Robb, J. R. Cheeseman, G. Scalmani, V. Barone, G. A. Petersson, H. Nakatsuji, *et al.*, Gaussian Inc., Wallingford, CA, 2016.
46 F. Neese, *Wiley Interdiscip. Rev. Comput. Mol. Sci.*, 2012, **2**, 73–78.
47 W. H. Miles, M. J. Robinson, S. G. Lessard and D. M. Thamattoor, *J. Org. Chem.*, 2016, **81**, 10791–10801.

List of Abbreviations

aq	Aqueous
Bpy	2,2'-Bipyridine
CV	Cyclic Voltammetry
d	Day(s)
DDQ	2,3-dichloro-5,6-dicyano-1,4-benzoquinone
DFT	Density-Functional Theory
DME	Dimethoxyethane
DMF	Dimethylformamide
DMSO	Dimethylsulfoxide
e.g.	*Exempli gratia* – for example
eq.	Equation
equiv.	Equivalent(s)
EtOAc	Ethyl acetate
i.e.	*Id est* – that is
GC	Gas Chromatography
HPLC	High Performance Liquid Chromatography
HRMS	High Resolution Mass Spectrometry
LDA	Lithium Diisopropylamide
MeCN	Acetonitrile
min	Minute(s)
MS	Mass Spectrometry
NaHMDS	Hexamethyldisilazane sodium salt
NFSI	*N*-fluorobenzenesulfonimide
NMR	Nuclear Magnetic Resonance
ppm	Parts per million
RT	Room Temperature (RT ≈ 295 K)
sat.	Saturated
SCE	Saturated Calomel Electrode
SFC	Supercritical Fluid Chromatography
TBAF	Tetrabutyl Ammonium Fluoride
$TBAPF_6$	Tetrabutyl Ammonium Hexafluorophosphate
Terpy	2,2':6',2''-Terpyridine
THF	Tetrahydrofuran
THI	Thermal Helix Inversion
TLC	Thin-Layer Chromatography
vs.	Versus

Summary (English)

Many properties of the objects around us, what they look and feel like, what they can do and what we can do with them depend on their molecular structure and activity. Picking up this thesis and reading these words involves movement of muscles, light reflecting off the page and being registered in your eyes, it all depends on molecular properties and chemical reactions. This thesis presents a part of the research that chemists do to develop materials and techniques to influence and to have control over what happens on the scale of molecules.

Molecular unidirectional motors are molecules that show movement, in this case rotation in one specific direction, when we shine light on them. Figure 1 shows an example of such a molecular motor. This motor operates by light and heat and rotates around a central C=C axis (indicated in blue). For clarification, a 3D model of the molecules is presented with red arrows representing the direction of movement of the ring. This ring corresponds to the red coloured ring in the central scheme.

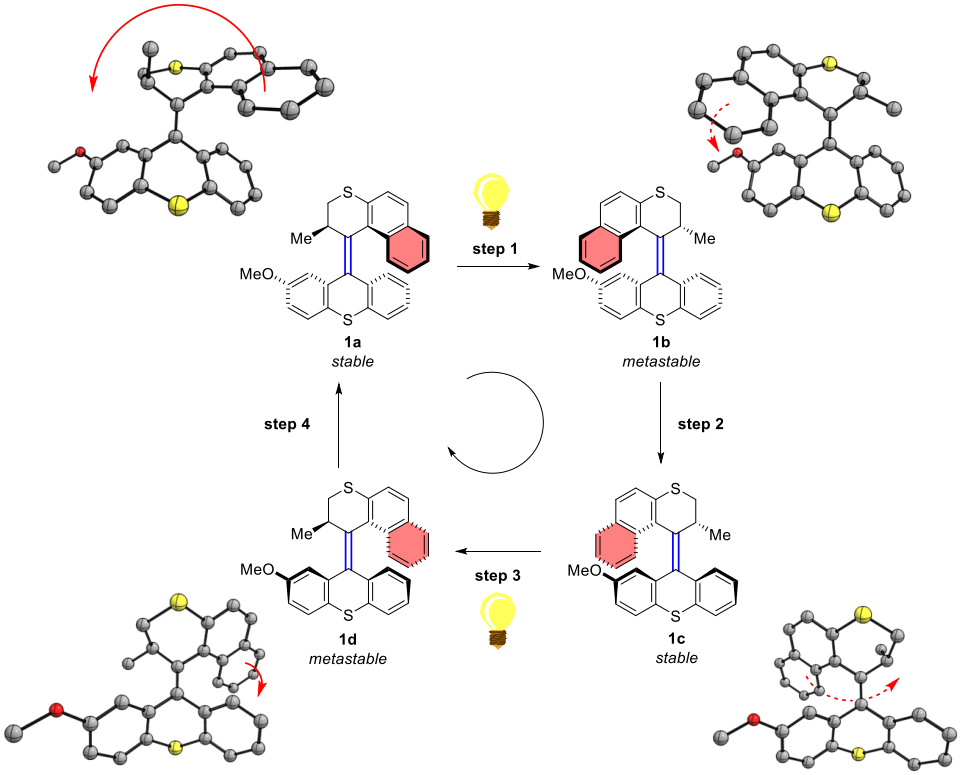

Figure 1. Rotation of a molecular motor.

In step 1, starting from **1a**, the top half moves with respect to the bottom half upon light irradiation, which is known as a photochemical *E*/*Z*-isomerisation. The interactions within the molecule make the newly formed conformation (**1b**) less stable, which is called the *metastable* state. With enough thermal energy (if the temperature is high enough) the molecule has sufficient energy to reorient to a more stable state and does so through a *thermal helix inversion* (THI, step 2). Which in our example in **1b** means that the red ring, pointed towards us, flips over the ring in the bottom half. This inverts the helix formed by these rings and importantly only goes in one direction (towards **1c**).

These two steps form a 180° rotation and repetition of these steps results in a full 360° rotation. Since the first discovery of molecular rotary motors, more molecules that share this property have been developed. Each modification of the molecule has an effect on all of these fundamental steps and influences what can be done with the molecule.

How rotary molecular motors work is described in Chapter 1, with a detailed look into both the photochemical step (e.g. steps 1 & 3) and the thermal step (e.g. steps 2 & 4). The effects that modifications of the molecules have on the functioning are discussed and a number of applications, such as influencing chemical reactions, are presented.

In Chapter 2 we synthesised new molecular motors with the introduction of an F atom or an alkyl group in order to develop a molecular motor that can operate with electricity instead of light. The positively charged versions of these molecules were not stable enough to achieve a molecular electromotor, but we have gained more insights in the requirements for such a motor.

Chapters 3, 4 and 5 are concerned with variations on bisthioxanthylidenes, a molecule (**2**, Figure 2) with two similar halves, consisting of three rings with a sulfur atom in the middle ring, connected by a C=C bond.

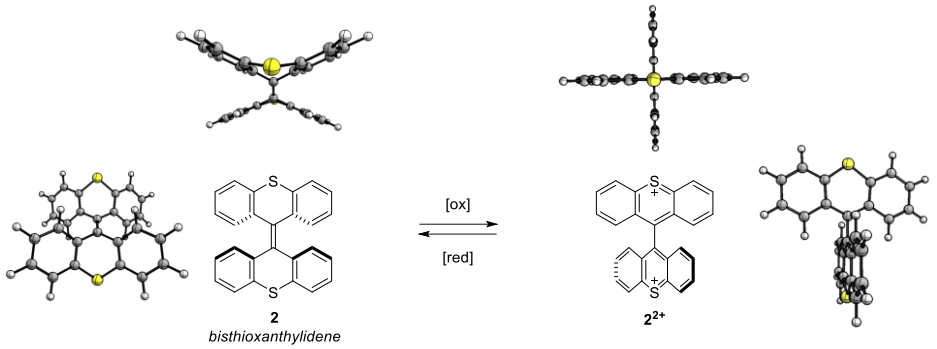

Figure 2. Bisthioxanthylidene, an electrochemical switch. Molecules presented with a 3D model of their front view on the side and a top view on top.

These *bisthioxanthylidenes* are interesting because of their shape and how this shape changes depending on the number of electrons in the molecule. When we oxidise this molecule, removing 2 electrons, the initially folded molecule (Figure 2, left) will adopt an *orthogonal* orientation where the two halves are flattened (Figure 2, right).

Chapter 3 presents a new synthesis method for these switches where they can be made in a fast way with a 20 minute reaction replacing two overnight reactions. With this reaction we have made a library of molecules with different substituents and shown that the electrochemistry of these switches is robust with the chosen variations.

Chapter 4 discusses molecules where a bridge is introduced between the two bisthioxanthylidene halves, consisting of a phenyl or anthracenyl group. This changes the geometries of the molecule and make it possible to observe a stable diradical, where two electrons are not paired up. On top of this radical state there are also a folded state and a dicationic state found as stable compounds. All of these states can be addressed selectively. This chapter mainly looks into the computational chemistry to understand what the folding and other geometry does to the molecular stability.

Chapter 5 has *bisthioxanthylidenes* with added arms with ligands, molecular parts that like to bind to metals. The synthesis of these new molecules is presented and we show that the electrochemistry of the core still functions normally. The addition of metals to the molecule have an influence on the fluorescence and, in one case, an influence on the geometry of the switch upon removing and adding electrons.

Further research presented in this thesis is concerned with other alkenes such as *isoindigo* (**3**, Figure 3) and *fluorenyl-helicene overcrowded alkenes* (**4**, Figure 3).

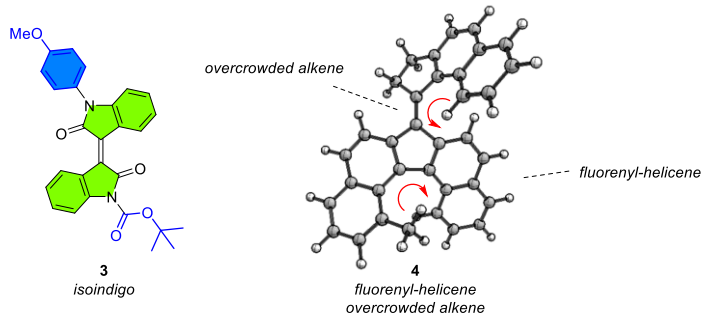

Figure 3. Isoindigo and fluorenyl-helicene overcrowded alkene.

Chapter 6 describes the computational method we developed, partly based on experimental data to understand the influence of substituents (blue) on the nitrogen atom of the isoindigo core (green). This method is developed to help to modify isoindigos to select the wavelength of light they absorb and how easy electrons can be added to them. This can be used, for example, to select the right molecules for the development of organic solar cells.

Finally, Chapter 7 investigated the synthesis and theoretical chemistry of *fluorenyl-helicene overcrowded alkenes*. These are molecules with a central alkene (C=C) bond with a lot of bulk around it. The bottom half is described as a fluorenyl-helicene as it is based on fluorenone and is helically chiral. This means that this shape has a helix that turns in a specific direction, as is the case in, for example, a screw. The whole molecule has two elements of helical chirality (the red arrows in Figure 3). The synthesis of the bottom half is given and we calculated the interactions of a number of examples of such molecules to investigate if we can use them as molecular switches or motors driven by either light or electricity.

Samenvatting (Nederlands)

Veel eigenschappen van objecten om ons heen, hoe ze eruit zien en hoe ze voelen, wat ze kunnen doen en wat we ermee kunnen doen, hangen af van hun moleculaire strucuur en activiteit. Het vasthouden en lezen van deze thesis bestaat uit beweging van spieren, licht dat reflecteert op de pagina en geregisteerd wordt via je ogen. Het hangt allemaal af van moleculaire eigenschappen en chemische reacties. Deze thesis presenteert een deel van het onderzoek dat chemici doen om nieuwe materialen en tools te ontwikkelen om invloed en controle te hebben op wat er gebeurt op de schaal van moleculen.

Moleculaire, unidirectionele motoren zijn moleculen die bewegen, in dit geval in één specifieke richting ronddraaien, als ze bestraald worden met licht. Figuur 1 illusteert een voorbeeld van zo'n moleculaire motor. Deze motor werkt met licht en warmte en draait rondom een centrale C=C as (aangegeven in blauw). Een 3D model van de moleculen is gepresenteerd ter verduidelijking, met rode pijlen die de richting van beweging van de ring aangeven. Deze ring correspondeert met de in rood aangegeven ring in het schema in het midden.

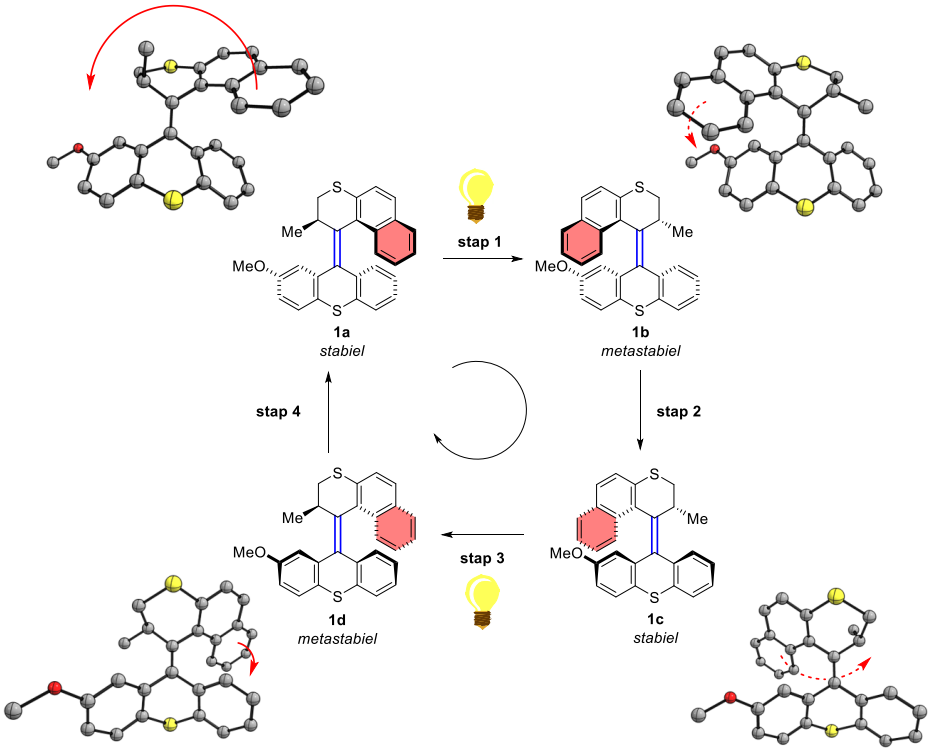

Figuur 1. Rotatie van een moleculaire motor.

In de eerste stap, vanaf **1a**, beweegt de bovenste helft ten opzichte van de onderste helft door bestraling met licht, wat we een fotochemische *E*/*Z*-isomerisatie noemen. De interacties binnen het molecuul zorgen ervoor dat deze nieuwe conformatie minder stabiel is, wat we de *metastabiele* staat noemen (**1b**). Met voldoende thermische energie (als de temperatuur hoog genoeg is) heeft het molecuul genoeg energie om naar een stabielere toestand te gaan en doet dit via een *thermische helix inversie* (stap 2). In ons voorbeeld vanaf **1b** beweegt de rode ring die naar ons toe wijst zich van ons af over de ring van de onderste helft. Dit draait de helix, gevormd door deze ringen, om. Belangrijk in deze stap is dat deze reactie uitsluitend in één richting gebeurt (naar **1c**).

Deze twee stappen leiden tot een 180° rotatie en een herhaling van deze stappen resulteert in een volledige 360° rotatie. Na de ontdekking van dit fenomeen, zijn er meer moleculen ontwikkeld die deze moleculaire rotatie laten zien. Elke verandering aan het molecuul heeft een effect op deze fundamentele stappen en heeft ook een effect op wat er met het molecuul kan worden gedaan.

Hoe deze moleculaire motoren werken is beschreven in hoofdstuk 1 met een gedetailleerde beschrijving van zowel de fotochemische (zoals stap 1 & 3) en thermische stap (zoals stap 2 & 4). Wat modificaties van het molecuul betekenen voor het functioneren is beschreven en een aantal toepassingen van moleculaire motoren, zoals het beïnvloeden van chemische reacties wordt besproken.

In hoofdstuk 2 hebben we nieuwe moleculaire motoren gesynthetiseerd met de introductie van een F atoom of een alkyl groep om een moleculaire motor te ontwikkelen die op elektriciteit werkt in plaats van licht. De positief geladen varianten van deze motoren waren niet stabiel genoeg om van een moleculaire electromotor te spreken, maar we hebben nieuwe inzichten gekregen voor verdere ontwikkeling van dit type motor.

Hoofdstukken 3, 4 en 5 betreffen variaties van *bisthioxanthylidenen*, een molecuul (**2**, figuur 2) met twee vergelijkbare helften, bestaande uit drie ringen met een zwavel atoom in de middelste ring, verbonden met een C=C binding. Deze *bisthioxanthylidenen* zijn interessant door hun vorm en hoe deze vorm verandert, afhankelijk van het aantal electronen in het molecuul. Als dit molecuul wordt geoxideerd, door 2 electronen eruit te halen, neemt de originele gevouwen vorm (figuur 2, links) een orthogonale vorm aan, waarbij de twee helften plat worden (figuur 3, rechts).

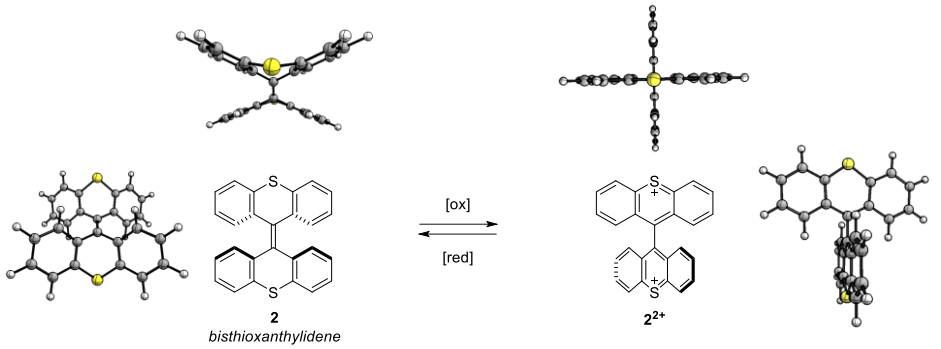

Figuur 2. Bisthioxanthylidene, een electrochemische schakelaar. Moleculen zijn gepresenteerd met een 3D model van een vooraanzicht aan de zijkant en een bovenaanzicht aan de bovenkant.

In hoofdstuk 3 wordt een nieuwe synthese methode gepresenteerd voor dit type schakelaar waarmee ze gemaakt kunnen worden met een 20 minuten durende reactie in plaats van twee reacties die elk een dag duren. Met deze nieuwe synthese hebben we een collectie van moleculen gemaakt met verschillende substituenten gemaakt en aangetoond dat de electrochemie van deze schakelaars robuust is met deze aanpassingen.

Hoofdstuk 4 gaat over moleculen waarbij een brug is geïntroduceerd tussen de twee helften van een bisthioxanthylidene, bestaande uit een fenyl of een anthracenyl groep. Dit verandert de geometrie van het molecuul en maakt het mogelijk om een stabiel biradicaal te hebben, waar twee electronen ongepaard zijn. Naast deze biradicale toestand zijn er ook een gevouwen toestand en een dicationische toestand te vinden als stabiele moleculen, waarbij al deze toestanden selectief te verkrijgen zijn. Dit hoofdstuk betreft voornamelijk de theoretisch chemische kant om te begrijpen wat de geometrie, zoals het vouwen doet met de moleculaire stabiliteit.

In hoofdstuk 5 worden *bisthioxanthylidenes* besproken met gekoppelde armen uitkomend in liganden, moleculaire onderdelen die graag aan metalen binden. De synthese van deze nieuwe moleculen wordt gegeven en dat het molecuul nog steeds als electrochemische schakelaar te gebruiken is wordt aangetoond. Het toevoegen van metalen aan het molecuul beïnvloedt de fluorescentie van het molecuul en in één geval ook de geometrie van de schakelaar tijdens het verwijderen en terug toevoegen van electronen.

Het verdere onderzoek in deze thesis betrekt zich op andere alkenen zoals *isoindigo* (**3**, figuur 3) en *fluorenyl-heliceen overvolle alkenen* (**4**, figuur 3).

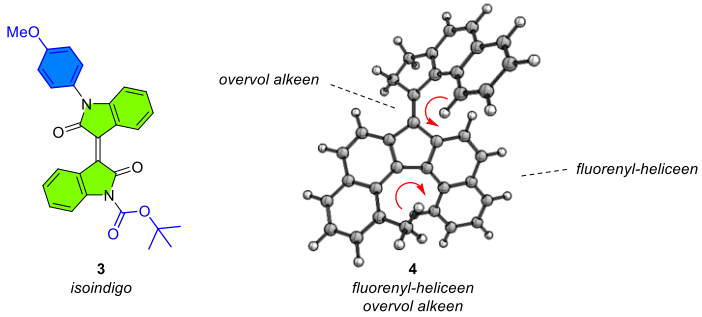

Figuur 3. Isoindigo en fluorenyl-heliceen overvol alkeen.

Hoofdstuk 6 beschrijft de computationele methode die we hebben ontwikkkeld, gedeeltelijk gebaseerd op experimentele data, om te begrijpen wat de invloed van substituenten op het stikstof atoom (blauw) is op de *isoindigo* kern (groen). Met de ontwikkeling van deze methode wordt het makkelijker om voor isoindigo's te kiezen wat voor golflengte licht ze absorberen en hoe gemakkelijk het is om electronen toe te voegen. Dit kan gebruikt worden in bijvoorbeeld organische zonnecellen.

Tot slot, wordt de synthese en theoretische chemie van *fluorenyl-heliceen overvolle alkenen* onderzocht in hoofdstuk 7. Dit zijn moleculen met een centrale alkeenbinding (C=C) met een grote hoeveelheid andere delen van het molceuul in de directe omgeving. De onderste helft kan worden beschreven als een *fluorenyl-heliceen* omdat het gebaseerd is op het molecuul fluorenon en het helische chiraliteit heeft. Bij helische chiraliteit heeft het molecuul een vorm met een draaiing in één vaste richting, zoals ook bij een schroef. Het gehele molecuul heeft twee elementen van helische chiraliteit (de rode pijlen in figuur 3). De synthese van de onderste helft is gepresenteerd en een aantal voorbeelden van dit type moleculen is onderzocht met berekeningen om te bepalen of ze gebruikt kunnen worden als moleculaire schakelaars of moleculaire motoren, aangestuurd door licht of elektriciteit.

Acknowledgements

After quite some years in Groningen there are many people who contributed to everything I have done here. So many in fact that I do not expect I will manage to construct a complete list of people in this acknowledgement. That does not take anything away from the fact that I am very grateful for all the good people around me. So firstly, to each and everyone who in any way added some positivity to the PhD journey; all the people mentioned here and also a great deal to everyone who I did not mention (or forgot to mention) here: thank you very much for everything!

Next, Ben, thank you for providing me with the opportunity to do all this research presented in this thesis. Over the years I have come to know you as an enthusiastic speaker and with a never ending, incredible amount of ideas. You truly have a strong passion for chemistry.

Sander, thanks for being my co-promotor. In the early times of my PhD you were the person to go to when there were things to ask and of course at the time many things were uncertain.

To the reading committee, profs. Nolte, Katsonis and Minnaard. I am very grateful that you took the time to go through my thesis.

My dearest paranymphs, Daisy & Cosima. Without holding back in sounding overly dramatic, there is not enough I can write in the back of my thesis to describe how much you have meant to me. In more down to earth terms, there should be many more songs written about you. Throughout the years, whenever there were good times and also, importantly, whenever there were bad times, you were there to share them and I thank you very much for that.

Tineke, the real boss around these parts. In my own mind, while writing this acknowledgement, two letters came bubbling up: EQ. I think these letters are fitting in two ways. On the one hand, in the meaning of emotional intelligence. On the other hand, EQ, in my audiophilic tendencies stands for equalizer, which can be used to provide a balanced tone and can remove sharp edges where necessary. Both are fitting as you provided compassion and balance to my experience in the group.

The invaluable lab managers, Romain & Anouk. I do not think that it would have been possible to finish this thesis without your help. You provided the required oversight in what was going on, what best to do and what direction the end of the tunnel was. I am sorry that many times when I came to your

office it was when there was something amiss. I hope our future encounters will be on more positive notes. Both your patience and understanding is praiseworthy.

Stefano, I think you would understand the detailed intricacies of a low grumbled sound with a meaningful look, a highly appreciated skill. Unfortunately, those are hard to get on paper. You helped me out of difficult situations many times and taught me a great deal of highly important things.

Filippo, you are a wise and kind man and a great listener. I am very grateful for your insights at the important moments. I think that most of the conversations we have had were in some way important to me, personally.

As I have spent so much time in the middle lab in 16, I have seen many people come and go. Firstly, Jana, my co-zaalassistent in the early days. I was happy to have someone else close by in the same lab who started on the exact same day. Then, Lotte, who was my next co-zaalassistent, thank you for helping me greatly in dealing with the problems that arose in the lab and keeping things manageable, especially in corona times. I hope the lab and the people stay manageable. Furthermore, I would like to thank everyone else with whom I have shared the lab. I have tried to provide people there with a balanced mix of music education with my proximity to the computer and I thank you all for letting me do this.

Rutger, we first met you as the quizmaster in a pubquiz and only later we found out that you were going to be the master student in our lab. Thanks for being my student as well, I have definitely learned from our interaction.

Marco, the man for electrochemistry in our group. Thanks for helping a lot with many bisthioxanthylidene related projects and your patience in holding electrodes in place.

I would also like to thank the people from downstairs, Wesley, Luuk, Jorn, for their insights in the many things that were up with the electrochemical mysteries. Wesley, thanks for your willingness to help and also for your insights on how things work in this institute.

To Renze, Monique, Hans, Pieter, Johan, you are all crucial parts of the research institute and I appreciate it very much that you were so helpful and approachable when trying to figure out what kind of molecules I was dealing with.

Verder wil ik ook iedereen van de BHV ploeg bedanken. Ik kijk nog steeds met een scherper oog naar situaties en naar wat er belangrijk is voor een veilige omgeving. Het gaf mij ook zeker een beter inzicht in wat er allemaal onmisbaar is in het runnen van een grote organisatie, maar veelal achter de schermen plaatsvindt.

Ik wil ook de mensen van de beveiliging en de receptie bedanken, omdat het altijd fijn was om iemand te groeten aan het begin en einde van een dag en soms even een praatje te maken.

To the well-spoken people from the lunchroom. Few things that were said there should be put into print, but these were often interesting insights in the human mind and a welcome and humorous escape.

To the climbing people, I enjoyed the frustrating attempts at difficult routes, the powering through heavy ones, the ostriches afterwards and the shared joy when things went well.

Johanna, thank you so much for all your support, the fun distractions and a very welcome amount of positivity. I am happy with all the good things we get up to, the delicious, the creative and the silly ones and whatever we will get up to in the future.

Finally I would like to express my appreciation to the collective of people who know what this means: Brian Buchannon, The Wizard of Gringard, The Climbing God, Protector of the Lab, Guardian of the Sonicator, Parter of the Party People.